

SOLPS Modelling of ELMing H-mode

THÈSE N° 4562 (2010)

PRÉSENTÉE LE 19 FÉVRIER 2010
À LA FACULTÉ SCIENCES DE BASE
CRPP ASSOCIATION EURATOM
PROGRAMME DOCTORAL EN PHYSIQUE

ÉCOLE POLYTECHNIQUE FÉDÉRALE DE LAUSANNE

POUR L'OBTENTION DU GRADE DE DOCTEUR ÈS SCIENCES

PAR

Barbora GULEJOVÁ

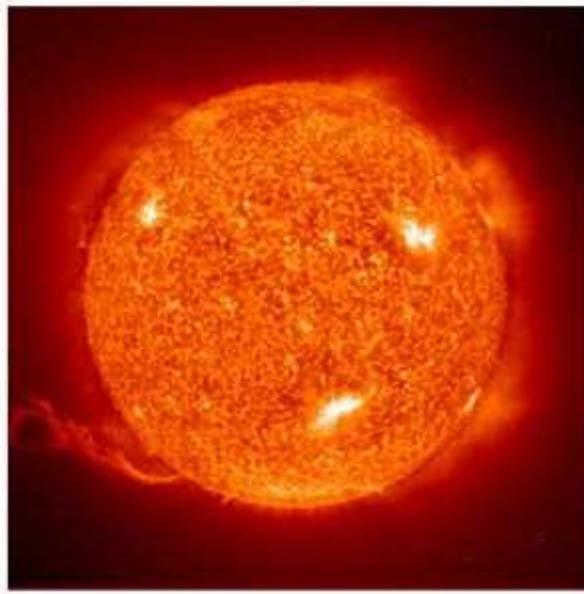
acceptée sur proposition du jury:

Prof. O. Schneider, président du jury
Dr R. Pitts, Dr O. Sauter, directeurs de thèse
Dr D. Coster, rapporteur
Dr J. Graves, rapporteur
Dr A. Kukushkin, rapporteur



ÉCOLE POLYTECHNIQUE
FÉDÉRALE DE LAUSANNE

Lausanne, EPFL
2010



I dedicate this thesis to all those who believe in fusion - clean energy of the future...

Contact: barbora.gulejova@epfl.ch

Abstract

Numerical simulation of the tokamak scrape-off layer (SOL) is an essential tool for the prediction of the conditions to be expected in future fusion reactors such as the ITER project, now under construction in Southern France. One particularly important issue regards the estimation of the expected transient power loads on plasma-facing components (PFC) due to magnetohydrodynamic plasma relaxations, known as Edge Localised Modes (ELMs). These loads are a major cause of concern for ITER owing to the very severe restrictions on PFC lifetime (especially the divertor targets) that they will impose if their amplitude is not maintained below a given size. Even though SOL plasma modelling has reached a comparatively high level of sophistication (the ITER divertor is being designed in part with complex edge plasma codes), the majority of simulations are performed for steady state conditions, necessarily excluding the description of transient events.

This thesis explores the utility and validity of the fluid plasma, Monte-Carlo neutrals approach to SOL and divertor modelling in the presence of time dependent ELM phenomena. It aims to test the most complex tool of this type currently available, the fluid (B2.5)-neutral Monte-Carlo (EIRENE) code package SOLPS5, against a variety of ELM sizes in two very different tokamaks, TCV and JET. Although the SOLPS package has been the modelling tool of choice for ITER design, it has not yet been systematically used for the study of ELM transients. A key element throughout is rigorous benchmarking – seeking the best possible agreement between both experiment and simulation and between different codes for the same experiment, using as many different measurements as possible to constrain the model. Such benchmarking attempts are still, unfortunately, comparatively rare on today's machines.

Fully time-dependent simulations (2-D plasma, 3-D neutrals) have been performed of four H-mode plasmas, two each on TCV and JET, covering Type III and Type I ELMs over a range of pedestal collisionality and energy expelled per ELM from $\Delta W_{\text{ELM}} \sim 0.005 \rightarrow 0.7$ MJ. The high end of this limit corresponds to the current maximum ΔW_{ELM} which is thought to be tolerable on ITER for acceptable divertor target lifetime. The two tokamaks differ radically in size, input power and divertor geometry, but share carbon as the main PFC material. The SOLPS5 simulations have thus been performed with all carbon charge states included but do not feature activated poloidal drift terms.

The approach is first to seek the closest match to experimental upstream, pedestal/SOL and downstream target profiles during the inter-ELM phase. This is achieved through the specification of radially varying perpendicular particle and heat diffusivities and/or convective radial velocity in order to account for the different transport levels in the edge and SOL regions. Poloidal variation of these transport coefficients is also applied to distinguish between main chamber SOL and divertor regions. This is important in a device like TCV with rather unconventional divertor geometry. Similar reasoning applies even more to the ELM itself, which is known to burst into the SOL in the outboard, unfavourable curvature region and is thus extremely poloidally localized. This has also been accounted for especially in the attempts to simulate the TCV ELM events.

The complexity of the ELM instability continues to prevent a complete theoretical description of the evolution of transport during the event. In SOLPS5, the simplest and currently only method by which the ELM can be simulated is to increase the anomalous transport coefficients used to simulate the pre-ELM state during a brief interval corresponding to the ELM duration, such that the total energy expelled during this time is compatible with that measured experimentally. In the case of TCV Type III ELM, where reasonable upstream and downstream data are available and for which the largest number of sensitivity studies have been performed in this thesis with SOLPS, agreement is good in the pre-ELM phase and reasonable, but less satisfactory during the ELM. This ELM is a largely convective event in terms of pedestal temperature collapse and is, by virtue of its low ΔW_{ELM} , the “least kinetic” of the four events studied. Nevertheless, comparison of the SOLPS5 simulation results at the divertor target with those from dedicated Particle-in-Cell kinetic transport code calculations for the same ELM, demonstrate that kinetic effects are important and must be properly accounted for (by appropriate adjustment of kinetic coefficients in the fluid simulations). This presumably becomes even more important as the ELM size increases, but can only be tested to the extent that the appropriate experimental data is available. As a consequence, the tentative conclusion from the work presented here is that the use of SOLPS in a predictive sense for ITER would at best provide indicative results.

In addition to the code-experiment benchmark, a code-code comparison has also been performed, checking SOLPS5 against published and well known time dependent Type I ELM simulations obtained with the dedicated JET code suite EDGE2D-Nimbus. A benchmark of this complexity has not previously been attempted and has been reassuringly somewhat successful, albeit with some unresolved discrepancies.

A key feature of ELM boundary physics occupying much current research are the energy deposition asymmetries observed at the targets, which favour the inner target during the ELM for forward toroidal field direction and which appear to reverse when the field direction is inverted. These trends are opposite to the behaviour seen in inter-ELM phases, behaviour which is conventionally understood to result from toroidal geometry and the contribution of poloidal drift physics. Added complexity comes from magnetic geometry, a prominent feature of the TCV-JET comparisons described in this thesis, the results of which seem to influence the simulation results (which do not include drift effects).

A recent development has been the suggestion that the ELM, in convecting plasma from pedestal to SOL regions, carries with it memory of the high toroidal rotation velocity known to characterise the H-mode pedestal on all devices. This hypothesis has been tested here in a preliminary manner, and for the first time in this kind of simulation, by imposing a toroidal velocity inside the magnetic separatrix in the simulations and studying the radial transport of this toroidal momentum into the SOL. Applied in the first instance to the TCV Type III ELM, the indications are that transfer of this rotation into the SOL can drive target asymmetries in the direction seen experimentally, though there are significant negative consequences for the resulting target profiles in other parameters for which a potential resolution would require protracted further study which has not been possible here.

Keywords: physics, plasma, fusion, tokamak, TCV, JET, numerical simulations, modelling, scrape-off layer, ITER, edge localised modes (ELMs), fluid, kinetic, SOLPS, B2.5, EIRENE, benchmark, pedestal, diffusive, convective, instability, transport, Particle-in-Cell, EDGE2D/Nimbus, target asymmetry, toroidal rotation

Version abrégée

Les simulations numériques du scrape-off layer (SOL) sont un outil essentiel afin de prédire les conditions attendues pour les futurs réacteurs de fusion tels que le projet ITER dans le sud de la France. Une question particulièrement importante s'intéresse à l'estimation des charges transitoires subies par les composants faisant face au plasma (PFC) et qui sont dues à des relaxations magnétohydrodynamiques du plasma connues sous le nom de Edge Localised Modes (ELMs). Ces charges sont une importante source d'inquiétude pour ITER en raison des très sévères limitations de la durée de vie des PFC (en particulier pour la cible du diverteur) qu'elles peuvent entraîner si leur amplitude n'est pas maintenue au-dessous d'un certain seuil. Même si la modélisation du plasma dans le SOL a atteint un certain niveau de sophistication (le diverteur d'ITER est conçu en partie à l'aide de complexes codes de plasma du bord), la majorité des simulations sont effectuées pour des conditions d'équilibre qui nécessairement excluent la description des événements transitoires.

Cette thèse explore l'utilité et la validité de la modélisation du SOL et du diverteur avec une approche fluide pour le plasma et Monte-Carlo pour les neutres en présence de phénomènes d'ELM dépendants du temps. Le but est de tester l'outil le plus complexe de ce type à l'heure actuelle, l'ensemble de codes SOLPS5 fluide pour le plasma (B2.5) et Monte Carlo pour les neutres (EIRENE) pour une variété de tailles d'ELM dans deux tokamaks très différents, TCV et JET. Même si l'ensemble de codes SOLPS5 a été choisi comme outil de modélisation pour le design d'ITER, il n'a pas encore été utilisé systématiquement pour l'étude des ELM transitoires. Un point crucial est le benchmarking en cherchant la meilleure correspondance entre l'expérience et la simulation, de même qu'entre différents codes pour la même expérience, en cherchant à imposer des contraintes au modèle en utilisant le plus grand nombre possible de mesures. Ce genre de tentatives de benchmarking sont malheureusement encore rare pour les machines actuelles.

Des simulations dépendantes du temps (plasma 2D, neutres 3D) ont été effectuées pour quatre plasmas en mode H, deux chacun pour TCV et JET, en couvrant les types d'ELM III et I sur un intervalle de collisionnalité au piédestal et d'énergie expulsée par ELM de $\Delta W_{\text{ELM}} \sim 0.005 \rightarrow 0.7$ MJ. La borne supérieure correspond au courant maximum ΔW_{ELM} que l'on pense tolérable pour ITER afin d'avoir une durée de vie acceptable pour la cible du diverteur. La taille, la puissance injectée ainsi que la géométrie du diverteur des deux tokamaks diffèrent radicalement, par contre le matériel utilisé pour les PFC est du carbone dans les deux cas. Les simulations avec SOLPS5 sont donc effectuées pour tous les états de charge du carbone inclus mais sans les termes de dérive poloïdale.

L'approche consiste en premier lieu à chercher la meilleure correspondance avec les profils cible en amont, en aval et sur le piédestal/SOL pendant la phase inter-ELM. Ceci est effectué en spécifiant les diffusions perpendiculaires des particules et de la chaleur qui varient radialement et/ou la vitesse convective radiale dans le but de tenir compte des différents niveaux de transport pour les régions du bord et du SOL. Une variation poloïdale de ces coefficients de transport est aussi utilisée afin de distinguer le SOL de la chambre principale et la région du diverteur. Ceci est important dans une

machine telle que TCV qui possède une géométrie atypique pour la région du diverteur. Le même raisonnement s'applique de manière encore plus prononcée pour l'ELM en lui-même. Il est connu pour se répandre dans le SOL de la région extérieure où la courbure est défavorable et il est donc extrêmement localisé. Il en a été tenu compte spécialement pour les tentatives de simulations des ELM de TCV.

La complexité de l'instabilité des ELM continue d'empêcher une description théorique de l'évolution du transport durant l'événement. Dans SOLPS5, la plus simple et actuellement la seule méthode qui permet de simuler des ELM est d'augmenter les coefficients du transport anomal qui sont utilisés pour calculer l'état pre-ELM pendant un bref intervalle correspondant à la durée de l'ELM de façon à ce que l'énergie qui est éjectée pendant ce temps est compatible avec les résultats expérimentaux. Dans le cas des ELMs de type III dans TCV, où des données raisonnables en amont et en aval sont disponibles et pour lequel le plus grand nombre d'études de sensibilité ont été effectuées dans cette thèse avec SOLPS, l'accord est bon dans la phase pre-ELM et raisonnable mais moins satisfaisant pendant l'ELM. Cet ELM est un événement largement convectif en terme d'effondrement de la température au piédestal et est, grâce à son ΔW_{ELM} qui est bas, le « moins cinétique » des quatre événements étudiés. Par contre, la comparaison des résultats obtenus avec SOLPS5 sur la cible du diverteur et ceux simulé à l'aide de code cinétique de transport Particule-in-Cell montre que les effets cinétiques sont importants et qu'il faut en tenir compte convenablement (en ajustant de manière appropriée les coefficients cinétiques dans les simulations fluides). Cela devient certainement encore plus important quand la taille de l'ELM augmente mais ne peut être testé qu'en disposant des données expérimentales appropriées. De ce fait, la conclusion tentante du travail présenté ici est que l'utilisation de SOLPS dans un esprit de prédiction pour ITER devrait au mieux fournir des résultats indicatifs.

En plus du benchmark code-expérience, une comparaison code-code a aussi été effectuée en vérifiant SOLPS5 avec la suite de codes EDGE2D-Nimbus dédié à JET et qui a obtenu des simulations publiées et bien connues d'ELM de Type I dépendantes du temps. Un benchmark de cette complexité n'avait pas été tenté auparavant et a été d'une certaine manière réussi, même si les raisons de certaines différences n'ont pu être identifiées.

Un point important de la physique des limites de l'ELM qui intéresse plus la recherche de nos jours est l'asymétrie de la déposition d'énergie observée sur les cibles qui favorise la cible intérieure pendant l'ELM dans la direction du champ toroïdal et qui apparaît opposée quand cette direction est inversée. Cette tendance est contraire au comportement observé durant les phases inter-ELM et qui est conventionnellement compris comme le résultat de la géométrie toroïdale et de la contribution de la physique des dérives poloïdales. Une complexité additionnelle vient de la géométrie magnétique, un sujet saillant des comparaisons entre TCV et JET décrites dans cette thèse, qui influence les résultats des simulations (qui ne contiennent pas d'effets de dérive).

Un développement récent est de suggérer que l'ELM, en convectionnant le plasma de la région du piédestal à celle du SOL, porte en lui la mémoire de la haute vitesse de rotation toroïdale connue pour caractériser le piédestal du mode H dans toutes les machines. Cette hypothèse a été testée de façon préliminaire et, pour la première fois dans ce genre de simulations, en imposant une vitesse toroïdale à l'intérieur de la séparatrice magnétique dans les simulations et en étudiant le transport radial de ce

moment toroïdal vers le SOL. Dans un premier temps, en appliquant ceci aux ELMs de type III dans TCV, les indications sont que le transfert de cette rotation vers le SOL peut mener à des asymétries sur les cibles dans la direction observée expérimentalement. Pourtant les profils obtenus pour les cibles dépendent significativement d'autres paramètres dont la résolution nécessiterait une longue investigation ce qui n'a pas été possible ici.

Mots clés : physique, plasma du bord, fusion thermonucléaire, tokamak, TCV, JET, simulations numériques, scrape-off layer, ITER, ELM, SOLPS, B2.5, EIRENE, benchmark, transport , diverteur

Contents

1. Introduction	15
1.1. Fusion - clean energy for the future	15
1.1.1. Current world energy situation	15
1.1.2. Currently available energy options – part of the solution	16
1.1.3. Thermonuclear fusion – principles and advantages	17
1.1.4. History and future of fusion	20
1.2. Tokamak- principles of magnetic plasma confinement	21
1.2.1. Tokamak efficiency	23
1.2.2. Plasma heating	24
1.3. Edge, scrape-off layer and divertor plasma	25
1.3.1. Limiter, X-point, Divertor	26
1.3.1.1. Modes of divertor operation	28
1.3.2. Edge transport barrier, H-mode	29
1.4. Motivation and aim of thesis	31
 2. SOL and edge plasma physics	 33
2.1. Fluid vs. kinetic treatment of plasma	33
2.1.1. Kinetic treatment of tokamak plasma	33
2.1.2. Fluid treatment of tokamak plasma	34
2.2. Parallel transport	39
2.2.1. Sheath boundary conditions	40

2.2.2. Heat flux limiters	43
2.2.3. Power deposited on divertor surfaces	44
2.3. Perpendicular transport	45
2.3.1. Perpendicular energy flux	47
2.3.2. Perpendicular transport of parallel momentum and viscosity	49
2.4. Volumetric processes in plasma and plasma-surface interactions	51
 3. Edge localized modes (ELMs)	 53
3.1. ELM classification	55
3.2. Current understanding of the ELM phenomenon	56
3.2.1. ELM cycle	57
3.2.2. Observations and theories of the ELM formation	59
3.2.2.1. Ideal MHD instability model- Model of Type I ELM	59
3.2.2.2. Resistive MHD instability model – Model of Type III ELM	61
3.2.2.3. Precursors of Type I and Type III ELMs	62
3.3.3. Observations and theories of ELM filament dynamics	63
3.3.3.1. ELM filament dynamics from closed to opened field lines	66
3.3.3.2. ELM filament transport models	67
 4. Modeling tool - SOLPS	 69
4.1. SOLPS5.0	70
4.1.1. Geometry	72
4.1.2. B2.5	74

4.1.2.1. Justification and limitations of the fluid description	74
4.1.2.2. Flux limiters	75
4.1.2.3. Anomalous cross-field transport description	76
4.1.2.4. Running B2.5	77
4.1.2.5. Impurities, Radiation	79
4.1.3. Neutrals	80
4.1.3.1. EIRENE	81
4.1.4. B2.5-EIRENE coupling	82
4.1.5. SOLPS hardware	83
 5. Experiment	 85
5.1. TCV and JET experiment	85
5.2. Diagnostics at TCV and JET	90
5.2.1. Diagnostics at TCV	90
5.2.2. Diagnostics at JET	96
 6. Simulations of ELMing H-mode at TCV	 99
6.1. Type III ELMing H-mode at TCV	99
6.1.1. Experiment	99
6.1.2. Settings, inputs, boundary conditions	100
6.1.3. Determination of anomalous transport coefficients	102
6.1.4. Simulations of inter-ELM phase	104
6.1.4.1. Diffusive approach	105

6.1.4.2. Convective approach	108
6.1.4.3. Targets	111
6.1.4.4. Energy analysis	116
6.1.5. Simulations of Type III ELM at TCV	119
6.1.5.1. Time-dependent phenomena in SOLPS5.0	119
6.1.5.2. ELM model with SOLPS5.0	120
6.1.5.3. Diffusive vs. convective approach	124
6.1.5.4. Simulations of targets	131
6.1.5.5. Time-dependent signals	135
6.1.5.6. Comparison with kinetic simulations	142
6.1.5.6.1. Ion vs. electron target power fluxes	148
6.1.5.6.2. The influence of flux limiters	152
6.1.5.7. Energy analysis	157
6.2. Type I ELMing H-mode at TCV	161
6.2.1. Settings	162
6.2.2. Simulation of Type I ELMing H-mode at TCV	163
6.2.2.1. Energy analysis	166
6.3. Toroidal pedestal rotation	171
6.3.1. Features of target power asymmetry in SOLPS	171
6.3.2. Toroidal pedestal rotation	172
6.3.2.1. Toroidal pedestal rotation in SOLPS	173
6.3.3. Simulation of TCV Type III ELM with toroidal pedestal rotation	174

7. SOLPS simulations of JET ELMing H-modes	179
7.1. SOLPS-EDGE2D-NIMBUS benchmark of JET Type I ELMing H-mode	179
7.1.1. SOLPS vs. EDGE2D/NIMBUS	179
7.1.2. Experiment and settings	180
7.1.3. Results of the benchmark exercise	183
7.1.4. Target power loads	188
7.1.5. Energy analysis and radiation	189
7.2. H-mode with large Type I ELMs at JET	193
7.2.1. Simulation of large Type I ELM at JET	195
7.2.2. Energy analysis and radiation	201
7.3. Simulations of JET ELM with toroidal pedestal rotation	205
 Summary and conclusions	 209
 References	 215

1. Introduction

1.1. Fusion – clean energy for the future

1.1.1. Current world energy situation

The technological society of today is powered by energy. By historical standards, the world in which we live has only just begun to consume it. The revolutions in industry, agriculture, medicine and hygiene have brought about an increase of the global population during the last four centuries by an incredible factor of ten! United Nations forecasts indicate that the present population of 6.5 billion people will grow to a value in the range 8-13 billions over the next 50 years. This unprecedented increase in population coupled with rising prosperity in the developing world, means that the global demand for energy continues to grow year by year. In the developing regions such as Asia and Africa, where the energy use per person is about one tenth of that in western world, economic development is urgently needed to improve their very low standard of living. The energy use required, especially in China and India, is increasing very fast. Despite the efforts of the industrialized nations to reduce their energy consumption, the worldwide energy demands are expected to double or even triple in the next half of the century [1].

The discovery of fossil fuels – gas, coal and oil – offered to humankind the huge reservoir of concentrated energy, created by nature during many millions of years from the remains of dead plants and animals. Presently, fossil fuels provide 80% of world total energy consumption. If nothing changes, we will have consumed in two hundred years most of the fossil resources accumulated over hundreds of millions of years. Currently known oil reserves are predicted to last no longer than half century [2-3]. The weakness of our present energy system, which is dominated by fossil fuels, is being highlighted ever more by the serious consequences, which are the major threats of our planet. Of particular concern is the significant increase of the dependency on energy imports from the foreign countries with scarce fossil sources and thus further addiction to fossil fuels. According to a Green Paper of European Commission [4] where the future energy supply is discussed, Europe currently imports about 50% of its energy and unless action is taken, this fraction is predicted to rise to 70% by 2030. Fossil fuels are not distributed evenly around the world; oil and gas in particular are extremely localized, with, for example, about 70% of all oil located in the Middle East. Such dependency holds great potential for international tensions, or even wars. “Energy independence” therefore implies “energy security” and represents one of the crucial needs of many countries.

Most crucial in the short term, however, is the environmental issue. Heavy use of fossil fuels has damaging effects, such as acid rain and smog in cities, with the resulting impact on health. Considerably more serious, however, is the release of carbon dioxide (CO₂) as a result of fossil fuel consumption, which retains the heat of the earth in the atmosphere through the greenhouse effect. It is now widely recognized scientifically that this is responsible for most of the current global warming trend and will be the cause of

(possibly catastrophic) further temperature increase, The recently released report issued by the International Panel on Climate Change (IPCC) of the United Nations [5], states that “the chance that the rise in temperature since 1950 is not caused by human interference is considered to be less than 10%”. In the last century, the average temperature on earth has risen by 0.6° C, while over the past 50 years the rise in temperature has taken place twice as rapidly as in the previous 50 years. If we do not curb our use of fossil fuels, this century will possibly see a temperature rise of up to 5.8°C. The temperature increase has a variety of consequences for the environment on the Earth, namely extreme weather conditions, such as heavy storms, rains, intense heat waves, change of ocean currents, rising sea levels, diminishing biodiversity etc. Needless to say, that the economic consequences of this are considerable. A global average temperature increase of greater than 2-3 degrees is generally considered to be highly threatening. To avoid exceeding this limit, CO₂ emissions will have to be reduced drastically - by at least 60-70% in the coming fifty years [6]. According to scientific predictions, the acceptable concentration of CO₂ is not more than 550 ppm, double of what was before the industrial revolution.

The world has entered a new “era of consequences and responsibility”. The future energy system must change completely, requiring a transition to low-carbon economy. The major challenge is to provide the population with affordable, clean and safe energy sources. There is no single solution to this challenge. No alternative energy source can currently fully replace fossil fuels. All viable energy sources that can contribute to a sustainable energy mix should be developed as soon as possible and supported with the appropriate allocation of funds.

1.1.2. Currently available energy options – part of the solution

The options, likely as a solution only for the first half of this century, are following: energy conservation, switching to renewable energy sources, increasing the share of nuclear energy for the generation of electricity and capturing CO₂ from power stations.

The most promising alternative options for transport are battery-powered electric vehicles and the use of hydrogen fuel generated by splitting water, recombining it to release energy in fuel cells or burning it directly. This will have the effect of increasing electricity demand, and its share in energy demand, particularly in developed countries.

Renewable energy sources such as biomass, solar, geothermal and wind energy have experienced rapid development over recent years, and have a great potential to contribute to a CO₂-free energy system, especially in the first half of this century. Hydropower is the largest renewable source: it provides over 17% of the world's electricity. Most of the suitable locations for hydropower have already been exploited, so the growth of renewable sources will have to come mainly from the rest of the sources, which currently contribute to only about 1% to the world energy demand. When considering their potential contribution to energy supply, the fact that renewable energy technologies suffer from isolated availability and are variable in nature is often neglected. Moreover, they are subject to sudden local climate change and require complex

management of the electricity supply network and often the additional cost of accompanying energy storage. They can make a large contribution in countries with a distributed population and lack of electricity network, but they can make only a minor contribution to the energy demand in regions currently occupied by the developed nations. According to the most optimistic predictions, they may be able to supply at most around 50% of the energy demands in 2100 [2-3].

Nuclear power, currently producing about 15% of the world's electricity (almost 7% of worldwide energy [7] demand), is the technology of nuclear fission. Long half-life nuclear waste (millions of years), transport of radioactive materials and fear of accidental release of radioactive material (e.g. Chernobyl) remain disadvantages even if nowadays the technology has reached a high level of technical advancement, safety and reliability. According to the predictions, the reserves of uranium are limited. Technology of new generation of fission reactors with breeders consuming most of their own high level waste is under development, but has risks and leads to the proliferation.

The development, acceptability and economics of CO₂ sequestration are still uncertain and it is not cheap technology. The increased energy requirements of capturing and compressing CO₂ significantly raises the operating costs of CCS (Carbon Capture and Storage) equipped power plants. Moreover there are additional investment or capital costs. The process increases the fuel requirement of a plant with CCS by about 25% for a coal-fired plant and about 15% for a gas-fired plant [1]. The cost of this extra fuel, as well as storage and other system costs are estimated to increase the costs of energy from a power plant with CCS by 30-60%, depending on the specific circumstances [8]. After all, the fact is that even with possibility of CO₂ capturing the fuel supplies are limited and thus the CO₂ sequestration is no long term solution.

1.1.3. Thermonuclear fusion – principles and advantages

Are there other options for clean and safe energy production? Fortunately yes: Thermonuclear Fusion - the energy which powers our sun and stars. In fact, all matter present in the universe was at one time formed by fusion of the lightest element, hydrogen. In the sun, hydrogen is converted into helium by fusion, providing enough energy to keep the Sun burning and to sustain life on Earth.

Fusion is one of the most promising technologies for both economic growth and sustainable environment. This safe, environmentally responsible and long-term energetic option has the potential to produce electricity continuously, on a large-scale and with competitive cost in the range predicted for the cost of renewable energy sources. In comparison to renewables, fusion is particularly suited for the centralized supply of base-load electricity all day and every day, rain or shine, without additional cost of storage. Fusion would be an ideal complement to other intermittent renewable sources in a sustainable and safe energy mix.

In an EU Green Paper published in 2000 – ‘Towards a European strategy for the Security of energy supply’ [4] and a progress report published in 2005 [3], the long-term role of fusion is recognized: ‘Thermonuclear fusion also bodes well for the future and could take over the reins from some existing energy sources towards the middle of the century’.

How does it work? Fusion is the “opposite” process to nuclear fission, in which neutrons split heavy nuclei into smaller components, leading to the production of further neutrons and a chain reaction. In fusion two light nuclei fuse together to form a larger one. From all possible reactions of light elements, the best candidate for the terrestrial fusion (the highest cross-section at the lowest temperatures) is between the two heavy isotopes of hydrogen, deuterium and tritium (**Fig.1.1**). The reaction generates a nucleus of helium (alpha particle) and a fast neutron with high kinetic energy. Approximately ~ 17.6 MeV of energy released by this reaction can be used to heat water or other medium and run electric power producing turbine generators. In fact, the half of percent of hydrogen mass is converted to this released energy according to Einstein’s equation $E=mc^2$, relating mass and energy.

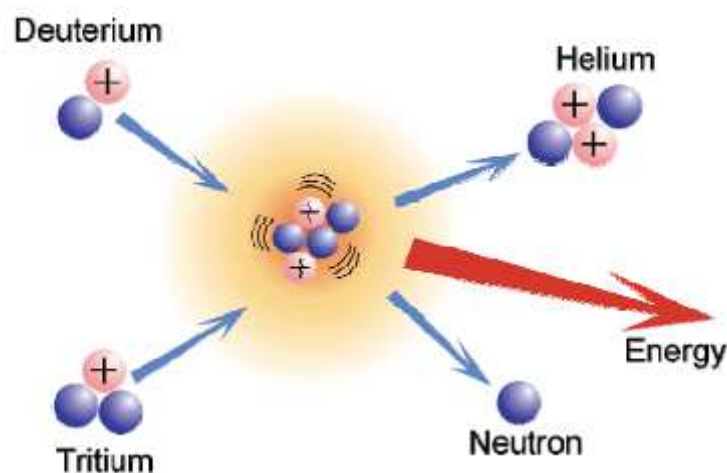


Figure 1.1. Schematic of fusion reaction

Both nuclei have a positive electric charge and therefore repel each other. In order to overcome the electrostatic repulsion and bring the nuclei close enough to fuse, they need to move very rapidly. This can be achieved at extremely high temperatures e.g. ~15 million degrees in the sun or in the range 100-150 million degrees in a terrestrial fusion reactor. Even at much lower temperatures, the initially gaseous fuel atoms are stripped of their electrons to form a gas of independently moving charged particles. This “soup” of charged particles is the fourth state of matter and is called “plasma”. It represents more than 99% of total mass of matter in the universe. The extremely strong gravitation force holding plasma in the Sun is substituted by strong magnetic force acting on the particles fusing in the ‘artificial suns’ on the Earth, the fusion reactors. The most advanced concept of such a reactor is called TOKAMAK, described in section 1.2.

Fusion offers several attractive advantages compared to the other alternative or conventional sources of energy.

Quasi- unlimited energy source: The fuels of this practically limitless source of energy are available abundantly everywhere around the globe in large enough quantities for millions of years of energy supply. These heavy forms of hydrogen (especially deuterium) are freely accessible for all nations. Each litre of ordinary water contains about 33 milligrams of deuterium, which can be easily extracted using electrolysis. If

fused with tritium, that is equivalent to some 340 liters of gasoline. Tritium is radioactive and has a half-life of about 10 years, which means that it disintegrates very rapidly. Therefore, it is hardly found in nature and has to be produced artificially. Inside a fusion reactor, tritium is produced from lithium, a light metal, which is used for example in batteries. The earth's crust contains enough lithium for thousands of years of energy supply at the present world wide level, and the world seas also contain a huge supply of lithium. The energy released from fusion reactions is enormous. To illustrate: the lithium from 1 laptop battery combined with deuterium from 100 litres of water can produce 200 000 kWh of energy, covering the electricity use of an average European citizen over 30 years. This corresponds to the energy released from the combustion of about 40 tons of coal. To operate for a whole year generating about 7 billion kWh of electricity, D-T fusion plants would use just 100 kg of deuterium and three tonnes of lithium.

CO₂-free energy source: Second crucial feature of fusion is its cleanliness. There are no CO₂ emissions, no long-lived nuclear waste and the ash of fusion, Helium, is an inert, non-radioactive and harmless gas. Typical coal-fired power station devours 3 millions of tones of fuel and produces some 11 millions of tones of CO₂ to yield the same annual output as fusion power plant.

Inherently safe energy source: Fusion being an opposite process to fission, doesn't involve a chain reaction. Therefore, no runaway reaction (explosion) is possible. In the reactor volume of 1000 m³ or more, there will be only 2g of fuel enough for just a few seconds of operation. The fuel must be continuously supplied to the fusion reactor. If fuel supply is closed, reaction stops and any deviation from normal conditions lead to its slowing down. Even in the worst possible in-plant driven accident scenario, the risk to the general public would be below the level at which evacuation of the area around the power plant is required. The highly energetic neutrons produced by fusion reactions can activate the structural materials of the vessel. However, the use of low-activation materials can limit the half-life of the resulting waste to about 10 years, what means, that after 100 years their radioactivity drops to a value of one 10.000th of its initial value (what is comparable to that of ash from coal power station) and they can be recycled. Even though Tritium is radioactive, it is produced inside of the reactor and no transport outside the plant is needed. Half-life of about 10 years is negligible compared to Uranium or Plutonium, fission reactor fuels.

Competitive price of fusion electricity: The most important conclusion of independent studies on economic aspect of electricity generated by nuclear fusion is that the cost will be comparable to that of electricity generated by other sustainable energy sources. According to European Fusion Power Plant Conceptual Study (PPCS) released by EFDA in April 2005 [9], the cost of future fusion electricity is estimated from the models to 5-10 Eurocents per kWh. This falls to the range of expected future costs of other renewable sources. The important economic asset is that most of the cost relates to capital amortization. The cost of fuel would represent a negligible percentage of the total cost of which at least 70% is an initial investment. Moreover, 'external costs' such as those associated with environmental damage or adverse impacts upon health, which are substantial part of coal-fired plants, are not included in cost of fusion plant. Unlike the fossil fuels-based electricity, which cost is dominated by the cost of primary fuels, fusion-based electricity is not expected to be very sensitive to economic or political events.

1.1.4. History and future of fusion

In 1920, Sir Arthur Eddington, English astronomer, was the first to propose that fusion of hydrogen powers the sun. In 1938, 18 years later, Hans Bethe, calculated the exact way, in which the protons in the sun fuse together to form helium. In 1950 the first small experiments were constructed to study magnetically confined plasmas, of the size that could easily fit on the top of the table. In sixties the ‘tokamak era’ was born. At the first world fusion conference, ‘Geneva Atoms for Peace Conference’, organized by International Atomic Energy Agency IAEA and held in United Nations in 1958, the fusion research was declassified. After it was understood that the minimal size that was thought to be sufficient for the fusion reactor was too small, a new generation of large-size tokamaks came into operation in late seventies and early eighties, including the European machine JET the experiments of which are one of the subjects of this thesis. In 1985 in Geneva and idea of international effort to develop fusion energy for the benefit of all mankind was launched by agreement between US President Reagan and General Secretary Gorbachev of the Soviet Union. In 1988 the design for the next generation machine ITER (International Thermonuclear Experimental Reactor) [10], was started between Europe, Russian Federation, Japan and the USA. Unfortunately, the design presented in 1998 was considered too expensive by the partners, and a reduced-cost design was requested. A smaller and less expensive version of ITER, but with the same overall scientific objectives, was designed and approved in July 2001. The ITER Agreement was officially signed at the Elysée Palace in Paris on 21 November 2006 by Ministers from the seven ITER Members. ITER is truly worldwide effort, including China, the European Union, India, Japan, Korea, Russia and the United States, representing over half of the world's population. ITER means the ‘the way’ in Latin and it is the biggest and most exciting global research project, and the first to demonstrate that it is possible to produce commercial energy from fusion. The partners of ITER project finally decided that the facility will be built at Cadarache in France. The construction will take about 10 years and it is scheduled to power up in 2019. ITER is designed to produce 500 MW of fusion power, while only 50 MW is required as an input for heating the plasma, which means an energy gain of a factor of ten. Compared to the largest fusion reactor existing today, JET, the plasma volume of ITER is almost ten times larger, which makes it easier to keep the plasma confined for a longer time. ITER aims to be the first fusion experiment to produce net thermal power and will open the path towards fusion-based power plants. In October 2008 at 22nd IAEA Fusion Conference in United Nations in Geneva fusion community celebrated the 50th anniversary and the fact that after the efforts of scientists worldwide, fusion is ready to move out of the laboratory. The construction of ITER, which will be followed by a twenty years research program, started in 2008 in Cadarache.

After ITER, a next step called DEMO is foreseen: a fusion power reactor that will demonstrate tritium self-sufficiency and first large-scale electrical power production. The so-called “fast-track” approach (proposed by EU Council Presidency in 2001) with testing of appropriate plasma-facing materials in parallel with development of prototype power plant DEMO/PROTO could achieve net electricity production about 35 years after the decision to construct ITER, after which commercial deployment of fusion energy

could start. If development steps are performed sequentially instead, the time to net electricity production will be extended to about fifty years.

During the last few decades, enormous scientific and technological progress has been achieved in research of nuclear fusion. This rapid progress is comparable to that of computer chips, described by Moore's law. The so-called 'triple product' measuring the performance of the fusion plasma doubled every 1.8 years while the number of transistors on computer chips doubles every 2 years. The increase of the triple product during last thirty years represents factor of 10.000 and only another factor of 6 is needed to attain the level required for power plant [11].

According to the predictions fusion has potential to cover upto 35 % of the world's electricity in 2100. The models, investigating the future energy scenarios show that the role of fusion in the energy market during this century will greatly depend on measures to reduce CO₂ emissions. For a reasonable emission limitations (at an average reduction of CO₂ emissions) fusion may provide up to 20% of the electricity requirements in 2100 [12].

Fusion being an extremely complicated technology, unfortunately suffers from the lack of awareness and interest by mainstream media, politicians and public. As a consequence of the combination of these factors it has been delayed by approximately 20 years. Despite of that the fusion power has a potential to arrive exactly at the time when the need will be the highest.

1.2. Tokamak –principles of magnetic plasma confinement

Since there are no materials that can withstand extremely high temperatures of fusion plasma, it is important to isolate it from the walls of the fusion reactor. Therefore strong magnetic field is used, with the magnetic field lines closing in themselves without touching the walls. The plasma charged particles are forced to spiral around the magnetic field lines run around in the circles for thousands of kilometers without ever encountering the wall as in a 'magnetic cage'. This approach called "magnetic confinement". Another way of producing fusion is an inertial confinement [13], where the fusion reaction is initiated by heating and compressing a fuel target typically in form of pellet containing mixture of D and T by using high-energy beams of laser light. So far it has been attractive for its possible military applications unlike the magnetic confinement fusion which is in addition usually considered more promising for energy production. The most advanced magnetic confinement approach is so far the fusion device called tokamak, what is a Russian acronym for 'toroidal chamber with magnetic field coils'. The plasma is heated in a ring-shaped toroidal metallic container (vessel) and kept away from the vessel walls by applied and self-generated magnetic fields (unlike another magnetic confinement concept, stellarator with only applied magnetic fields). In a magnetic field, charged plasma particles are forced to spiral along the magnetic field lines. This is necessary also to avoid the cooling down of plasma by contact with wall materials and stopping the fusion process. Moreover, the isolation of the plasma minimizes the release of impurities from the vessel walls into the plasma that would contaminate and further cool the plasma by radiation. The tokamak principle is illustrated schematically in **Fig.1.2**. From

geometrical point of view there are two parameters characterizing the size of each tokamak, the major radius of the torus, R and the minor radius, a defining the plasma cross-section.

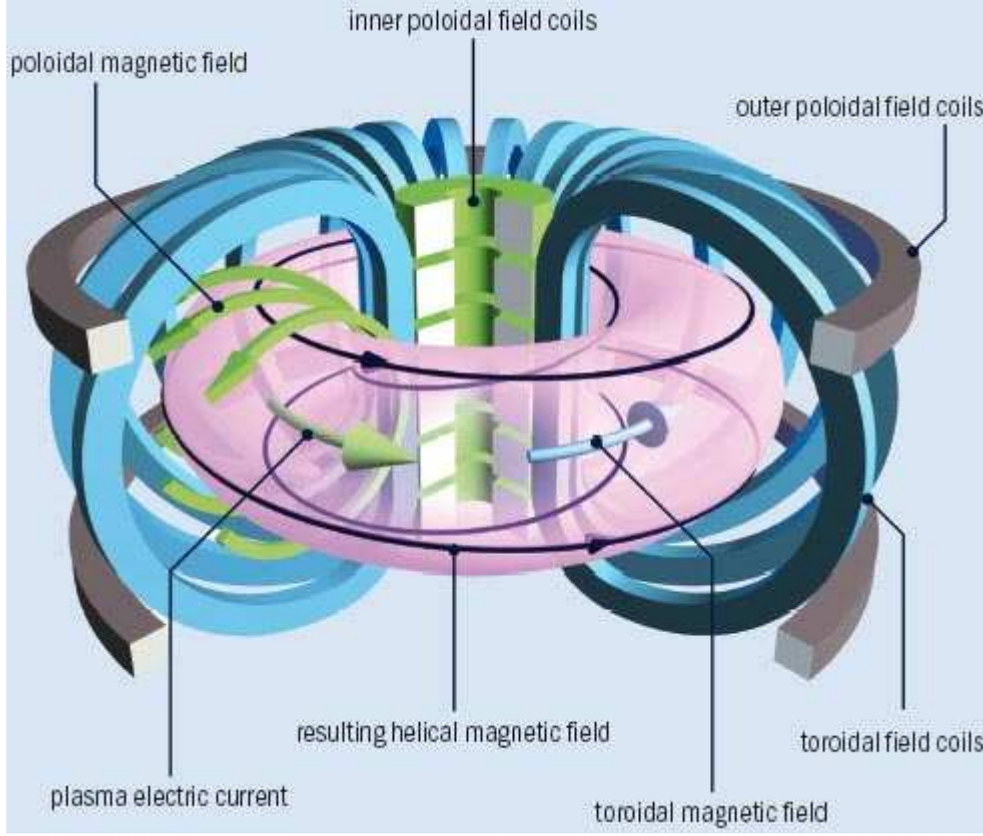


Figure 1.2. Tokamak principle Extracted from [14].

The magnetic field has toroidal (B_Φ) and poloidal (B_θ) components, which together form a resulting helical field (B).

$$\vec{B} = \vec{B}_\Phi + \vec{B}_\theta \quad (1.1)$$

The toroidal field, which guides the particles around the torus (“long way”), is maintained by magnetic field coils surrounding the vacuum vessel. The toroidal field provides the primary mechanism of confinement, but cannot confine the plasma on its own. The radial decay of the toroidal field ($B_\Phi \sim 1/R$) results in the $\vec{V}B \times \vec{B}$ drift [15] which causes the charge separation. This generates a vertical electric field which leads to radial movements of the plasma column through $\vec{E} \times \vec{B}$ drift. A poloidal field must therefore be added, guiding the particles around the plasma cross section (“short way”):

$$B_\theta \approx \frac{\mu_0 I_p}{2\pi a} \quad (1.2)$$

It pinches the plasma away from the walls and maintains the plasma's shape and stability. The helical field, characterized by a pitch angle, θ_{pitch} enables a single field line to cover almost the entire doughnut-shaped surface.

$$\theta_{\text{pitch}} \approx \frac{B_{\theta}}{B_{\phi}} \approx \frac{B_{\theta}}{B} \quad (1.3)$$

It plays an important role in particle and energy deposition on the plasma facing components (PFC) especially divertor plates (see section 1.3.1). The number of toroidal rotations made by a given field line in order to complete one poloidal rotation is expressed by the so-called safety factor and can be written, in the large aspect ratio (R/a), circular approximation as:

$$q = \frac{rB_{\phi}}{RB_{\theta}} \quad (1.4)$$

The poloidal field is induced both internally, by the toroidal plasma current driven in the plasma, I_p (which is induced by the coils passing through the centre of the torus representing the primary winding of the transformer), and externally, by coils that are positioned around the perimeter of the vessel. The powerful toroidal plasma current acts as the secondary winding of the transformer and can reach high values (e.g. up to 7MA has been reached on the one of the largest tokamaks JET and up to 17 MA will be possible on the next generation device, ITER, with I_p on the order of 21 MA being required in most tokamak reactor designs).

The neutrons without electric charge escape the confining field and are captured in the walls of the tokamak. They carry the most of the energy released by fusion reaction and by collisions with walls generate heat, which is removed by the coolant (i.e. helium or water). In real fusion power plant this will flow to the heat exchanger to produce steam powering the turbine coupled to electrical generator as in conventional power station.

1.2.1. Tokamak efficiency

The ratio of fusion power to the input power required to raise the plasma temperature for fusion reaction to run, so-called “fusion gain” Q_{DT} . If the fusion power exceeds the power required to heat and sustain the plasma, the “breakeven” is achieved ($Q_{DT}=1$). Future power plants aim to attain of course much higher values of Q_{DT} (e.g. ITER $Q_{DT}=10$) and if fusion reaction becomes self-sustained, plasma ignites and $Q_{DT}=\infty$. In order to achieve a power-generating fusion reactor and ensure that plasma exceeds “breakeven”, the so-called Lawson Criterion (formulated in 1955 by British scientist John Lawson) must be satisfied by ensuring that product of pulse duration and plasma density exceeds a given threshold for a fixed temperature. More usual expression used nowadays for fusion reactors is given as:

$$Tn\tau > 3.10^{28} \text{ Km}^{-3}\text{s} \quad (1.5)$$

The product of plasma temperature T , central density n and energy confinement time τ (measure of how long the energy in the plasma is retained before being lost) on the left side of Eq.1.5 is so-called “triple product”. The confinement time increases dramatically with plasma size because large volumes retain heat much better than small ones. An ultimate example is Sun whose energy confinement time is massive. The number of fusion reactions per unit volume is roughly proportional to the square of the density.

Therefore the density of fuel ions must be sufficiently large for fusion reactions to take place at the required rate. For sustained fusion to occur, the following plasma conditions need to be maintained simultaneously:

- ✓ T: 100-200 million °C (for D-T reaction to occur at JET over 100 million °C is needed, other fusion reactions (e.g. D-D, D-He³) require even higher temperatures).
- ✓ τ : 4-6 s
- ✓ n : $1-2 \times 10^{20} \text{ m}^{-3}$ (approximately 10^{-3} g.m^{-3} , i.e. one millionth of the density of air)

A significant fraction of losses in magnetically-confined plasma is due to radiation. The fusion power is also reduced if the fuel is diluted by impurity atoms or by the accumulation of Helium ions from fusion reaction itself. In order to achieve high enough temperatures required for fusion, different heating methods are used in research devices as described in section 1.2.2. However, the next step machine ITER and the commercial fusion reactors will require the self-heating.

The alpha particles (He⁴) (second product of fusion reaction apart from neutrons) are confined by magnetic field and transfer their energy to the plasma fuel ions (D, T) through Coulomb collisions. If this process, called **alpha-heating**, is sufficient to maintain the density and temperature of plasma at required levels by itself, the fusion reaction becomes self-sustained. This condition is called ignition and is six times more demanding than the condition for breakeven in terms of confinement time and plasma density.

The effectiveness of the fusion reactor in terms of fusion power density is expressed by the measure of plasma pressure normalized to the magnetic field strength, β . Fusion power density varies roughly as β^2 at constant magnetic field and in configurations with externally driven plasma current as $(\beta/(I/aB))^4$ where the fraction of so-called bootstrap current, I_B is constant. I_B is a net current, which occurs due to the banana-shaped orbits of particles in the plasma with strong density and temperature gradients. This bootstrap current plays an important role in the advanced scenario of the future power plant, where it dominates over the plasma current driven by pulsed solenoid. By avoiding the inefficient and expensive cooling down of plasma between the pulses of I_p tokamak becomes economically viable.

1.2.2. Plasma heating

The basic heating which is generated naturally in tokamak plasma is the **ohmic heating** produced by the strong toroidal plasma current I_p . This current inherently resistively heats the plasma electrons and ions by collisions in the toroidal direction. In order to increase the confinement and of the plasma thus performance of the reactor several forms of additional (external) heating are used.

One way to transfer energy to plasma particles in general is to provoke their collisions with the neutral atoms (in fusion reactor D or T) of high energy which are injected into the plasma. Accelerated beams of energetic ions are neutralized before injection into the plasma in order to be able to penetrate the confining magnetic field. This is called **neutral beam injection** heating (NBI) and, for example at JET, can deliver an additional heating power in excess of 20 MW.

Another method is **electron-cyclotron resonance** heating (ECRH). Electromagnetic waves of a frequency matched to rotation frequency of the electrons, spiraling around the magnetic field lines in tokamak, are able to resonate its wave power into the plasma particles. This heating system has advantage of being localized at a particular location in the plasma. Energy is transferred to the plasma at the precise location where the electromagnetic waves resonate with the ion/electron rotation.

1.3. Edge, scrape-off layer and divertor plasma

Most of the field lines in the tokamak are so ‘**closed**’, because they reside on magnetic flux surfaces which do not intersect any of the solid surfaces bounding the tokamak plasma. However, close to the walls, some of the magnetic field lines intersect the solid materials of the vessel at some location and the particles following these field lines are guided into collisions with the first wall and deposit their energy onto the plasma-facing material. These are ‘**open**’ field lines. The volume entirely filled by the closed field lines is called **confined volume**. Particles escaping this region comprise the ‘**plasma exhaust**’. The border of the confined region is known as the **Last Closed Flux Surface (LCFS)** or **separatrix (Fig.1.3)**. The narrow region outside this border, usually only few cm wide, is the area where the plasma is essentially scraped off from the core plasma. In this so-called **Scrape-Off Layer (SOL)**, all magnetic field lines are open and particles reaching these field lines will directly intersect material surfaces. This region of tokamak between the solid materials of the vessel walls and the main plasma volume, often referred to as **plasma edge**, is a considerably researched area of fusion plasma physics, which studies the phenomena related to the existence of the opened field lines at the edge of the confined plasma volume. However edge plasma is used in the fusion community mostly to discuss the plasma inside the separatrix (in the pedestal region for H-mode plasmas –see section 1.3.2; and where most of the radiation occurs for L-mode). The properties of plasma edge control the power and particle exchange between the burning plasma and the vessel walls.

The behavior of plasma edge and SOL is strongly coupled with the **plasma-wall interaction**. The plasma-facing components (PFC) are subject to **particle and heat fluxes** that strike the first wall continuously and transiently in bursts (see chapter 3). They lead to **erosion**, releasing surface material into the plasma where it acts as an **impurity**, which can migrate into the core plasma, causing radiation loss and plasma fuel dilution. Eroded impurities can also be confined in the SOL plasma, often migrating to locations remote from the point of release. The main mechanism for plasma erosion is **sputtering** [16], of which two main types can be distinguished. Physical sputtering, is the process by which atoms from material surfaces are ejected due to the bombardment by energetic plasma ions and neutrals (with energy above the sputtering threshold energy). Chemical sputtering occurs through the chemical reactions of the wall material and plasma. It is a particular problem when carbon is used as first wall material (as it is in both of the tokamaks studied in this thesis TCV and JET) – deuterium ions and neutrals react readily with carbon to form hydrocarbons with sputtering yields generally much higher than those common to physical sputtering (more details see in chapter 2).

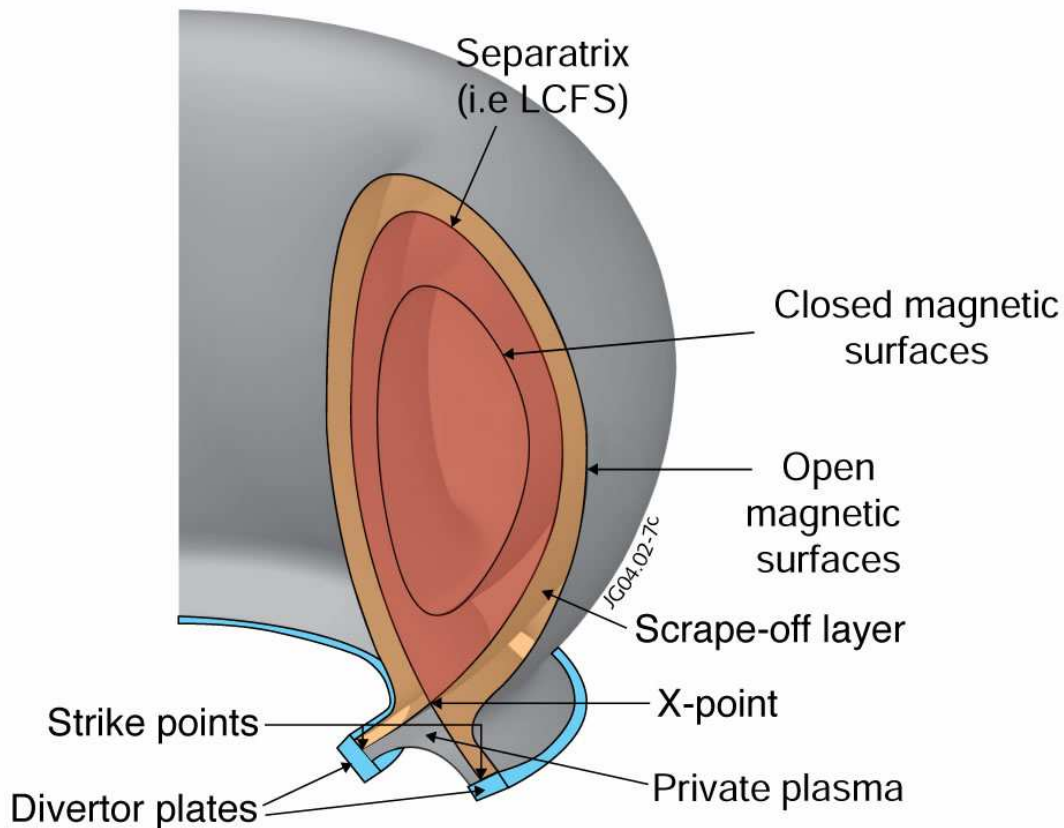


Figure 1.3. Geometry of field lines in tokamak [3]

At sufficiently high energy densities, **melting** (for metals) or sublimation (for carbon) of solid material can occur, causing very rapid erosion of the surface. High ion fluxes on metals can cause blistering. Another potential source of local wall erosion is **arcing**, which occurs when the electric potential between plasma and first wall materials exceeds a critical level.

1.3.1. Limiter, X-point, Divertor

The fusion processes in burning plasma must be protected from the cold reactor components. To guarantee sufficiently high plasma purity, low fuel dilution and the highest performance, the plasma-wall interaction must be localized and controlled. This is achieved in a tokamak by forcing the interaction to occur at specific material surfaces which then define the last closed flux surface and separate open from closed magnetic surfaces. In the historically earlier and simpler option, objects called **limiters** are placed on the walls to limit the confined region by defining the LCFS (**Fig.1.4**). This concept has two main disadvantages. Firstly, material released by impact of the plasma on the limiter can penetrate straight into the core and degrade its properties. Secondly, most of the ionisation occurs inboard of the LCFS in a limiter configuration. As a result, the very

high T_e and T_i at the plasma edge (due to the absence of local ionization cooling) causes too high power fluxes at limiters. These are unacceptable for fusion reactor, unless strongly radiating edge is used, which in turn requires injection of extrinsic impurities degrading core performance. A third important problem of limiter configuration is that only L-mode (see section 1.3.2) can be obtained and therefore a very large size of machine would be required to gain back confinement through the size.

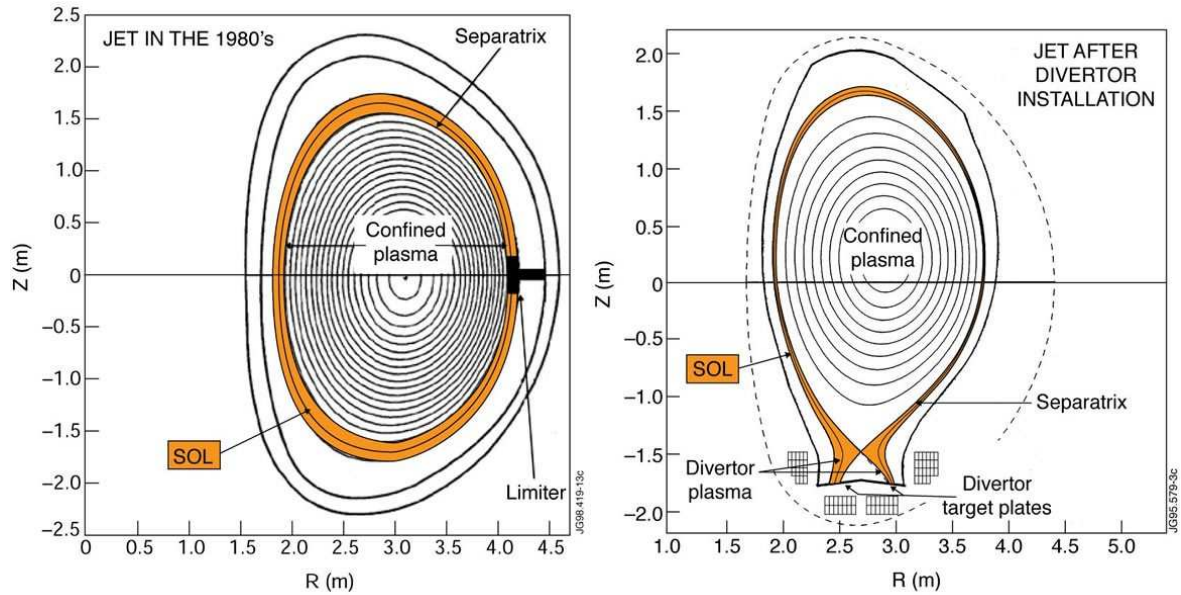


Figure 1.4. Example of limiter and divertor configurations from the JET tokamak ([3])

Most tokamak designs (including TCV and JET, which are the main focus of this work (see Chapter 5), and ITER) opt for more a sophisticated solution developed more than 20 years ago. This concept is based on the modification of the magnetic field lines at the plasma edge, so that the field lines of the SOL are diverted into a region more remote from the confined plasma, where the plasma-surface interaction and particle exhaust are localized. This configuration is achieved by using the poloidal magnetic field coils or even dedicated internal coils to generate an ‘X-point’ (see Fig.1.3), where the poloidal magnetic field is zero. The resulting magnetic field topology is also referred to as a **divertor** configuration (see Fig.1.4). The region of SOL adjacent to the confined plasma is defined as **upstream** and the region neighbouring the target plates **downstream**. The intersections of the separatrix with divertor plates are called **strike points**. An important advantage of divertor over limiter is that the materials facing the plasma exhaust are not generally in direct contact with the main plasma, reducing the probability that impurities released by the plasma-wall interaction can penetrate to the core. In addition, the use of a divertor generates regions of amplified particle recycling (see Section 1.3.1.1), in which cold neutral gas cushions can naturally develop, reducing charged particle fluxes to the divertor plates and assisting in power handling. Moreover, this high recycling region improves in turn impurity screening, making it harder for eroded material to reach the confined plasma. This reduction of particle and energy flux is known as divertor detachment (see section 1.3.1.1) and will be mandatory on the ITER

tokamak and future DEMO reactors if the high steady state power flux densities that will be experienced there are to be maintained within engineering limits.

The weak poloidal field near the X-point (zero-field point) forces magnetic field lines in this region to make many transits around the torus before terminating on the divertor targets. This long particle residence time promotes energy loss (due to collisions with ions, neutrals and electrons), assisting in divertor action. The path of the exhaust particles along a field line from their entry point in the SOL to their intersection with a solid surface is known as the **connection length**. In the symmetric divertor configuration with the equal distances from X-point to the both targets it can be approximated as:

$$L_{\text{con}} \approx \pi R q \approx \pi a B_{\theta} / B_{\phi} \quad (1.6)$$

The distance along magnetic field in the SOL between 2 points of contact with the solid surfaces is $\sim 2.L_{\text{con}}$. In divertor configurations, this path is longest for the particles residing in the immediate proximity of the separatrix (since in this region the field lines pass closest to the magnetic field null). In fact, the X-point represents the perpendicular projection of a field line with zero pitch. The connection length can be very long (from target to target at separatrix $\sim 30\text{m}$ in TCV, $\sim 60\text{m}$ in JET, $\sim 200\text{ m}$ in ITER). This results in the cooling down the plasma at the targets what allows electrons and ions to recombine to neutral atoms and locally extinguish the plasma ‘flame’.

1.3.1.1. Modes of divertor operation

There are different modes of the divertor operation, depending principally on the SOL density, input power, connection length and divertor geometry. If the plasma density in SOL (and core) is low, input power high and/or the connection length short, the plasma temperature remains high from upstream to downstream regions and most of the power entering SOL reaches the strike point regions. Under these conditions, the plasma sheath (see chapter 2) controls the exhaust of power and particles to the targets. In this so-called **sheath-limited regime**, the heat is simply proportional to the product of the particle flux and temperature at the sheath entrance.

For constant SOL input power, as the plasma density is raised, the plasma flux to the targets rises. An increase in density in the SOL affects the plasma collisionality which leads to finite electron conduction and thus to a temperature drop. This promotes an increased energy loss through ionization and excitation. In addition the increased recycling due to the flux amplification near the targets occurs also (charged particles encountering solid first wall recombine on the surfaces). This increases the convective flux and temperature dependence and adds to the conductive temperature drop. This is called **recycling regime**. The temperature drop may be further enhanced by presence of the impurities (due to increased radiative losses) or extending the connection length between upstream and downstream. Since the pressure (being proportional to the product of the density and temperature) is constant along the each particular field line, the downstream density increases as temperature at the targets drops. Even though the power flux to the targets is still controlled by sheath, it is reduced with temperature drop. In contrast to sheath limited regime more energy is dissipated volumetrically.

If plasma density is increased even further the number of charged particles reaching divertor plates diminishes to negligible levels. The release of impurities and subsequent radiation losses drop, temperature decreases and recombination forming neutrals occurs over a large volume and measured particle flux at the target plates drops by more than an order of magnitude. Neutrals transporting the residual power and particles deposit these over broad areas reducing the peak values to acceptable levels for materials to sustain the bombardment. Neutral particles can create a ‘cloud of gas in the divertor region’ what can cause that plasma becomes completely separated from the solid surface, the regime referred to as **divertor detachment**. With the low temperatures in the divertor a region of high neutral pressure can develop and this enables helium ash to be pumped out efficiently. Such a removal of the exhaust is crucial for the functioning of a reactor. If plasma is not detached, is it referred to as attached.

1.3.2. Edge transport barrier, H-mode

Most of the particles in the plasma are **transported parallel** to magnetic field lines due to their natural feature to follow the field lines (see section 2.2). However, there are processes which force plasma particles to leak out from the confined volume, and diffuse across the magnetic field. Particles enter the SOL only by this **cross-field transport** which occurs at low rates compared with transport along the field lines (see section 2.3). They may leave the confined volume simply due to the fact that their orbit around each field line has a finite radius or they can ‘jump’ from one guiding line to another due to collisions with other plasma particles or due to fluctuating electric fields causing so called turbulent cross-field transport.

At fixed temperature the fusion rate is proportional to the square of pressure. One can basically distinguish between two different operation modes. The case when the pressure falls off smoothly to zero at the edge of the plasma is referred to as low confinement mode (**L-mode**). When the pressure drops off very steeply at the edge, and is uplifted elsewhere by the ‘height’ of this drop, high-energy confinement mode (**H-mode**) is achieved. This regime is a ITER operation baseline scenario. H-mode is associated with strong edge transport barrier (ETB), the region of very high pressure gradient near the plasma edge which is naturally produced by X-point configuration. This barrier against cross-field transport significantly reduces the turbulent transport of particles onto the open field lines thereby increasing the density and temperature of the core plasma. The different upstream profiles of plasma density and temperature in H-mode and L-mode are depicted in **Fig.1.5**.

Despite of much progress made over the past two decades in the description of an H-mode, an understanding of the basic mechanisms that lead to an H-mode is one of the a major topics of fusion research around the world.

The improved confinement and high performance provided by insulation at the edge in H-modes comes at the price of violent energy emissions from the plasma, that can heat surfaces to several thousands degrees in a fraction of a second. The strong pressure gradients across the H-mode transport barrier can lead to instabilities and strip off the outer layer of the plasma and throw out violent bursts of particles and energy, which are thus ejected out of the region of closed field lines. These bursts, called **Edge Localized Modes (ELMs)** are double-edged swords. On one hand, they help particles to escape the

plasma and would inhibit the accumulation of helium ash in a working reactor. On the other, if they are not controlled, they would erode the plasma-facing surfaces too rapidly for a power plant to be viable. The subject of ELMs is addressed in detail in chapter 3.

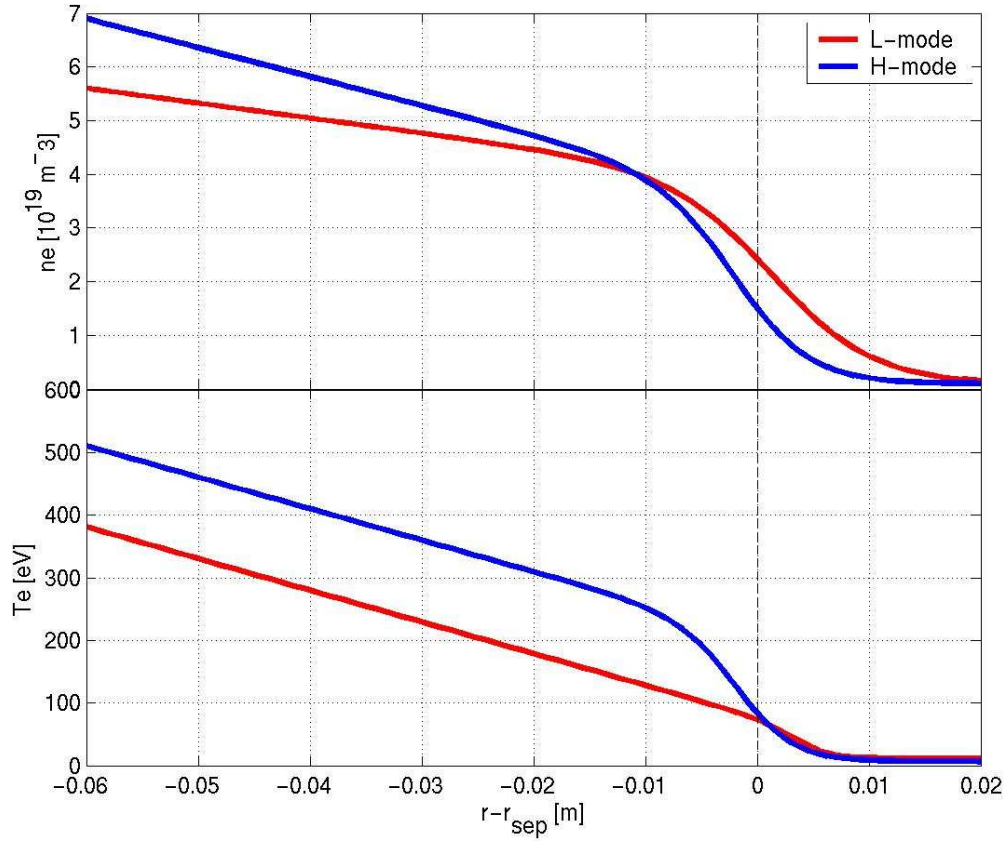


Figure 1.5. Upstream radial profiles of density and temperature of typical L-mode (red) and H-mode (blue) at TCV tokamak.

1.4. Motivation and aim of thesis

Fusion is one of the future energy options, which can play an important role in the sustainable energy mix. There are nevertheless several issues to be resolved both by the new next step device ITER and by ongoing research in the period of its construction. Of particular interest is the physics in probably the most complex region of a fusion reactor where plasma physics and surface/atomic physics meet: the scrape-off layer (SOL) and divertor plasmas. Understanding SOL transport and plasma-wall interaction is extremely important as they determine the particle and power exhaust, plasma fuelling and the erosion rate of the first wall materials and thus set the boundary conditions for the confined plasma.

A powerful instrument for both improvement of understanding the plasma edge and prediction of the conditions to be expected in ITER, is numerical modeling. Although the code packages to simulate the SOL plasma are still slightly simplified in terms of the true physical situation, they are ever more sophisticated and in many cases are able to capture the experimental observables. The biggest and most complex edge plasma physics code package, the SOLPS suite [17], has long been used for simulations of the ITER divertor and SOL [18]. However, attempts to carefully match the code output against experimental data for specific tokamak discharges on today's machines are still relatively scarce. And still, the comparison with real experimental measurements is a crucial element in the validation of any numerical modeling. Benchmarking of the different codes against each other is an equally important task, checking the overall level of consistency of the codes which solve the same problem with different numerical schemes. This is particularly important for SOLPS4, which is the principal edge modeling tool used to predict the ITER divertor performance [19]. A good level of agreement between simulation and experimental data from present machines significantly contributes to the building of the confidence of predicting the future tokamak operation.

The ELMs, associated with transient power loads on plasma-facing components (PFCs), represent an issue which is one of the major concerns for ITER. Their transport in SOL has been lately subject of considerable research activity [20]. If ELM-size scalings derived on the basis of today's experiments prove to be correct, ELM-target interactions will cause unacceptable divertor target erosion and thus significantly reduce the expected lifetime of the ITER divertor [21- 22]. As a result, much research on present devices is focused on ELM elimination or mitigation. Understanding these modes, from formation to interaction with the divertor targets and first wall surfaces, is a critical element in devising mitigation strategies and in quantifying the level of material interaction (and hence component lifetime) to be expected in the ITER Baseline operating scenario.

Even though several numerical codes have tried to model the ELMs transiently, they have been so far rarely used for modelling of SOL and divertor part of the tokamak plasma during these events. This thesis represents one of the first attempts to do so by extensive time dependent SOLPS simulations of ELMs. This work aims to address the key question of whether fluid codes such as SOLPS can be reliably used to model high energy kinetic transient events.

2. SOL and edge plasma physics

The introduction of the important terms and definitions of the edge and SOL plasma was given in the section 1.3. This chapter aims to describe the basics of SOL and edge plasma physics needed for understanding of the work presented in this thesis. The special focus here will be of the physics treatment of the particles and heat transport in this region on tokamak plasma.

2.1. Fluid vs. kinetic treatment of plasma

In general, magnetically confined plasma can be treated either as a fluid or as kinetic ionized gas which is associated with electro-magnetic fields. These two approaches are applicable in different conditions and for different phenomena and are described in more details in the following text.

2.1.1. Kinetic treatment of tokamak plasma

If plasma is viewed as an ionized gas, the kinetic treatment is fundamental in the description of its motion. Kinetic treatment of plasma can be imagined as a combination of the simple kinetic theory of gases, electromagnetic effects and collisions of the charged particles. If the plasma is in thermal equilibrium, velocity distributions are Maxwellian. In plasma treated as kinetic phenomenon, discrete particles with non-thermal velocity distributions can be included in the plasma description if non-Maxwellian behaviour is present.

Plasma motion in toroidal magnetically confined systems generally evolves in three orthogonal directions: parallel (\parallel), diamagnetic (\wedge) and radial (\perp), where the flux surfaces are defined by \parallel and \wedge directions. In a toroidally axisymmetric system, \parallel and \wedge can be combined into single poloidal direction and thus the problem of plasma transport can be treated only in two directions, poloidal (θ) and radial (\perp). However, for simplification throughout this thesis the parallel and poloidal terms are used with the same meaning and the diamagnetic direction is omitted. The geometry of SOL transport is discussed in [16, 23-24]. Most of the equations stated in this section are closed in the direction parallel to magnetic field, a simplification originating from the fact that in most cases the transport along the field lines dominates the transport across them. Cross-field transport plays an important role in tokamak plasma and especially in the SOL (see section 2.3.).

The equations describing the kinetic approach are known as Fokker-Planck-Poisson system [25]. The Fokker-Planck equation is

$$\left(\frac{\partial}{\partial t} + v_{\parallel a} \nabla_{\parallel} + \frac{e_a (\vec{E} + \mathbf{v}_a \times \vec{B})}{m_a} \cdot \nabla_{\mathbf{v}} \right) f_a(s, \mathbf{v}_a, t) = \sum_{b \in (e, i)} \vec{C}_{ab} + \vec{S}_a \quad (2.1.)$$

and the Poisson equation is

$$\nabla_{\parallel}^2 \phi = -\nabla_{\parallel} E_{\parallel} = -4\pi(e_e \int f_e dv_e + e_i \int f_i dv_i) \quad (2.2.)$$

where s is parallel distance, ϕ is electrostatic potential and v_a , e_a , m_a and f_a the velocity, charge, mass and distribution function of species a (electrons or ions), respectively. $\sum \bar{C}_{ab}$ is term due to inter-species collisions other than events where the particles appear or disappear and \bar{S}_a represents the net volumetric source (+) or sink (-) of the particles. The term $e_a \cdot (\bar{E} + v_a \times \bar{B})$ is the Lorentz force with \bar{E} and \bar{B} electric and magnetic field respectively. Perfect absorption at the plasma-solid interface ($s=L_{\text{con}}$) is typically assumed when applying these fundamental equations to the SOL plasma.

$$f_i(s = L_{\text{con}}, v_{\parallel i} > 0, t) = f_e(s = L_{\text{con}}, v_{\parallel e} > 0, t) = 0 \quad (2.3.)$$

This assumption excludes secondary and thermal electron emission from the surface which is generally present in the experiment and can strongly influence the deposited heat loads [26].

Neglecting the collisional effects (no $\sum \bar{C}_{ab}$ in Eq.2.1) yields the Vlasov-Poisson problem and neglecting the Coulomb force by setting $E_{\parallel}=0$ on the left side of Fokker-Planck equation (Eq. 2.1.) reduces it to the force-free Vlasov equation.

$$\left(\frac{\partial}{\partial t} + v_{\parallel} \cdot \nabla_{\parallel} \right) f_a = \frac{d}{dt} f_a = S_a \quad (2.4.)$$

In this case the Lorentz force is purely magnetic and thus vanishes for parallel motion and decouples the ion and electron distributions. Hence, the ion and electrons are distinguished only by their masses with parallel motion regardless of their charge. This is identical to the kinetic theory of gases [27] which is an important starting point in plasma kinetic analysis.

The treatment of plasma transport using the Fokker-Planck-Poisson system of equations is quite complicated and codes using this approach (e.g. BIT1 see in section 6.1.5.6) are extremely CPU intensive.

2.1.2. Fluid treatment of tokamak plasma

In this section the fluid approach to plasma transport is presented, which is in general relatively simple (compared to the kinetic approach) and therefore is usually used as a first candidate for the numerical solution of plasma evolution. However, if the fluid description is applied to kinetic phenomena, approximations must be used as for instance to the highest moment of particle distribution equation or to parallel heat flux in form of kinetic corrections (section 6.1.5.6.2).

Tokamak plasmas are usually treated as electrically conducting, collisional magnetic fluids and their dynamics are described by magnetohydrodynamics (MHD). MHD theory is a fluid (continuum) theory and, unlike the kinetic approach, cannot treat discrete particles. Since this approach is built on fluid, thermodynamic equilibrium, it considers averaged values of the plasma parameters without requiring details of the velocity distribution function $f(x,v)$. It is important to note that in an ionized plasma, particle collision times vary strongly with plasma temperature. The normalized neo-

classical collisionality, ν^* is inversely proportional to the electron-electron collisional mean free path λ_{ee} and is thus directly proportional to density while decreasing as the square of the temperature.

$$\nu^* = \frac{Rq}{\varepsilon^{3/2} \lambda_{ee}} \quad (2.5)$$

$$\lambda_{ee} \approx \lambda_{ii} \approx 1.727 \times 10^{17} \frac{T_e^2}{n_e \cdot \ln \Lambda} \quad [\text{m}] \quad (2.6)$$

where ε is inverse aspect ratio (a/R), $\ln \Lambda$ is Coulomb logarithm (for typical edge plasma parameters in range $\sim 15-17$ [16,28]), n_e density and T_e temperature of electrons. In Eq.2.6 temperature is expressed in electronvolts [eV] (obtained from joules [J] when multiplying by electric charge $e=1.62 \cdot 10^{-19}$ C), however in some equations T_e will be given in degrees kelvin [K] (when conversion to J is done by multiplying by Boltzmann constant $k=1.38 \cdot 10^{-23}$ J.K⁻¹). In general throughout this thesis, if not stated differently, the equations including Boltzmann constant k include the temperature expressed in degrees kelvin and in those equations without Boltzmann constant it is expressed in electronvolts. In general the collisional mean free path are defined as,

$$\lambda_{ee,ii} \approx v_{th,e,i} \cdot \tau_{e,i,col} \quad (2.7)$$

where $v_{th,e,i}$ is the thermal velocity for electrons and ions

$$v_{th,e,i} = \left(\frac{kT_{e,i}}{m_{e,i}} \right)^{1/2} \quad (2.8)$$

with $T_{e,i}$ being temperatures of electrons and ions and $\tau_{e,i,col}$ are the collisional times

$$\tau_{e,i,col} \sim \frac{T_{e,i}^{3/2}}{n_e \cdot \ln \Lambda} \quad (2.9)$$

As plasma gets hotter the distance of closest approach of charged plasma particles decreases so that both electrons and ions offer much smaller cross-sections for Coulomb collisions. The net result is that such collisions become far less frequent and the collision times increase. Hence, as plasma is heated it becomes less collisional very rapidly. Therefore fluid approach is usually valid in colder and denser plasmas with higher collisionalities ($\nu^* \geq 1$). For the plasma to be collisional the spatial scales of collisions $\lambda_{ee,ii}$ must be shorter than other characteristic scale lengths of system L_{\parallel} including the typical scale lengths of thermodynamic parameters (density n , temperature T and pressure p) and magnetic field B , $L_{\parallel,B} = (\nabla_{\parallel} B/B)^{-1}$.

$$L_{\parallel} \gg \lambda_{ee,ii} \quad (2.10)$$

In the SOL, these characteristic lengths usually approximately equal the connection length L_{con} . In general the fluid description is usually reasonably valid in SOL plasma in steady state. However, during transient events, like ELMs, this is no more the case.

The set of MHD equations is formed by the combination of the equations of fluid dynamics (Navier-Stokes equations - applying Newton's second law to the fluid motion and assuming that fluid stress is the sum of a diffusing viscous term proportional to the gradients of velocity and pressure terms) and equations of electromagnetism (Maxwell's equations – Gauss' law, Faraday's law of induction, Ampere's law where the charges and currents are affected by the fields through the Lorentz force). They consist of the particle

conservation equation (continuity equation), the momentum conservation equation, energy conservation equation, Ampere's law.

The simplest form of MHD is ideal MHD, where the resistivity of the fluid is sufficiently small that the fluid can be treated as a perfect conductor. In this case, Ampere's law contains no electric field and no electric diffusivity. However the plasma as an imperfectly conducting fluid must be treated by resistive MHD, where the finite resistivity/diffusion coefficient is included. In other words, Ampere's law contains an extra term representing the collisional resistivity.

If only parallel motion of plasma is considered, the plasma fluid conservation equations represent a 1D, 2-fluid (electrons and ions considered) system of velocity moment equations derived from the collisional Fokker-Planck kinetic vector equation. Here it is written as a function of position in direction parallel to magnetic field lines denoted as x .

$$v_x \cdot \frac{\partial f_a}{\partial x} + \frac{eE}{m} \frac{\partial f_a}{\partial v_x} = \sum C_{a,b} + S(x, \vec{v}) \quad (2.11)$$

In the high collisional limit the plasma fluid equations mentioned above reduce to famous Braginskii equations [16,29], which are here given in the direction parallel to magnetic field.

$$\text{Particle conservation – (continuity)} \quad \frac{d(nv)}{dx} = S_p \quad (2.12)$$

$$\text{Momentum conservation} \quad \frac{d}{dx} [(m_i v^2 + 2kT)n] = -m_i (v_i - v_n) v_{in} n \quad (2.13)$$

$$\text{Energy conservation} \quad \frac{d}{dx} \left[\left(\frac{1}{2} m_i v^2 + 5kT \right) nv - q_{||e} \right] = Q_R + Q_E \quad (2.14)$$

with S_p the particle source, x the parallel coordinate and $v_{i,n}$ are the velocities of ions and neutrals. Furthermore $n=n_e$, $p_{e,i}=nkT_{e,i}$, total pressure $p=p_e+p_i$ and a current free plasma ($j_{||}=0$) are assumed. The basic plasma condition of quasi-neutrality is satisfied $n_e=\sum Z_i n_i$ (with Z_i charge of ion species). Other terms will be explained below. Electric field \vec{E} is assumed parallel to \vec{B} and thus the expressions for $\vec{E} \times \vec{B}$, $\vec{v} \times \vec{B}$ effects are avoided [16]). Further simplifications are the assumptions of equipartition ($T_e=T_i$) and the neglect of viscosity Π_i (see later).

Eq.2.12-2.14 represent a sum of both electrons and ions, where terms involving the electron mass are omitted as small, and in the following text more details will be given on how these equation are derived from the collisional Fokker-Planck kinetic vector (Eq.2.11), which is multiplied by the zeroth, first and second order of velocity moment. The particle conservation equation is obtained by multiplication of Eq.2.11 by the zeroth order velocity moment $d\vec{v}$ and by integrating over the entire velocity space to get the average thermodynamical values:

$$n = \int_{v=-\infty}^{v=\infty} f(v) \cdot dv \quad (2.15.)$$

The momentum conservation equation is obtained by multiplication of Eq.2.11 by the first order velocity moment $mv_x d\vec{v}$. At this point it is important to distinguish between pressure in parallel and perpendicular directions, $p_{\parallel} = nkT_{\parallel}$ and $p_{\perp} = nkT_{\perp}$, where the \parallel and \perp denote the direction parallel to the magnetic field and perpendicular direction corresponding to the gyro-motion of the particles, respectively. If self-collisionality is weak, the increase of momentum flux (mnv^2) representing the acceleration of the plasma flow tends to be caused by T_{\parallel} rather than T_{\perp} . For this reason the gyration effects are ignored and it is assumed that flow of momentum grows at the expense of p_{\parallel} (strong pressure anisotropy: $p_{\parallel} \gg p_{\perp}$). This is actually expressed by the first part of the momentum conservation equation arising from the first term of Eq.2.11 $\frac{d}{dx}(mnv^2 + p_{\parallel})$.

Multiplication of the second term of Eq.2.11 by the first order of velocity moment results in the force due to electric field E , $F_E = -eEn$. The third term of Eq.2.11, representing collisions, involves three components including the term for ion-neutral momentum loss collisions $m_i(v_i - v_n)v_{in}n_n$ where v_{in} is ion-neutral collision frequency, the term for momentum transfer between electrons and ions, corresponding to the friction force $F_f = m_e(v_e - v_i)v_{ei}^{mom}n$ (with $v_{ei}^{mom} \propto Z_i n_e T_e^{3/2}$) and, in the case of $dT_e/dx \neq 0$ a second collisional force $R_T \equiv -0.71n(dkT_e/dx)$. The latter arises due to the fact that electrons from colder side with larger collisional frequency v_{ei}^{mom} tend to push ions in the direction of increasing T_e and ions act oppositely on electrons with the same force.

If collisionality is not weak but rather intermediate, it is necessary to take into account not only p_{\parallel} but also p_{\perp} (intermediate pressure anisotropy $p_{\parallel} \neq p_{\perp}$). They are commonly coupled by the force on the plasma exerted by parallel gradients in the perpendicular pressure $-\nabla_x p_{\perp}$, the so called parallel stress tensor Π .

$$\Pi \equiv \frac{2}{3}(p_{\parallel} - p_{\perp}) \quad (2.16)$$

$$p \equiv (p_{\parallel} + 2p_{\perp})/3 \quad (2.17)$$

In this case, an additional term must be present in the momentum equation which is especially important for ions since self-collisionality of electrons is usually assumed to be strong enough to ensure that electron pressure isotropy ($p_{\parallel e} \approx p_{\perp e}$) is satisfied. For ions it is expressed as

$$\Pi_i = -\eta_{\parallel} \frac{dv}{dx} \quad (2.18)$$

where η_{\parallel} is the parallel viscosity coefficient. It is worth noting, that in situations of low-collisionality, Π_i becomes unphysically large ($\Pi_i \rightarrow \infty$) and it is necessary to apply kinetic corrections, which are introduced as viscous stress limiter in the codes like SOLPS used in this thesis (see Chapter 4) with values usually

$$\Pi_{i,lim} \approx -0.5p_i \quad (2.19)$$

Multiplication of the last fourth term of Eq.2.11 by first order of velocity moment gives rise to the last term of momentum conservation equation describing the ions created by ionization of neutral population with a drifting Maxwellian distribution $m_i v_n S(x, \vec{v})$.

Thus, while anticipating pressure isotropy, the full momentum conservation equation for both ions and electrons can be presented as follows.

$$\frac{d}{dx}(m_i n v^2 + p_{\parallel i}) - eEn = -m_i (v_i - v_n) v_{in} n + m_e (v_e - v_i) v_{ei}^{\text{mom}} n + 0.71n \left(\frac{dkT_e}{dx} \right) \quad (2.20)$$

$$\frac{dp_e}{dx} + eEn = m_e (v_e - v_i) v_{ei}^{\text{mom}} n - 0.71n \left(\frac{dkT_e}{dx} \right) \quad (2.21)$$

By multiplying of Eq.2.11 by second order of the velocity moment $0.5v^2 d\vec{v}$, the energy conservation equation is obtained. Multiplication of the first term of Eq.2.11 yields

$$\frac{d}{dx} \left[\frac{1}{2} m n v^3 + \frac{3}{2} p_{\parallel} v + q_{\parallel}^{\text{cond}} \right] \quad (2.22)$$

where $q_{\parallel}^{\text{cond}}$ denotes the parallel conduction heat flux, arising from parallel temperature gradient $\nabla_{\parallel} T$, which is very important, especially under conditions of high collisionality (see section 2.2). The second term of Eq.2.11 gives $-enEv$, which is energy transfer from electrons to ions as a result of the ambipolar electric field (assuming $v_i = v_e$). Multiplication of the third term of Eq.2.11 results in the energy from collisions associated with heat transfer. There are three resulting terms and for simplification they involve only the collisions of charged particles. First of these three terms is the heat transfer due to self-collisions which couple T_{\parallel} and T_{\perp} , $Q_{\perp \rightarrow \parallel}$. This term is negligible for low collisionalities, but for intermediate collisionality the contribution of p_{\perp} through Π_i must be included and the term thus becomes

$$\frac{d}{dx} \left[\left(\frac{5}{2} p_i + \frac{1}{2} m_i n v^2 + \Pi_i \right) v + q_{\parallel}^{\text{cond}} \right] \quad (2.23)$$

The second term of energy from collisions associated with heat transfer is the Joule Heating due to net drift of electrons against the dissipative collisional force R , $Q_R = -R(v_e - v_i)$. Since $m_e \ll m_i$ this heating is transferred to the electron fluid. Finally third term of the energy from heat transfer collisions comes from equilibration collisions between electrons and ions

$$Q_{eq} = \frac{3m_e}{m_i} n v_{eq} (kT_e - kT_i) \quad (2.24)$$

where $v_{eq} \propto n \ln \Lambda T_e^{-3/2}$. The multiplication of the fourth term of Eq.2.11 by second order of velocity moment results in the ionization source of Maxwellian neutrals

$$Q_{E\parallel} = \frac{1}{2} k T_n S_p(x) \quad (2.25)$$

Thus by dropping terms with m_e and assuming isotropic electrons, the energy conservation equations for ions and electrons become:

$$\frac{d}{dx} \left[\left(\frac{5}{2} p_i + \frac{1}{2} m_i n v^2 + \Pi_i \right) v + q_{\parallel i}^{\text{cond}} \right] = envE + Q_{eq} + Q_{E\parallel i} \quad (2.26)$$

$$\frac{d}{dx} \left[\frac{5}{2} p_e v + q_{\parallel e}^{\text{cond}} \right] = -envE - Q_{eq} + Q_R + Q_{E\parallel e} \quad (2.27)$$

where parallel conduction heat fluxes $q_{\parallel,e,i}^{\text{cond}}$ represent a closure to the Braginskii equations [29] in the direction parallel to magnetic field and will be addressed in more details in the next section.

2.2. Parallel transport

It is well known that heat can be transferred by three different mechanisms, convection, conduction and radiation. In terms of heat transported parallel to magnetic field lines there are always two components: the heat flux arising from the parallel temperature gradient, the **conductive** heat flux (already mentioned in section 2.1.2.) and the one connected with the movement of particles within the plasma fluid, the **convective heat flux**. Heat convection is due to the bulk motion of fluids, where the mass is actually transferred together with the heat. It refers to the sum of heat transfer due to diffusion (generally defined as the random Brownian motion of particles in the fluid) and advection (generally defined as transport of matter or heat by the large scale motion of flows in the fluid). It is the transfer of thermal energy between neighboring particles in a fluid due to a temperature gradient

The net conductive heat flux due to random particle motion is

$$q \equiv -\chi \frac{dT}{dx} \quad (2.28)$$

where χ is the heat conduction coefficient

$$\chi = n \frac{kT}{m\nu_s} \quad (2.29)$$

with the self-collision frequency $\nu_s \propto m^{-1/2} n T^{-3/2}$. Therefore the heat conduction coefficient χ is a very strong function of temperature and can be written as

$$\chi = \kappa_0 T^{5/2} \quad (2.30)$$

where κ_0 is a constant. It is important to note, that since $\chi \propto m^{-1/2}$ electron heat conductivity is much larger than ion heat conductivity $\chi_e > \chi_i$ and consequently parallel convection is often more important than conduction for ions.

The parallel conductive heat fluxes for electrons and ions are expressed as follows:

$$q_{\parallel,e}^{\text{cond}} = -\chi_e \frac{dT_e}{dx} = -\kappa_{0e} T_e^{5/2} \frac{dT_e}{dx} \quad [\text{Wm}^{-2}] \quad \kappa_{0e} = \frac{30692}{Z_i \ln \Lambda} \approx 2000 \quad (2.31)$$

$$q_{\parallel,i}^{\text{cond}} = -\chi_i \frac{dT_i}{dx} = -\kappa_{0i} T_i^{5/2} \frac{dT_i}{dx} \quad [\text{Wm}^{-2}] \quad \kappa_{0i} = \frac{1249}{Z_i^4 m_i^{1/2} \ln \Lambda} \approx 60 \quad (2.32)$$

where $Z_i=1$, $m_i=2\text{amu}$ and Coulomb logarithm $\ln \Lambda=15$ have been assumed to derive numerical values [16]. $T_{e,i}$ are expressed in [eV] and $dT_{e,i}/dx$ in [eV.m⁻¹].

The parallel convective heat flux for electrons and ions are usually expressed as follows:

$$q_{\parallel,e}^{\text{conv}} = \frac{5}{2} k T_e n v_e \quad (2.33)$$

$$q_{\parallel,i}^{\text{conv}} = \left(\frac{1}{2} m_i v_i^2 + \frac{5}{2} k T_i \right) n v_i \quad (2.34)$$

The total parallel heat flux is

$$q_{\parallel} = q_{\parallel}^{\text{cond}} + q_{\parallel}^{\text{conv}} \quad (2.35)$$

where the total conduction and convection heat fluxes including both ions and electrons are:

$$q_{\parallel}^{\text{cond}} \approx -\kappa_{0e} T_e^{5/2} \frac{dT_e}{dx} \quad (2.36)$$

assuming $\kappa_{0e} \gg \kappa_{0i}$ and T_e in [eV]

$$q_{\parallel}^{\text{conv}} = \left(\frac{1}{2} m_i v^2 + 5kT \right) n v \quad (2.37)$$

assuming the local ambipolarity $v_e = v_i = v$ and $T_e = T_i$.

2.2.1. Sheath boundary conditions

The parallel heat fluxes closing the fluid conservation equation in direction parallel to the magnetic field are linked with the interaction of the plasma flowing in SOL with the surfaces of divertor targets where the sheath is formed between plasma and the wall. The sheath problem is a purely kinetic phenomenon and it is very important in the context of work described in this thesis, since the plasmas analyzed here are assumed to be always attached (see section 1.1.3.1.). This and the following section deal with the sheath problem and the kinetic corrections introduced to the set of fluid equations for parallel heat conductivity.

When plasma is in contact with solid surface, a **sheath** is formed between the plasma and the surface and the heat transported along field lines is limited by that which can cross this sheath. Edge fluid codes, such as the B2.5 code used throughout this thesis, do not explicitly contain sheath physics (which requires a fully kinetic treatment, as in the PiC numerical treatments) and thus they use the fluid equations up to the last numerical grid cell bordering solid surfaces (for example the divertor targets). To bridge the gap between the plasma grid and the surfaces, sheath transmission coefficients are applied to describe the kinetic processes of energy and particle filtering accomplished by the sheath. The sheath problem is one of the oldest in plasma physics and has been extensively studied analytically and numerically [16, 30-31]. In the sheath problem the velocity distribution functions for ions and electrons $f_i(v)$, $f_e(v)$ evolve according to Fokker-Planck and Poisson equations (section 2.1.2).

In terms of kinetic/fluid phenomena the SOL divides into a narrow ($\sim 30\mu\text{m}$) region in front of the wall (sheath), which requires a kinetic treatment, and the rest of the plasma between two sheaths at inner and outer targets, which is also called pre-sheath. The sheath represents the sink of particles and energy for the SOL plasma. Since electrons are more mobile than ions, any surface in contact with plasma charges negatively compared to the plasma potential ($V_p=0$) and quasi-neutrality (valid elsewhere in plasma) is not satisfied in the sheath. An electric field arises, which pulls in ions to

satisfy quasi-neutrality until currents balance (unless surface is biased) to satisfy the charge balance equation

$$e_i \int f_i v_{\parallel i} dv_i + e_e \int f_e v_{\parallel e} dv_e = 0 \quad (2.38)$$

Ions and electrons move parallel to the electric field which is perpendicular to the solid surface. The electrostatic sheath in direct contact with the divertor surfaces (where $n_i > n_e$) has size defined by Debye length, λ_{DB}

$$\lambda_{DB} \equiv \left(\frac{5.53 \times 10^7}{n_e} T_e \right)^{1/2} \quad (2.39)$$

and it is called Debye (or Langmuir) sheath. In the presence of magnetic field, this electrostatic Debye sheath is combined with an approximately quasi-neutral magnetic Chodura sheath [30] with width of the order of the ion Larmor radius (radius of ions gyrating around magnetic field lines), ρ_i

$$\rho_i = \frac{m_i v_{\perp}}{eB} \cong \frac{m_i c_s}{eB}, \quad \rho_i > \lambda_{DB} \quad (2.40)$$

where c_s is a sound speed, a speed of ion fluid moving towards any sink defined as:

$$c_s = \left(\frac{k(T_i + T_e)}{m_i} \right)^{1/2} \quad M = \frac{v_{se}}{c_s} \geq 1 \quad (2.41)$$

where M is so-called Mach number. The values of c_s are typically in order $\sim 10^4$ m.s⁻¹ for D⁺ ions. It is also often expressed as

$$c_s = \left(k \frac{Z_i T_e + \gamma T_i}{m_i} \right)^{1/2} \quad (2.42)$$

where the polytropic parameter $\gamma=1$ for isothermal flow, $\gamma=5/3$ for adiabatic flow with isotropic pressure and $\gamma=3$ for 1D adiabatic flow with no perpendicular heat flux. In SOLPS it is usually assumed to be adiabatic.

The potential between the pre-sheath and the sheath entrance is called pre-sheath potential V_{se} .

$$V_{se} \cong -0.7 T_e \quad (T_e \text{ in [eV]}) \quad (2.43)$$

This potential causes the plasma flow towards the surface such that the so-called Bohm-Chodura criterion is satisfied [16].

$$v_{se} \geq c_s \quad (2.44)$$

This means that for a stable sheath to form (where quasi-neutrality is guaranteed), the velocity at which plasma particles enter the sheath, v_{se} must be at least as high as the sound speed, c_s .

The particle flux to the targets is

$$\Gamma_{se} = n_{se} v_{se} \quad (2.45)$$

where the density of electrons at the sheath entrance is obtained from the Boltzmann relation as

$$n_{se} = n_0 \cdot \exp(V_{se}/T_e) = 0.5 n_0 \quad (T_e \text{ in [eV]}) \quad (2.46)$$

where n_0 is density in the SOL plasma at $V=0$ and a factor of 0.5 in the right side of Eq.2.46 results from using Eq.2.43. While the ions are accelerated in the sheath, the electrons need to have energy sufficient to be able to overcome the potential barrier. This

potential barrier consists of the potential difference between pre-sheath and Debye sheath V_{se} (Eq.2.41) and the potential difference between sheath edge and the surface V_{sf} (if the surface is unbiased (floating) V_{sf} corresponds to the floating potential)

$$\frac{V_{sf}}{T_e} = 0.5 \ln \left[2\pi \left(\frac{m_e}{m_i} \right) \left(1 + \frac{T_i}{T_e} \right) \right] \left(\frac{1}{(1 - \delta_e)^2} \right) \quad (T_e \text{ in [eV]}) \quad (2.47)$$

Here δ_e is the coefficient of secondary electron emission which is usually ignored. Thus if $T_i \approx T_e$ is assumed,

$$V_{sf} \approx 3T_e \quad (T_e \text{ in [eV]}) \quad (2.48)$$

In the sheath limited regime the total heat transported parallel to the field lines is determined by the heat which is allowed to cross the sheath. The net energy flux through the sheath for electrons is defined as

$$q_{se,e} = (2kT_e + |eV_{se}| + |eV_{sf}|) \Gamma_{se} = \gamma_e kT_e \Gamma_{se} \quad (2.49)$$

where the first term represents the net electron heat flux density at the sheath-solid interface $q_{ss,e} = 2kT_e \Gamma_{se}$. The coefficient γ_e , called electron sheath heat transmission coefficient is defined as

$$\gamma_e \approx 2 + \frac{|V_{sf}|}{T_e} + \frac{|V_{se}|}{T_e} \approx 2 + 3 + 0.7 = 5.7 \quad (T_e \text{ in [eV]}) \quad (2.50)$$

The situation with ions which are accelerated across the sheath is much more complicated. They have non-Maxwellian distribution but in order to ease the analysis, they are treated kinetically assuming a Maxwellian distribution drifting with the ion sound speed. The net ion energy flux through the sheath can thus be expressed as

$$q_{se,i} = \left(\frac{5}{2} kT_i + \frac{1}{2} m_i c_s^2 \right) \Gamma_{se} = \gamma_i kT_i \Gamma_{se} \quad (2.51)$$

If $T_i = T_e$,

$$q_{se,i} = \frac{7}{2} kT_i \Gamma_{se} \quad (2.52)$$

and the ion sheath heat transmission coefficient $\gamma_i \approx 3.5$. However detailed kinetic analyses and calculations predict that it is more appropriate to consider

$$q_{se,i} \cong 2kT_i \Gamma_{se} \quad (2.53)$$

yielding $\gamma_i \approx 2$ [16]. If $T_e = T_i$, the total heat transferred across the sheath is thus

$$q_{se} = \gamma \cdot kT_e \Gamma_{se} \quad (2.54)$$

with $\gamma \approx 7 - 9$ the total sheath heat transmission coefficient ($\gamma_e \approx 5 - 6$ and $\gamma_i \approx 2 - 3.5$).

2.2.2. Heat flux limiters

As the previous section has discussed, the presence of the sheath places a limit on the heat flux which can be transmitted by the plasma to the surface on any given field line. Nevertheless, this is strictly the case only in the sheath-limited regime when the collisionality is low and the parallel temperature profiles flat. Thermal conduction plays almost no role and the heat transfer happens mostly by the convection, almost the entire SOL is stagnant with regard to flow and all the flow acceleration occurs very near to the solid surface. This is not true in a high recycling divertor, where flat gradient of temperature exists in the region between the X-point and target due to the plasma temperature cooling in the region of the targets and beyond, reducing gradients and preventing conduction. The transport is almost all convective in this case. Conductivity is what allows the temperature to drop from upstream to the X-point (provided collisionality high enough). At this point strong, usually ionization driven flows form to convect material to the targets. But the sheath still exists (if attached) and controls the ultimate energy flow out of the flux tube.

In sheath heat flux limited regime, if $\gamma = 7$ is assumed, the heat flux density through the sheath is

$$q_{sh} \approx 7kTnv \quad (2.55)$$

For $M=1$ (the condition on the flow speed at the sheath edge required for a stable sheath to form) the parallel convected heat flux density can be expressed as

$$q_{||}^{conv} = \left(\frac{1}{2} m_i v^2 + 5kT \right) nv = 6kTnv \quad (2.56)$$

When collisionality is not sufficiently high, strong parallel temperature gradients $\nabla_{||}T$ develop and the conductive heat flux can become an important component of the total parallel heat flux to the targets. In this case, which is referred to as conduction regime, the simple sheath expressions no longer suffice as a description of the total heat exhausted from the plasma and, if a fluid description is being used to model the SOL, kinetic corrections in the form of parallel heat flux limiters must be introduced into the set of fluid MHD (Braginskii) equations.

Apart from the standard expression given by Eq.2.28, valid for any medium, the conduction heat flux can be expressed also by the formula derived by Spitzer-Harm, valid for fully collisional situations:

$$q_{SH} \approx -2.9 \times 10^{-19} n_{e,i} v_{th,e,i} \lambda_{e,i} \frac{dT_{e,i}}{dx} = \chi_{e,i} \frac{dT_{e,i}}{dx} = \kappa_{||,SH} \cdot \frac{\partial T_{e,i}}{\partial x} \sim T^{5/2} \quad (T_e \text{ in [eV]}) \quad (2.57)$$

where $\kappa_{||,SH}$ is the Spitzer-Harm heat conduction coefficient. When the collisionality (proportional to T_e^{-2}) decreases, the heat flux becomes unphysically large ($q_{SH} \rightarrow \infty$) and since the scale-lengths of $\nabla_{||}T$ are not free to evolve, but are limited to the size of the system ($L_{||}$), the temperature gradients must steepen in order to enable the transfer of heat along the field lines by conduction. Thus the heat flux conduction coefficients $\chi_{e,i}$ are limited to some fraction α of the free-streaming heat flux. A simple kinetic correction in the form of electron and ion heat flux limiters, $\alpha_{e,i}$ can then be used to reproduce the effect of this steepening of the $T_{||}$ profile at intermediate and low collisionalities:

$$q_{lim} = \alpha_{e,i} n_{e,i} v_{th,e,i} kT_{e,i} \sim T^{3/2} \quad (2.58)$$

Typical values of heat flux limiters are $\alpha_e \approx 0.2-0.3$ and $\alpha_i \approx 0.6-1.5$. Choosing the best values to use in modeling a given situation is not straightforward. A more informed choice can be made through comparison with experimental data or with the results of kinetic simulations (such as the BIT1 code [32], see section 6.1.5.6).

In B2.5 and other fluid codes the parallel conductive heat flux is conventionally defined as a geometric combination of limited and Spitzer-Harm heat fluxes:

$$\frac{1}{q_{\parallel}^{\text{cond}}} = \frac{1}{q_{\text{lim}}} + \frac{1}{q_{\text{SH}}} \quad (2.59)$$

In order to understand what is actually represented by the application of heat flux limiters it is useful to write both in terms of their dependence on temperature:

$$q_{\text{SH}} \approx q_{\parallel}^{\text{cond}} = \chi_{\parallel} \frac{dT}{dx} = \kappa_0 T^{5/2} \frac{dT}{dx} \propto T^{5/2} \frac{dT}{dx} \quad (T \text{ in [eV]}) \quad (2.60)$$

$$q_{\text{lim}} = \alpha \cdot n \cdot v_{\text{th}} kT = \alpha \cdot n \left(\frac{kT}{m} \right)^{1/2} kT \propto T^{3/2} \quad (T \text{ in [K]}) \quad (2.61)$$

The “combined” heat flux density thus increases more slowly with temperature with flux limiters ($T^{3/2}$) than without them ($T^{5/2}$). The conduction heat flux limiters, $\alpha_{e,i}$, are known also as the free streaming multipliers (ratio of the heat flux to the free-streaming value) [16]. Without flux limiters the parallel heat transport is always limited by the classical Spitzer-Harm value at one end (conductive flux) and by the kinetic free-streaming value at the other (convective flux).

2.2.3. Power deposited on divertor surfaces

As the introductory discussion of Chapter 1 has already made clear, the particle and energy loads on the plasma-facing surfaces are amongst the most important tokamak parameters since, if not controlled, they can damage and considerably reduce divertor target lifetime. This is less of an issue in current research devices, where steady state power loading is often of insufficient duration to be a concern and in which stored energies are usually too low to be the cause of significant PFC damage. In next step devices such as ITER, however, PFC lifetime will become a serious threat if power fluxes are left uncontrolled. For this reason, credible predictions of the likely heat loads are required. The SOLPS code has long been used to assess these loads during the ITER design process and it therefore becomes increasingly important to pursue cross-checking and benchmarking of these code predictions on current devices. This is one of the aims of the work described here.

There are several terms contributing to the total power flux deposited on solid surfaces intercepting the tokamak plasma. The first and most important is the heat transmitted by electrons and ions across the sheath – given by expression Eq.2.54. The ions bring a directed kinetic energy across the sheath equal to their thermal energy plus that gained through acceleration in the sheath potential fall $Z_i e V_{\text{sf}} \sim 3 Z_i k T_e$ and thus the flux term including both these contributions can be written as

$$\frac{1}{2} m_i c_s^2 + 3 Z_i k T_e \quad \text{with } E_{\text{kin}} = \frac{1}{2} m_i c_s^2 \quad [\text{J}] \quad (2.62)$$

The third important contribution to deposited power is the potential energy released by fuel ion recombination to neutrals at the surface which is an exothermic process and releases heat. The neutrals subsequently recombine to form molecules so that the total energy released is the combination of the ionization and dissociation energies. For deuterium atoms $E_{\text{ion}} = 13.6\text{eV}$ and $E_{\text{diss}} = 4.52\text{eV}$ and so the recombination term is

$$q_{\text{rec}} = \left(\sum_{\text{ions}} E_{\text{ion}} + \sum_{\text{ions}} E_{\text{diss}} \right) c_s n_i \quad (\text{E in [J]}) \quad (2.63)$$

If $T_i = T_e$, the total heat flux deposited at the targets is

$$q_{\parallel, \text{dep}} = (\gamma kT + E_{\text{kin}} + E_{\text{ion}} + E_{\text{diss}}) \Gamma_{\text{se}} \quad (\text{E in [J]}) \quad (2.64)$$

where the term $\gamma kT \Gamma_{\text{se}}$ includes both $q_{\text{se},e}$ (Eq.2.49) and $q_{\text{se},i}$ (Eq.2.51).

Kinetic energy can be included also in the sheath heat transmission coefficient and the total deposited heat load can be approximated as:

$$q_{\parallel, \text{dep}} = (7kT/e + 18.1)e \Gamma_{\text{se}} \quad (\text{T in [eV]}) \quad (2.65)$$

It should be noted that since the target surface normal is not generally aligned with the magnetic field vector \vec{B} , the real deposited heat flux is corrected by multiplication by $\cos\Psi$, where Ψ is the angle between the magnetic field vector and the surface normal.

2.3. Perpendicular transport

When the plasma escapes across the separatrix to open field lines in the SOL of a diverted configuration, the power is transported both in the parallel direction towards the divertors and across the field towards the first wall surfaces. Since parallel transport is much faster than radial transport it is responsible for most of the power deposited on the targets. The slower radial transport determines to some extent the width and shape of power deposition perpendicular to the field at the targets and the extent to which residual power is deposited on the main walls.

Although the physics of parallel transport is reasonably well understood in the SOL, the same does not apply to cross-field or radial transport [16]. With respect to 1D parallel transport the cross-field transport represents both its source (when plasma crosses separatrix and gets to the SOL where it is subject to parallel transport) and to some extent the sink (when plasma moves cross-field outwards from flux tube until it hits the limiter walls). In the radial direction, the conservation of particles can be written as:

$$\frac{d\Gamma_{\perp}}{dr} = S_{p\perp} < 0 \quad (2.66)$$

where Γ_{\perp} is the radial particle flux and the radial source of particles S_p is negative in the sense that the parallel removal to the solid surfaces ($S_{p\parallel}$) constitutes a radial particle sink $S_{p\perp}$ for cross-field particle flux density:

$$S_{p\parallel} = -S_{p\perp} \quad (2.67)$$

The radial particle balance equation can be written also in more general form

$$\frac{d\Gamma_{\perp}}{dr} = -\frac{n}{\tau_{\parallel}} + S_{\text{ion}} \quad (2.68)$$

including the ionization source S_{ion} . The parameter τ_{\parallel} is a parallel loss time:

$$\tau_{\parallel} \cong 2L_{\text{con}}/c_s \quad (2.69)$$

The standard way of describing the cross-field particle flux is a combination of diffusive and convective fluxes which are controlled by cross-field diffusion coefficient D_{\perp} and radial velocity v_{\perp} respectively. In this case:

$$\Gamma_{\perp} = -D_{\perp} \frac{dn}{dr} + v_{\perp} n \quad (2.70)$$

Assuming diffusive motion, the cross-field particle flux density satisfies Fick's law

$$\Gamma_{\perp} = -D_{\perp} \frac{dn}{dr} \quad (2.71)$$

where the approximation is often used of $dn/dr \approx n/\lambda_n$ with λ_n being the characteristic radial scale length of the density (\sim radial decay length defined by the radial exponential decay of density $n(r) = n(0) \cdot \exp(-r/\lambda_n)$).

Radial transport in SOL is very definitely not classical, since classical cross-field diffusion of particles is far too slow to match SOL measurements of the diffusion coefficient. Classical cross-field diffusion from electron-ion collisions only maybe expressed as:

$$D_{\perp}^{\text{class}} = 8 \cdot 10^{-4} T_e^{-3/2} n k (T_e + T_i) / B^2 \quad (2.72)$$

In the SOL plasma this is typically in the range $\sim 10^{-3} \text{m}^2 \cdot \text{s}^{-1}$. Diffusion coefficient D_{\perp} is generally anomalous compared with classical rates and therefore it is not possible to calculate it from the first principles. It is usually obtained from experiment inferred by using the Fick's law (assuming pure diffusion with constant D_{\perp}). Almost all measurements in the tokamak SOL have found exponential behaviour in the density profile [33-38] as would be expected in the simple SOL on the basis of the diffusive description of cross-field transport. Approximating the transport in the way of diffusive ansatz allows simple estimates of the characteristic radial width of the SOL, λ_{SOL} in terms of a characteristic diffusion distance which a particle travels cross-field beyond the separatrix,

$$\lambda_{\text{SOL}} \cong (D_{\perp} \tau_{\text{SOL}})^{1/2} \quad (2.73)$$

where τ_{SOL} is the characteristic particle dwell time in the SOL. Assuming $\tau_{\parallel} \approx \tau_{\text{SOL}}$ and neglecting SOL ionization sources yields

$$S_{p\perp} = -D_{\perp} \frac{n}{\lambda_{\text{SOL}}^2} \quad (2.74)$$

If simple collisional diffusion is considered, D_{\perp}^{class} , very thin SOL is found $\lambda_{\text{SOL}}^{\text{class}} \cong 1 \text{mm}$. When compared with typical SOL width [33-38] found on many tokamaks including TCV [39],

$$\lambda_{\text{SOL}} = 10 - 30 \text{mm} = \lambda_{\text{SOL}}^{\text{class}} \cdot \sqrt{\frac{D_{\perp}}{D_{\perp}^{\text{class}}}} \quad (2.75)$$

experimental value of D_{\perp} in a range $\sim 1 \text{ m}^2.\text{s}^{-1}$ is found. This is consistent with the radial diffusion coefficient empirically obtained from measurements in non-toroidal plasmas expressed by the well known Bohm scaling [40].

$$D_{\perp}^{\text{Bohm}} = 0.06 T_e / B \quad (2.76)$$

which is usually $\sim 1\text{-}2 \text{ m}^2.\text{s}^{-1}$ for typical TCV plasma.

It is well known that the cross-field transport process throughout the tokamak cross-section is largely turbulent driven, both in the core and the SOL. Only under certain circumstances does neo-classical cross-field transport adequately described measured cross-field transport rates (for example cross-field ion diffusivities are often consistent with neo-classical transport rates in the core of the plasma or in H-mode transport barrier regions). Electron radial transport is always anomalous and turbulence driven. In the SOL, radial transport seems to be a mixture of drift wave type turbulence ([41]) and electrostatic interchange driven type turbulence (with the former seeming to occur closer to the separatrix and the latter further out radially in the SOL). The latter has been shown to operate directly on the TCV tokamak ([39,42]), a machine on which much of the work described here has concentrated. Because of this turbulent nature of radial transport, D_{\perp} alone or $D_{\perp} = \text{constant}$ does not represent it appropriately and the real description is one of radially varying D_{\perp} and v_{\perp} . Nevertheless, the field is still some way from a quantitative ability to prescribe the transport rates driven by these processes, especially where predictions to next step devices are concerned. Even though it is now clear that the main process of cross-field transport is not diffusive, this ansatz is still used in much fluid modeling to approximate the real situation in the absence of a more quantitative alternative description. Most modeling approaches, including the work to be presented later in this thesis, rely on simplistic descriptions of the transport, either as purely diffusive or convective when it is known that neither is a complete description of the true driving mechanism(s). In the simulations with fluid code like SOLPS, where only the value of particle flux is important and the details of the nature of D_{\perp} , v_{\perp} components are not required, it is practical to write the particle flux density using the effective diffusion and convection coefficients D_{\perp}^{eff} , v_{\perp}^{eff} , as follows.

$$\Gamma_{\perp} = D_{\perp}^{\text{eff}}(r) \frac{dn}{dr} \quad (2.76)$$

$$\Gamma_{\perp} = n v_{\perp}^{\text{eff}}(r) \quad (2.77)$$

Typical values for D_{\perp}^{eff} found experimentally are in the range $0.1\text{-}10 \text{ m}^2.\text{s}^{-1}$.

2.3.1. Perpendicular energy flux

The power from core enters the SOL through radial transport where usually the main part of it ends up deposited at the divertor targets (as discussed in section 2.2.3), and the remaining part is divided into the power deposited on the walls and the radiation. For example, from $\sim 100 \text{ MW}$ of power entering the SOL in ITER, the fraction of 65-70% is expected to be dissipated in the divertor by volumetric radiation. In common with the parallel heat flux, the flux of plasma energy in the perpendicular direction can be expressed as a sum of conductive and convective energy flows which are themselves the sum of contributions from electrons, ions and neutrals. Assuming the quasi-neutrality, the expression for radial conductive energy flux of electrons and ions is as follows:

$$q_{\perp,e,i}^{\text{cond}} = -n(\chi_{\perp,e,i} \nabla_{\perp} T_{e,i}) \quad (2.78)$$

where $\chi_{\perp,e,i}$ is the coefficient of cross-field heat diffusivity for electrons and ions. The SOL $\chi_{\perp,e,i}$ are extremely important since they control the power decay width, which is one of the key parameters determining the power deposited on solid surfaces (e.g. divertor targets). Like the other cross-field transport coefficients, the $\chi_{\perp,e,i}$ are anomalous and cannot yet be derived theoretically from first principles but must be extracted from experimental data. Very often for modelling purposes (and because very little information is ever available experimentally concerning T_i in the SOL) $\chi_{\perp,e} = \chi_{\perp,i}$ is assumed and the typical values derived from experiment are in the range $0.1\text{-}10 \text{ m}^2\text{s}^{-1}$ [16]. If CX collisions are an important factor, the conducted neutral heat flux must also be considered. In this case, if the CX neutral collision mean-free-path, λ_{CX} is shorter than the temperature gradient scale length, it is possible to treat the neutrals as a fluid:

$$q_{\perp,n}^{\text{cond}} = -\kappa_{\text{CX}} \nabla_{\perp} T_i \quad (2.79)$$

where $\kappa_{\text{CX}} \approx n_0 \lambda_{\text{CX}}^2 \nu_{\text{CX}}$ is estimated from the random walk with collisional frequency ν_{CX} . Within SOLPS, the neutrals are simulated by the Eirene Monte-Carlo code which follows the trajectories of test neutrals in a plasma background and properly accounts for the neutral heat transport (see chapter 4).

Perpendicular heat convection by electrons, ions and neutrals may be expressed by analogy with the parallel convected heat flux.

$$q_{\perp,e,i,n}^{\text{conv}} = \frac{5}{2} k T_{e,i,n} n v_{\perp,e,i,n} \quad (2.80)$$

where the $v_{\perp,e,i,n}$ are the radial velocities of the electron, ion and neutral fluids.

It is worth noting that the net radial convective energy flux to the walls due to the ion outflux can be quite small even if the ion particle outflux is large. This can happen if the density is high enough for $T_n \sim T_i$ due to CX collisions with $\lambda_{\text{CX}} < \lambda_{\text{ion}}, \lambda_n$. In such a case, the energy fluxes due to ions and neutrals will balance out ($n_i v_{\perp,i} = n_n v_{\perp,n}$).

Comparisons of experiment and simulations with radially increasing v_{\perp} and constant χ_{\perp} [41,43-44] conclude that depending on density, different energy transport channels are dominant. If the upstream density is high and CX plays an important role, the biggest contribution to radially transported energy in far SOL is from electron convection and neutral conduction due to CX collisions. In contrast, at low density diffusion dominates and most of the cross-field power is transported by this mechanism. In this case the total cross-field power flux may be expressed as the sum of convective and conductive contributions for both electrons and ions.

$$q_{\perp}^{\text{tot}} = q_{\perp}^{\text{cond}} + q_{\perp}^{\text{conv}} = \chi_e n k \nabla_{\perp} T_e + \chi_i n k \nabla_{\perp} T_i + \frac{5}{2} k T_e n v_{\perp} + \frac{5}{2} k T_i n v_{\perp} \quad (2.81)$$

$$q_{\perp}^{\text{conv}} = \frac{5}{2} k T n v_{\perp} = \frac{5}{2} n k T \frac{D_{\perp}}{\lambda_n} \quad (2.82)$$

$$q_{\perp}^{\text{cond}} = \chi_{\perp} n k \nabla_{\perp} T \sim \chi_{\perp} n k \frac{T}{\lambda_T} \quad (2.83)$$

If the radial particle and energy transport is assumed diffusive and the radial decay lengths for both density (λ_n) and temperature (λ_T) are known, the total perpendicular heat flux on walls can be estimated as:

$$q_{\perp}^{\text{tot}} = \chi_{\perp e} n k \frac{T_e}{\lambda_{Te}} + \chi_{\perp i} n k \frac{T_i}{\lambda_{Ti}} + \frac{5}{2} D_{\perp} \frac{n_e k T_e}{\lambda_n} \quad (2.84)$$

In terms of the distribution of the total power in SOL from the core into the parallel and radial transport channels, the transport in both directions is strongest close to the separatrix. The radial transport is naturally highest there because this is the point at which the power enters the SOL. However, the separatrix vicinity is also the place with highest temperatures and the resulting high parallel heat conduction ($\propto T^{5/2}$) means that parallel energy transport usually dominates over radial heat transport. As a consequence, the power deposited on the main chamber walls usually represents only around one quarter of the total power which enters the SOL from core and the majority is directed to the divertor targets [41].

2.3.2. Perpendicular transport of parallel momentum and viscosity

In this section the influence of cross-field transport on the pressure constancy in parallel flux tubes will be addressed. Cross-field transport is not only a source of particles and heat to the flux tubes just outside the separatrix in the SOL. It represents also the source of parallel momentum to the flux tubes neighbouring at the outer side of the flux tube, which on the other hand experiences a loss of parallel momentum by the cross-field transport.

The total pressure is constant along flux tubes in the SOL and this pressure constancy is expressed as

$$\frac{d}{dx} (mnv^2 + p_e + p_i) = 0 \quad (2.85)$$

assuming no cross-field transport of momentum into the flux tube. However, this is not strictly true for individual flux tubes subject to an influx due to cross-field transport. The parallel momentum conservation equation for individual flux tube should in fact strictly be written as:

$$\frac{d}{dx} (mnv^2 + p_e + p_i) = S_{\text{mom}} \quad (2.86)$$

If radial flow is assumed only radially outwards from separatrix to the walls, the momentum source S_{mom} is positive for the tube further out (gaining the momentum) and negative for the tube closer to the separatrix (losing momentum) and averaged over entire SOL, $S_{\text{mom}} = 0$.

If parallel velocity is assumed to be radially constant in the SOL ($dv_{\parallel}/dr=0$), the momentum source due to cross-field particle transport has diffusive nature [16]:

$$S_{\text{mom}, D_{\perp}} = mv_{\parallel} S_{p\perp} = mv_{\parallel} D_{\perp} \frac{dn^2}{dr^2} = mv_{\parallel} \frac{D_{\perp} n}{\lambda_n^2} \quad (2.87)$$

And, if integrated over the whole length of the flux tube:

$$\int S_{\text{mom}, D_{\perp}} dx = L_{\parallel} \overline{nv_{\parallel}} D_{\perp} \frac{m}{\lambda_n^2} \quad (2.88)$$

with $\overline{nv}_{\parallel}$ the average flux density along the SOL. In reality however, v_{\parallel} varies radially and the resulting dv_{\parallel}/dr gives rise to additional cross-field transport of momentum due to perpendicular shear stress at the rate proportional to $\eta_{\perp} dv_{\parallel}/dr$, where η_{\perp} is the perpendicular shear viscosity coefficient. As with other cross-field coefficients, η_{\perp} is anomalous and little is known about its value. It is usually approximated as $\eta_{\perp} \approx nmD_{\perp}$ based on analogy with classical transport [16]. The momentum source due to the cross-field transport of viscosity is expressed as:

$$S_{\text{mom}, \eta_{\perp}} = \frac{v_{\parallel} \eta_{\perp}}{\lambda_v^2} \quad (2.89)$$

where λ_v is parallel velocity radial decay length ($\lambda_v \sim \lambda_n$). This momentum source is of order of $S_{\text{mom}, D_{\perp}}$ and since both make only small contributions to pressure balance, they are often neglected [16]. In other words cross field transport does not greatly influence pressure constancy along field lines.

At this point now that the viscosities in both parallel (see section 2.1.2) and perpendicular direction have been mentioned, it is useful to distinguish between them in terms of their influence on the parallel velocity. In a magnetized plasma, the viscosity tensor represents a sum of several component tensors, although the parallel and perpendicular viscosities are the most important within the frame of this work. The parallel viscosity controls the variation along magnetic field-lines of the velocity component parallel to field-lines. It arises due to the collision-induced, random-walk diffusion of particles, with frequency ν , and step-length l_{par} . The perpendicular viscosity controls the variation of the velocity components perpendicular to magnetic field-lines. It corresponds to a collision-induced random-walk diffusion of particles, with frequency ν , and step-length l_{perp} . Compared to the parallel viscosity it is smaller by a factor $(l_{\text{perp}}/l_{\text{par}})^2$. Thus, it is the greatly reduced step-length in the perpendicular direction, relative to the parallel direction, which accounts for the smallness of the perpendicular viscosity compared to the parallel viscosity. Both the parallel and perpendicular viscosity coefficients will be addressed in section 6.3.3.

2.4. Volumetric processes in plasma and plasma–surface interactions

The plasma is full of particles (charged or neutral, atoms or molecules, photons...) which are subject to different inter-species volumetric processes. The most relevant for tokamak divertor physics are electron impact ionization, charge exchange, three-body recombination (electron impact recombination), radiative recombination and molecular dissociation.

Extensive reviews of atomic and molecular data for hydrogen, hydrocarbons and atomic impurities can be found in the series [45]. Relevant surveys of atomic and molecular data for fusion including data for line and other radiation for hydrogen and impurity atoms and ions are published in [46].

Part of the energy in SOL is always lost by radiation, especially when impurities are present. The radiation loss rate, P_{rad} , is the rate at which energy is lost by radiation per unit volume [16] and is experimentally measurable (for example using bolometers). P_{rad} must be distinguished from the electron cooling rate P_{cool} , at which plasma electrons lose energy by inelastic collisions with ions and atoms. Although not directly measurable, it is used in modelling as a component of the energy balance. At low temperatures, typical of the divertor plasma, P_{rad} is dominated by radiative cascade and continuum radiation, while P_{cool} is dominated by the rate at which recombining electrons lose their kinetic energy. In this case $P_{\text{rad}} > P_{\text{cool}}$ (see Eq.2.91).

The powers associated with ionization and recombination inside P_{cool} should be distinguished. Beginning with ionization:

$$P_{\text{cool,ion}} = P_{\text{rad,ion}} + E_{\text{ion}} \cdot \alpha_{\text{ion}}^{\text{eff}} \quad (2.90)$$

where $\alpha_{\text{ion}}^{\text{eff}}$ is an effective ionization rate and E_{ion} the ionization potential energy ($E_{\text{ion}}(\text{H})=13.6\text{eV}$). Non-photon energy cost to the electron population is only E_{ion} . **Tab.1.1** compiles the ionization potentials for the charged states of Carbon, the principal impurity in the JET and TCV plasmas modelled in this thesis.

State	C^0	C^+	C^{2+}	C^{3+}	C^{4+}	C^{5+}
$E_{\text{ion}} [\text{eV}]$	11	24	48	64	392	490

Table 1.1. Ionization potentials for charged states of C

At very low temperature, however ($T_e < 1\text{eV}$), recombination dominates over ionization.

$$P_{\text{cool,rec}} = P_{\text{rad,rec}} - E_{\text{ion}} \cdot \alpha_{\text{rec}}^{\text{eff}} \quad (2.91)$$

where $\alpha_{\text{rec}}^{\text{eff}}$ is the effective recombination rate (dependent on n_e). The potential energy of recombination heats the electrons (at least for three-body collisional recombination).

The total amount of energy radiated by single particle during its lifetime in the plasma is defined as a radiation potential $E_{\text{rad,pot}} [\text{J}]$. This quantity depends strongly on plasma temperature and radiating species and is typically in range of $\sim 1\text{-}10 \text{ keV} \sim 10^{-16} - 10^{-15} \text{ J}$ for low Z. Total radiated power $P_{\text{tot,rad}}$ expressed using the radiation potential is:

$$P_{\text{tot,rad}} = E_{\text{rad,pot}} \Phi_Z [\text{W}] \quad (2.103)$$

where Φ_Z is impurity particle influx rate due to sputtering or artificial injection.

In addition to the processes occurring in the plasma volume there are plasma-wall interactions, which are responsible for impurity production and recycling. The former appears when the particles after striking the surface release the surface material through chemical and physical sputtering (as briefly mentioned in section 1.3.). To do so the incident particle must have enough energy to overcome the surface binding energy, E_B . This energy is $E_B \sim 7.4\text{eV}$ for C and the threshold energy for physical sputtering of graphite walls is $\sim 30\text{eV}$ and $\sim 42\text{eV}$ for D and C respectively [16]. The physical sputtering yield, the number of impurities released by impact by one particle, is calculated by Roth-Bodansky formula [47], but can be strongly influenced by the different surface properties like roughness. If the vessel has graphite walls, in chemical sputtering hydrogenic atoms break C-C bounds and create C-H bounds while hydrocarbon impurities are released. Chemical sputtering yields are studied in [48] and like physical sputtering yields they strongly depend on surface properties like roughness, presence of amorphous carbon layers etc. and are generally higher than those of physical sputtering. The experimentally reported values lie usually between 1-5% and depend strongly on surface properties. In the SOLPS code these processes are treated by the sputtering coefficients. There are three processes which plasma and neutrals undergo during the interactions with the wall, contributing to fuel recycling. The particle is absorbed and trapped by the surface, or it is reflected or it is absorbed/adsorbed by surface and subsequently released as thermal particle with velocity dependent on the surface temperature. The coefficients relevant to these processes are available in the TRIM database used by Eirene part of SOLPS code and they are derived from calculations in [49].

3. Edge localized modes

The transition from L-mode to H-mode is normally accompanied by the appearance of edge localized modes, ELMs [50]. The “ELMing H-mode” is the reference scenario in which ITER will attempt to reach burning plasmas with fusion gain of ~ 10 (the $Q_{DT} = 10$ baseline). Without the confinement improvement afforded by the H-mode, the required fusion performance cannot be obtained. The high confinement is produced by the formation of an edge transport barrier (the H-mode pedestal), which “insulates” the core plasma but which is associated with high plasma pressure, built up over a very narrow region at the edge of the plasma (pedestal widths are typically a few cm). This region of high pressure gradient is destabilizing for MHD modes, known, for evident reasons, as Edge Localised Modes (ELMs). These modes are both beneficial, in allowing the pressure gradients to relax, simultaneously expelling particles, allowing impurities (including He ash in a reactor) to be flushed out and plasma density to be controlled and a threat, due to the high transient energy densities they deposit on PFCs posing material damage and lifetime issues [51-52]. Large amplitude ELMs can also seriously deteriorate the core confinement [53].

The most serious consequence of the ELMs is the high peak heat loads with values ~ 10 times higher than the time-averaged levels. According to present models and empirical scalings of experimental data from various divertor tokamaks, the expected value of energy expelled by uncontrolled ELMs in ITER is $\Delta W_{ELM} \sim 20$ MJ. However, evaluation of the expected characteristics of power fluxes to the divertor during the ELMs in ITER and experimental measurements of plasma material erosion under such loads has shown that an acceptable divertor lifetime can only be ensured for ELMs causing an energy loss of $\Delta W_{ELM} \sim 1$ MJ. This is a factor of 20 smaller than the expected natural ELM size and has determined the requirements for ELM control in ITER [52]. Therefore the elimination and mitigation of these transient events is a crucial task for the fusion community. The method envisaged also in the original ITER design (2001), uses frozen pellets of deuterium injected into the edge of the plasma at high frequencies in order to fix the ELM frequency to values required for low ELM energy. It has been since realized that this might not be enough to do the job completely, so new design incorporates an additional way of the taming ELMs by applying a weak magnetic field via external coils employed near the plasma edge which mix-up the magnetic surfaces in order to increase particle transport and thus mitigate the ELMs. In other words, this method represents plasma edge ergodisation by resonant perturbations of the magnetic field. One of the major investments of ITER is to the in-vessel coils which should ensure, that the size of ELMs is acceptable for the planned operation of the reactor. As already mentioned in the motivation of this thesis (section 1.4), the aim of this work is to verify by the comparison with existing experiments, that the existing fluid numerical codes are able to predict how the ELMs at ITER will behave.

The ELMs are manifest as repetitive bursts of particles and heat in the SOL with quasi-regular or irregular periodicity and represent a temporary breakdown of the H-mode edge confinement barrier (**Fig.3.1**). With appropriate diagnostics (for example fast, wide angle imaging of the plasma in visible light) they can be observed as helical filamentary structures in the SOL (**Fig.3.2**).

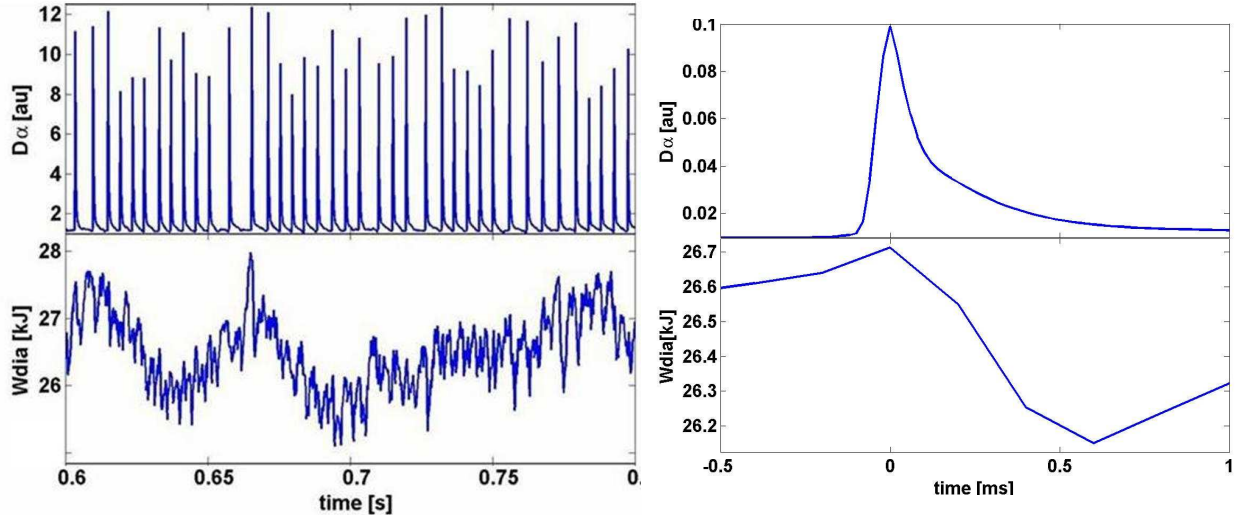


Figure 3.1. *Left:* Typical TCV Type III ELM signals from D_α and the energy stored in the plasma measured by diamagnetic loop (see chapter 5), $W_{\text{plasma}} = W_{\text{dia}}$, *Right:* coherently averaged data from many ELMs to reproduce one ELM as a mean of these events averaged on a common timebase.

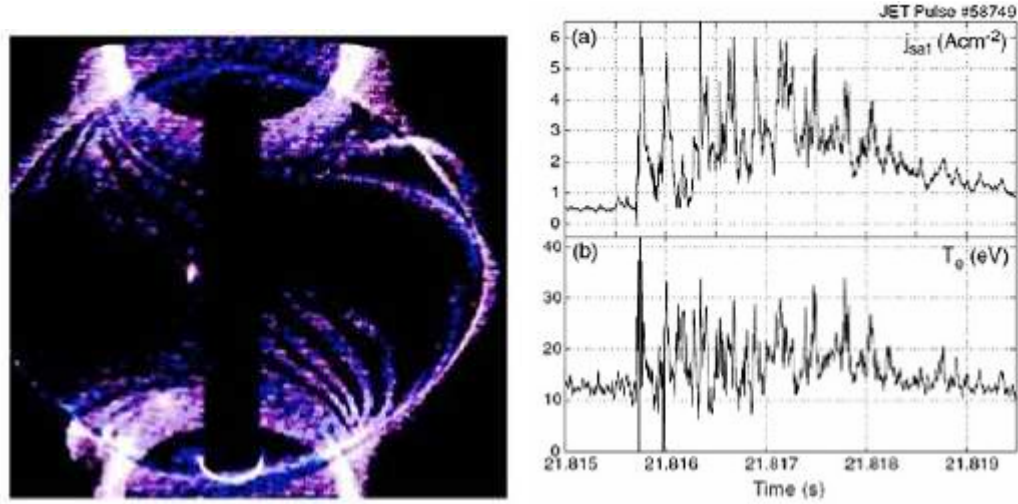


Figure 3.2. *Left:* Multiple plasma filaments obtained by high speed visible light camera imaging on the MAST tokamak (from [54]). *Right:* Evidence of filament fine structure from JET fast reciprocating turbulent transport probe located in far SOL. Extracted from [55-56].

The severity with which ELMs can reduce material lifetime, even in ITER (not to mention DEMO reactors, with higher stored energy and thus higher ELM energy transients) has focused the fusion community's attention onto this phenomena in recent years. Understanding the physical mechanism responsible for the particle and power exhaust due to the ELM and developing predictive capability with regard to ITER is an

issue of highest priority. This thesis contributes to this research effort in attempting to model the ELM transient evolution in the SOL and the subsequent effect at the divertor target. Before describing in subsequent chapters the methodology of this approach and presenting simulation results, the following sections outline some of the key features of ELM classification, the ELM cycle and a brief description of some aspects of the theory of ELM formation.

3.1. ELM classification

A variety of ELM types have been observed in tokamaks [50]. The main ELM classification is in terms of dependence of ELM frequency on heating power P . An important parameter characterizing the ELMs is their size in terms of expelled energy per event ΔW_{ELM} , which is often expressed in terms of drop in total plasma diamagnetic energy W_{dia} during an ELM, and its fraction of the energy stored in plasma, $\Delta W_{\text{ELM}}/W_{\text{plasma}}$ [57] (see **Fig.3.1**). The basic classification including the most common ELM types is described briefly in the following:

- 1.) **Dithering ELMs** occur in the vicinity of the L-H transition threshold power $P_{\text{L-H}}$, and are thought to be transitions back and forth between L- and H-mode confinement.
- 2.) **Type III ELMs**, referred to often also as “small” ELMs, appear after the L-H transition when heating power P is increased. The bursts are small ($\Delta W_{\text{ELM}}/W_{\text{plasma}} \sim 1\text{--}3\%$) and frequent with repetition frequency of ELM events $f_{\text{ELM}} \sim \text{few } 100 \text{ Hz}$, which decreases with increasing input power above $P_{\text{L-H}}$. Type III ELMs are usually associated with reduced H-mode confinement (compared with Type I ELMing H-mode – see below).
- 3.) **Type I ELMs**, called also ‘large’ or ‘giant’ ELMs occur when more heating power is added to a Type III ELMing H-mode [58]. They do not have a definite threshold in terms of energy loss, but usually $\Delta W_{\text{ELM}}/W_{\text{plasma}} > 2\%$ is found. Even if most machines have very steady Type I ELMing H-modes with periodic ELMs, also large isolated and irregular bursts are observed. Unlike Type III ELMs, f_{ELM} of Type I ELMs increases with rising heating power P .
- 4.) **Type II ELMs**, known also as “grassy” ELMs, are associated only with strongly-shaped plasmas (high plasma triangularity) and high pedestal pressure. In comparison with Type I ELMs, they have lower magnitude and higher frequency, though plasma confinement is similar to that in the Type I regime. Type II ELMs are almost never seen alone and come usually mixed with ELM-free periods inside Type I phases.

Typical examples for three of the above ELM Types can be seen in **Fig.3.3**.

Type I and Type III ELMs are by far the most commonly observed in tokamaks and are of high relevance to ITER. It is now known, however, that Type I ELMs lead to unacceptable plasma-facing component lifetime. Type III ELMs, which occur at lower pedestal pressure and hence lower confinement, are not suitable for ITER’s baseline, unless the confinement is gained back by operating at higher I_p . The key problem is the risk if the Type I ELMs turn out to be unmitigatable (whilst still retaining confinement). In that case the solution might be to revert to edge plasma with Type III ELMs and hence suffer the penalty of reduced confinement. The drop of 20% confinement means a drop of fusion gain to around $Q = 5$, a 50% of $Q=10$ mission goal. Hence the study of both these

types of ELMs is very important. **Tab.3.2** offers the main parameters of the four typical ELMs found at TCV and JET which are simulated in this work (see chapter 6, 7).

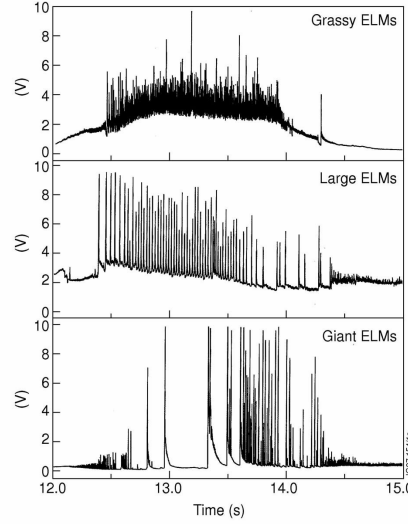


Figure 3.3. Examples of D_α signals obtained for different ELM Types [3].

	Type III TCV	Type I TCV	Type I JET	Big Type I JET
ΔW_{ELM}	700 J	3 kJ	200 kJ	750 kJ
$\Delta W_{\text{ELM}} / W_{\text{plasma}}$	2.5 %	12%	5%	12%
f_{ELM}	200 Hz	50 Hz	30 Hz	1-2 Hz – irregular
v_{ped}^*	0.7	0.15	0.12	0.09

Table 3.1. ELM characteristic parameters for typical Type I and Type III at TCV and JET, v_{ped}^* is the normalised neo-classical pedestal collisionality (see Eq.2.5).

3.2. Current understanding of the ELM phenomenon

ELMs are among the most intensely studied and relatively poorly understood phenomena in tokamak edge plasmas. They were first discovered on the ASDEX tokamak in 1980 [59] (as a phenomenon accompanying the H-mode) and since then have been a subject of steady research activity. Over recent years, this activity has taken on new urgency with the realisation that ELM-induced PFC erosion will be too severe for the “natural” ELM amplitudes expected on ITER to be tolerated (see the introduction of this chapter). Several reviews of the topic [28,60-71], including studies describing the behaviour and theories of the ELMs [50,58,62] exist in the literature. The phenomenology of ELMs together with various signatures of the physics processes involved, are reviewed in [62], where the observations common to studies of ELMs on

the different machines are summarized. In the following sections the most important observations and existing theories on the current understanding of these complicated transient phenomena are summarized, with emphasis on a discussion of the following issues:

- 1.) Where, why and how the ELMs arise? – “origin”
- 2.) What do they look like? - “structure”
- 3.) How they propagate from the place of their origin out into the SOL? – “perpendicular transport”
- 4.) How they propagate to the divertors? – “parallel transport”
- 5.) How they interact with PFCs, especially divertor targets – “heat loads”

In the description of the ELM phenomenon there are two important terms, **instabilities**, which are most likely the origin of the ELM event and **filaments**, which are associated with the evolution of the ELM after its onset and expelling to the SOL. The stability of plasma represents the primary limitation on the effectiveness of the fusion reactor expressed by β and thus on fusion power density. All models (theories) use pedestal plasma instabilities to explain the ELM origin and behavior [61-62]. In other words, simply said, the plasma goes through a cycle where it is destabilized and then stabilized again. The stability against these instabilities governs the behavior of the edge plasma [58] and is based on the MHD energy principles.

3.2.1. ELM-cycle

The time between two ELMs is usually much longer than the ELM event itself. The ELM phenomenon as an event during the ELMy H-mode can be pictured schematically as a cycle consisting of five phases (from large part described in [72]), which are depicted on **Fig 3.4**. Note that the terminology used to denote each particular phase is not generally used in literature, but is used here as a useful reference for discussion of the simulation results to be presented in chapters 6 - 7.

Phase ‘1’ corresponds to the situation before the ELM, the so called ‘**steady state**’ or **pre-ELM** phase, when plasma pedestal is stable and H-mode is ELM-free. The steep pressure gradient at the edge is maintained by the edge transport barrier.

Phase ‘2’ represents the ‘**growth**’ stage, when the precursors of the ELM appear in the pedestal before the plasma crosses the separatrix. Development of flute-like ripples in the pedestal ($\tilde{n}/n \ll 1$, where \tilde{n} and n are averaged thermodynamic values of these perturbations and of ambient plasma respectively) is accompanied by the linear growth of the small perturbations. This process is considered as MHD activity (in case of Type I ELMs with origin in the ideal MHD peeling-ballooning modes (see section 3.2.2.1).

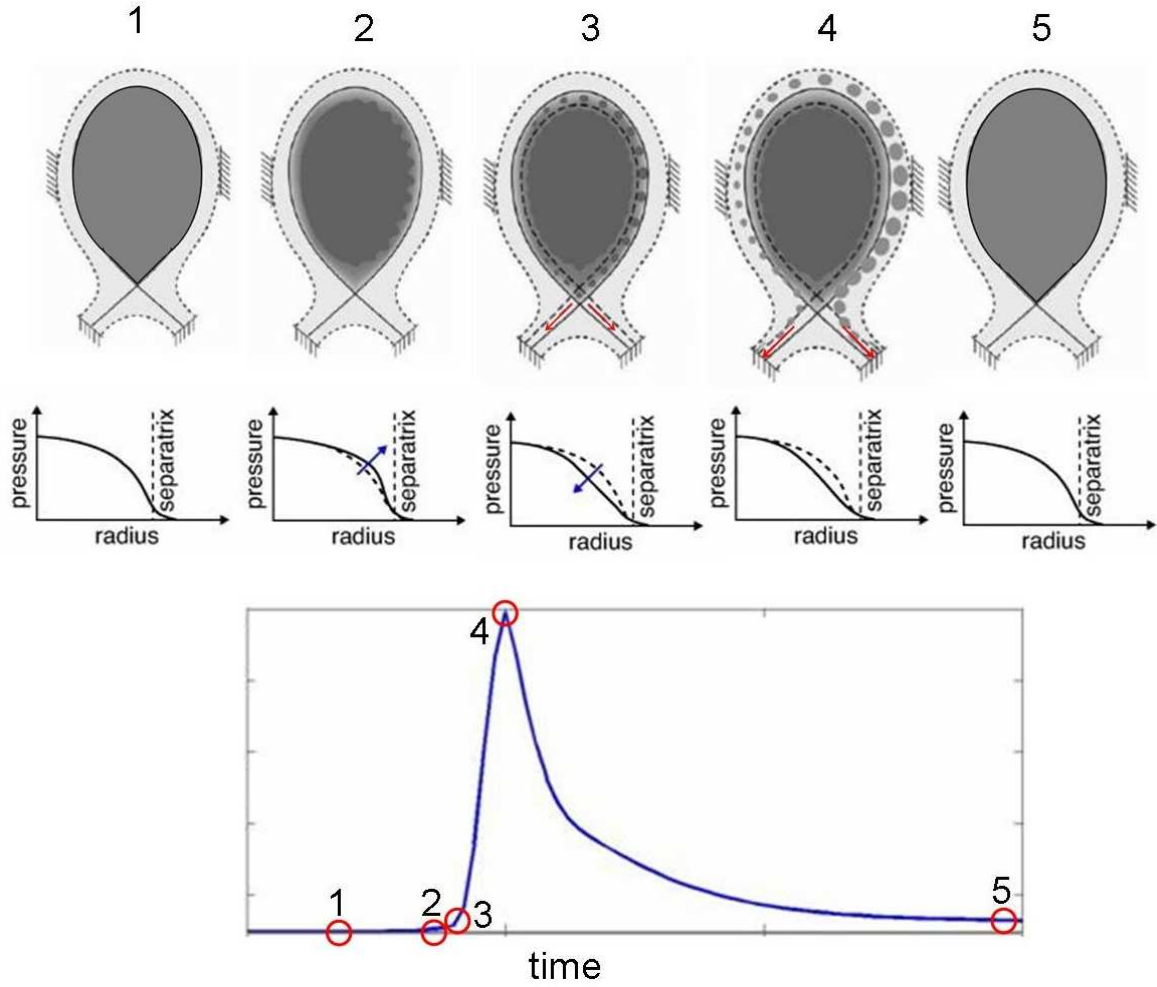


Figure 3.4. ELM cycle including 5 subsequent stages corresponding to the red circles on the top of the D_α signals during the ELM cycle (*lower*). Top: The poloidal cross-sections with the ELMs indicated as grey circles moving radially outwards from the core to SOL [72]. Red arrows indicate their movement towards the targets. Middle: The corresponding upstream outer midplane radial pressure profiles.

Phase ‘3’ is a ‘**saturation**’ phase when the onset of the ELM occurs by the growth of instability and ELM crosses the separatrix. The instability increases in magnitude until the linear growth saturates. Simultaneously, the pressure gradient builds up and when it exceeds a critical value for stability, flute-like perturbations change into non-linearly evolving distinct plasma filaments ($\tilde{n}/n \sim 1$). The pressure itself does not necessarily cause this instability, but it can be triggered by an electric current driven by the pressure gradient, so-called bootstrap current, I_B (see section 1.2.1). The filaments are accelerated outwards and they consequently intersect the separatrix and enter into the SOL. The pedestal pressure collapses and after very short time the D_α signal starts to rise (see **Fig.3.4.lower**). The mechanism by which filaments cross the separatrix (which would appear to require magnetic reconnection) is not yet fully understood and will be addressed later. Formation of the non-linear plasma filaments is most probably a

consequence of transport (drift-ordered) effects or non-linear MHD ordered effects (see section 3.3.3).

Phase ‘4’ is the ‘**exhaust**’ stage, during which the filaments, once in the SOL are subject to strong parallel losses along the field lines to divertor targets. The evolution of the ELM filament involves strongly non-linear perturbations ($\tilde{n}/n \geq 1$). The particle, momentum and energy content of filaments, together with the current density associated initially with the pedestal plasma are conveyed by parallel (poloidal) convection and conduction to the divertor targets. During this phase the plasma dynamics in the SOL are the result of competition between radial propagation and **parallel losses** which in turn also determines the distribution of particles, current and energy deposited on the PFCs. In the D_α temporal signal this exhaust stage corresponds in terms of plasma-wall interactions to the **ELM rise** phase and when the expelled plasma ends up in a form of the intense heat loads at the divertor plates the distinctive peak in the D_α radiation is produced.

The last phase ‘5’ is the ‘**recovery**’ or **post-ELM** phase. In this ‘**relaxation**’ phase, corresponding to the whole period after the ELM peak has been reached (in **Fig.3.4. lower** between points 4 and 5), the pressure gradient decreases until the plasma becomes stable again and thus identical to pre-ELM phase. The cycle is then repeated until the pressure gradient once again reaches the stability limit and another ELM occurs.

3.2.2. Observations and theories of the ELM formation

Since this thesis focuses only on the Type I and Type III ELMs, the following section aims to describe the main features and differences between them, concentrating especially on the phase of the ELM formation and confronting the theories summarised above with experimental observations.

The integrated model of the ELM contains phases with very different nature evolving on different timescales and thus also the underlying physics for them is different and they must be treated by different approaches. It is important to distinguish between the ELM as a coherent MHD instability and individual ELM filaments which are effects of that phenomenon in SOL [67-68].

The theories of ELM formation are based on the appearance of underlying instability, usually within ideal or resistive MHD to describe the ELM cycle (qualitatively in terms of periodic build-up of the plasma edge conditions to the point at which they trigger the instability, the consequent loss of the plasma and recovery phase for the cycle to repeat). Although MHD instability theory is generally known to successfully describe the linear stage of ELM evolution [73], the non-linear phase is considerably more complex [74].

3.2.2.1. Ideal MHD instability model – Model of Type I ELM

The model for the origin of Type I ELMs based on the experimental observation suggests that they are triggered by a combination of two MHD instabilities, ballooning modes with high toroidal mode number n and low-to intermediate- n peeling modes [75-76] (driven by pressure gradient α and current gradient respectively). This is confirmed

by several analyses of experimental data from different tokamaks [58,77] at AUG, [78] in DIII-D, [79] in JT60U, where general agreement with the predictions of the peeling-ballooning (P-B) model is found. These two radially localized instabilities are studied in detail in [75] and are briefly described in the following text.

The ballooning mode is driven by pressure gradient α ,

$$\alpha = 2Rq^2 \frac{dp}{dr} / B^2 \quad (3.1.)$$

and appears at critical pressure gradient α_c . All theories involving the ideal MHD ballooning limit predict $f_{ELM} \propto P$ where P is sufficiently large to dominate the transport losses, since the heating time to reach the critical gradient is inversely proportional to P . They remove an amount of plasma energy given by $\Delta W_{ELM} / W_{plasma} \propto \alpha_c$, which is independent of P [75]. Moreover, the ELM transport is observed to have a ballooning character and thus during the ELM, the particles and energy are expelled on the outboard unfavourable curvature side of the torus (LFS) [80-83]. However, while ideal ballooning limits the critical pressure gradient at which Type I ELM occurs ($\alpha \sim \alpha_c$) an additional trigger is required for the ELM to appear. Thus, other phenomenon – peeling mode with low toroidal mode number n – is responsible for the ELM itself [62]. The peeling mode, driven by edge current density and stabilized by edge pressure gradient, has features which are consistent with several properties of tokamak behavior in H-mode during ELMs. The appearance of the peeling or “kink” mode in the edge pedestal is supported by the fact that there is always a finite current density at the plasma edge, either due to a finite edge temperature to ensure the flow of the ohmic current, I_Ω or due to a finite edge pressure gradient in which case the pressure gradient driven Pfirsch-Schlüter (I_{PS}) [16] and I_B currents can contribute. The latter is parallel to the magnetic field and is clearly destabilizing, while I_{PS} is parallel to the field on the outboard side of the torus and antiparallel on the inboard side and as a result is stabilizing at the inboard and destabilizing at the outboard side. The peeling mode is expected to emerge at low edge collisionality while for higher collisionality it can be stabilized by sufficiently high pressure gradient [75]. As the plasma is heated the stability depends on the competition between the destabilizing effects from increase of T_e (which increases the I_Ω and if the collisionality is reduced, the I_B) and stabilizing effects of pressure gradient from for example I_{PS} .

Fig 3.5 depicts schematically the ELM cycle evolution in terms of the edge current density/edge pressure stability diagram for coupled peeling ballooning modes proposed by [61,75]. With a steep enough pressure gradient α and high enough current density J , the pedestal plasma reaches the low-to-intermediate- n stability limit and an ELM is triggered. In the stability analysis [58], the plasma was found to cross this stability limit just before an ELM. The mode structure of the ELM triggering instability can extend radially across the entire pedestal. The edge stability varies during the ELM cycle. Just before the ELM, the plasma is stable (in the ‘low shear’ region). Following the curve (1) on **Fig.3.5** first, the peeling boundary is crossed, the pressure gradient rises (as the edge pedestal develops after previous ELM crash) to the ballooning limit ($\alpha=\alpha_c$ – in **Fig.3.5** denoted as “ballooning boundary”), which restricts the further increase of pressure gradient. Meanwhile, as seen in curve (2), the edge current rises due to the rise in I_B and I_Ω until it reaches the right top corner of the stable ‘triangle’ (indicated as point 3 on **Fig.3.5**). This rise occurs on slower, resistive time scale. This eventually leads to

destabilizing effects and the low-to intermediate- n peeling mode instability occurs and triggers the ELM when the stability boundary is crossed. This is depicted on **Fig.3.5** as curve (4), representing the ‘ELM crash’ with loss of edge confinement and pressure gradient drop. During the ELM crash the edge pressure gradient flattens and the plasma becomes stable again. Between the ELMs the pressure gradient steepens, I_B builds up, the pedestal density and temperature increases and later during the ELM crash, they usually both collapse (sometimes only one of them).

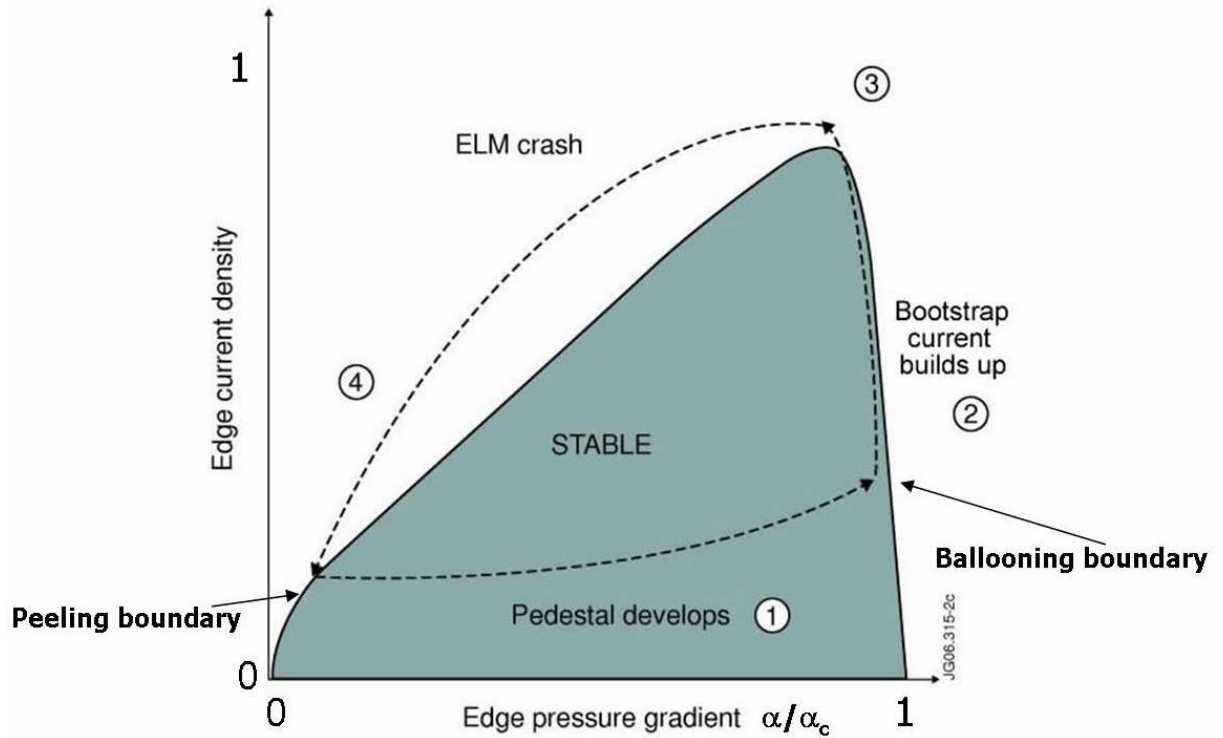


Figure 3.5. Type I ELM model extracted from [75]

3.2.2.2. Resistive MHD instability model – Model of Type III ELM

Unlike in the case of Type I ELMs, under the conditions in which the Type III ELMs exist, not enough I_B is driven in the edge region. Consequently the pressure gradient is significantly lower than in Type I ELM plasmas. Type III ELM plasmas are far from the low-to intermediate- n peeling ballooning stability boundary and it is unlikely that they are triggered by the same mechanism as the Type I ELMs. Compared to Type I ELM plasmas, the pedestal plasma of H-modes with Type-III ELMs is characterized by high collisionality. These instabilities are current driven and appear when plasma resistivity is rather high and thus the edge temperature rather low, generally below a critical temperature (e.g. 300 eV in ASDEX Upgrade [84]). This is consistent with the reduction of their frequency f_{ELM} with P , particularly at higher density and suggests a role of resistivity. Thus, these ELMs require a resistive (and not ideal) MHD model. The high

resistivity implies that the behaviour of Type III ELMs is more fluid-like (than that of Type I ELMs). This means that the use of fluid-based model (like the one in the SOLPS code) could be appropriate as a treatment of the Type III ELMs (at least more appropriate compared to kinetic Type I ELM).

Different resistive MHD instabilities based on observations from several machines have been proposed as the origin of Type III ELMs. A model based on data from ASDEX Upgrade [85] predicts resistive peeling modes with poloidal mode number $m=3$ and toroidal mode number $n=1$ and resistive ballooning modes with $m=3-20$ whilst resistive ballooning modes with $n \geq 10$ have been invoked to explain Type III ELMs on JET [86]. The resistive peeling $m=3, n=1$ modes are destabilized by an increase of edge current gradient and resistive ballooning $n > 2$ modes by rising pressure gradient. This observation is consistent with the feature of Type III ELMs, that they are known to stabilize with increasing power since plasma temperature and hence conductivity rise and thus f_{ELM} decreases because greater values of pressure gradient are required to destabilize the ELM at these higher T_e .

The other group of theories [81] is based on ideal ballooning modes with validity limited by $P \geq P_{L-H}$. Another possible theory [87] involves stabilization of peeling modes by increasing of the pressure for $\alpha < \alpha_c$. Based on resonant magnetic perturbations, micro-tearing modes have also been proposed as a trigger for Type III ELMs [88,89]. These modes, driven by the electron temperature gradient, are unstable in the steep density gradient region of the H-mode pedestal. They have growth times in the range 80-320 μs . Another possible candidate leading to Type III ELMs are the interchange instabilities driven by magnetic curvature and thermodynamic gradients (with the growth time $\sim 0.5 \tau_A$) [87].

3.2.2.3. Precursors of Type I and Type III ELMs

A variety of fluctuations are observed in conjunction with the ELM phenomenon. Of particular interest are ‘**precursors**’ which may have a causal relationship to, or act as a trigger for, the ELM burst of magnetic fluctuations and transport. There is a clear distinction between the ‘precursors’ for Type I and Type III ELMs. The main characteristics observed for the precursors of typical ELMs at TCV and JET are listed in the Table 3 and will be addressed in the following text for both Type III and Type I ELMs. This information helps to define what the “real ELM start time” is, which can be used as an indication for the simulations (see section 6.5.1).

	$\Delta W_{\text{ELM}} / W_{\text{ELM}}$	Precursor frequency	Precursor growth time τ	Precursor toroidal number n
JET Type I	2-9%	15 kHz	100 μs	0-4
TCV Type I	3-11%	50 kHz		
TCV Type III	2-6%	120 kHz	50 μs	5-8

Table 3.2. Typical ELM precursors observed at TCV and JET [62]

The Type I ELM onset takes place on the Alfvénic time $\sim \tau_A = L_{\parallel}/v_A$, where v_A is Alfvén speed (speed of typical plasma oscillation of ions and magnetic field, an MHD wave), which is much shorter than resistive time scales. Compared to the obvious Type III ELM precursors (see later), the precursors for Type I ELMs are less evident, slowly rotating or not even detectable. Turbulence is observed to grow on ideal MHD timescales, although toroidal asymmetries suggest that some other mode acts as a trigger. Type III ELMs have obvious magnetic precursors with high $n \sim 5-15$, ballooning structures, $f_{\text{ELM}} \sim 50-150$ kHz and they are slowly growing on the resistive time scale $\tau_{\eta} = L_{\perp}/D_{\eta}$, with L_{\perp} being the transverse gradient scale length of the electromagnetic field in which lines diffuse across the width of the erupting structure of the developing ELM [90-92].

3.3.3 Observations and theories of ELM filaments dynamics

The observation of filamentary structures associated with ELMs on several tokamaks [93-99] is a relatively recent development. Many ($\sim 10-20$ for Type I ELMs) plasma filaments appear during the exhaust stage of ELM. These filaments are \vec{B} -field aligned (flute-like) perturbations (observed to follow the pre-ELM magnetic field lines) with average thermodynamic quantities well in excess of the ambient values, so that $\tilde{n}/n \geq 1$. They are localized in the plane perpendicular to the magnetic field (drift plane) and have characteristic length scales along the field which are much longer than those across the field. The filaments can thus be pictured as isolated, field aligned plasmoids, whose pressure greatly exceeds the ambient background and are therefore driven mainly by their own field and pressure gradients. ELM filaments are bursts of particles expelled onto the open field lines moving collectively across the field to the main vessel wall and traveling to the divertor targets by parallel motion. They rotate toroidally and travel radially deep into far SOL and are detected long after the end of magnetic activity (for instance at JET $\tau_{\text{filament}} \sim 2\text{ms} \gg \tau_{\text{MHD}} \sim 200\mu\text{s}$). As the filaments move radially, they may stretch and shear in the perpendicular plane or even disintegrate into ever smaller filaments [100-102]. This filamentary break-up is consistent with the frequent observation, notably using electric probes in the SOL plasma, of a sharp “front” followed a slower “trailing wake” of smaller events [103]. (**Fig.3.2 right** and **Fig.3.6**). The filaments are usually observed to rotate toroidally at some fraction of the pedestal toroidal velocity and the combination of this toroidal rotation with radial movement appears, in experimental measurements at fixed poloidal/toroidal location in the SOL as a succession of arriving filaments, with intensity decreasing with the time. Analysis of the ‘exhaust’ stage in terms of the filaments and theory of ELM filament dynamics in terms of pedestal heat loss from filamentary object is performed in [103]. **Fig.3.6** shows an example from ASDEX Upgrade demonstrating how different filaments become visible at different times in the ELM evolution.

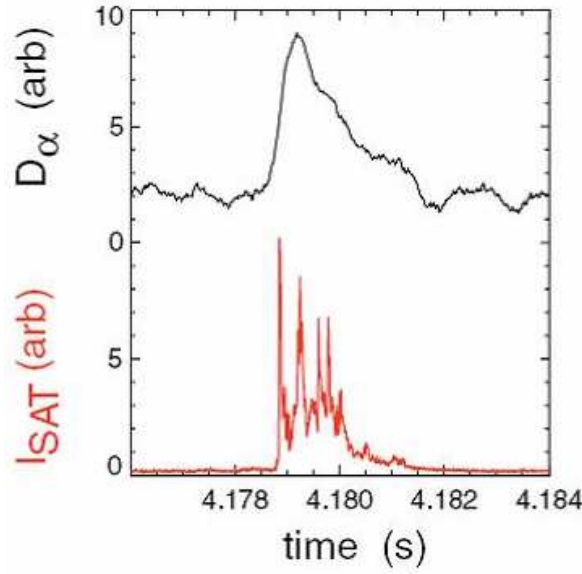


Figure 3.6. ELM filaments. ASDEX Upgrade target D_α and j_{sat} measurements temporal evolution of the ELM. Extracted from [104]

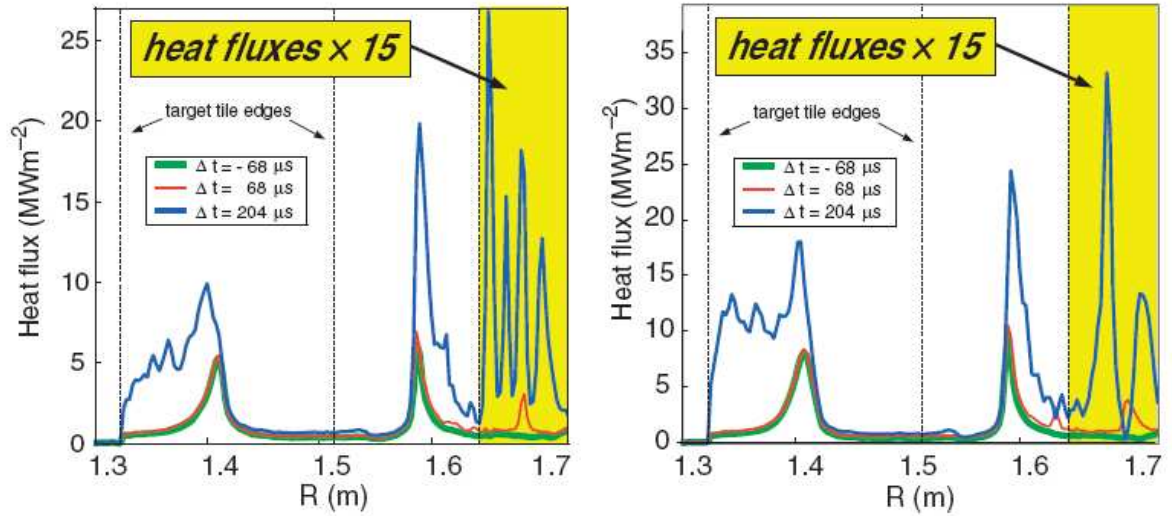


Figure 3.7. Time evolution of two ELM heat flux profiles at ASDEX Upgrade (#16724). The location and the amplitudes of the individual stripes vary strongly for each ELM. The yellow region defines the ‘remote tiles’ area with increased sensitivity. Extracted from [98]

The succession of filaments is observed not only in time, but also spatially, for example as discrete field aligned bands on divertor targets [105]. The filaments rotating with different fractions of radial velocity and being moved radially outwards differently and thus hit the target in the different distances from the strike point. The pattern of power deposition at the target plates invariably consists of an intense footprint at or near the separatrix, with individual filamentary bands located usually further out in the

divertor SOL. In cases where filaments are clearly detected far from the strike zones, they usually carry only a small fraction of the total ELM power [98]. If the filamentary picture of the ELM formation is correct (see **Fig. 3.4**), then the intense power deposition profile at the strike point is in fact itself composed probably of many filaments with the difference being that the geometry of the magnetic field (proximity to the X-point null) pushes the filaments extremely close together such that in the absence of a diagnostic capable of extremely high spatial resolution, the individual filaments cannot be distinguished. Only those filaments which propagate far into the main SOL are sufficiently separated to be clearly visible as bands at the target, by which time parallel transport has exhausted much of the filament energy. **Fig. 3.7** shows a recent example from ASDEX Upgrade, demonstrating the presence of filaments in the target power deposition profile.

The key feature of this picture as far as the modelling to be presented later is concerned is that, although the ELM appears, in reality, to be a composite event made up of many individual filaments, it can reasonably be treated from the point of the SOLPS simulations (which cannot account for the filamentary character) as a prompt increase in radial transport in the SOL.

The key observables pertaining to the evolution of the ELM filaments, which are based on the available experimental data from all large tokamaks are summarized in [106-107]. The radial velocity v_{\perp}^{ELM} of the filaments in SOL is strongly subsonic (much smaller than the pedestal sound speed): $v_{\perp}^{\text{ELM}}/c_s^{\text{ped}} \sim 0.01-0.1 \ll 1$. The measured time-of-flight values of v_{\perp}^{ELM} across many machines are $\sim 1\text{km/s}$ with both accelerating [54] and decelerating [55,108] filaments reported. Experimentally, v_{\perp}^{ELM} is in good agreement with radial velocity calculated from local gradients of electric potential obtained from reciprocating Langmuir probes (LP). Moreover the propagation velocity of turbulent filaments (blobs) in the SOL of L-mode discharges, corresponds well to the values of v_{\perp}^{ELM} . Even though initially the Type I ELM filaments rotate at the pedestal velocity, this rotational velocity decreases by factor of 10 across the SOL. This dissipation like the toroidal momentum is most likely due to the collisional dissipation of viscous friction with the background SOL plasma or due to sheath dissipation or resistivity caused by contact of filament with divertor targets [103]. The averaged v_{\perp}^{ELM} has been observed to scale with ELM size such that small Type III ELMs propagate more slowly than large Type I ELMs and consequently deposit a smaller fraction of their initial energy on the walls [55]. In the only existing analysis of Type III ELMs at TCV, rather high values of $v_{\perp}^{\text{ELM}} \sim 1\text{km.s}^{-1}$ have been found [109].

The delay between the onset of magnetic activity and arrival of hot electrons to the divertor targets

$$\tau_e \sim L_{\text{con}}/v_{\text{th,e}} \quad (3.2)$$

correspond to the prompt electron losses at the electron thermal speed $v_{\text{th,e}}$ and the values for JET ELMs are $\sim 10 \mu\text{s}$ observed in [110] by divertor target soft X-ray emission inferring the presence of hot electrons. Nevertheless the bulk energy pulse arrives at the targets with delay which corresponds approximately to ion pulse propagation at the pedestal sound speed c_s^{ped} ,

$$\tau_i \sim L_{\text{con}}/c_s^{\text{ped}} (\sim 100-300\mu\text{s at JET}) \quad (3.3)$$

Depending on the symmetry /asymmetry of the parallel connection length from the outboard midplane (\sim ballooning point) to the each target, there can be a delay in the arrival of pulses at the different targets $\Delta t_{\text{in-out}} \sim L_{\text{con,in}} - L_{\text{con,out}} / c_s^{\text{ped}}$. For example, at JET with $L_{\text{con,in}}/L_{\text{con,out}}=2$, the pulse arrives earlier on outer target ($\Delta t_{\text{in-out}} \sim 50\text{-}300 \mu\text{s}$). However for typical TCV magnetic equilibria $L_{\text{con,in}} = L_{\text{con,out}}$ and thus no delay is expected.

After the loss of the TB (\sim pedestal collapse) during the ELM, the radial SOL profiles of ELM filaments density and/or temperature closely resemble L-mode profiles and are about two times less steep compared to the inter-ELM H-mode phase. Note, that this observation suggests that radial ELM filament propagation is driven by similar mechanism as ohmic, L-mode and inter-ELM H-mode turbulence in the SOL [39].

The ELM filament ion temperature in the far SOL have been found to be much higher than the electron temperature ($T_i/T_e \approx 3$ at JET), indicating that electrons in the filament have cooled substantially compared with the ions (for instance at JET $T_e^{\text{ELM}} \sim 25 \text{ eV} \ll T_e^{\text{ped}} \sim 1 \text{ keV}$) [72].

Most (60-90%) of the total energy expelled during the ELM is deposited on the divertor targets [66-67,110]. The rest is deposited on the main chamber walls (up to $\sim 25\%$ in JET [108]) or can be radiated. The energy deposited on walls increases with ELM size and decreases as the separatrix-wall gap increases. The radial profiles of the power deposited on the divertor targets are comparable to the pre-ELM profiles in terms of the strike point location and profile width, which broadens typically by less than factor of 2 during the ELM compared with the inter-ELM situation.

3.3.3.1. ELM filaments dynamics from closed to opened field lines

From the previous section it is clear that the origin and formation phase of the Type I and Type III differ, however the exhaust stage is believed to be very similar. It should be noted that since the phase of ELM formation in terms of its precursors (origin) and also the exhaust phase in terms of radial and especially parallel motion of the plasma filaments are quite well understood, this is by far not the case of the process by which plasma moves out from closed to opened field lines and crosses the separatrix. There are number of ideas but no specific picture of this transition to the SOL exists.

Various models of ELM filament dynamics are analyzed in [77], where the important criterion to distinguish between two groups of theories is whether the observed filaments are carried along within magnetic flux tubes (MHD) or whether they drift across magnetic field lines (drift-ordered scheme described by drift hydrodynamics (DHD)). The ideal MHD filament theory is based on an extension of the linear MHD model developed for ELM stability (as described in section 3.2.2) into the non-linear MHD model of ELM dynamical evolution (transforming the linear ballooning theory into a non-linear dynamical ballooning theory) [74,111]. It can be imagined as an explosive growth of local fluid quantities appearing as an exploding flux tube radially protruding on the LFS, which remains connected to pedestal. This approach is valid only for the ELM filament explosion and not in the far SOL. It is restricted to the early non-linear phase without any drift-ordered effects until the separatrix is crossed. Once, the flux tube crosses the pre-ELM separatrix it accelerates to $v_{\perp}^{\text{ELM}} \sim c_s^{\text{ped}}$ and has drift-ordered dynamics. According to [77] the plasma which is already in the SOL would diffuse

across the boundaries of the flux tube with particle and heat diffusivities D_{\perp} , χ_{\perp} , due to some unspecified transport mechanism (for instance micro-turbulence driven by steep pressure gradient at the filament front or compression of magnetic flux surfaces due to flux tube propagation [103]). After the plasma has diffused, onto the open field lines, it is transported by convection and conduction with parallel velocity v_{\parallel} and heat flux density q_{\parallel} along the unperturbed magnetic field lines to the divertor plates. On the basis of the analysis performed in [77] it can be concluded that the integrated ELM model is best described by ideal DHD which is capable of describing the evolution of the edge-SOL turbulence and its suppression during the L-H transition, the evolution of the edge plasma pedestal profiles during the inter-ELM phase and also the MHD instability most probably responsible for the onset of the ELM.

The information above reinforce the justification of the assumption that the filaments near the separatrix all merge together and transport their energy to the targets as one.

3.3.3.2. ELM filament transport model

In general both fluid and kinetic approaches are used for the treatment of parallel transport of plasma during the ELM. A kinetic description solving the full Fokker-Planck Poisson system is included in 1-D particle in cell (PiC) simulations, such as in [112-113]. Kinetic simulations of the ELM transient with the BIT1 PiC code performed for JET relevant conditions including binary treatment of Coulomb collisions are described in [32]. The electron and ion heat fluxes are reported to rise on the electron (Eq.3.3) and ion (Eq.3.3) timescales, in accordance with the observations mentioned in the first part of the section 3.3.3. More details are given also in chapter 6 where a comparison of kinetic simulations with those of fluid SOLPS code of ELMs at TCV and JET is presented.

Simple models of parallel energy loss driving the transients have been developed in [103], where both fluid and kinetic approaches are used. An analytic approximation of kinetic parallel losses from ELM filaments has been derived using a 1D model of parallel transport along open field lines where the transition of the filament from the closed to open field lines (from pedestal to SOL where it is connected to divertor targets) is imposed as a free parameter – radial pedestal velocity ($v_{\perp}^{\text{ped}} = v_{\perp}$), estimated from the radial ELM propagation in terms of average velocity of ELM filament front ($v_{\perp}^{\text{ELM}} \sim 500\text{--}1000 \text{ m.s}^{-1}$ at JET) [102,115-119]. In this time-dependent transport model, time is converted into distance through velocity, v_{\perp} is fixed and model is used to see if experimental measurements are reproduced. The particles diffusivity radial transport coefficient D_{\perp} is also assumed to be known. This kinetic model describes the collisionless transport of transient particles and energy flux onto the surface (e.g. free streaming particles). It is derived from the simplest possible form of the Boltzmann equation neglecting both forces and collisions. The temporal evolution of the ELM filament is approximated through the Green's function approach, describing the response of the dynamic equations to an impulse source given by the Dirac delta function. The violation of quasi-neutrality as a direct consequence of neglecting the Coulomb force in Vlasov-force free equation is eliminated by gradually imposing weak quasi-neutrality ($n_i \sim n_e$) within the Maxwellian model (using the delay on the ion thermal transit timescale),

which allows the electron and ion densities to evolve independently in the initial phase of the ELM ($t \ll \tau_{||,i}$), but requires the re-establishment of quasi-neutrality on the timescale of ion thermal time ($t \geq \tau_{||,i}$). This model successfully reproduces the delay observed in experiment [94,120] and in 1D kinetic simulations of ELM pulse propagation [26,32]. Despite the simplifications the simple kinetic model captures the relevant ELM features produced by numerical solution of the Fokker-Poisson system used in PiC code BIT1.

In the fluid parallel transport model, which should be valid normally only in a collisional system, the even velocity-moment coupled density and energy equations including ion-electron collisional energy exchange (see chapter 2) are numerically solved [103]. Unlike the collisionless kinetic approach, the effects of the collisions important especially as filament evolves (in presence of subthermal particles), are easily included in the fluid model by appropriate relaxation times. The sheath limited regime characterized by $M_{||}=1$ and constant γ_e, γ_i is valid only for low collisionality and is not a good candidate to model ELM transient with fluid approach. However, the fluid description with some kinetic corrections does capture the parallel loss of particles down a flux tube.

The 2D multi-fluid, 3D neutral Monte-Carlo suite of codes, SOLPS, used throughout this thesis, solves the fluid equations in both parallel and radial directions and includes the neutral particles in 3 dimensions. More details are found in the next chapter. The capability of this fluid code to satisfactorily describe the inherently kinetic ELM events, is questioned in this thesis by comparison with kinetic 1D PiC model and experimental data (see chapters 6,7).

4. Modelling tool – SOLPS

Simulating experiment according to the rigorous principles of mathematics and physics is an important part of research, fusion being no exception. ‘Computer modelling’ has a very distinguished role of mediator between experimental data and physics theories. Computer codes represent powerful modelling tools.

Plasma is modelled as a large set of free charged particles that move chaotically at very high velocities and are subject to electromagnetic interactions. Even though the fundamental plasma physics theory used in the models is well understood and validated, the real plasma in tokamaks is an extremely complex system and it is beyond the means of any model to follow the positions of vast number of particles moving rapidly in electromagnetic fields that are self-generated by these particles. Moreover with respect to high velocities of plasma particles, the volume of plasma to which the simple model of infinite homogeneous plasma could be applied, would be hardly realistic.

The major challenge when modelling high temperature plasma behaviour is the particle and energy transport, which are by nature turbulent and thus non-linear. While the rate of change of the parameters in the linear system is proportional to the current state of the system, a slight change of input parameters in a non-linear system can lead to substantial modification of the solutions. Edge plasma modelling must account for a further significant complication – the continuous exchange with the external environment (PFCs) together with the presence of large quantities of neutral atoms and molecules associated with processes occurring at the solid-plasma interface. In addition, steep gradients of the basic parameters (like temperature, density, electric and magnetic fields...) play an important role and thus must be accounted for. Moreover, the spatial scales are very wide (~ 10 m for the SOL lengths vs. ~ 1 μ m for the sheath width).

The performance of future facilities like ITER is usually based on the scaling-laws – the measured dependencies of plasma parameters collected on existing tokamaks. Even though these are purely empirical they have been proven to be quite robust and thus it can be assumed that they are based on the dominant physical mechanism which can be modelled despite of turbulent nature of plasmas. Successful models validated by experimental data contribute not only to the increasing confidence of the performance of the future machines but in addition improve the understanding in the plasma physics. The efforts of the fusion modelling community are increasingly directed towards “integrated tokamak modelling”, in which a package of models consisting of many interlinked tools modelling the different regions of plasma is being developed. The biggest challenge in this respect is modelling of the plasma edge.

If the plasma is simulated at the individual particle level, the transport of the particles and energy is due to particle collisions and particle drifts due to gradients in plasma (potential gradients producing electric fields, pressure gradients producing diamagnetic drifts, B-field gradients causing grad B drifts) and is treated by kinetic codes. These are tremendously CPU intensive already at the level of 1D. Two-dimensional kinetic treatments for charged particles are only feasible on small spatial scales and usually restricted to a rather simple geometry and developed for specific problems such as the electrostatic sheath. One of the most advanced 1D kinetic codes is

the particle-in-cell (PiC) code BIT1, the results of which will be compared with the 2D fluid simulations that form the core of this thesis (more details see in section 6.1.5.6).

A less CPU intensive approach is to study the plasma as a fluid and model it as a continuum consisting of an effectively infinite number of particles whose transport can be described by diffusion and convection. The transport described by turbulence is captured in fluid turbulence codes such as 2D ESEL [42] or 3D turbulent code TOKAM-3D code developed recently [121]. Since the SOL is characterized by the competition of transport perpendicular to the magnetic surfaces and parallel transport to the material boundaries intercepting open field lines, a two-dimensional description of the edge plasma, assuming toroidal symmetry, is the minimum requirement if volumetric processes (which are so important in capturing much of divertor plasma behaviour) are to be captured.

Three 2D fluid code packages, UEDGE [122], EDGE2D [123] and B2 [124] have seen the most widespread use in tokamak edge modelling over the past 15 years or so. More recently, the Japanese code SOLDOR [125] has been developed. These codes solve different multi-fluid versions of the 2D Braginskii equations [29], which in principle contain all information necessary to describe collisionally dominated magnetically confined toroidal plasmas. Only the newer versions of the code packages, like B2.5 include the typical neoclassical effects and allow the activation of current and drift related terms.

To include the neutral species and model the neutral-plasma interactions, the fluid codes usually contain a simplified fluid approximation of the neutral model where no molecular and other effects are considered [126]. More realistic simulations are possible when the plasma codes are coupled to dedicated Monte-Carlo neutral transport codes such as DEGAS2 [127], NIMBUS [128-129], EIRENE [49,130] and NEUT2D [131]. The coupled packages are EDGE2D-NIMBUS [13], B2 (and B2.5)-EIRENE [133-134], UEDGE-DEGAS2 [135], UEDGE-EIRENE [136] and SOLDOR-NEUT2D [131], where the first two represent the biggest and the most comprehensive edge plasma code packages and are benchmarked in this work. In these code packages, the set of neutral particle histories is simulated on a plasma background provided by the fluid code or specified by the user. The use of Monte-Carlo codes considerably increases the CPU consumption of the simulations. In fact for example, over the past 15 years, although computing power has doubled around 7 times, a complete SOLPS simulation of an ITER edge plasma still requires the same CPU time (~2 months) today as it did in the early '90s [137]. This is because with each increase in computing power, there is a compensating increase in the sophistication of the code package.

4.1. SOLPS5.0

The code package SOLPS5.0, including the coupled B2.5 plasma and EIRENE Monte-Carlo neutral codes, is the principal tool used in this thesis to simulate the ELMing H-mode SOL of JET and TCV. The **Scrape-Off Layer Plasma Simulator** (SOLPS) code suite can be used for a variety of purposes, such as understanding the basic physics concepts, deriving scalings for various quantities, integrating all available experimental measurements and making predictions for future devices [17]. It comprises a number of separate components [138] – a manual can be found online [139]:

- 1.) DG – graphical interface for the establishment of the configuration of simulated discharge used as input for the code [139].
- 2.) CARRE – grid generating code [140]
- 3.) B2.5 – two-dimensional fluid code for SOL and edge plasma [141-143] including fluid treatment for the neutrals [126].
- 4.) EIRENE – three-dimensional Monte-Carlo code for neutrals [49]
- 5.) b2plot – tool for visualizing the code output [139]

A comprehensive description of the B2 code can be found in the PhD thesis of M. Baelmans [133] and the edge plasma physics in the B2-EIRENE package is extensively described in [17]. Additional useful documentation of the SOLPS code suite, including the two above mentioned reports, and others such as manuals of DG, CARRE, SOLPS introductory course slides, etc can be found on each server where SOLPS is installed in the user's personal code directory /doc/.

As shown in **Fig.4.1**, elements from quite different fields of physics must be combined in a model able to properly describe the SOL. Several of these issues have already been addressed in the previous chapters and they will be revisited below.

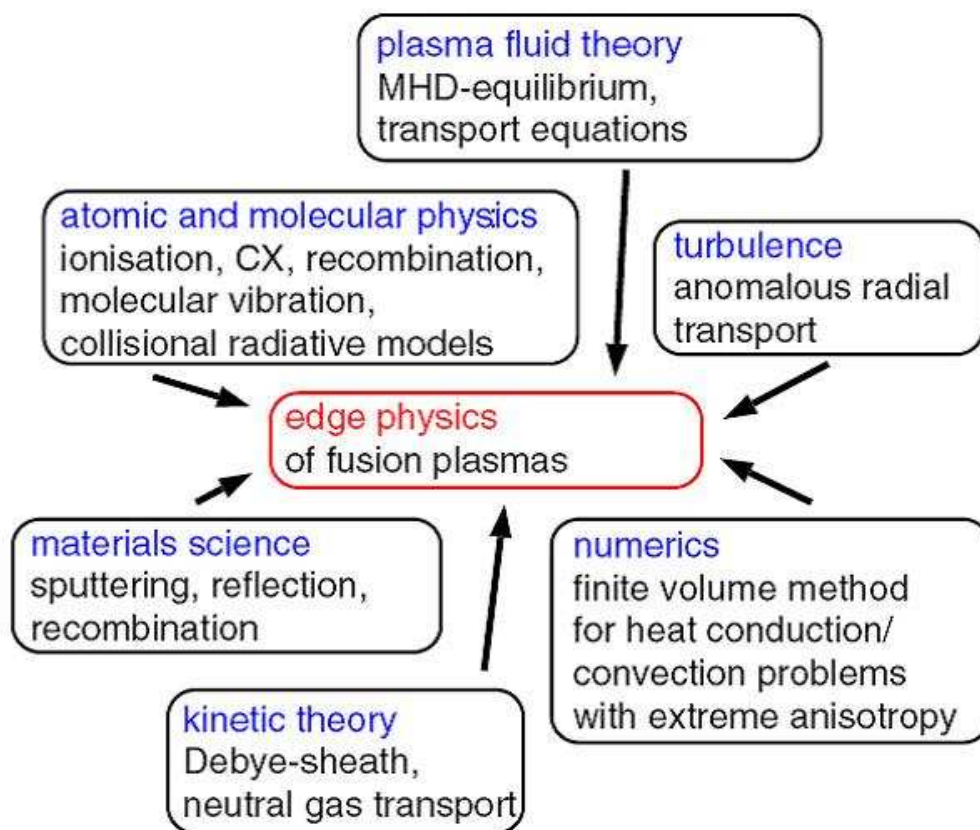


Figure 4.1. Ingredients for model to describe SOL; extracted from [17]

4.1.1. Geometry

Two-dimensional fluid models make use of the tokamak toroidal axisymmetry to describe the plasma parameters in the poloidal cross-section. In principle, there are two basic coordinate systems, illustrated schematically in **Fig. 4.2**: toroidal-poloidal-radial (ϕ - θ - r , referred to as ‘poloidal’) and parallel-diamagnetic-radial (\parallel - \wedge - r , referred to as ‘parallel’). The Braginskii transport equations are closed in the parallel direction aligned with the magnetic field \vec{B} and anisotropic fluid viscosity and thermal conductivity are easier specified in a parallel coordinate system. Since the three characteristic directions of the plasma motion are parallel to magnetic field, diamagnetic (perpendicular to magnetic field) and radial (normal to flux surfaces), the ‘parallel’ coordinate system is also historically predominant. However, the toroidal symmetry is easier imposed in the ‘poloidal’ coordinate system, where it is more computationally convenient. The transformation of the Braginskii equations from the parallel to poloidal coordinate systems is derived in [133], where all relevant fluid equations, expressed in poloidal coordinates assuming toroidal symmetry are defined. In such a two-dimensional model the plasma is described using an orthogonal poloidal-radial coordinate system (θ, r) with ignorable toroidal coordinate ϕ .

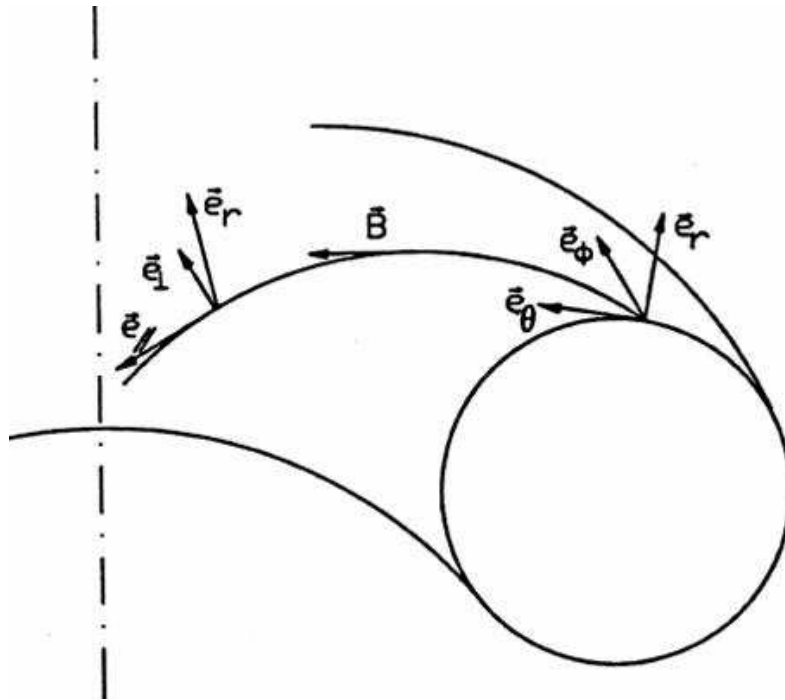


Figure 4.2. Two basic coordinate systems for tokamak application; note that \perp corresponds to \wedge in this drawing. Extracted from [133]

In order to generate the simulation grid, the poloidal cross-section of the plasma configuration to be modelled is required. The SOLPS code includes a database of the 2-D poloidal cross-sections of the most commonly used experimental geometries from a variety of tokamaks to which SOLPS has been applied. If a new configuration is needed,

it is generated using DG from the technical drawing file in HPLG format. Poloidal flux surfaces are provided by magnetic equilibrium reconstruction codes solving the Grad-Shafranov equation (the EFIT [144] and LIUQE [145] codes are used to generate the poloidal magnetic flux for JET and TCV respectively). When these are uploaded to DG, the type of divertor (for example SNL - see later in chapter 5) and grid spatial resolution is defined by the user. The latter is performed through the choice of the number of poloidal surfaces and radial cells in the core, SOL, PFR and divertor leg regions of the grid. Higher resolution is used where strong gradients in the plasma are expected, such as radially in the separatrix vicinity and poloidally close to the targets and X-point. From a practical point of view, the magnetic surfaces are by default allowed to intersect the wall surfaces only at the targets and thus intersections with the main chamber walls are not included.

The output file created by DG is then used by the program CARRE to generate the curvilinear, quasi-orthogonal grid, strictly aligned with the magnetic field lines, which represent the so-called ‘physical domain’ used by B2.5 and EIRENE. The output of CARRE includes the metric coefficients required to transform this physical geometry to the topologically rectangular mesh, referred to as ‘computational domain’ on which the numerical calculations are performed. **Fig.4.3.** illustrates the computational and physical domains, where the different regions are colour coded.

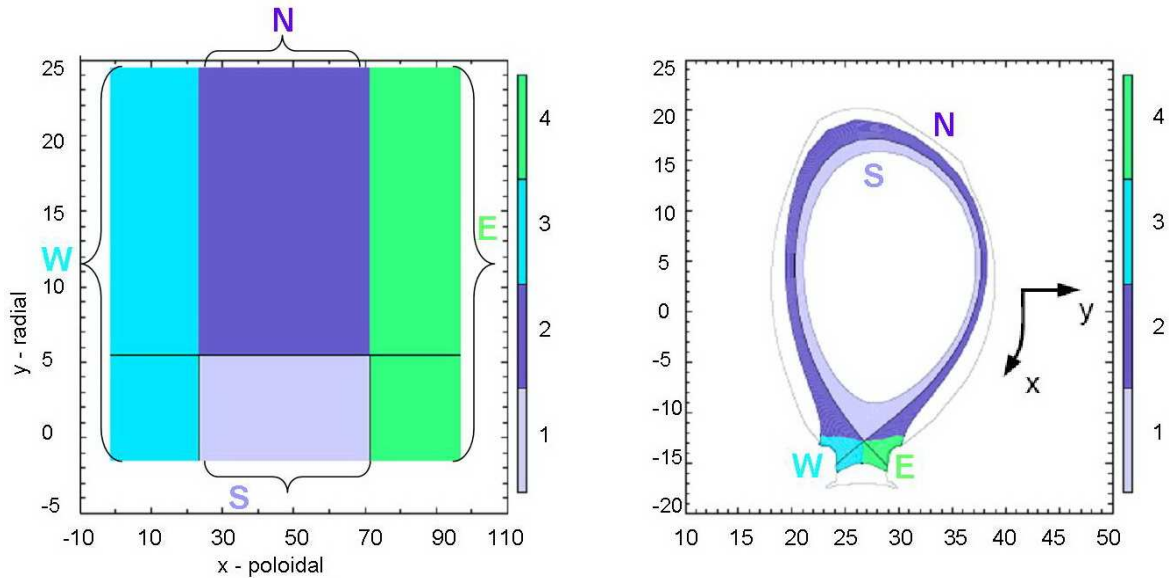


Figure 4.3. Computational (left) and physical (right) domains with boundaries

There are four main boundaries, denoted east ‘E’, west ‘W’, north ‘N’ and south ‘S’. By default the positive direction of flow in B2.5 is from inner to outer target (‘W’ to ‘E’) and from core plasma radially outwards perpendicularly to the magnetic flux surfaces (‘S’ to ‘N’). The ‘south’ boundary represents the innermost boundary which is often referred to as ‘core’ boundary. The ‘north’ boundary represents the furthestmost extension of the grid towards the main chamber and it is called also ‘outer’ boundary. The SOLPS grid uses an (x,y,z) coordinate system with x being the poloidal coordinate, y the radial coordinate orthogonal to the flux surfaces and z is the (ignored) toroidal

coordinate. The coordinate \perp corresponds to the direction perpendicular to the magnetic field and the y-axis. The directions of magnetic field and plasma current correspond to the normal operation conditions of ASDEX-Upgrade tokamak (FWD $B_\phi = \text{ion } \nabla B$ drift directed towards the X-point of an SNL equilibrium - downwards). However, this becomes important only if SOL flows are activated in the simulations (to study the influence of drifts), which is not the case in this work, or in the case of inclusion of a parallel velocity at the inner core boundary. The latter has been attempted in this thesis to study such a component as a mechanism for driving ELM in-out asymmetries in target power loads (see section 6.3).

4.1.2. B2.5

The B2.5 code is the latest version of the B2 code originally written by Braams [124]. It is written in FORTRAN 90 using dynamic memory allocation. B2 is the plasma code in the SOLPS4 package which has been used exclusively to date by the ITER team to simulate the ITER divertor [18]. It solves the multi-species fluid equations including the continuity equation, momentum and energy conservation equations.

For the purposes of edge plasma modelling, modifications to the neoclassical fluid equations are made. Certain simplifications are used in the fluid model (B2.5) in order to render the model computationally easier to solve whilst retaining a sufficiently accurate description of edge physics phenomena. For example, many mixed derivatives and velocity gradients in the viscous stress term are typically neglected in order to reduce its contribution to conductive type. Magnetic field gradients and metric coefficients are usually neglected.

In the old B2 version of the fluid code, transport in a given flux tube is assumed to be dominated by parallel flow and drifts are neglected. Moreover the approximation of ambipolar flow is used to eliminate the electric currents which removes many terms from expressions for the tensor fluxes and it is not necessary to solve Ohm's law in conjunction with the set of transport equations [133]. In B2.5, both electric currents and perpendicular flows are introduced, the latter resulting in mixed derivatives in the continuity and energy equations. The set of equations in B2.5 is thus extended by current continuity and charge conservation equations in comparison with B2. For a detailed description of the equations in B2.5 see [141-142]. Drift terms are also included in B2.5 where they can be switched on by the user. The activation of such terms, however, requires significant efforts and is typically used only by experts.

4.1.2.1. Justification and limitations of the fluid description

The validity of the fluid approach in the boundary layer of the tokamak plasma may be questionable. In general, however, the fluid description can be successfully applied to edge plasma modelling. As described in section 2.1.2, the condition of validity of the fluid approach is met when inequality Eq. 2.10 is satisfied. When examining the validity of Eq.2.10 for the characteristic scale length for magnetic field B , $L_{\parallel,B}$ which approximately equals the connection length in SOL, L_{con}

$$L_{\parallel,B} = \left| \frac{\nabla_{\parallel} B}{B} \right|^{-1} \gg \lambda_{ee}, \lambda_{ii} \text{ (where in orders of magnitude : } L_{\parallel,B} \sim 10\text{m and } \lambda_{ee,ii} \sim 0.1\text{-}1\text{m)},$$

an examination of this criterion concludes that the plasmas in the boundary layer of all TCV and JET discharges analyzed in this thesis are likely to be sufficiently collisional for the fluid equations to be valid. This is not true, however, in the collisionless sheath region with steep gradient of n . Even if fluid treatment up to the sheath edge gives the results of plasma parameters of proper order of magnitude [146] it does not describe properly the physics in this region. This issue is treated in the fluid codes, including B2 and B2.5, by taking the sheath entrance as a boundary to the computational domain and imposing appropriate boundary conditions, such as sonic flow ($M_{\parallel} = 1$) and prescribing energy transfer coefficients. Since the full fluid treatment in the edge gives better results than expected from the purely theoretical considerations [147], the pragmatic approach of imposing boundary condition at the sheath entrance deduced from kinetic models appears to be justified.

4.1.2.2. Flux-limiters

In order to account for the kinetic effects at the sheath where steep gradients exist, the parallel electron (and possibly ion) thermal conductivity is flux-limited in the fluid codes [148]. This ensures that the heat conduction as calculated from the classical formulation is maintained below the maximum physically possible value. This upper limit for the parallel electron heat conductivity is given by the corresponding maximum convection provided by electrons, corresponding to a directed velocity equal to their thermal speed [133]. The heat flux limit of electron parallel heat conductivity is formulated as

$$\kappa_{\parallel} = \frac{\kappa_{\parallel,SH}}{1 + \left| \frac{q_{SH}}{q_{lim}} \right|} \quad (4.1.)$$

where q_{SH} is the classical Spitzer-Härm heat flux (Eq.2.57) with $\kappa_{\parallel,SH}$ the classical Spitzer- Härm heat conduction coefficient and q_{lim} the heat flux limit (Eq.2.58), the electron flux limiting factor inside q_{lim} is usually set to $\alpha_e = 0.2$, based on the results of kinetic calculations. The situation for ions is less clear [17], but usually high flux limiters, such as $\alpha_i = 10$ are chosen, corresponding effectively to no limit at all. The corrected parallel electron heat flux is given by

$$-\bar{q} = \frac{\bar{\nabla} T_e}{\left| \bar{\nabla} T_e \right|} \cdot \frac{1}{\left| \kappa_{\parallel,SH} \nabla T_e \right|^{-1} + q_{lim}^{-1}} \quad (4.2)$$

A similar procedure applies to the derivation of a parallel momentum flux limit

$$\eta_{\parallel} = \frac{\eta_{class}}{1 + \left| q_{class}^m / q_{lim}^m \right|} \quad (4.3)$$

where the classical momentum flux is

$$q_{\text{class}}^m = -\eta_{\parallel, \text{class}} \frac{\partial u_{\parallel, a}}{\partial x} \quad (4.4)$$

with u_{\parallel} the velocity of the species a (ions and electrons). The flux limit is

$$q_{\text{lim}}^m = \alpha \cdot p \quad (4.5)$$

with the pressure p and parallel momentum flux (or viscosity) limiting factor usually set at $\alpha = 0.5$.

In general, if these kinetic corrections become important, quantitative conclusions are questionable, because the fluid model is no longer strictly valid. However, prescriptions of particle, energy and momentum conservation still guarantee a qualitatively correct description. The flux limiters are designed to give the correct answer in the collisional regime. More details on this subject can be found in section 6.1.5.6.2.

4.1.2.3. Anomalous cross-field transport description

Although parallel transport is relatively well understood, radial transport is in general determined by turbulence and is therefore complex and anomalous. Models of edge turbulence are discussed for example in [39] and substantial progress in understanding of the radial particle turbulence driven transport in SOL has been made of late. **Turbulence** in tokamaks is determined by small scale, low frequency drift wave turbulence involving eddies, waves and vortices of the $\bar{E} \times \bar{B}$ velocity [16]. These eddies advect (transport) the background thermal gradient to produce disturbances in all the thermodynamic state variables. These are then carried with the flow while the eddies persist and then are picked up and carried further by new eddies. If the size and lifetime of eddies are small and short compared to the scales of the background plasma, the above described mechanism has the character of a diffusive process. If the turbulence is local, the net time-averaged transport does indeed scale with the background gradients.

In a code (like e.g. B2.5) the turbulent nature of radial transport is captured by the calculation of the radial fluxes, Γ_{\perp} represented by a combination of diffusive and convective terms as expressed by Eq.2.70. Such a model can adequately describe the time-averaged turbulent flux even if the underlying process is not necessarily diffusive. If the convective radial velocity v_{\perp} and diffusion coefficient D_{\perp} are related in a simple way as

$$v_{\perp} = \sqrt{D_{\perp} / \tau_{\parallel}} \quad (4.6.)$$

the assumption of pure convective or pure diffusive cross-field transport in Eq. 2.76 is in principle, equivalent. Unfortunately, as a result of the turbulent nature of radial transport, neither D_{\perp} nor v_{\perp} can be simply parameterized with the macroscopic measurables such as distance from the separatrix or LCFS, collisionality or line-averaged density. Within typical tokamak operational windows (for example variation in density) the measured D_{\perp} and v_{\perp} can vary by orders of magnitude. When modelling the SOL with fluid codes like B2.5, the diffusive and convective terms in the transport ansatz defined by Eq.2.70 serve only to prescribe the radial transport in terms of a flux, and do not address the underlying origin of the turbulence [149].

In principle, the ion momentum equation in the diamagnetic direction employed in B2.5 could be used to obtain the neoclassical radial ion velocity v_{\perp}^{neo} . However, since in the SOL relative fluctuation levels are generally orders of magnitude higher than in the

core, neoclassical transport theory [28], which does not take into account turbulence, can be applied only inside LCFS. As a consequence, this velocity, v_{\perp}^{neo} deviates from the observed ‘anomalous’ experimental values, and therefore the neoclassical radial velocity is in B2.5 replaced by an anomalous value v_{\perp} according to an expression consistent with experimental data as a diffusive Fick’s law,

$$v_{\perp} = -D \frac{d}{dr} \ln(n), \quad (4.7)$$

and the anomalous transport is introduced in the edge modelling as a phenomenological description [133].

When prescribing radial particle transport in SOLPS, usually only the diffusive term is considered, assuming the flux to be proportional to the density gradient as expressed by Eq.2.76 and even often taking the D_{\perp}^{eff} to be constant both radially and poloidally. However, extensive measurements in C-Mod tokamak [150] have shown that SOL density profiles can only be explained in terms of a radially strongly varying effective diffusivity if a purely diffusive ansatz such as Eq.2.76 is assumed. In the case of a purely convective ansatz (see Eq. 2.77) a radially varying v_{\perp} is observed [151] (see **Fig.6.8**). On the other hand, the principal conclusion of [39] is, that the diffusive description of radial particle flux in the tokamak SOL should be abandoned in favour of a convective ansatz, the absolute magnitude and radial variation of which is determined by large scale fluid interchange cross-field motions of plasma blobs. Even though the convective approach appears to be better than diffusive in the sense of being a more realistic description of the true transport process, it is still an incomplete description: parametrization of the effective radial velocity is very difficult. Although convection seems to be a more appropriate description of the mid to far SOL transport, the situation closer to the separatrix is likely closer to a diffusive process, particularly in H-mode situations. At some point in the SOL, a transition appears to occur between different transport processes. Especially closer to the pedestal the transport is not described by a single mechanism. This thesis contains an extensive series of attempts to simulate both the stationary and time-dependent SOL by using the convective transport ansatz either as pure convective velocity or as a combination of both convective and diffusive terms in Eq. 2.70 (see chapter 6).

4.1.2.4. Running B2.5

Two of the primary inputs required by SOLPS are the simulation grid, derived from magnetic equilibrium of the particular experiment to be simulated – see the **Fig.4.1** for the grids used in this thesis and a set of boundary conditions. The latter are specified for energy, continuity, potential and momentum equations in terms of the fluxes or derivatives of the fluxes. These imposed boundary conditions are translated by the code as sources and sinks of particles, momentum and energy. Among the standard boundary conditions, described in more detail below, are the kinetic boundary condition for the sheath at the target plates and density or heat fluxes at the core boundary. The boundary conditions are discussed in the following separately for each boundary.

I) At the targets ('E' and 'W' boundaries) the standard boundary condition is the Bohm criterion for the formation of a stable sheath (see Eq.2.42) requiring that the flow be at least sonic at the sheath entrance [152]. In the code this is translated as:

$$v_{\parallel} \geq c_s - \frac{b_z}{b_x} v_{\perp} \quad (4.8)$$

where c_s is local sound speed and b_z/b_x the inverse field line pitch with b_z and b_x respectively the toroidal and poloidal components of the magnetic field. The pitch angle at the plates is limited from below to be no less than one degree. In order to ensure that no unphysical flows are generated, the code solves the parallel momentum equation using the electric potential. The boundary condition for the current continuity equation at the plates corresponds to the sheath voltage characteristics:

$$j_x = en(b_x c_s - b_x \frac{1}{\sqrt{2\pi}} \sqrt{\frac{T_e}{m_e}} \exp\left(-\frac{e\Phi}{T_e}\right)(1 - \gamma_e)) \quad (4.9)$$

where j_x is the poloidal current density, Φ the potential and γ_e the secondary electron emission coefficient. The electron and ion heat fluxes from the grid are [17]:

$$q_{ex} = b_x \frac{n}{\sqrt{2\pi}} \sqrt{\frac{T_e}{m_e}} \exp\left(-\frac{e\Phi}{T_e}\right)(1 - \gamma_e) \left(T_e \frac{1 + \gamma_e}{1 - \gamma_e} + e\Phi\right) \quad (4.10)$$

$$q_{ix} = \frac{5}{2} n T_i c_s b_x \quad (4.11)$$

The acceleration of ions in the sheath before hitting the wall by the potential drop must be accounted for in the creation of the neutrals. The ion energy may also be partly reflected as energy of the recycled neutral atoms, while electrons in general deposit all their energy at the wall. This will be discussed also later in section 6.1.5.6. Impurity production (see section 4.1.2.5) is determined by applying the local sputter models.

II) At the inner (core) flux surface currents are set either to the divergent part of the diamagnetic current or to zero, both guaranteeing that the net current integrated over the inner flux surface is zero. It is standard in SOLPS to fix the main plasma ion density and power fluxes. Impurity and neutral fluxes are set to zero or are forced to ionize into the higher ionization stages. The parallel momentum is either fixed (to zero or to the value of the measured experimental rotation) or a momentum flux is set.

III) At the outer boundaries of the computational domain, representing the walls or plasma close to walls, the boundary conditions are imposed usually in the form of decay lengths or outflows representing the main chamber wall pumping or effective boundary conditions replacing the outer SOL (since the current version of B2.5 does not support gridding to the walls)

Apart from magnetic equilibrium for the simulation grid and boundary conditions, other inputs required by the code include the choice of anomalous transport coefficients (see section 6.3.1), a set of volume sources (either heating or gas puffs) and feedback schemes, allowing the strength of the gas puff to be adapted such that the midplane separatrix density or core density are controlled and maintained at the requested values.

In addition to setting the boundary conditions, the user must also specify the numerical time step, Δt and number of internal and external iterations for each simulation. At each external iteration, corresponding to single time step, the volumetric and surface sources are computed by solving the momentum, particle and energy

conservation and finally again the continuity equation. Before the next time step (external iteration), this procedure is repeated for a number of internal iterations (usually fixed as ~ 10) in order to relax the solutions of the equations. This process is repeated until the convergence is reached (\sim achieving the steady state), which means that no major variation of plasma parameters (including densities, temperatures, energy and particle fluxes at various locations and total particle and energy content of the plasma) is observed. The level of convergence can be estimated from analysis of the residuals of each equation in B2.5. Provided that the internal iterations are well converged, each time step corresponding to the chosen Δt provides a solution in real time. The use of time-dependent SOLPS simulations is a particular feature of this thesis work which will be discussed in the result chapters 6,7.

4.1.2.5. Impurities, Radiation

For quantitative comparison with the experiments, the impurities (which are always present in the plasma) can be included in the model. These can be the wall material released by plasma-surface interaction - intrinsic impurities (C, W, Be...) or extrinsic “seeded” impurities (Ne, Ar, Kr, N₂...) used in experiment to increase radiation losses and hence reduce plasma power fluxes onto material surfaces. In this thesis only carbon has been included as an additional species in addition to the electrons and fuel ions.

The biggest problem to overcome with carbon in terms of the simulations is that even at low plasma temperatures, where the physical sputtering switches off, carbon chemical sputtering continues [153], producing methane and other hydrocarbons, which finally break up into carbon atoms and ions [154]. This sputtering process is a surface effect and has a reasonably strong surface temperature dependence, with a maximum yield at about 600 K (~ 0.05 eV). Carbon produces hydrocarbons what leads to a surface temperature effect. However, a realistic model of the chemical sputtering process is not yet included in SOLPS and the absolute yield is sensitively dependent on the type of surface (e.g. pure graphite or co-deposited layer). It should be also pointed out that SOLPS (EIRENE) does not properly model the full hydrocarbon chain process. Radiation losses due to low Z elements like carbon are dominated by line radiation for temperatures below 100eV and by Bremsstrahlung above several keV. Due to their radiation characteristics, the low Z elements will contribute more to SOL and divertor radiation ($T < 100\text{eV}$) than the higher Z elements.

In order to account for the effects of impurities in B2.5, a simple model is employed as a starting point to estimate the radiation losses on closed field lines (main chamber) [155]. The radiation loss of impurity Z must equal the divergence of the radial heat flow q_{\perp} .

$$\frac{\partial q_{\perp}}{\partial r} = -n_e n_Z L_Z(T_e) \quad (4.12)$$

where $L_Z(T_e)$ is radiation function of the impurity Z. This simple model is extended for the open field lines as described in [17], yielding an upper limit for the radiated power on open field lines.

In simulations with SOLPS5.0 carbon is produced at the target plates (and side walls) by physical and chemical sputtering. The chemical sputtering coefficients can be

chosen by the user with different values for different surfaces and in this thesis they are fixed at the same value (0.035) [48] everywhere and for all charge states. When comparing with experiment, the missing background due to radiation in the core not covered by the B2.5 grid must be subtracted.

4.1.3. Neutrals

In all but the simplest situations, in order to define the SOL properties self-consistently, a description of neutral behaviour must be included along with the plasma transport. The presence of neutrals in the code is very important since they serve as a primary fueling source for the plasma and thus influence the global particle confinement. Neutral sources are important for the plasma, while the neutral particle transport (and thus the neutral source distribution) is determined by the plasma background. Neutral recycling in the edge also strongly influences the plasma properties near surfaces, such as divertor targets.

There are three basic energy exchange channels, including charge exchange, atomic radiation and volume recombination. The latter becomes important for plasma temperatures below $\sim 2\text{eV}$. The recombination of an electron and an ion into a neutral atom needs a second body to account for energy and momentum conservation during the process. This can be either a photon in case of radiative recombination or an additional electron in case of three-body recombination.

The penetration of neutrals into the plasma is characterized by two different regimes. For regions with temperature $T > 10\text{ eV}$, such as the main SOL, the neutrals are in a kinetic regime, where the mean free path of charge exchange (CX), λ_{CX} and ionization λ_{ion} are about the same ($\lambda_0 \approx \lambda_{\text{CX}} \approx \lambda_{\text{ion}}$) and after a few CX collisions the neutrals are ionized. In the divertor where temperature can be $\ll 10\text{eV}$, diffusive processes occur with a very large number of CX events taking place resulting in a random walk before ionization ($\lambda_{\text{CX}} \ll \lambda_{\text{ion}}$, $\lambda_0 = \sqrt{\lambda_{\text{CX}} \cdot \lambda_{\text{ion}}}$) [17].

Neutral particle behavior can be described in SOLPS either by simple analytic approximations with the fluid neutral model included in B2, or can be treated kinetically by iterations with the Monte-Carlo code, as EIRENE, to which B2.5 is coupled to form SOLPS5.0. The fluid neutral model is applicable if the neutral ionization mean free path is less than typical gradient lengths for neutral and plasma parameters. In this fluid model for neutral species only atomic species are present and the neutral temperature is set to be equal to T_i . In order to better account for the distribution of neutrals away from material surfaces, a “first-flight” approximation is used in neutral model, which is described in [126] together with the most appropriate settings to be used in fluid neutral model deduced from comparison of results from the SOLPS package, where B2.5 is coupled to EIRENE. Compared to the kinetic description provided by the EIRENE code, the use of fluid neutrals in B2.5 is computationally faster and introduces no additional convergence problem. Due to the lack of “Monte-Carlo noise” it is easy to monitor. However, it is a much less complete physics description (for example neutrals are only 2D in this model) and is strongly dependent on the geometrical features of the modelled area. Another disadvantage is the influence of the neutrals on the profile of the ion temperature, which

sensitively depends on neutral flux limits, neutral thermal diffusivity, neutral conductive heat flux limits and boundary conditions in the vicinity of the main chamber walls.

4.1.3.1. EIRENE

The kinetic Monte-Carlo neutral description in Eirene is a comprehensive neutral model of neutrals and incorporates detailed geometric considerations and complex atomic, molecular and surface physics. The Monte-Carlo code, EIRENE (coupled to B2.5) is used in this work for the proper description of neutral transport. Eirene solves the full 3-D Boltzmann time-dependent or stationary transport equations for the neutral distribution function.

$$\frac{\partial f(\vec{x}, \vec{v}, t)}{\partial t} + \vec{v} \cdot \nabla f(\vec{x}, \vec{v}, t) = C(f(\vec{x}, \vec{v}, t)) \quad (4.13)$$

with C the collision term, which can also include neutral-neutral collisions, creating already a non-linear problem for the neutral transport itself. These collisions can be accounted for through the BGK-approximation [156-157]. They have been used to simulate high density JET divertor plasmas [158] and are now routinely used in SOLPS simulations of the ITER divertor where neutral densities are extremely high. However, as is the case throughout the work described here, self-collisions between particles of the test species are normally excluded, yielding the linear problem.

In SOLPS5, the test particle trajectories are followed in EIRENE on the plasma background supplied by B2.5. The Monte-Carlo principle is used for computation of statistical expectation values of complex processes between test particles and the plasma and the first attempts developed for neutron transport calculations can be found in [159-160]. The Monte-Carlo method is used to integrate the particle transport equation statistically using discrete Markov-chains [49,159-160]. The N test particles are launched with certain direction and velocities (eventually with prescribed distribution) from a particle source with strength S . Each test particle is then followed along its trajectory with the length l defined as

$$l = -\lambda \ln R \quad (4.14)$$

where λ is mean-free-path of the test particles and R is a random number between 0 and 1. At the end of the trajectory the particle is either absorbed at a material surface or ionized and thus becomes a species of the plasma background. During the simulation with EIRENE, the N particle histories are used to derive average values, for example of density, with statistical uncertainty $\sim 1/\sqrt{N}$:

$$n = \frac{t \cdot S}{V \cdot N} \quad (4.15)$$

where t is time which a given particle spends in the cell of volume V . Rate coefficients of volumetric processes are provided by databases like AMJUEL [49], HYDHEL [161] or METHAN [49]. The vessel geometry, grid and atomic and molecular data are specified in a rather complicated EIRENE input file "input.dat". In addition to the atomic physics data, the surface reflection data are necessary and are provided also by Monte-Carlo codes like TRIM [162] where the surface reflection of ions and neutrals are calculated using the binary collision model. These can be also included into the boundary conditions describing the plasma-surface interactions [163].

Like the fluid part of SOLPS5.0, B2.5, the EIRENE code is written in FORTRAN (77 and 90) and it can be used ‘stand-alone’ or coupled to plasma codes other than B2.5. The version ‘99 of EIRENE, so-called new EIRENE, which is used throughout this work, includes friction between molecules and ions and the possibility for multiple molecular species.

4.1.4. B2.5 – EIRENE coupling

When B2.5 is coupled to EIRENE, the neutral source terms of the B2.5 fluid model are rescaled by 10^{-10} . Even in coupled cases there is still a remnant fluid neutral population followed by B2.5 and thus it is necessary to scale down the source terms relevant to this fluid neutral population so that it exist only as a trace and does not influence the solution. The kinetic neutral population does not see this scaling factor and is fully taken into account [164].

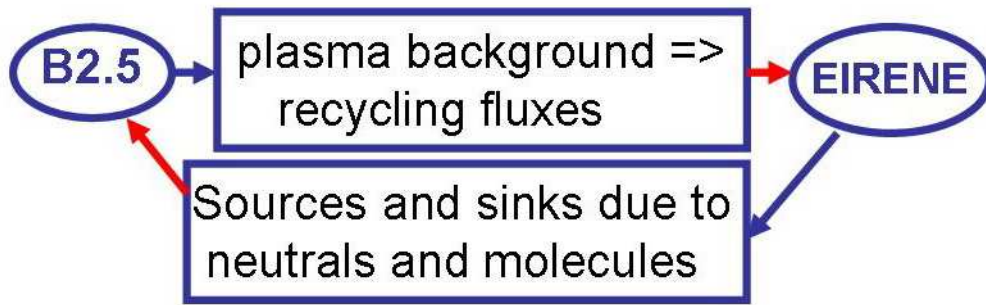


Figure 4.4. *Coupling between B2.5 and EIRENE parts of SOLPS5.0*

The coupling between these plasma fluid and Monte-Carlo neutral parts of the SOLPS5.0 package is done by means of passing arrays in both directions. The B2.5 code delivers a plasma background on which the neutral trajectories are computed and the associated particle momentum and energy sources and sinks are computed. Once EIRENE has completed the simulation of the set of N neutral particle histories, these sources and sinks are transferred to B2.5. In order to translate the total energy sources from the Monte-Carlo code into the internal energy sources needed for the plasma fluid solution, conversion rules [165] are applied. B2.5 relaxes the solution from EIRENE through several internal iterations and provides EIRENE with a new plasma background. Among the values given to EIRENE is also the particle flux at the boundaries of the grid which serves as information with which the surface and volumetric neutral sources for coupled EIRENE are deduced. The iteration scheme, illustrated schematically in **Fig.4.4**, is repeated until satisfactory convergence is obtained. Normally at least ~ 1000 external iterations are required to reach the converged steady state which corresponds approximately to 24 hours of CPU time.

4.1.5. SOLPS hardware

The SOLPS5 code package is a very sophisticated SOL and divertor simulation research tool which has been developed over more than two decades by a number of collaborating specialists in Europe. The code is under continuous development at the Max Planck Institute for Plasma Physics in Garching, Germany (while EIRENE is developed mostly in Juelich (EURATOM Association FZ-Juelich, Germany)).

The simulations presented in this work for TCV plasmas have been performed using a SOLPS5.0 package installed on the IPP Garching cluster consisting of a growing number of PCs operating under Linux (/afs/ipp-garching.mpg.de/). The cluster is accessible remotely and the code is constantly updated while keeping track of all previous ‘subversions’.

Users run the code from their own directories using personal compiled versions of the code. Each user can modify the local source code and choose which of the modifications from the newest subversion of the code are required when compiling. The simulations of JET discharges included in this thesis were performed on the JET Analysis Cluster (JAC) for which the same rules as those in force on the IPP Garching cluster apply. The JAC cluster is accessible online through the web interface Citrix [166]. The personal directory on the IPP Garching cluster containing the work performed for this thesis is:

```
“/afs/ipp-garching.mpg.de/home/b/bug;  
p01.bc:scratch/bug/solps_subversion/src/Braams/b2/runs/ TCV/ “  
and on the JAC cluster at:  
“jac:work/bgule/solpscode/src/Braams/b2/runs/JET”.
```

The output of every successful simulation performed on either of two clusters is saved on the centralized MDS database located on the server at IPP Garching [167] under different simulation numbers and in the same way as tokamak experimental data is stored. Data in individual nodes can be accessed with a variety of software. The fifth generation language, Matlab [168] has been used throughout this work.

The SOLPS5 code has been installed and is in use at CRPP since 2001 and has been the principal modelling tool used for the simulation of divertor plasma detachment on TCV [149]. It is run at CRPP on a cluster of 5 PC's under a Linux platform and managed by the Openmosix [169] software. Only the first simulations during the thesis have been performed on this cluster. For practical reasons all subsequent important run directories were migrated to the IPP Garching cluster which, like the JAC cluster, has the advantage of permanent maintenance and archiving.

5. Experiment

In this thesis the SOLPS5.0 code package has been used to simulate four ELMing H-mode discharges on two machines, TCV and JET. This chapter summarizes these experimental situations, together with the diagnostics whose data are used to constrain and compare with the simulations.

5.1. TCV and JET

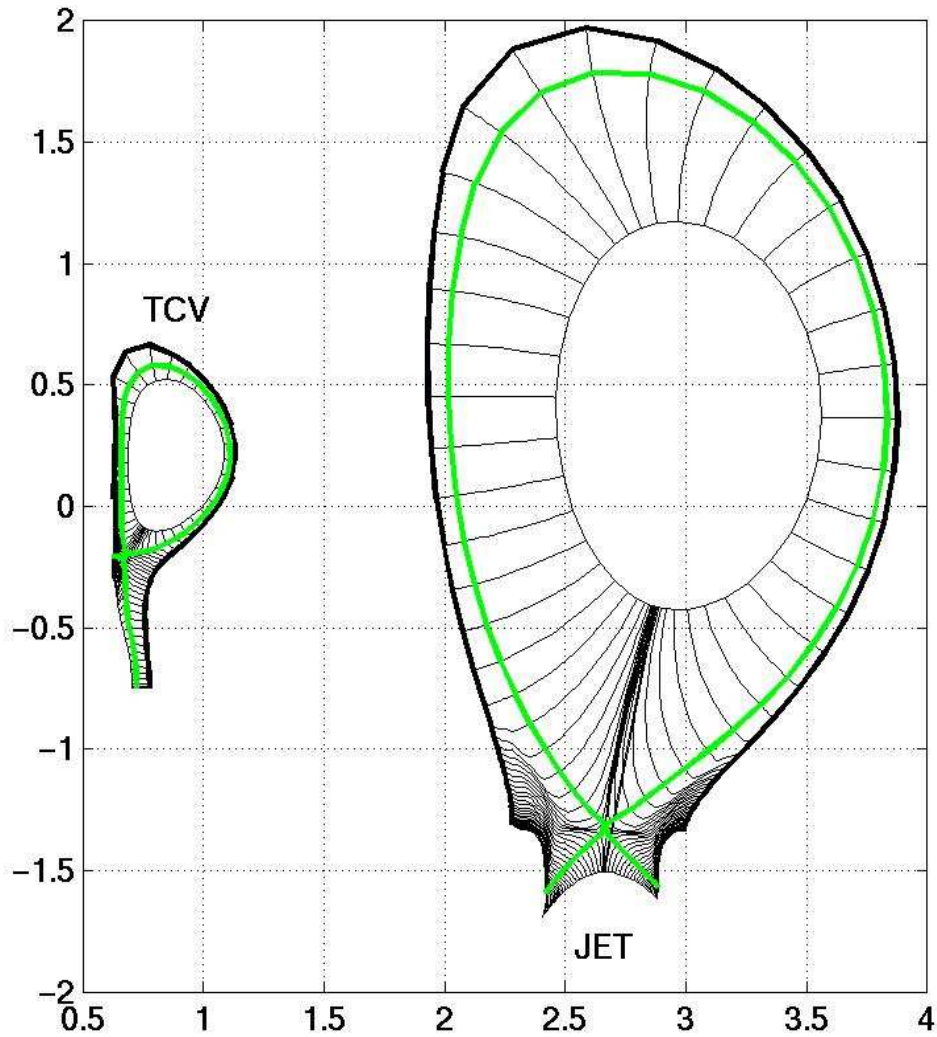


Figure 5.1. Comparison of size and magnetic equilibria of TCV and JET used for the SOLPS5 simulations. The radial extent (in the core part) of the equilibria on this figure is limited to the radial extent of the simulation grid used in this thesis and the green lines correspond to the separatrix; The discharges depicted here are # 26730 (TCV) and #58569 (JET).

Fig. 5.1 illustrates the difference in size and shape of equilibria of TCV and JET used for SOLPS5 simulations in this thesis. An attempt has been made in this work to draw conclusions on the nature of the ELMy H-modes (including both steady state and transient ELM event) in each of the two machines by comparing the code simulations with experiment. This will be the content of the following chapters.

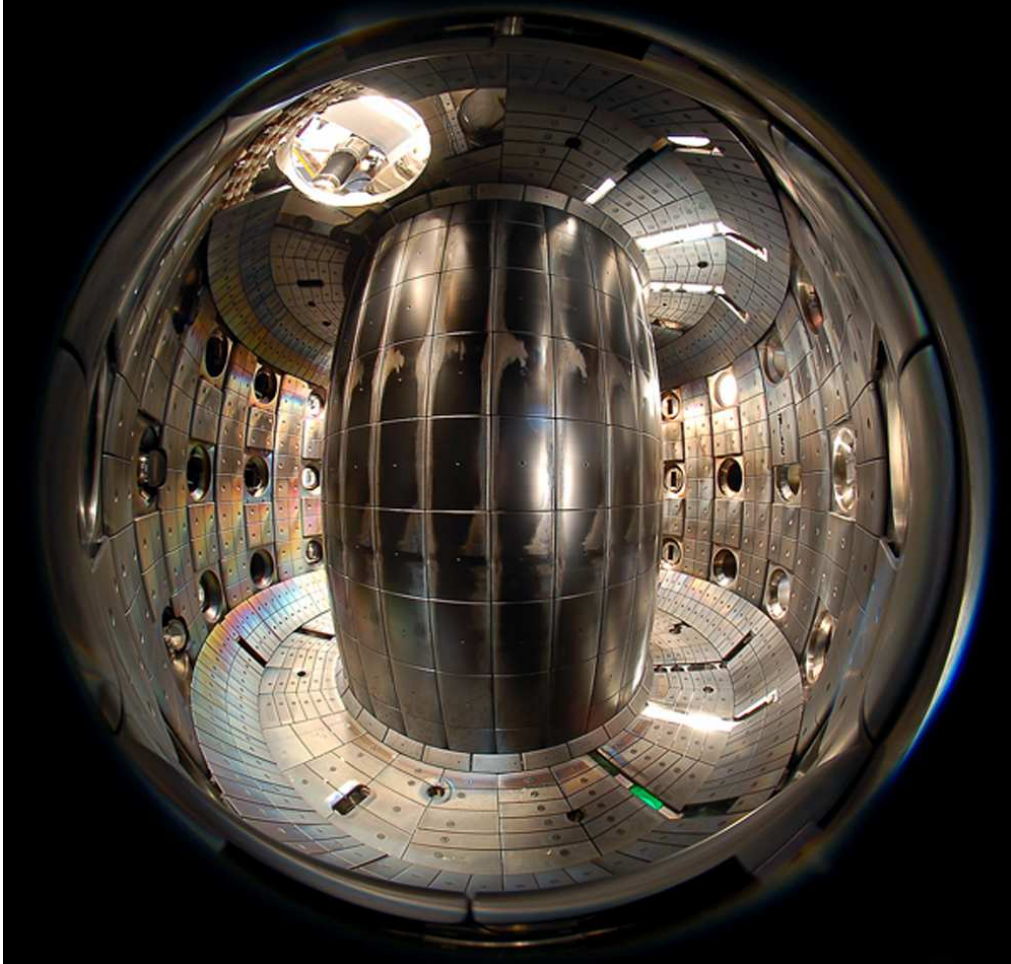


Figure 5.2. TCV interior with main chamber walls graphite coverage (carbon ~ 90% of total surface coverage).

The fusion device of the research centre of plasma physics in Lausanne, Switzerland, CRPP, TCV, stands for ‘Tokamak à Configuration Variable’. It is a medium sized tokamak with a set of 16 independently controllable poloidal field coils, allowing a wide range of magnetic equilibria to be studied [170]. The first wall contains ~1600 protection elements manufactured in high purity polycrystalline graphite. The interior of TCV with graphite walls is shown in **Fig.5.2**. The PFCs are inertially cooled and the vacuum vessel is conditioned 2-3 times per year including vessel bake-out at ~250°C and boronisation by plasma chemical vapor deposition in a 10% B₂D₂, 90% He gas mixture depositing a reasonably homogeneous boron layer of ~10nm thickness on an internal surfaces. In between D plasma discharges, He-glow discharge is used to establish similar short term surface properties before each plasma shot [171]. Another particularity of

TCV tokamak is the world record plasma elongation (ratio of height and width of plasma) of up to ~ 3 [170].

To date, the majority of ohmic H-modes have been obtained in reversed toroidal field, B_ϕ , (ion $B \times \nabla B$ drift direction upwards). This is historical and essentially a consequence of H-mode avoidance since with the more conventional forward B_ϕ operation, ohmic H-mode is easily obtained, even at low plasma current, but often without frequent ELMs, making density control difficult. The latter is particularly important for the low density second harmonic ECRH experiments which constitute a large fraction of the TCV experimental programme.

The second machine of interest in this work, JET, the “**Joint European Torus**”, is situated at the Culham Science Centre, Oxfordshire, UK. The JET device is currently the world's largest tokamak and the world's largest nuclear fusion research facility. A view inside the JET vacuum vessel with a snapshot of the plasma in D_α emission included can be seen on **Fig.5.3**.

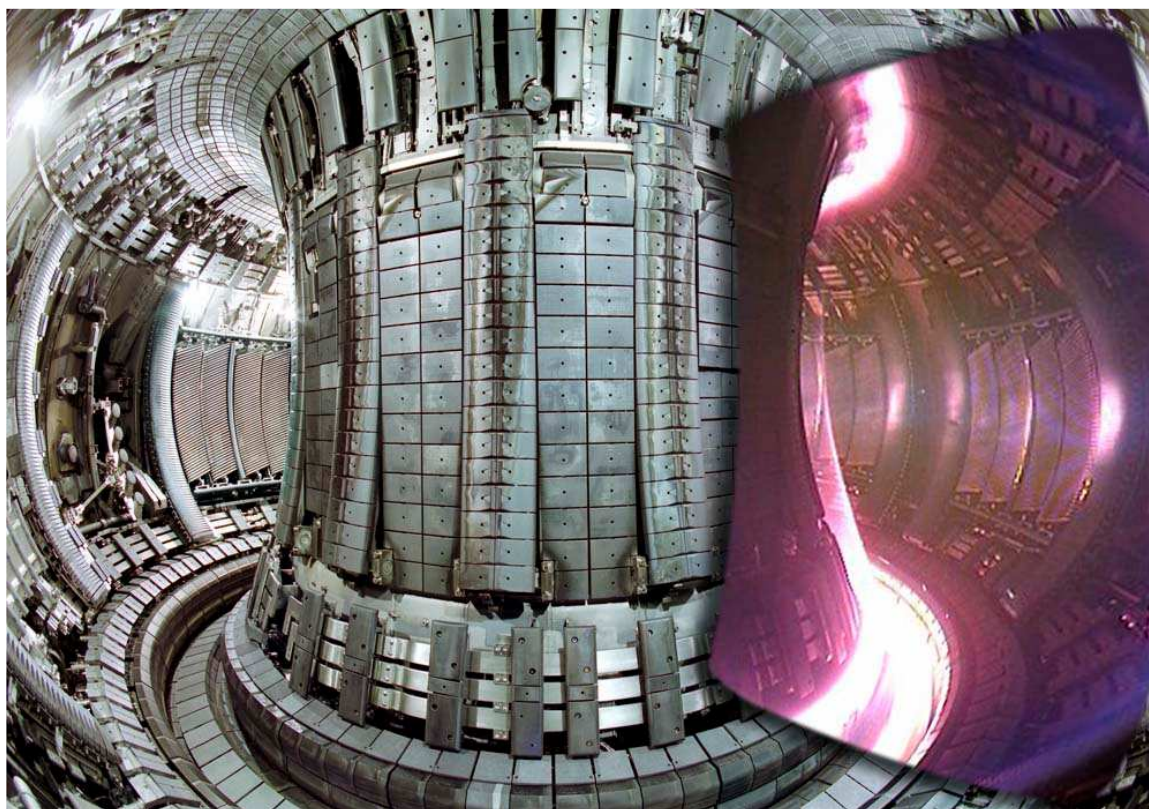


Figure 5.3. JET chamber with plasma discharge on the right side; [14],[3]

Tab.5.1 lists many of the important parameters of TCV and JET tokamaks contrasting their relative differences, especially in terms of size and divertor geometry. The configurations and the parameters presented in **Tab.5.1** correspond, unless stated otherwise, to the typical discharges used in this thesis. The material of the JET walls is CFC. Regular beryllium evaporation and deuterium glow discharges are used to reduce impurity levels.

	TCV	JET
Typical R [m]	0.875	3.05
Typical a [m]	0.25	0.915
Typical B_ϕ [T]	1.43	2-3
Maximum I_p [MA]	up to 1.2 (usually 0.5)	2-3 (max. 4)
Typical direction of B_ϕ	REV	FWD
Plasma volume [m ³]	~1	~100
LCFS area [m ²]	~10	~100
$L_{\text{parallel,total}}$ [m]	~ 32	~ 129
$L_{\text{parallel,outmid,outtarg}}$ [m]	~ 17	~ 42
$L_{\text{parallel,outmid,intarg}}$ [m]	~ 15	~ 87
$L_{\text{par,outmid,outtarg}}/L_{\text{par,outmid,intarg}}$	~ 1.2	~ 0.5
$L_{\text{parallel,X-point,outtarg}}$ [m]	~ 15	~ 19
$L_{\text{parallel,X-point,intarg}}$ [m]	~ 3.5	~ 11
$L_{\text{par,X-point,outtarg}}/L_{\text{par,X-point,intarg}}$	~ 4.3	~ 1.7
$L_{\text{poloidal,total}}$ [m]	~ 2.6	~ 8.4
$L_{\text{poloidal,outmid,outtarg}}$ [m]	~ 1.2	~ 2.5
$L_{\text{poloidal,outmid,intarg}}$ [m]	~ 1.4	~ 6
$L_{\text{pol,outmid,outtarg}}/L_{\text{pol,outmid,intarg}}$	~ 0.9	~ 0.4
$L_{\text{poloidal,X-point,outtarg}}$ [m]	~ 0.6	~ 0.3
$L_{\text{poloidal,X-point,intarg}}$ [m]	~ 0.05	~ 0.3
$L_{\text{pol,X-point,outtarg}}/L_{\text{pol,X-point,intarg}}$	~ 11.8	~ 1.1
Strike point position	Outer SP-vessel floor Inner SP – vertical targetcentral column (vert. target)	Both SP – vertical targets
Strike point vs. X-point	Inner SP- similar vertical position as X-point Outer SP–below X-point	Both SP – below X-point
Divertor geometry	Open divertor, no baffling structure	Baffled (closed) divertor
Divertor configuration type	SNL	SNL (here DOC-L)
Maximum pulse length [s]	4 (usually 2)	80 *
Max. heating power [MW]	5 (4.2 additional)	~30 (20 NBI)
Power density [MW.m ⁻³]	~ 1-5 (max. 4.5)	~ 0.2- 0.3
Density control	no active pumps only wall pumping	Divertor cryo-pumping

Table 5.1. Important parameters of TCV and JET tokamaks. Estimated of the parallel and poloidal connection lengths are made on the flux surface closest to the separatrix (from outside) for the plasma equilibria depicted on Fig.5.1. * Even if the pulse length is long the flattop length is approximately ~10s, depending on I_p and B_ϕ

The important part of the **Tab.5.1** deals with the comparison of the geometry of the two machines. Different geometry especially in the divertor configuration plays quite

an important role in the explanation of the different effects (for example in terms of asymmetries) on these two devices. Therefore these geometrical differences deserve more attention.

One very striking difference is the asymmetry in the poloidal lengths of the inner and outer divertor legs in the ‘unconventional’ TCV configuration. In JET, with a more conventional poloidal divertor configuration, the strike points are symmetrically disposed on the vertical targets for the equilibrium modelled here. In contrast to the almost equal inner and outer X-point to target poloidal connection lengths in JET, the distance from X-point to the outer target in TCV $L_{\text{poloidal,X-point,outarg}}$ is approximately 10 times longer than to inner target $L_{\text{poloidal,X-point,intarg}}$. The same comparison for parallel connection lengths from X-point to inner and outer targets $L_{\text{par,X-point,outarg}}/L_{\text{par,X-point,intarg}}$ yields the ratios 4.3 and 1.7 for TCV and JET respectively. These geometries are, of course, reflected in the relative connection lengths from the outer midplane towards the targets, where for TCV one obtains the ratio close to unity (in terms of both poloidal and parallel connection lengths) while at JET the connection length from outer midplane to outer target is only about half of that to the inner target (again for both poloidal $L_{\text{pol,outmid,outarg}}/L_{\text{pol,outmid,intarg}}$ and parallel connection lengths $L_{\text{par,outmid,outarg}}/L_{\text{par,outmid,intarg}}$). SNL stands for single-null lower divertor configuration and it is standard TCV divertor configuration as seen in **Tab. 5.1** and **Fig. 5.1**. The SNL configuration at JET, DOC is the ‘Diagnostic Optimized Configuration’ developed for the study of pedestal and SOL physics during ELMing H-mode [110]. This is a configuration optimized for the JET edge profile diagnostics (especially edge LIDAR and Li-beam – see section 5.2.2) which provides much higher quality composite radial profiles than in other conventional configurations. DOC-L is a variant of this shape (triangularity $\delta=0.27$) with strike points located on the lower vertical tiles of the divertor and optimized for infra-red power flux measurements.

Tab.5.2 offers an overview of the main plasma parameters of the four discharges simulated in this thesis. On TCV, the radiation in the core is quite strong, while at JET the radiation from core is low such that almost the whole injected heating power crosses the separatrix into the SOL. It is clear that this set of four discharges offers a rather wide range of operating conditions and therefore the study presented in this work brings quite comprehensive comparison of code and experiment for the ELMing H-modes and offers a test for the SOLPS code across a wide range of parameters.

Both of the TCV discharges in **Tab 5.2** are ELMing H-mode pulses with very similar magnetic SNL equilibrium (see **Fig.5.1**). Discharge # 26730 is an ohmic H-mode with Type III ELMs (see section 6.1.) whilst #32713, is an ECR heated pulse with much larger ELMs, probably Type I (see section 6.2). The ion $B \times \nabla B$ drift is directed towards the X-point – downwards (FWD field) in #32713 and upwards (REV field) in #26370.

Two high power JET H-modes have also been simulated in this work. The pulse #70224 is a high I_p , ~8 MJ stored energy plasma with ELMs approaching $\Delta W_{\text{ELM}}=1$ MJ, modelled for the first time with SOLPS (see section 7.2). A second pulse, with lower stored energy and smaller Type I ELMs, originally considered in detail by Kallenbach with the EDGE2D-NIMBUS code package [172], has been modeled as a benchmarking exercise featuring a high level of complexity including carbon impurities and the full ELM cycle (see section 7.1. and [173]). The two JET discharges considered here are very similar in terms of magnetic configuration, both close to the Diagnostic Optimized Configuration (DOC) plasmas mentioned above. They are both vertical target equilibria

with moderate triangularity ($\delta \sim 0.25$) and separatrix-to-wall gaps of ~ 5 cm at the outer midplane.

	# 26730	#32713	#58569	#70224
Machine	TCV	TCV	JET	JET
ELM Type	Type III	Type I	Type I	Type I
I_p [MA]	0.43	-0.37	2	3
B_ϕ [T]	-1.43	1.43	2	3
P_{IN} [MW]	0.6	1	14	17
P_{SOL} [MW]	0.4	0.75	12	14
q_{sep} [kW/m ²]	46	75	120	140
\bar{n}_e [10^{19} m ³]	6	5.5	4	6
n_e^{sep} [10^{19} m ³]	1.6	2	2	1
W_{dia} [MJ]	0.026	0.022	4	8
v_{ped}^*	0.7	0.15	0.12	0.09

Table 5.2. Main plasma parameters of four discharges simulated in this thesis, where q_{sep} is the power flux crossing the separatrix, \bar{n}_e is line averaged density, n_e^{sep} is the density at the outer midplane separatrix, P_{IN} is injected heating power, P_{SOL} is the power crossing the separatrix which is used as an input parameter for the simulations and is calculated as $P_{IN} - P_{RAD,CORE}$, where P_{RAD} is the core radiated power.

5.2. Diagnostics at TCV and JET

The simulations of the TCV and JET discharges have been effectively constrained by the available experimental data. The SOL is a radially narrow region with strong gradients and often strong poloidal variations in plasma parameters and particle sources. Therefore good spatial resolution is ideally required. Unfortunately, however, the SOL is the region in which the measurements with good spatial coverage are very often hard to make and thus the extent to which the edge code modelling can be constrained is slightly limited.

5.2.1. Diagnostics at TCV

Both simulated discharges at TCV have been constrained largely by experimental data from the diagnostics which are schematically depicted in **Fig.5.4**. Upstream profiles of electron density and temperature are provided by combination of the core and edge Thomson scattering (TS) systems [174], and reciprocating Langmuir probes (RCP). Unfortunately, charge exchange recombination spectroscopy (CXRS) measurements of

edge ion temperature were unavailable during the period of this thesis work for the magnetic equilibria used in these H-mode studies. Such measurements are available for TCV plasma centered on $z=0$ [175], but even there do not extend into the SOL, nor is the pedestal coverage adequate to constrain the simulations. As will be discussed later, in the absence of T_i data, energy equipartition ($T_i \approx T_e$) is assumed to constrain the simulations.

The inner and outer target profiles of ion saturation current, electron temperature and density are provided by fixed Langmuir probes. Additional diagnostics include the system of foil bolometers and AXUV cameras which measure the poloidal distribution of the total radiation. A system of photodiodes provides a few lines of sight of D_α emission. The diamagnetic loop provides a measurement of the plasma stored energy, from which the energy lost per ELM (ΔW_{ELM}) can be straightforwardly extracted if the energy loss is high enough to be detected. Outer target power loads are provided by a fast infrared camera (IR), viewing the vessel floor [105]. Very recently, a second IR camera, on temporary loan from the MAST tokamak, has provided the first fast IR measurements during ELMs at the inner target [176]. Analysis of the power fluxes necessary for the constraint of SOLPS5 simulations was, however, unfortunately unavailable in the time horizon of this work.

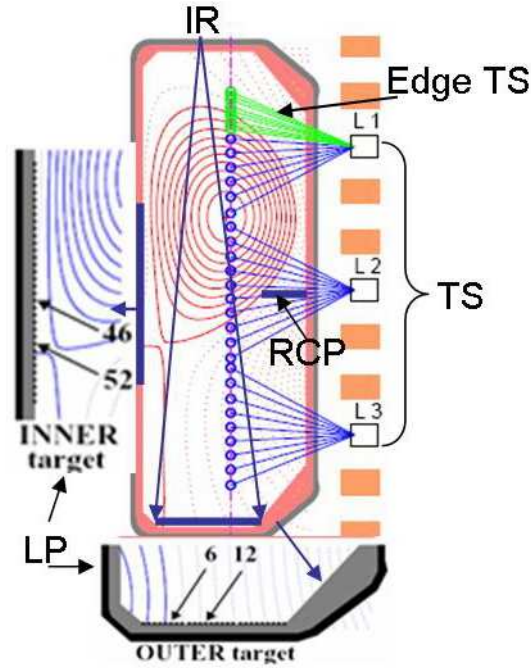


Figure 5.4. *Diagnostics at TCV*

Fig.5.4 illustrates the viewing chords of the edge and core TS superimposed on the standard divertor configuration. The main (core) TS system is optimized for plasma parameters typical in the confined region of the plasma with T_e in range of 50eV – 20keV (while TCV plasmas reach values usually up to 10 keV). The edge TS system can measure T_e in the range 5eV-1keV for n_e down to $5 \times 10^{18} \text{m}^{-3}$ and benefits from the region of high flux expansion at the top of SNL configurations to provide some measurement points in the SOL plasma, as well as reasonably high resolution in the pedestal region.

A small degree of vertical plasma sweeping is required to improve the profile quality given the extremely narrow pedestal width. The SOL measurements are invaluable in providing a comparison between data from the RCP and allowing profiles to be shifted to account for uncertainties in the separatrix position. The spatial resolutions and accuracies of the TS systems are 10mm (edge) and ≤ 35 mm (core) and $\sim 15\%$ and $15\%-25\%$ for T_e and n_e respectively.

The divertor LP diagnostic [177] consists of 34.4 mm diameter graphite single probes embedded flush in the central column tiles with probe spacing of 17.2 mm and 26 button probes in the vessel floor with probe spacing of 11.4 mm. There are 48 amplifiers so that in total 48 probes can be acquired at any time. Standard acquisition frequency is ~ 100 kHz. When in sweep mode, the probe voltage is typically swept at 100 Hz. Each probe measures the ion saturation current i_{sat} from which, knowing the projected probe surface area, A_{\perp} (depending on the probe geometry and magnetic field line impact angle) the ion saturation current density, j_{sat} is derived:

$$j_{\text{sat}} = i_{\text{sat}} / A_{\perp} \quad (5.1.)$$

The electron temperature is derived by applying standard fitting procedures (non-linear least squares) to the equation describing the probe sheath current-voltage characteristics,

$$I_{\text{pr}}(V) = i_{\text{sat}} [1 - \exp(-\frac{(V_{\text{pr}} - V_f)}{kT_e})] \quad (5.2.)$$

where I_{pr} , V_{pr} are the probe current and voltage respectively, and V_f is the probe floating potential which the probe adopts when the net current is zero. The ratio of electron to ion saturation current should normally be much greater than 1. In a weakly magnetized plasma it is close to the ratio $\sqrt{m_i/m_e}$ (~ 60). In strongly magnetized plasma, due to anomalous transport, it is more often ~ 10 and in detached plasmas, it is very often closer to 1, for reasons not yet really understood. Particularly in situations close to detachment/high recycling, where j_{sat} in fact can be extremely high, but T_e is quite low, the saturation current can diverge from the exponential behaviour leading to failed analysis [178]. In fact almost all strongly magnetised plasmas exhibit this behaviour, at least for probe voltages higher than the floating potential [179].

Furthermore, it is very often observed that especially under high recycling or detached conditions, tokamak divertor target probes yield T_e values higher than those measured by alternative methods [180]. Knowing j_{sat} and T_e , the local density is derived as:

$$j_{\text{sat}} = en_e c_s \quad (5.3.)$$

when isothermal assumption $T_i = T_e$ for c_s with $\gamma = 1$ is used. Atomic number $Z=1$ and Mach number at the targets is set to unity ($M_{\parallel}=1$).

As already mentioned, the derivation of n_e and T_e from the probe characteristics involves a number of interpretative difficulties [181], and thus their values are to be treated with some caution. The use of probe sweeping also severely reduces the time resolution of the diagnostic since each sweep yields only a single point for T_e and n_e . Sweep frequencies for the divertor system cannot generally exceed ~ 1 kHz at maximum before hardware issues render the data difficult to use. Such frequencies are far too slow to be of use in extracting parameters occurring on the ELM timescale (rise times in the range of ~ 100 μs). The most robust quantity and the best candidate for the meaningful

comparison with the code results is the j_{sat} , which is directly measured by the diagnostic and acquired at high rates, easily sufficient to provide many data points during the ELM itself. Inspection of the results provided in [149] indicates the statistical errors on j_{sat} and n_e of $\sim 7\%$ and $\sim 15\%$ for T_e . Even though an estimate of the true inherent error in deriving n_e and T_e from the probe characteristics using the standard sheath theory is complicated it most probably doesn't exceed $\sim 20\%$ in non-detached conditions.

As shown in **Fig.5.4**, the 5-pin fast reciprocating LP system [177] is located on the vacuum vessel midplane situated ~ 23 cm below the magnetic axis of the standard SNL diverted discharge on TCV. In a typical discharge the RCP reciprocates twice into the plasma, passing in each case first through a “wall shadow region” where field lines connect to the main chamber walls, before continuing through the SOL across field lines connected to the targets (see [39]). The upstream profiles of n_e and T_e are computed from RCP data using similar assumptions as for the fixed probes (there is a factor of 0.5 in the derivation of the density to account for flow acceleration such that the far field density is derived). However in the upstream region it is less likely that $T_i = T_e$ since the T_i is normally higher than T_e there [182]. If, for example $T_i = 2T_e$ the density would be overestimated by $\sim 20\%$. Therefore these data should be used with caution. Care must also be taken to properly account for uncertainties in the separatrix position.

The total radiated power and its poloidal distribution derived through tomographic inversion, is obtained with a system of foil bolometric cameras, consisting of 5 cameras with 64 viewing chords covering the entire poloidal cross-section of the TCV vessel. These bolometers are sensitive to both photons and neutral particles representing a shortcoming for the tomographic inversion technique (see below) in a sense that the assumption that plasma is transparent to the escaping radiation is violated by the presence of neutrals. Consequently, the reconstructed distribution becomes increasingly unreliable at high plasma densities when the neutral density increases especially in the divertor region. Tomographic inversion of the multichord camera signals to produce a two-dimensional poloidal reconstruction of the radiation intensities was obtained in collaboration with researchers from Hungarian Fusion Association (HAS). Such data represents an important test of the SOLPS5 simulations, which model the 2D plasma emission in the edge and SOL regions.

In 2005 the installation of a new system of radiation detectors based on absolute extreme VUV (AXUV) diodes has been completed on TCV. These AXUV diode detectors have the advantage of being semiconductor devices sensitive to photons and insensitive to neutrals. They are also capable of extremely high time resolution compared with a few ms for conventional foil bolometers (typically 100 kHz on TCV, limited essentially only by the modular transimpedance amplifier electronics mounted onto printed circuit boards which plug directly onto the vacuum feedthroughs). These cameras have been designed with the help of SOLPS5.0 simulations of recycling light emission intensities. They are arranged in a 7 camera array providing complete poloidal coverage of the TCV cross-section at a single toroidal location [183]. Each camera initially contained two identical diodes, one for bolometry allowing the measurement of total photonic plasma radiation (at energies in the range $\sim 10\text{eV} - 6\text{keV}$) and a second filtered for Lyman alpha (L_α) radiation at 120 nm resulting from excitation of hydrogenic atoms located in the cool plasma periphery. Filtering is achieved using VUV absorption filters mounted directly in front of the diodes. These are pinhole cameras using slit apertures

and their design is a modification of the concentric cylinder, re-entrant mechanical structure employed for many years on TCV for the soft X-ray tomography diagnostic [184]. With 7 cameras, the system provides a total of 280 viewing chords, 140 for each of the two diode sets (bolometry and L_α), giving unprecedented coverage for tomographic inversion of total radiation and recycling emission.

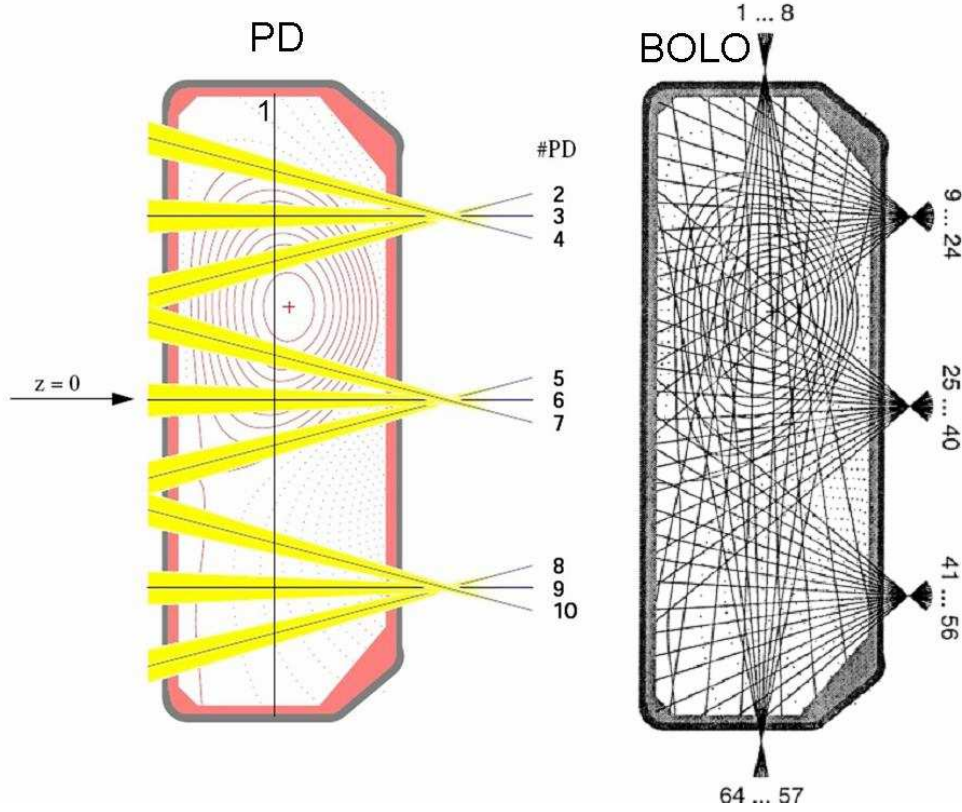


Figure 5.5 System of photodiodes (left) and foil bolometers (right) at TCV. Vertical chord #1 is unapertured and has much larger angular divergence compared to the lateral counterparts.

The author of this thesis was originally responsible for this new diagnostic and associated fast multi-channel acquisition system. Initially it was hoped to obtain new and unique experimental data from TCV using the L_α filtered diode sets, which would detect the radiation only from the edge and divertor regions and thus could be compared with edge plasma simulations (SOLPS5). The primary aims of the AXUV diagnostic were the investigation of fast transient events (ELMs and disruptions) through their radiation characteristics and, in conjunction with modelling using SOLPS5 code package, the study of neutral recycling distributions. In addition, by combining the total radiation from tomographic inversion from both foil and AXUV data, it was hoped that some idea of the spatial distribution of neutral particles might be obtained experimentally. However, estimating the true photonic component from AXUV is non-trivial, owing to the reduced

sensitivity of the diodes to radiation from lower photon energies, in the visible to UV region, where substantial emission can be present in fusion edge plasmas. First results in this respect have been presented by G. Veres at the Hefei Plasma-Surface Interactions conference [185].

Unfortunately, regarding the L_α filtered system, experiments on TCV quickly revealed a lack of signal on all but a handful of diodes. The conclusion of subsequent laboratory tests conducted on the cameras by the author during the 2006 TCV summer shutdown was that the low peak transmission of the L_α absorption filters (10%) and the strong angular dependence of this emission (only 1% at incidence angle $\sim 60^\circ$), means that insufficient L_α emission is gathered from even the highest density TCV plasmas for the filtered diodes to be useful. A few small scratches on one or two of the filters (the absorption layer is extremely thin – of the order of microns), which likely occurred during initial mounting of the filters inside the camera systems, were allowing plasma light to penetrate to several diodes. It also turns out that the diodes are subject to a relatively strong ageing effect (due both to exposure to boronisation, He glow discharge and plasma operation), a feature observed quickly on the unfiltered diode set. Further work in 2007 has demonstrated that the new cameras will not be useable for the specific detection of hydrogenic recycling emission and they are now being used for a different purpose.

The direction of the thesis has thus refocused more on the SOLPS5 simulations of H-mode in general and the original thesis title “Particle sources in the TCV tokamak edge” has been changed to “SOLPS5 modeling of ELMing H-mode”. Moreover, the quality of data from even the unfiltered cameras during the ELMing H-modes simulated here turned out to be insufficient for comparison with the modelling.

For the measurements of the radiation in the visible part of the spectrum the system of photodiodes (PD) including 9 detectors installed on the lateral ports and one on the top of TCV is used (see **Fig.5.5**). They provide the signals of D_α local recycling emissions from viewing lines and are compared with the simulated D_α radiation integrated over the lines of sight corresponding to the viewing chords of the PDs (more details see in section 6.1.5.5).

Outer target heat flux profiles are deduced from the tile surface temperature rise using a vertically viewing fast infrared (IR) [186] camera in conjunction with the THEODOR finite difference heat flux calculation code [187]. This data was used to investigate the divertor target heating due to ELMs on TCV and are compared with the SOLPS output. The experimentally measured deposited heat loads can be used to estimate the sheath heat transmission coefficients through the formula:

$$P_\perp = \gamma T_e j_{\text{sat}} \sin \alpha \quad (5.4)$$

where the P_\perp is the measured quantity obtained from IR and j_{sat} , T_e are obtained from the LPs. The α is the angle of the total magnetic field on the surface obtained from the magnetic reconstruction.

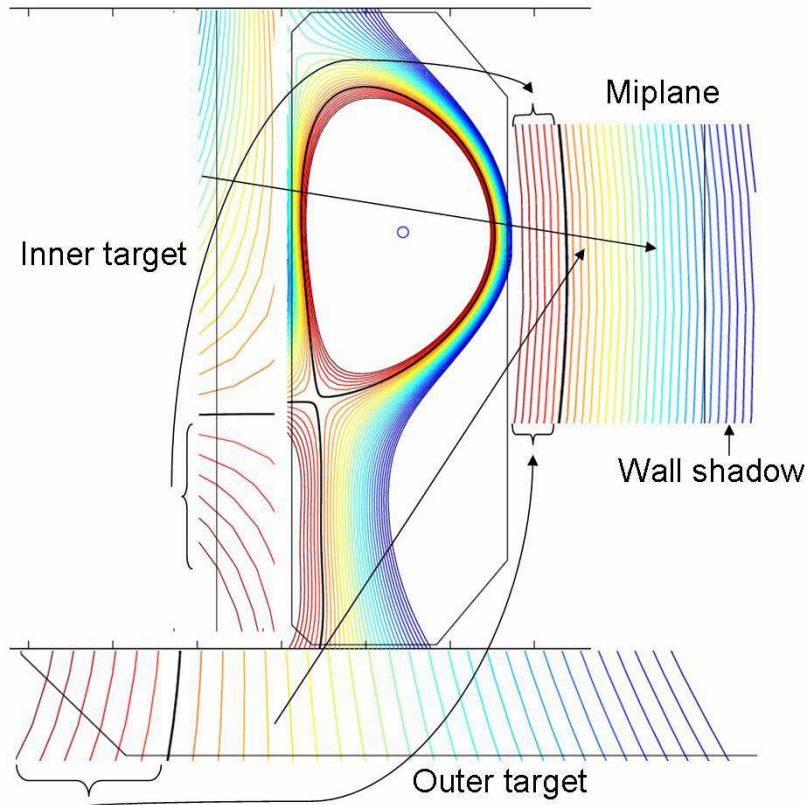


Figure 5.6. Schematic of mapping on the midplane

If not explicitly stated otherwise, all radial upstream and target profiles shown in the next chapters are mapped to the outer midplane and presented in terms of the distance from the separatrix ($r-r_{\text{sep}}$, where r_{sep} represents the radial position of the separatrix at outer midplane and r the radial position of the mapped point at outer midplane). A schematic of the mapping on the midplane for TCV is depicted in **Fig.5.6**.

5.2.2. Diagnostics at JET

Since very similar diagnostics have been used at JET and TCV for the code-experiment comparisons, the JET diagnostic set is only described briefly here, with appropriate references where details can be sought. The positions and viewing chords of most of these diagnostics are shown in **Fig.5.7**. Upstream profile measurements of n_e and T_e are provided by diagnostics depicted in upper part of **Fig.5.7**, Lithium-beam (KY63) [188], edge high resolution Thomson scattering spectroscopy HRTS (KE9D) [189], core LIDAR TS [190] and edge LIDAR [188,191], electron cyclotron emission diagnostics ECE [192-194]. Upstream ion temperatures are measured using CXRS [195]. Ion particle fluxes (j_{sat}) and T_e at the inner and outer targets are measured using fixed Langmuir probes [196] and infrared (IR) thermography [197]). The radiation power is provided by the system of fast bolometric cameras [198-200]. A recent upgrade [200] to the JET bolometer system has enabled radiated power measurements on ~ 1 ms timescale,

allowing ELM induced radiation to be studied [201-202]. It should be noted that there are often significant uncertainties in the magnetic separatrix position at JET. Coupled with positional uncertainties on some of the profile diagnostics, considerable empirical shifting of the radial profiles is sometimes required in order to allow quantitative comparison of composite profiles with simulations (a similar procedure was required in [172] for comparison with EDGE2D simulations).

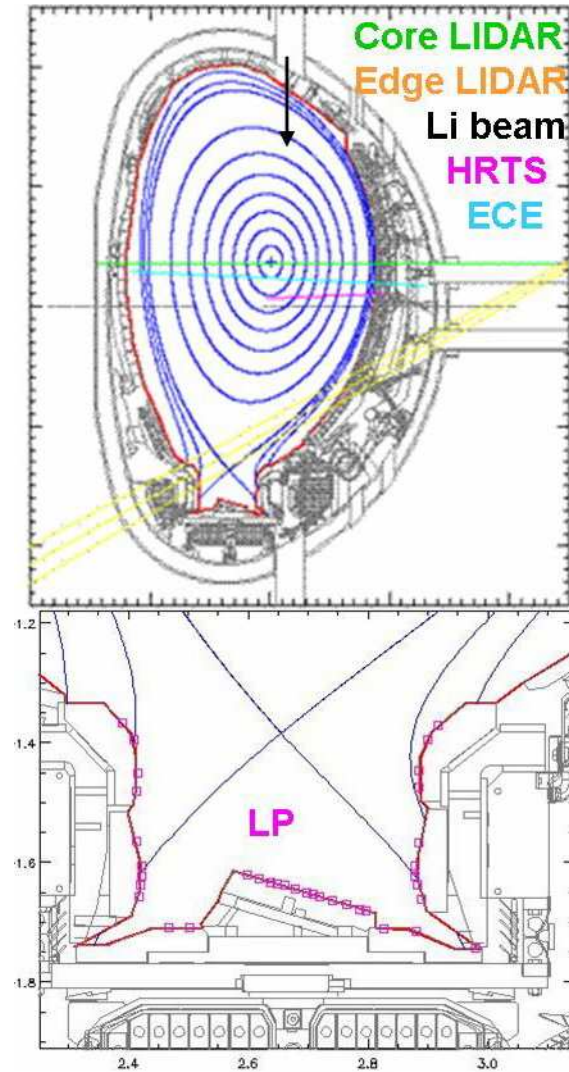


Figure 5.7. Diagnostics at JET producing data for comparison with SOLPS5 simulations

6. Simulations of ELMing H-mode at TCV

Although ohmic H-modes have long been produced on TCV and the effects of ELMs at the divertor target studied in some detail, no attempt has yet been made to model the scrape-off layer (SOL) in these plasmas. This chapter describes details of the first such efforts in which simulations of both inter-ELM and ELM phases using the coupled fluid-Monte Carlo SOLPS5 code (without drifts) are constrained by experimental data obtained from diagnostics described in chapter 5.

The code/experiment comparison for both Type III and Type I ELMing H-mode on the TCV and JET tokamaks is presented in this chapter, while the major part summarizes the results of simulations of the Type III ELMing H-mode #26730 (sections 6.1 and 6.3) and section 6.2 gives a brief description of Type I ELMing H-mode #32713.

6.1. Type III ELMing H-mode at TCV

The first part of this section summarizes the essential information which is relevant to all the simulations presented in this thesis, but the focus is especially on the Type III ELMing H-mode at TCV. The challenge is to reproduce the experimental observations with the SOLPS5 simulated ELMs. The settings, inputs and boundary conditions are listed and also the way of determining the anomalous transport coefficients discussed in detail. Different approaches to the simulation of both steady state and the ELM event are also presented. In the second part, the simulation attempts to reproduce the observed experimental data are described. Sensitivity studies have been performed on the various boundary conditions and parameters, including the effects of variations in the heat flux limiters. The focus then switches to time-dependent modelling of the ELM cycle. Following an introduction to the technique of such a simulation in SOLPS, different ELM models and approaches to simulations are discussed. The simulations are compared with the available data and in addition benchmarked with the kinetic 1D PiC code BIT1.

6.1.1. Experiment

Simulations described here have been performed for a typical deuterium single null lower (SNL) ohmic Type III ELMing H-mode target discharge (#26730) at TCV with plasma current $I_p = 430$ kA, reversed field $B_\phi \sim 1.43$ T, line averaged electron density $\bar{n}_e = 6 \times 10^{19} \text{ m}^{-3}$ ($n/n_{GW} \sim 0.3$; n_{GW} is the Greenwald density) and stored energy of ~ 20 kJ. The magnetic equilibrium reconstruction of this SNL configuration corresponds to the simulation grid shown in **Fig. 6.1**, illustrating the short high field side (HFS) divertor leg on the central column and low field side (LFS) strike point on the vessel floor. This rather unconventional diverted configuration is characteristic of TCV. The plasma has elongation and triangularity of $\kappa_{95} = 1.65$, $\delta_{95} = 0.4$ respectively, and $q_{95} = 2.5$. The time evolution of a few relevant plasma signals are shown in **Fig. 6.2**. Since not all required data are available for this particular discharge data from several very similar discharges have been combined to provide the simulation benchmark dataset. Thus, radiated power

from #20703 is combined with edge and SOL profiles from #26730 (TS and RCP), #31832 and #31837 (RCP), #31838 (LPs) and #31835 (IR).

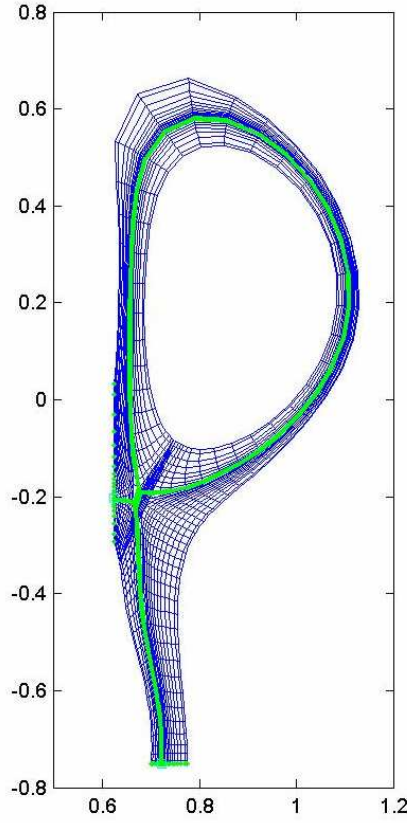


Figure 6.1. Grid used for the simulation of the TCV discharge #26730 and Type III ELM; green lines represents the separatrix

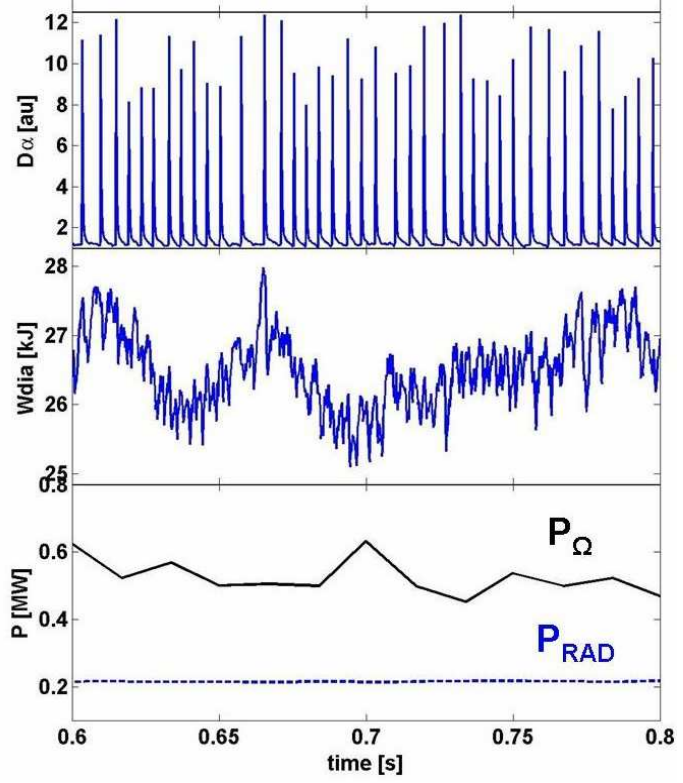


Figure 6.2. Time-traces of the main parameters of the discharge #26730 simulated in this chapter. It can be seen on the signal of D_α that the ELMs are very regular and similar. While ohmic power P_Ω is depicted for #26730, the P_{RAD} is taken from similar shot #20703, for which bolometry data of better quality are available.

6.1.2. Settings, inputs, boundary conditions

In the next section the input parameters and assumptions which have been adopted to simulate type III ELMing #26730 are summarized. In the simulations presented in this thesis the approach has been to systematically introduce increasingly sophisticated options inspired by the observations. The initial simulations thus begin with the simplest input parameters and boundary conditions. Once converged solutions are obtained, new options and boundary conditions are added. Therefore, the results presented here are only the “final product” and the selection of the best of the hundreds of the simulations which have been launched and analyzed in order to give meaningful solutions on the issues addressed.

Experimentally obtained inputs given to the code are magnetic equilibrium, upstream density at the separatrix and power entering the grid from core boundary. The power crossing the core boundary, P_{SOLPS} is assumed to be equally shared between electrons and ions. This is taken from the experiment as a difference between the input power P_{IN} (in this case \sim ohmic power P_{Ω}) and power radiated in the core part of the grid $P_{\text{RAD,CORE}}$. The values of P_{SOL} in **Tab.5.2** correspond to the values of P_{SOLPS} chosen for the simulations. For the simulations of discharge #26730, $P_{\text{SOLPS}} = 400\text{kW}$, while 200 kW belongs to electrons and 200 kW to ions. The value of $P_{\text{SOL}} = 400\text{ kW}$ estimated as a difference between $P_{\Omega} = 555\text{ kW}$ and $P_{\text{RAD,CORE}} = 155\text{ kW}$ (see **Fig.6.2**), while the radiated power was taken from very similar discharge #20703 for which the data of better quality were available. Although the plasma parameters of the two shots #26730 and #20703 are very close they were performed at different times with respect to separate vessel boronisations. Since on TCV proximity to boronisation is usually associated with lower impurity levels and hence lower radiation, it is expected that P_{RAD} for the simulated shot (performed sooner after boronisation than #20703) would be at least as low as and likely even lower than that assumed (based on #20703). Since $P_{\Omega} = 500\text{ kW}$ of the simulated discharge #26730 is slightly lower than the one of #20703 (555 kW), the value P_{SOLPS} is expected to be at least $\sim 555 - 155 = 400\text{ kW}$. The power crossing the core boundary in SOLPS, adapts to match P_{SOLPS} .

Other experimentally obtained inputs given to the code is the upstream density at the outer midplane separatrix obtained from edge TS, n_e^{sep} is prescribed as the value in **Tab.5.2** (for this simulation $n_e^{\text{sep}} = 1.6 \times 10^{19}\text{ m}^{-3}$) and the feedback mechanism is used on a gas puff which increases the input particle flux if the computed density at the separatrix is below required density and reduces it otherwise. Simulations of this nature are also frequently performed by prescribing a flux at the inner core boundary. This makes more sense in predictive simulations for a machine like ITER, where there is no data to guide the prescription of a separatrix density. Separatrix density feedback is used throughout here given that data are available to guide the choice of n_e^{sep} .

The gas puff is described inside the EIRENE input file as a point source of D_2 , placed on the vessel floor from where it is introduced to the divertor as in experiment. A particle recycling coefficient of $R=1.00$ is used on all surfaces including the divertor targets and the core boundary is fully absorbing for neutrals. The total ion outflux from the core is equal to the neutral influx into the core and it is redistributed equally over the entire core boundary. The Mach number is set as $M_{\parallel} \geq 1$ at both targets and a decay length of 3cm is fixed at the north boundary for densities of all species and temperatures T_i and T_e . With the exception of simulations reported in section 6.3. the parallel velocities at the north and south boundaries are, as an adhoc assumption, set to zero. Physical sputtering is implemented according to the Roth-Bodansky formula and chemical sputtering from D^+ and D impact is set to 3.5% on all surfaces. Both physical and chemical ion sputtering occur only at the divertor targets and therefore no ion sputtering is assumed at the north boundary, corresponding to an absence of impurity release at the main chamber walls. Carbon impurities in all ionization states are assumed to be deposited on material surfaces with a sticking coefficient of unity.

Quite an important part of this work is devoted to the study of the boundary conditions (sheath heat transmission coefficients and heat flux limiters) representing the

approximation of the kinetic effects in the fluid B2.5 code. They are discussed in more detail in the section 6.1.5.6, where the comparison of fluid SOLPS5.0 and kinetic PiC BIT1 code is presented. Here only the values which are usually used in the simulations will be given. The sheath heat transmission coefficient for electrons γ_e is in SOLPS defined as

$$\gamma_e = \gamma_e^* + \frac{V}{T_e} \quad (6.1)$$

where V is the potential at the targets, T_e is the temperature at the targets and γ_e^* is a constant given in the input file (with boundary conditions specified in B2.5) and in all the simulations in this thesis is set to $\gamma_e^* = 2$, giving $\gamma_e \sim 5$. The ion sheath heat transmission coefficient is set to a constant value, $\gamma_i = \gamma_i^*$ and in all simulations $\gamma_i^* = 3.5$. Thus the total sheath heat transmission coefficient is around $\gamma_e = \gamma_e + \gamma_i \sim 8$. For these pre-ELM simulations and unless otherwise stated elsewhere, the electron and ion heat flux limiters are fixed as $\alpha_e = 0.3$ and $\alpha_i = 10$ respectively, with the latter corresponding effectively to no heat flux limit for the ions. The viscous stress limiter is set to $\alpha_v = 0.5$. Quite an extensive sensitivity study of the effects of the flux limiters has been performed in this work and is presented in section 6.1.5.6.2.

The simulation grid for TCV discharge #26730 shown in **Fig. 6.1**, has been reconstructed from the magnetic equilibrium of this discharge at 0.7s and extends radially from -2.5 cm inside and +2 cm outside the midplane separatrix. This grid extent is sufficient to encompass the edge transport barrier (ETB) region, which is rather narrow in TCV (see below). It has 72 poloidal cells (in SOLPS numbered ix) including the guard cells at the inner and outer targets and 24 radial cells (numbered iy), also including the guard cells at the inner and outer grid boundaries. The first 11 poloidal cells cover the inner divertor, the next 40 (ix=12-51) the main SOL and the last 21 (ix=52-72) the outer divertor. The separatrix is located between the radial cells 9 and 10 and outer midplane is at poloidal cell 36. Carbon is the dominant impurity in TCV away from boroization and is included in the simulation, with transport coefficients assigned as for the fuel species. The fluid code simulations thus contain 9 species. These are the neutrals of deuterium and carbon, D and C; and ion species which include D^+ and all charge states of carbon, C^+ , C^{2+} , C^{3+} , C^{4+} , C^{5+} , C^{6+} . No drifts have been included in the simulations presented in this thesis.

6.1.3. Determination of anomalous transport coefficients

Several approaches are possible to determine the anomalous transport coefficients used for calculation of radial fluxes in SOLPS. The first is the direct comparison with experimental measurements. Effective diffusion coefficients can be derived from experimental profile measurements (as done for example in C-Mod [41]). The convective radial velocity, v_\perp can be obtained from direct measurements from turbulence. However, this is not always possible, since the turbulence measurements of energy fluxes are rarely (if ever) available. Moreover, the turbulence on ion energies is never measured and T_i in the SOL only rarely. The second possibility is coupling with a turbulence code, in which

the fluid transport code passes temperature and density profiles to the turbulence code. The latter calculates the turbulent radial fluxes (on typical turbulence timescales of order of the plasma frequency 1-100 μ s) and these enter the transport code as particle and thermal diffusivities, D_{\perp} and χ_{\perp} [203-204] with timescales of 1-1000 ms (related to ion and parallel neutral transport or wall processes for saturation and pumping or equilibration of the core). It would be incredibly expensive to run the turbulence codes for long transport timescales and therefore the most convenient and most often used approach, employed also throughout this thesis, is to systematically adjust the anomalous transport coefficients until the best possible agreement with the experimental profiles is achieved.

The anomalous transport coefficients used for calculation of radial fluxes in SOLPS can be in general space and/or time dependent. There are several possible models of these anomalous transport coefficients in the code:

- constant in real or flux space
- poloidal variation representing the ballooning nature of the turbulent driven fluxes
- radial variation for pedestal and/or SOL studies
- poloidal variation of the radial profiles in the different regions of the grid in order to account for the different ansatzes of radial profiles of transport coefficients in main plasma and divertor regions
- time-dependent for ELM studies including the space variation possibilities mentioned above

The possibilities of the radial and poloidal variation of the transport coefficients in the code are schematically shown on **Fig.6.18**. The radial variation of transport coefficients in H-mode is basically expressed by the division of the SOL radial profile into three regions. One is on closed field lines, the second is the transition region close to the separatrix, representing the steep H-mode pedestal and the third is the outer SOL which seems to be dominated by rather large radial plasma transport creating rather flat plasma profiles extending to the main chamber walls [17]. This might be created by flute-like turbulence with rather high $\vec{B} \times \vec{\nabla} B$ and $\vec{E} \times \vec{B}$ drifts causing the plasma filaments to propagate rapidly outwards as explained in Chapter 3.

The introduction of poloidally and radially varying transport coefficients potentially produces a large number of free parameters. Despite the fact that SOL modelling is very successfully able to identify the basic physics mechanisms and in many cases represent even quantitatively the experimental results, the largest uncertainty in the SOL description is the question of the anomalous transport. Consequently, the major difficulty in predicting divertor conditions for future tokamaks is the uncertainty in the magnitude of the anomalous transport of energy and particles. One way of doing this is to take the experimentally measured gradient lengths of power, temperature and density from existing machines and extrapolate these quantities for future machines and then compare these values with those predicted by the code and, if necessary, adjust the transport coefficients in the code to produce better match. Another approach is to attempt to find the scaling of transport coefficients directly. SOLPS5.0 has been used to determine the appropriate transport coefficients for various experimental discharges and find the scaling of these coefficients [205-207]. This is very important also in case of transient events such as ELMs, the prediction of which is crucial in designing next step devices.

6.1.4. Simulations of inter-ELM phase

The first step in the simulation of the ELM cycle is to establish a “steady-state”, pre- or inter-ELM model to provide a starting point for the more complex time dependent ELM simulations. In order to use the steady state solution as a starting point for the time-dependent ELM simulation, it must, however, also be time-dependent. For a truly self-consistent solution, the time steps for the plasma fluid code (B2.5) and the EIRENE neutral code must be matched if artificial compression of the neutral timescale is to be avoided [208]. Establishing this concordance of time steps required considerable effort and was eventually solved.

This section contains the results presented in [209] but with the addition of new material offering a more complete picture of the simulation study which has been performed, including sensitivity studies (on the input power, ballooning effects and the effect of changing transport levels in the divertor and PFR regions) and analysis of additional issues compared to the published work.

As it was already mentioned in the previous section, the anomalous coefficients represent the biggest uncertainty in the SOLPS simulations. Different approaches to choose the ansatz for these coefficients are discussed in the following text.

The SOL radial particle and heat flux includes not just diffusive but also convective components, for which there is yet no experimentally verified physical model with which the values of the transport coefficients can be specified for use in the SOLPS5 simulations. However, the only important quantity concerning the results of the code is the total radial particle flux Γ_{\perp} and thus choosing a radially dependent D_{\perp} , v_{\perp} or their combination for describing this flux is equivalent. Thus the transport can be specified by diffusion alone, or an adhoc combination of diffusivity and convection, or by convection alone using the convective velocity v_{\perp} . In this work three different approaches have been attempted, the results of which are summarized in this section:

- 1.) “**Diffusive approach**” with D_{\perp} , $\chi_{\perp i, e}$ radially varying and $v_{\perp}=0$
- 2.) “**Convective approach I**” with D_{\perp} having radially flat profile with small values (~ 0.1), $\chi_{\perp i, e}$ radially varying as in 1.) and finite, radially varying v_{\perp}
- 3.) “**Convective approach II**” with both D_{\perp} and $\chi_{\perp i, e}$ having radially flat profiles with small value (~ 0.1) and radially varying v_{\perp}

Since the contribution of D_{\perp} , $\chi_{\perp i, e}$ in both convective approaches is very small in Eq.2.70, v_{\perp} represents the effective radial velocity v_{eff} (see Eq.2.77).

In the absence of experimental data for the ion temperature profile (since the edge charge exchange measurements on TCV became available only at the end of the PhD work), $\chi_{\perp i} = \chi_{\perp e}$ was assumed in all the simulations in this chapter.

6.1.4.1. Diffusive approach

In the first simulation attempts in this work referred to as “diffusive approach” the approach used in the JET EDGE2D-Nimbus study in [172], was broadly followed. Coefficients, D_{\perp} , $\chi_{\perp,e}$ controlling the rate of perpendicular particle and energy diffusion are systematically adjusted in order to obtain satisfactory agreement between experimental and simulated midplane profiles.

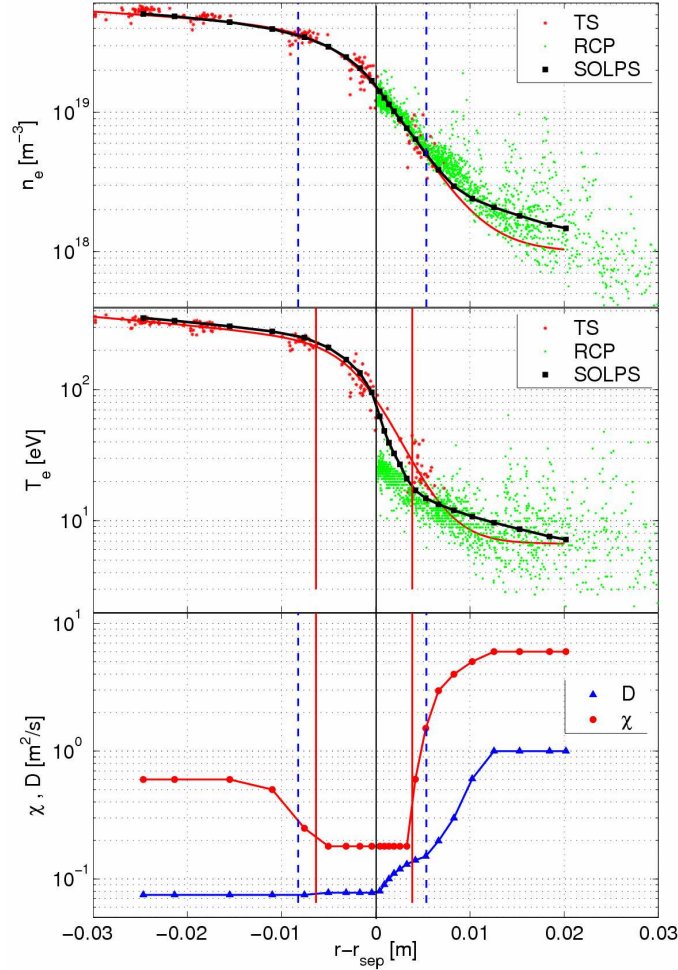


Figure 6.3. Density n_e and temperature T_e profiles from SOLPS5 (black squares), edge TS (red points) and RCP (green dots). The perpendicular particle and heat transport coefficients D_{\perp} (blue triangles) and χ_{\perp} (red circles) used to obtain the upstream match are shown in the lower plot. It is assumed that $\chi_{\perp,e} = \chi_{\perp,i}$ and $v_{\perp} = 0$. All data have been mapped to outer midplane and expressed in terms of distance from the separatrix – see section 5.2.1. The black vertical line marks the separatrix location ($r - r_{sep} = 0$). The blue dashed lines and red full lines indicate respectively the width of the pedestal for n_e and T_e estimated from TS data. The RCP data are from shots #26730, #31832 and #31837 and the TS data from #26730. SOLPS simulation number is 27195.

Fig.6.3 compiles the results for the upstream profiles of T_e and n_e in comparison with the edge TS and RCP data. The TS profiles are compilations of a number of laser

pulses through the discharge, filtered to exclude ELM events. The composite profile has been fitted using a tanh function which identifies the experimentally measured midplane pedestal height and width [210] as $3.6 \times 10^{19} \text{ m}^{-3}$, 1.36 cm and 179 eV, 1.02 cm for n_e and T_e respectively. Where the data overlap there is generally very good agreement of upstream n_e and T_e experimental profiles from the two diagnostic systems. For density, the RCP data have been multiplied by a factor of 0.5 to account for the known overestimation due to finite Larmor radius effects which increase the projected collection area of the Langmuir probe pins. No radial shift has been applied to the profiles [209].

The SOLPS5 model profiles of the inter-ELM simulation, following the first “diffusive approach”, are also shown in **Fig.6.3**, superimposed on the experimental data. Invoking only a radial variation of D_\perp , χ_\perp (to account for the very differing transport rates in the edge pedestal and main SOL regions) with $v_\perp = 0$ keeping edge transport barrier (ETB) everywhere, the SOLPS density profile matches experiment rather well. In the case of T_e it has not been possible to match the full shape of the pedestal even if the separatrix values are close. The diffusion coefficient D_\perp does not require much variation in the region through the confined and ETB regions. However, a gradual decrease of $\chi_{\perp,i,e}$ is required from just inside the inner boundary of the simulation region right through the ETB. In the main SOL, both D_\perp and $\chi_{\perp,i,e}$ are increased up to a values of $1 \text{ m}^2 \text{ s}^{-1}$ and $6 \text{ m}^2 \text{ s}^{-1}$ respectively. A higher value of $\chi_{\perp,i,e}$ than D_\perp in the main SOL has been applied in order to flatten the temperature profile there. An ansatz with a transport barrier in the radial profiles of particle and heat diffusivities thus allows the steep pedestal region inside the magnetic separatrix to be satisfactorily reproduced. Interestingly, results of a similar study on the ASDEX-Upgrade tokamak using SOLPS5 have also very recently been published and are in good agreement with those from TCV regarding the SOL and pedestal region transport in both radial shape and magnitude [211]. It seems clear that the foot of the ETB extends somewhat (~0.5 cm at the midplane) into the SOL itself. This is similar to the JET findings in [172]. Unlike the analysis in [172], however, in these simulations no inward pinch has been found necessary to obtain a good match to experiment.

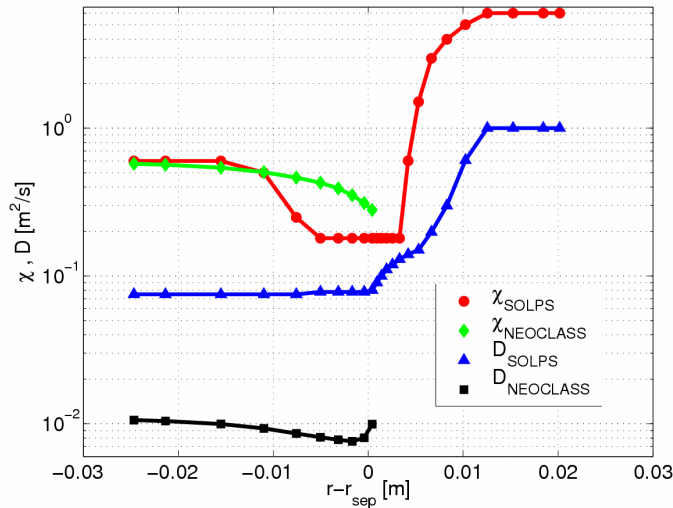


Figure 6.4. The perpendicular particle and heat transport coefficients D_\perp and χ_\perp used to obtain the upstream match shown in **Fig.6.3** in SOLPS compared with the ion neoclassical values calculated using the parameters T_e , T_i , n_e from SOLPS [212].

Furthermore, the derived SOLPS5 transport parameters D_{\perp} , χ_{\perp} have been compared with ion neoclassical values in the pedestal region (calculated using the density and temperature data from SOLPS since pedestal measurements of ion temperature were not yet available on TCV at the time of doing this analysis [212]) and found to be very similar. As it can be seen in **Fig. 6.4**, the SOLPS5 TCV simulations show transport levels of ions near to neo-classical in the pedestal region. This is not the case for electrons, for which always higher anomalous coefficients are observed.

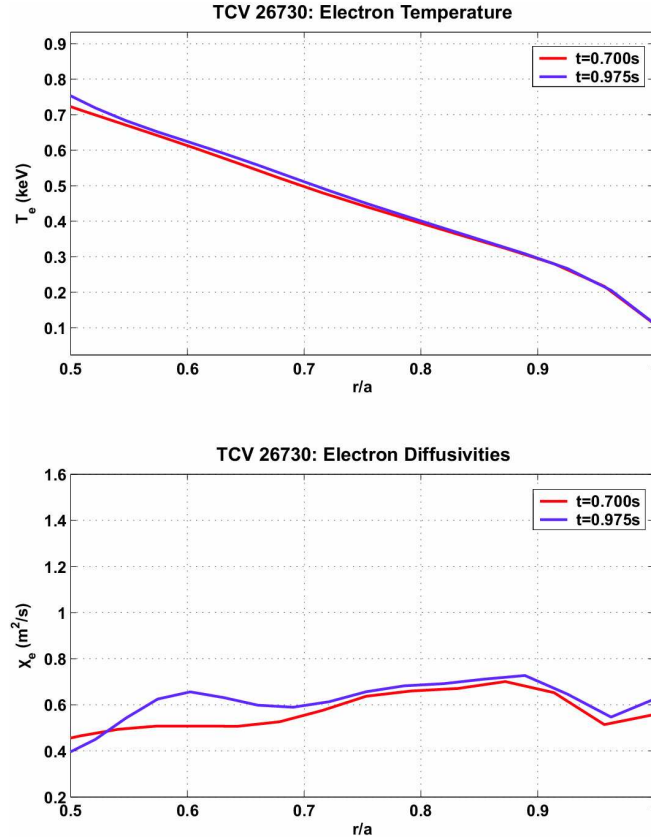


Figure 6.5. *Upper:* The profiles of upstream midplane T_e from ASTRA code fitting the experimental TS profiles including both core and edge TS data for #26730 at different times (0.7 and 0.975s). *Lower:* Corresponding values of electron heat diffusivity coefficients calculated by ASTRA. Note, that the data are plotted against r/a and not against $r-r_{sep}$ mapped to the midplane as in figures with SOLPS results. Here $r/a=1$ corresponds to separatrix ($r-r_{sep}=0$). The values of $\chi_{\perp e}$ found by ASTRA close to the separatrix $\sim 0.5 m^2.s^{-1}$ are nicely compatible with those found by SOLPS within a factor of ~ 2 (see **Fig.6.3**). Supplied by Dr. Elina Asp and Dr. Olivier Sauter.

Based on the experimental T_e profiles from TS system the heat diffusivity coefficients were calculated using the core transport code ASTRA [213] for the simulated discharge #26730 in steady state. **Fig.6.5** compiles ASTRA results in which the temperature profiles from different times were matched by the code and corresponding $\chi_{\perp e}$ obtained. Within the variety of discrepancies one might expect for comparison between such different codes, the values of $\chi_{\perp e}$ in the pedestal region required by SOLPS to provide the

best fit to TS edge profiles, are to a satisfactory extent (within a factor of ~ 2) consistent with those found by ASTRA ($\sim 0.5 \text{ m}^2.\text{s}^{-1}$). The values of $\chi_{\perp i}$ could not be obtained from ASTRA for lack of T_i profile information.

6.1.4.2. Convective approach

Direct measurements of turbulent driven $\vec{E} \times \vec{B}$ radial particle fluxes compared with 2D fluid turbulence simulations of the TCV SOL using the ESEL code [214] show that in the mid to far SOL at least, interchange turbulence is responsible for the observed transport. In this case, convection as the main contributor to particle flux is more appropriate, but it is not clear which mechanism drives the cross-field transport in the near SOL. The experimental observations of turbulent perpendicular transport in the TCV SOL, in particular the strong dependence of average radial intermittent particle flux on local mean density [215], are a good basis for the assumption that the purely diffusive description of the radial transport in SOLPS is inadequate, especially at high density. It therefore seems reasonable to invoke the convective component via v_{\perp} in Eq.2.70 representing the intermittent nature of the observed turbulent flux. In favour of the introduction of radially dependent perpendicular convective transport into the simulations are also the simulations by UEDGE for C-MOD [216] and DIII-D [217-219]. Encouraging also are the considerable improvements in the code-experiment match during the detached regime on TCV when using the radially dependent convective v_{\perp} while maintaining spatially constant D_{\perp} [149].

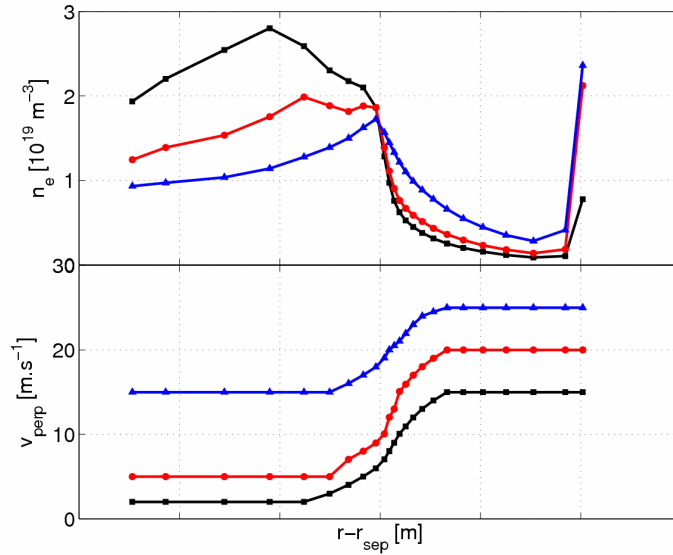


Figure 6.6. The radial profiles of density together with the anomalous perpendicular velocity v_{\perp} in the simulations with $D_{\perp} \sim 0.1 \text{ m}^2.\text{s}^{-1}$ where the same boundary conditions as in “diffusive” simulations are set.

In contrast to the diffusive case, convective transport, described as $\Gamma_{\perp}^{\text{conv}} = n.v_{\perp}$, does not contain any a priori information on $\nabla_{\perp} n$ and can therefore lead to density

radially increasing in the SOL. An example of this behaviour which is not observed in experiment, is shown on **Fig. 6.6** for a simulation with the same boundary conditions for density as used for the diffusive approach (zero particle flux density at inner boundary and decay length for density of 3cm at outer boundary). To overcome this problem, the boundary conditions for density at the inner and especially the outer boundary need to be modified. One possibility is to follow the approach in [149] and define the maximum permissible value of $\Gamma_{\perp}^{\text{conv}}$ and calculate v_{\perp} from this flux.

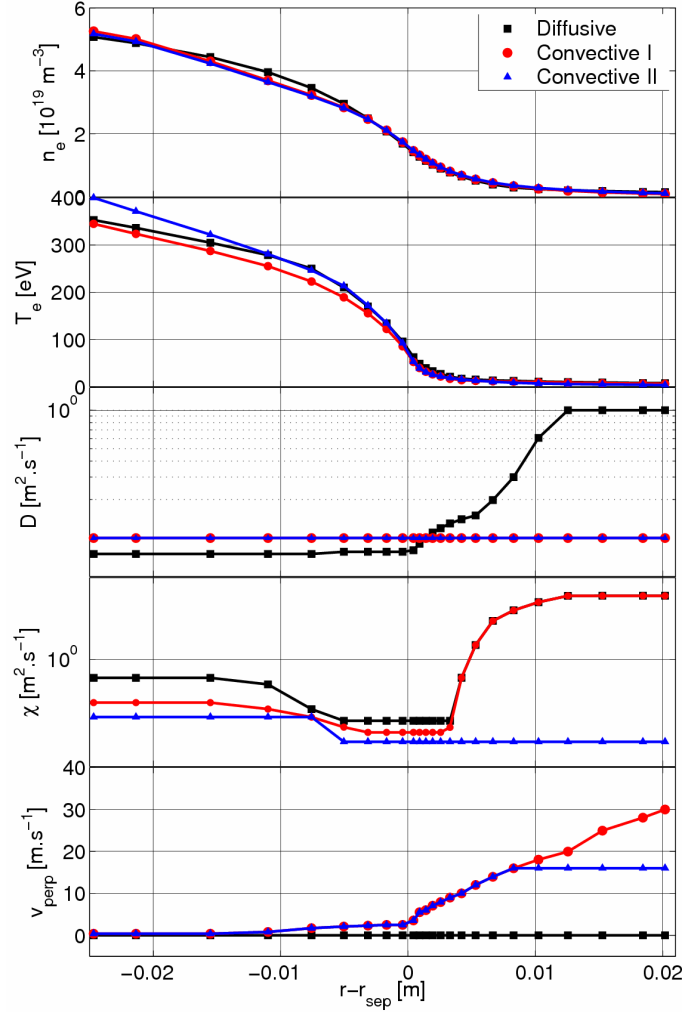


Figure 6.7. The upstream profiles n_e , T_e simulated by SOLPS and corresponding anomalous transport coefficients D_{\perp} , χ_{\perp} , v_{\perp} which were required to obtain the best agreement with experiment. Three different ansatzes are shown, in black squares the “diffusive” (identical to one shown in **Fig.6.3**), in red circles “convective I” (simulation 27722) and blue triangles “convective II” ansatz (simulation 27302). All of them give very good agreement with experimental profiles of n_e , T_e but also among each other. Note, that the χ_{\perp} in “convective II” had to be lifted slightly in the inner part of the radial profile in order to fit the temperature profile there. In addition, the v_{\perp} in the outer part of the radial profile had to be flattened so that the profile of n_e would match better.

Using this scheme the best results in the simulations were obtained with a decay length for the density of D^+ ions of -8cm at the outer boundary and a zero density gradient condition for all carbon ions at the inner boundary, which is consistent with the H-mode flat density profiles in the core and the absence of a carbon core source in the simulated plasma. At the outer boundary the leakage option for density was set with leakage factor α in loss flux $\Gamma_{\text{loss}} = \alpha c_s n$, while the deuterium species were given $\alpha = -0.001$ and carbon species $\alpha = -0.025$. These conditions were chosen on the basis of experimental measurements [164]. Moreover, a zero gradient for Mach number at outer boundary was set (in contrast to purely diffusive cases where a zero parallel velocity is used as boundary condition). With these parameters, the runs show a density profile very similar to that obtained in the purely diffusive ansatz.

The simulated upstream profiles from all three approaches (Diffusive, Convective I and Convective II) are compiled in **Fig. 6.7**. This comparison illustrates that there is a certain arbitrariness to the choice of the anomalous transport coefficients, since closely similar results can be found with different approaches. It is interesting, however, that the values of v_{\perp} which have been found necessary to obtain agreement between code and experiment are increasing functions of radial distance in the SOL (approximately from 0 to 30 m.s^{-1}). This is very similar to the effective convection velocities obtained directly from measurements of turbulence in low density TCV L-modes [220] where the radial velocity v_{\perp} rises from about 0 to $\sim 100 \text{ ms}^{-1}$ across the midplane mapped SOL width from separatrix to wall radius (see **Fig. 6.8**).

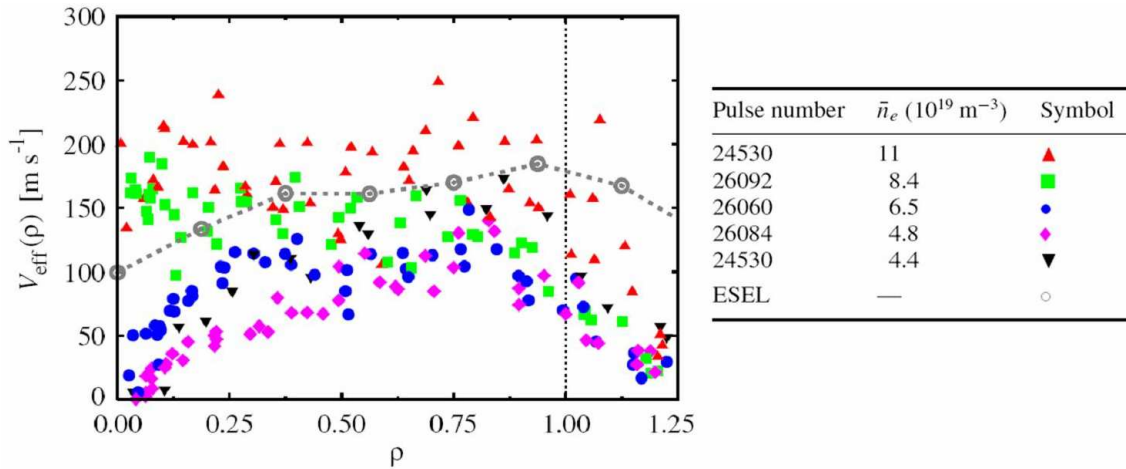


Figure 6.8. Radial profiles of the effective radial convection velocity in the SOL defined by Γ/n for the density scan of L-mode discharges in TCV including the predictions from the 2D fluid turbulence code ESEL. Extracted from [220].

The L-mode discharges described in [220] have $I_p=340 \text{ kA}$ (compared to $\sim 430 \text{ kA}$ in this simulated H-mode) and $\bar{n}_e = 5 \times 10^{19} \text{ m}^{-3}$, slightly lower than in the H-mode simulated here ($\bar{n}_e = 6 \times 10^{19} \text{ m}^{-3}$). The slightly higher convective velocities seen in the L-mode (compared with those required in SOLPS to match H-mode profiles) is unsurprising given the increased confinement in H-mode. Although indirect, this SOLPS result points to a similar convective type far SOL transport in between ELMS in H-mode. Indeed, the few measurements available during H-modes (similar to the Type III

discharges discussed here) show very similar inter-ELM turbulence statistics as for L-mode [220]. Thus, although the classical code SOLPS cannot account for the turbulence as such, in order to achieve the match with the experimental upstream profiles, a convective profile is required which matches the measured turbulent v_{\perp} in both radial profile shape and absolute magnitude. This result is self-consistent and rather satisfying. **Fig. 6.9** shows an example of the different shapes of v_{\perp} which did not provide satisfactory agreement of SOLPS with experiment, leading to the conclusion that the rising shape of v_{\perp} is the only possibility to achieve a satisfactory match. The fact that in the pedestal region the v_{\perp} is not a good description is also shown since the high values there provide too low n_e .

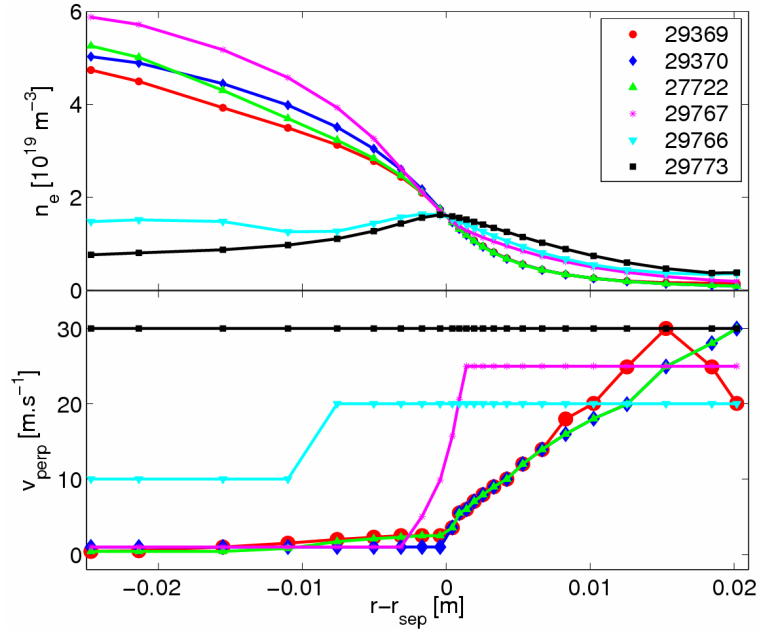


Figure 6.9 Example of radial n_e profiles from SOLPS by using different values of v_{\perp} (while keeping flat $D_{\perp} \sim 0.1 \text{ m}^2.\text{s}^{-1}$). The reference case #27722 is the one shown in **Fig.6.7** which fits the experimental n_e well. It appears that also the profiles with v_{\perp} decreasing towards the outer wall as indicated from measurements and ESEL simulations shown in **Fig.6.8** would lead to satisfactory match with experimental n_e . However, from #29767, #29766 and #29773 it is clear that only a rising profile of v_{\perp} can lead to the agreement with experimental profiles.

6.1.4.3. Targets

So far only the upstream profiles were of interest and in the following part the target profiles will be analyzed in details. Two single Langmuir probe (LP) arrays with sampling rate 100 kHz provide good coverage of electron temperature T_e , electron density, n_e and ion flux density, j_{sat} at inner and outer targets (see section 5.2.1). During this particular simulated discharge #26730 the probes were operated in fixed negative bias mode, generating j_{sat} on a fast timescale. In further, identical discharges, pre-programmed outer divertor strike point sweeps in conjunction with both voltage

sweeping and constant bias modes, allowed profiles of ion flux, n_e and T_e with higher spatial resolution to be generated. Outer target heat flux profiles are deduced from the tile surface temperature using the vertically viewing infrared (IR) thermography system with time resolution 20 ms (see section 5.2.1).

It is important to note that SOLPS5.0 computes the fluxes across cell surfaces but n_e and T_e at cell centres. For this reason the simulated j_{sat} which is compared here with experiment is not the particle flux which is an output of the code, but calculated according to the formula Eq.5.3 with the values of n_e , T_e and T_i are taken at the targets (the poloidal cell just before the last guard cell). Normally the output from SOLPS and j_{sat} calculated like this should have approximately the same values. However, if strong poloidal gradients appear at the last cell surface, the SOLPS flux there can be quite overestimated. After quite extensive analysis of this in the simulations presented here it was concluded that the best values of j_{sat} to be compared with the experiment are those estimated according Eq.5.3 [221].

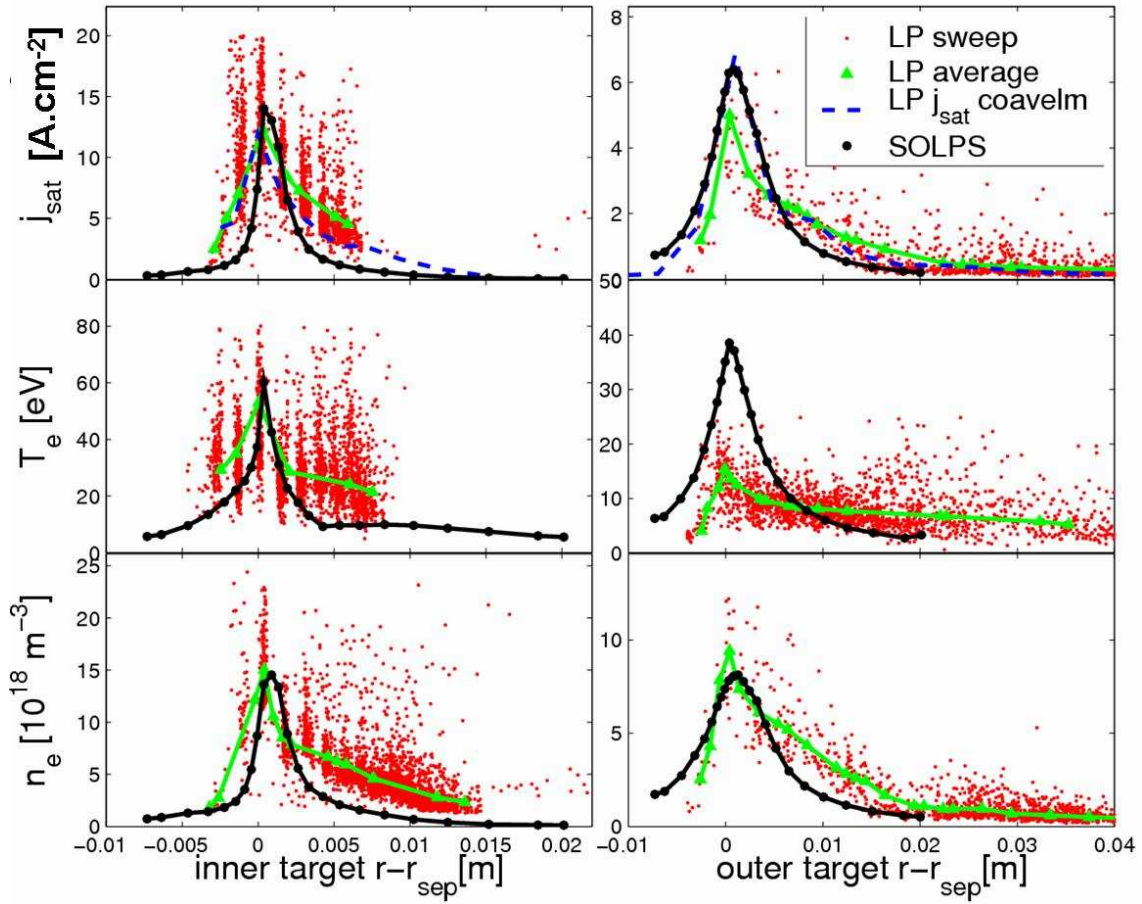


Figure 6.10. The profiles of j_{sat} , T_e and n_e at inner (left) and outer target (right) from SOLPS simulation obtained using the “diffusive approach” (black circles) and LP (red dots). Probe data at the outer target are obtained during an outer divertor leg sweep (#31838) with an exception of the j_{sat} points marked with blue dotted line, which result from a coherently averaged ELM (“coavelm”) in a separate discharge without strike point sweeping. They act as a cross-check of the swept data.

Fig. 6.10 presents the measured inner and outer divertor target j_{sat} , n_e and T_e profiles compared with the simulation for the upstream match obtained according to the “diffusive approach” shown in **Fig. 6.3**. At the outer target the experimental parallel ion fluxes have been obtained both from fast voltage sweep of the probes as the divertor leg itself is swept across the target during the steady ELMing phase and by extracting the pre-ELM j_{sat} value obtained from coherent averaging (following the technique reported in [177]) on a probe by probe basis for a case with the outer strike point fixed in time (in a separate, identical discharge). The two techniques provide similar profiles, though the divertor leg sweep clearly has the advantage of offering higher spatial resolution. It does this, however, at the price of averaging over the ELM peaks, which occur on a much faster timescale than the voltage sweep frequency. Data at the inner target are of lower quality – floating potentials of the inner target LP, especially in the strike point region, are very negative (due to the presence of strong thermoelectric currents [177]) and insufficient bias potential often makes it difficult to extract T_e reliably, particularly during ELMing phases.

With the same radial ansatz of transport coefficients (as in **Fig.6.3**) applied everywhere in the SOL of the SOLPS grid, far worse agreement with experiment than upstream is obtained at the divertor targets, where, for example, the code overestimates the experimental data of j_{sat} by factor of 3. Apart from the effects of fluid drifts (not yet included in the simulations), one obvious explanation are the differences between the main SOL and divertor cross-field transport rates. This has been tested by inclusion of poloidal variation of the transport coefficients such that the transport is specified differently in the main chamber SOL and divertor regions and it was confirmed that poloidal variation of transport coefficients is really necessary. This is extremely important in TCV, where the unconventional divertor geometry, particularly the outer leg, means that care must be taken in presence of the steep H-mode barriers to tailor differently the transport in this region compared with core. This refinement of the poloidal distribution of transport coefficients was applied by ‘switching off’ the transport barrier in the divertor regions and setting increased, fixed values of D_{\perp} , χ_{\perp} in divertor SOL and private flux regions (PFR). Removing the TB in the divertor legs by keeping D_{\perp} , χ_{\perp} constant at the same values as those in the core of the computational domain, leads to significant improvement. However it should be noted that the satisfactory simulation experiment match as presented on **Fig.6.10** has *only been possible* by both “switching off” the transport barrier in the divertor regions and increasing setting values of D_{\perp} and $\chi_{\perp, \text{e}}$ in the divertor to $6 \text{ m}^2 \text{ s}^{-1}$ (cf. $D = 1 \text{ m}^2 \text{ s}^{-1}$ and $\chi_{\perp, \text{e}} = 6 \text{ m}^2 \text{ s}^{-1}$ in the main chamber SOL – **Fig.6.3**). As can be seen from the model profile widths at the outer target, the PFR transport should probably be decreased to steepen the profile there. **Fig.6.11** compiles the result of the sensitivity study with different values of radially constant transport coefficients in the divertor legs.

The effects of the ballooning and rescaling the transport levels in the divertor SOL vs. PFR regions have been studied and it was concluded that none of them show remarkable differences in the target profiles and therefore they have not been used in the simulations.

The poloidal variation of the transport coefficients provides a satisfactory match between experiment and simulation at the targets given that drift effects (which are of course always present in experiment) might be expected to provide a further correction to

the non-drift code runs. In this sense, it is somewhat artificial to seek too close a match. Drifts very likely are playing a role in TCV, but the situation is complicated by the unconventional divertor geometry combining a short and long divertor leg. In reversed B_ϕ (the case considered here), observations made elsewhere (e.g. on the JET [222] and Alcator C-Mod [223]) tend to find that although T_e at the inner usually stays lower than at the outer, the difference is significantly reduced compared with forward B_ϕ , where T_e is always much higher at the outer target. This is also of course due to toroidal geometry which automatically ensures that more power flows to the outer SOL whatever the field direction.

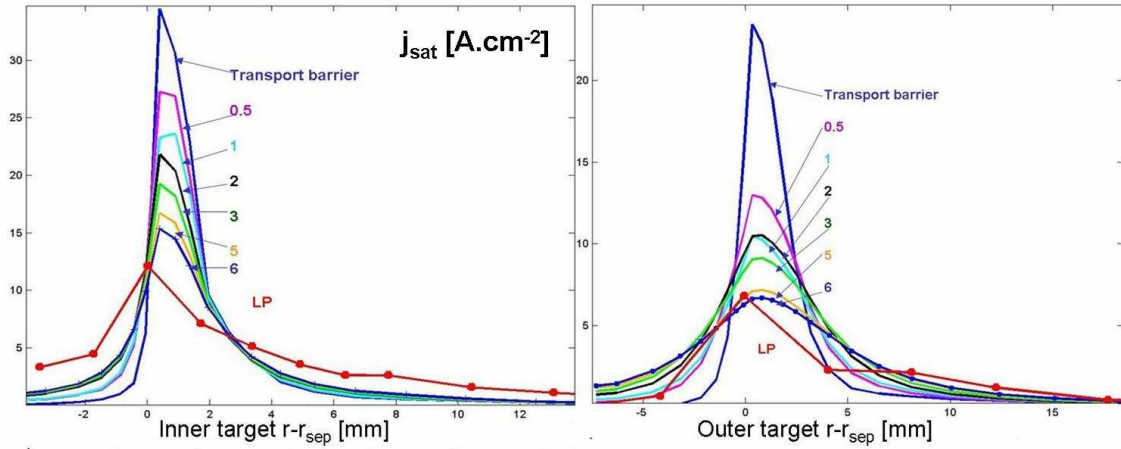


Figure 6.11. Profiles of j_{sat} on inner and outer target with different anomalous transport coefficients D_\perp , χ_\perp in the divertor legs. The lower blue curves correspond to the case with radial transport barrier (as plotted on Fig.6.3) everywhere poloidally including the divertor legs. All the other profiles are with flat radial profiles of D_\perp , χ_\perp in the divertor legs. With increasing values of transport coefficients the j_{sat} values decrease.

In TCV, the experimental data in Fig.6.10 indicate a hotter inner divertor in reversed B_ϕ , a consequence both of the effect of drifts and the short inner divertor leg. In the strike point regions, the code matches reasonably the inner target T_e and overestimates that at the outer by about a factor of ~ 2 . The modelled densities are also in reasonable agreement with data at both targets, albeit slightly underestimated at the outer target due principally to the higher simulated T_e . The experimental density is computed assuming $T_i = T_e$ (since no measurements of T_i are available there), but the code indicates that this is a reasonable approximation. Switching on drifts would very likely decrease the predicted outer target T_e but have only a small effect at the inner target (for the geometrical reasons mentioned above). The reasonably good match at the inner target may in fact indicate that the short divertor leg in fact dominates over any drift effect. In fact, recent experimental observations of forward B_ϕ ohmic H-modes at TCV, albeit at lower current ($I_p = 330$ kA) than the discharge considered here do indicate the importance of drift effects by showing that the experimental outer target T_e in this shot is increased by almost a factor of 2 over the values of the case in REV field #26730 shown here

(**Fig.6.10**), which would match these drift-free SOLPS simulations. Furthermore, the reversed field discharge simulated here has narrower flux expansion and hence higher power load at outer target (higher T_e).

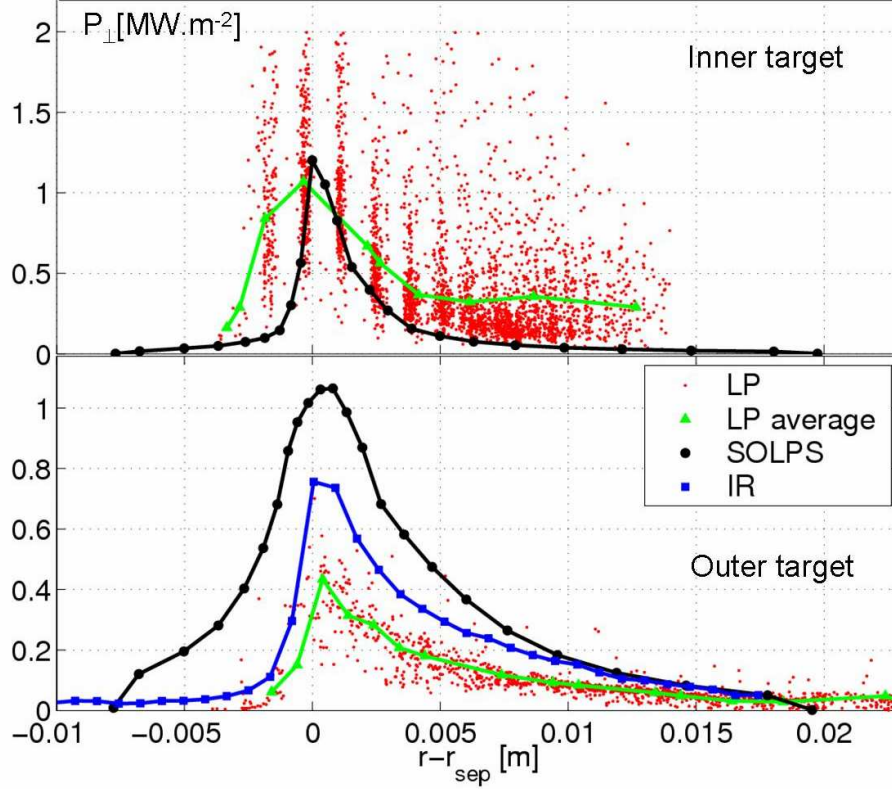


Figure 6.12. The profiles of perpendicular power fluxes P_{\perp} on inner (upper) and outer (lower) targets from SOLPS “diffusive” case (black circles) with data derived from target LP (red points) shown also averaged (green triangles). Blue line represents data derived from IR camera measurements of surface temperature at outer target.

Fig. 6.12 compares simulated perpendicular target power fluxes, P_{\perp} with data derived from the target Langmuir probes according to Eq.5.4 and at the outer target only, from IR camera measurements of surface temperature (from which power flux densities are derived using the THEODOR code [187]). A sheath heat transmission coefficient of $\gamma = 7.5$ has been assumed for the calculation of P_{\perp} from LP data (guided by the study on TCV reported in [186]), but comparison with the IR profile shows that slightly higher values would be more appropriate in this case. SOLPS data superimposed on these LP and IR experimental data in **Fig.6.12** are calculated in the code as it will be described later (section 6.1.5.4). Due principally to the overestimate of target T_e , SOLPS5 overestimates the outer target power (\sim factor 2.4), but is only a factor 1.3 above the measured IR profile and slightly underestimates the inner target values. From **Fig.6.12** it appears that conducted power is found quite symmetrically at both targets in this configuration. However, the profiles are mapped on the midplane and in SOLPS simulations the inner target surface is larger than outer target surface (see **Fig.6.1**) and

thus integrating the power under the profiles in **Fig. 6.12** at the targets themselves shows that the inner target is slightly favoured in terms of deposited power (see section 6.1.4.4).

The same ansatz of transport coefficients has been applied to the divertor legs in all three cases discussed above (Diffusive, Convective I and II), and the target data from the simulations performed with “convective approaches I and II” are very similar to those shown on **Fig. 6.10**.

6.1.4.4. Energy analysis

Energy balance of steady state of simulated Type III ELMing H-mode is analysed in this section.

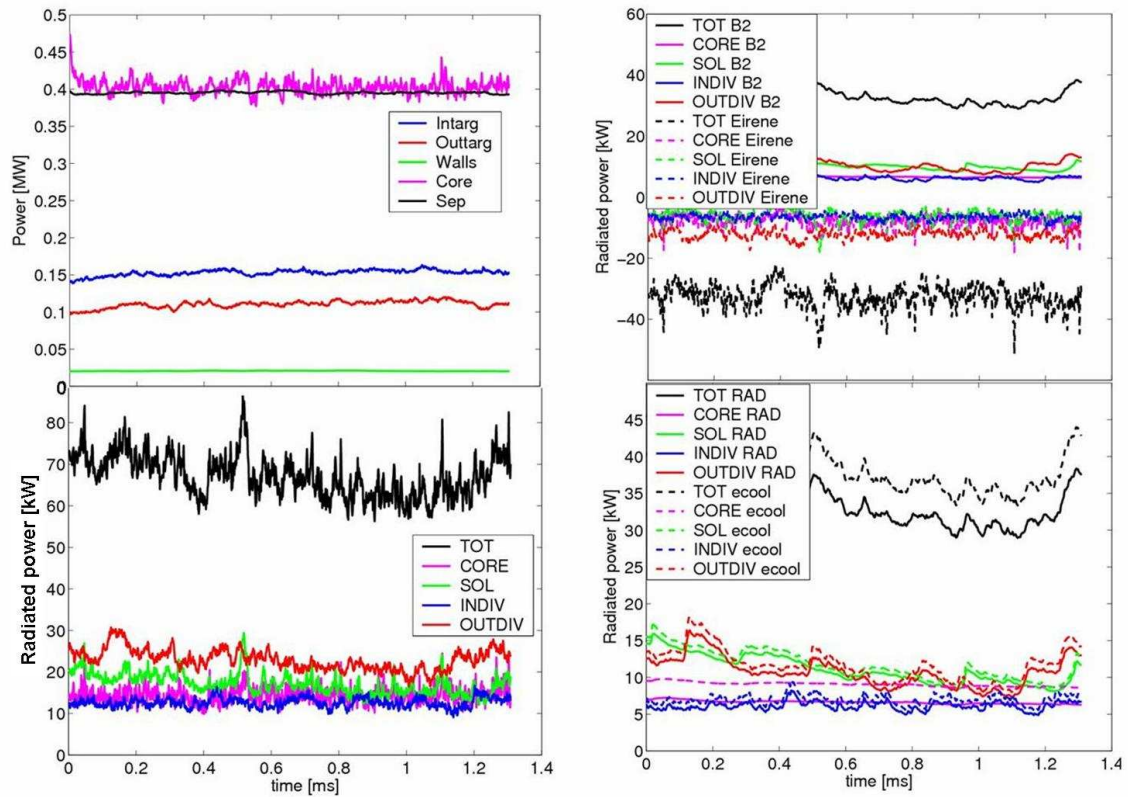


Figure 6.13. *Left upper: SOLPS powers crossing the boundaries, Left lower: Total radiated power as a sum from the grid regions. Right upper: SOLPS radiated powers from photons (B2.5) plotted as positive and from neutrals (EIRENE) plotted as negative (only for the clarity), Right lower: Electron cooling rate vs. power radiated from impurities (B2.5)*

Fig 6.13 left shows the power crossing the boundaries of the SOLPS grid including the core (inner) boundary, outer boundary (walls), and both inner and outer divertor target boundaries. The power crossing separatrix is also included. The contributions to the radiated power are compiled in **Fig. 6.13 left lower** and **Fig. 6.13 right upper**, where both contributions from photons and neutral atoms are plotted

separately. The electron cooling rates compared to the power radiated from impurities in B2.5 are depicted in **Fig.6.13 right lower**. The power crossing the core boundary corresponds to the grid input power given to the code as an input parameter, $P_{\text{SOLPS}} \sim 400$ kW. As it is seen on **Fig.6.13 left**, the smallest contribution to this power comes from the power deposited on the walls (~ 20 kW) and largest part, more than 80%, is deposited on the targets (~ 310 kW), as would be expected. It should be, however, noted that since the grid does not cover the whole plasma volume up to the walls, all of this power crossing the outer boundary of the grid does not have to be necessarily deposited on the walls. The rest, about 20%, is lost by radiation (~ 90 kW).

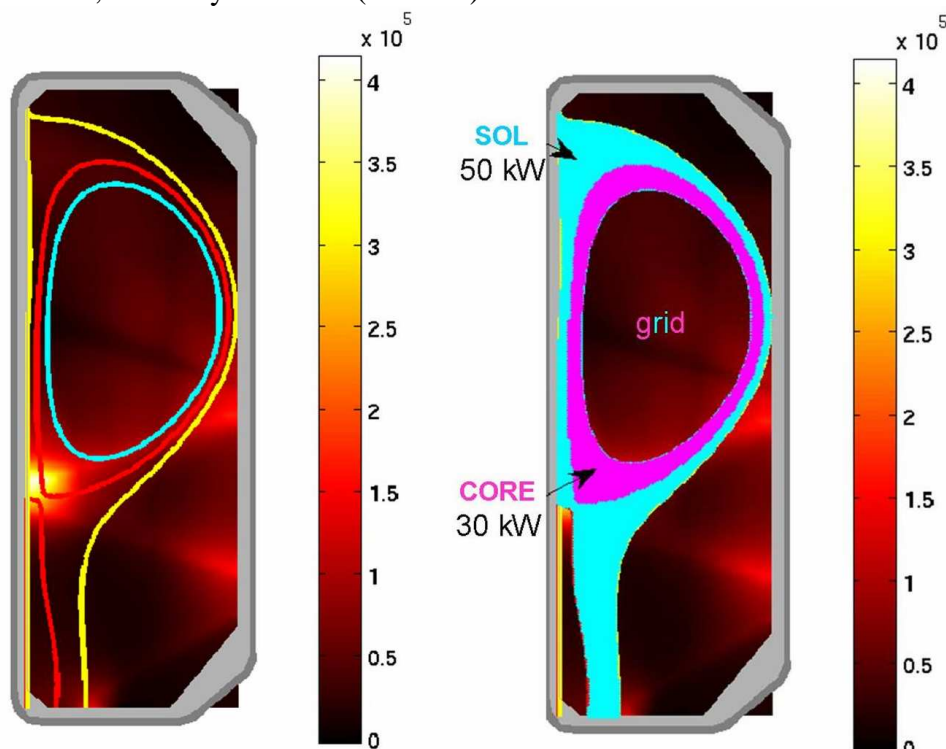


Figure 6.14. *Left: Radiated power during pre-ELM phase of #26730 from foil bolometers. Lines indicate the approximate extend of the SOLPS grid.*

Right: Superimposed areas corresponding to the radial extent of the simulation grid where the radiation have been calculated using TI. Corresponding radiated powers are indicted as light blue ~ 50 kW coming from SOL including divertor legs, and in magenta ~ 30 kW was radiated from core part of grid. Supplied by B.Tal, Hungarian association (HAS).

While higher power is deposited on the inner target compared to outer in SOLPS ($P_{\text{IN,DEP}}/P_{\text{OUT,DEP}}=1.38$), the situation with radiation is opposite. **Fig.6.13 left lower** shows the radiated power from the different regions of the grid and distinguished for photons and neutrals (the total radiated power is also included). The contributions from B2 (photons) and EIRENE (neutrals) are about the same, while more than twice as much power is radiated at outer divertor compared to the inner divertor. About the same amount of power is radiated from short inner divertor volume as from the SOL and core regions. Even if the tomographic inversion of chordal radiation measureme from foil bolometers (see **Fig 6.14 left**) shows the strongest radiation zone to be located at the X-

point (and hence in the inner target vicinity), one must take into account the uncertainty of TI and much lower spatial resolution of bolometer cameras compared to the SOLPS simulations. Moreover the radiation powers are from #26730 for which (as mentioned above) the data of inferior quality (compared to #20703) have been obtained and the set of the chords acquiring the signals during this discharge was rather incomplete. Therefore one should take these data only as an indication. In **Fig. 6.14 right** the areas corresponding to the radial extent of the SOLPS simulation grid are superimposed on this experimental data distinguishing between SOL and core part where TI is to be applied to calculate radiation. Since the foil bolometers are sensitive to both photons and neutrals this experimental data are to be compared with total radiation from SOLPS including the contributions from both B2.5 and EIRENE. The part of experimental radiation within the limits of the grid is ~80 kW, to be compared with the value from SOLPS ~ 90 kW. Of this ~80kW the fraction ~30 kW coming from the core part highlighted on **Fig.6.14 right** is slightly less compared to SOLPS power radiated in the core ~ 20 kW. The SOL part in the same figure including the divertor legs radiates ~50 kW in experiment a little bit less than the code-predicted value of ~ 65 kW.

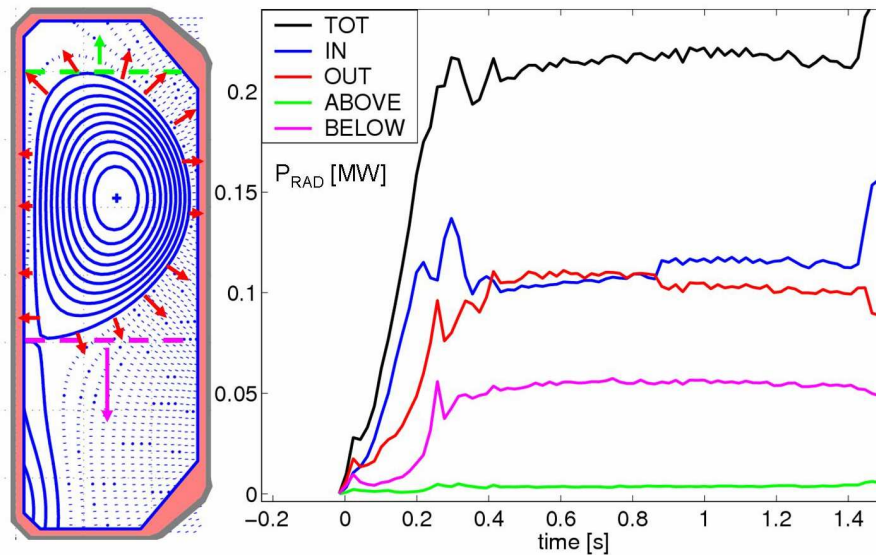


Figure 6.15. Radiated power from foil bolometers in different regions of the plasma in discharge #20703. “IN” stands for inside the separatrix, “OUT” stands for outside the separatrix, “BELOW” and “ABOVE” means the radiation below and above the main plasma. “IN” stands for inside the separatrix, “OUT” stands for outside the separatrix, “BELOW” and “ABOVE” means the radiation below and above the main plasma. One can also assume that $P(IN)=P(CORE)$; $P(OUT)-P(BELOW)\sim P(\text{Inner divertor})$; $P(BELOW)\sim P(\text{Outer divertor})$.

Fig 6.15 shows the total radiated power from #20703 (for which bolometry data is of better quality than that for the discharge simulated here (corresponding to #26730), even if the radiation levels are slightly higher), is separated into components corresponding to areas below X-point, above the main plasma and inside and outside of the separatrix. Here, again one can see that the radiation below X-point represents quite an important fraction of total radiated power ~ 50 kW, what is in quite reasonable

agreement with $\sim 30\text{kW}$ from outer divertor leg in SOLPS, taking into account the difference between the two discharges.

6.1.5. Simulation of Type III ELM at TCV

A typical Type III ohmic ELMIg H-mode at TCV (see **Fig. 6.2**) has a stored energy of $W_{\text{plasma}} \sim 25\text{ kJ}$ with $f_{\text{ELM}} \sim 200\text{ Hz}$ and $\Delta W_{\text{ELM}}/W_{\text{plasma}} \sim 1\text{-}2\%$, so that each ELM exhausts a few 100 J. Regarding the magnitude of target power fluxes etc., such these ELMs cannot be compared with the more commonly studied larger Type I ELM events seen on bigger machines, but their behaviour with respect to transport in the SOL and interactions with the targets appears to be similar. The smaller ELM size, associated with a generally higher pedestal collisionality (see **Table 3.1**) might also be more appropriate to a fluid type of treatment, such as that used here with the SOLPS5 suite. The comparisons with the PiC simulations (see section 6.1.5.6) will show, however, that even for these smaller ELMs, they are sufficiently kinetic for the fluid treatment to fail in some respects.

As for the pre-ELM simulations described in the previous section, the emphasis on the time dependent modelling to be treated in this section will be on matching upstream Thomson Scattering (TS) measurements of the T_e and n_e profile evolution during the ELM cycle and comparing with particle fluxes at the outer divertor target from Langmuir probe and IR power flux measurements on the ELM timescale. Unfortunately since not all required diagnostics are available at the required time resolution in any given shot, signals from several discharges have again been combined for comparisons with the simulations. The target data from discharge #26730 has been used to simulate the inter-ELM pedestal and SOL plasma (see section 6.5.1) using coherently averaged upstream core and edge TS data. In this section where the time-dependent data on the fast scale are required, the TS data from the very similar discharge #26393 is used to benefit from the fast consecutive pulsing of the TS lasers which allows two pedestal profiles to be measured in quick succession ($\sim 1\text{ ms}$) during the same ELM (see [174]).

6.1.5.1. Time dependent phenomena in SOLPS5.0

When modelling any time-dependent phenomenon the timescale of the modelled event is an important factor. In the tokamak plasma, timescales range from a few microseconds to a few seconds. If one is interested in simulating an event with relatively long timescale, it often makes sense to use multiple steady state snapshots. However, for fast phenomena like ELMs, time dependent modelling is required. In fact the complete ELM event contains different timescales, where the fastest is of order $\sim 10\text{ }\mu\text{s}$ and longest of order of 10s or even 100s of ms, corresponding to relaxation between two ELM events. As indicated in **Tab.6.2.** for the analysis of the effect of the ELM on SOL and divertor properties with SOLPS code, the several different time-scales have to be considered and it is clear that not only plasma but also neutrals must be treated time-dependently [17].

Underlying ELM perturbation	10-100 μs
Enhanced transport	0.1-1 ms
Parallel transport of fast tail electrons	1-10 μs
Parallel transport of ions	0.1-1 ms
Flight time of neutral atoms	0.1 ms
Flight time of neutral molecules	1-10 ms
Period of ELM repetition	1-1000 ms

Table 6.2. Timescales associated with ELM modelling

6.1.5.2. ELM model with SOLPS5.0

Many features of ELMs are captured by existing theory, although some of the observations indicate the need for additional ingredients in these models. Most of the models of ELM cycle are spatially local. Fully time-dependent and spatially resolved simulations (as in [85]) are necessary to describe the complex ELM phenomenon. It has now been established through measurements on many tokamaks, including TCV, that the ELM is a filamentary plasma structure expelled toroidally asymmetrically from the edge barrier region, localised in the outboard midplane region of the poloidal cross-section and probably rotating in the SOL plasma (see chapter 3). There is currently no convincing ELM model describing how energy released from the edge pedestal is transferred to the divertor targets. It is likely, though not yet proven, that the mechanism involves a magnetic reconnection process by which hot pedestal plasma on closed field lines can reach the targets via parallel transport.

The complexity of the ELM transport cannot yet be captured in a code package such as SOLPS5 so an approximate ansatz (invoked also by [172,211,224-225]) is used in which the ELM is simulated by simple enhancement, over a short timescale, of the radial transport in the edge. This is performed by repeatedly (at frequency f_{ELM}) elevating the values of transport coefficients of diffusion and/or convection from the pre-ELM, steady state values ($\sim 0.1\text{-}1 \text{ m}^2\cdot\text{s}^{-1}$) to much higher ELM values ($1\text{-}10 \text{ m}^2\cdot\text{s}^{-1}$). The second important constraint is the measured value of ΔW_{ELM} . In addition to these two key parameters (f_{ELM} , ΔW_{ELM}) the other inputs required for the time dependent simulation are listed before and will be discussed in more detail below. All these other parameters are “free” or “semi-free”, as they can be approximately estimated from the measurements while making assumptions and choices in order to obtain the closest match with experiment.

- Duration of enhanced transport, t_{ELM}
- Radial extent of enhanced transport
- Poloidal extent of the increased transport
- Form of the poloidal function applied on the poloidal region with enhanced transport
- Ansatz of the ELM model – diffusive (increase of D_{\perp} , χ_{\perp}) or convective (increase of v_{\perp})
- Magnitude of the enhanced transport

As indicated schematically in **Fig. 6.16**, the ELM cycle, from the point of view of the time dependent simulations, can be divided into 3 intervals. The first corresponds to the steady state and is referred to as pre-ELM phase, which has been discussed at length in the previous section. The second part is the “ELM rise time”, t_{ELM} , (corresponding roughly to the experimentally observed time over which the associated MHD activity is high or the interval over which target recycling emission or power fluxes rise). During this period in the simulations, the transport coefficients are increased radically in SOLPS to simulate the ELM. The third part of the ELM cycle is so-called “post-ELM time”, and normally corresponds to the time of relaxation of the solution until the next ELM event is experimentally seen or until the solution converges back to the pre-ELM state. In this part of simulation the transport coefficients are set to be identical to those used for the pre-ELM phase.

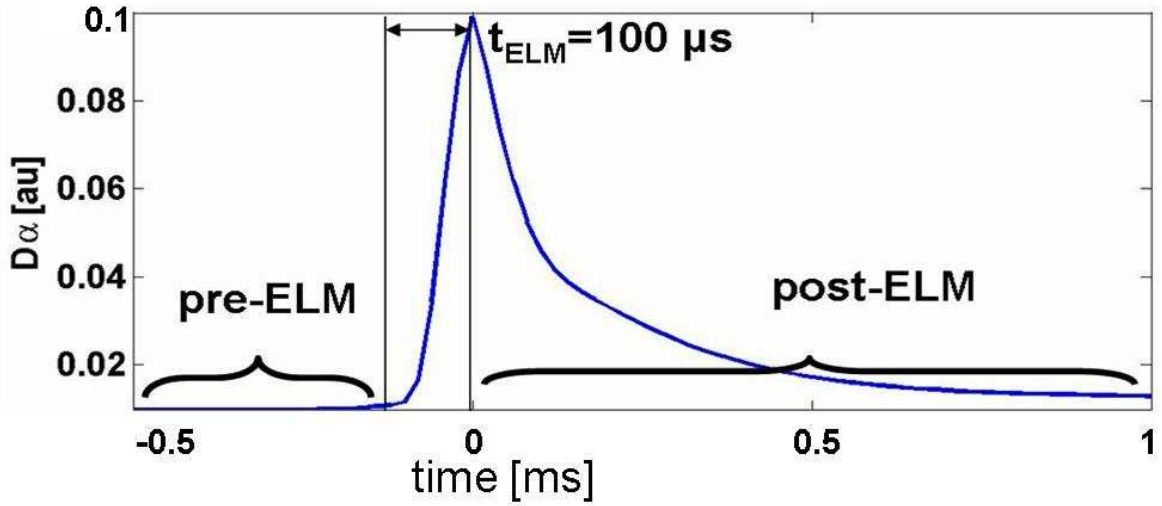


Figure 6.16. Schematic description of the ELM cycle using the time dependence of the response of recycling emission to illustrate division into three intervals for the ELM simulation; here the result of coherent averaging from many ELM events inside of the discharge # 26730 is shown from which $t_{\text{ELM}} \sim 100\mu\text{s}$ has been estimated for the simulation in the section 6.5.1.5.

If the ELM is considered as a Type I event associated with ideal ballooning instability, the event starts as soon as pressure gradient reaches the critical value α_{crit} and the transport in the unstable region enhances. This kind of transport avalanche stops at the radial position where the pressure gradient profile falls below α_{crit} , which actually determines the so-called ELM-affected area and is seen as the region with collapsed TB in the radial pressure profiles (as indicated on **Fig.6.17.**). Normally, an attempt to estimate this radial extent is made from the comparison of the pre-ELM and ELM (or after ELM peak) upstream profiles of T and n, if these are available.

Another free parameter used in this work is the poloidal extent of the region with enhanced transport coefficients during the ELM. Guidance in this area is relatively poor and only a few indirect experimental indications exist. As shown in chapter 3, however, the ELM is known to have strong ballooning nature and thus the transport coefficient

enhancement is expected to occur primarily in the outboard midplane region. This is therefore the region in which the transport coefficients are enhanced in the simulations. Since the transport coefficients are normally only applied in a poloidally uniform sense in SOLPS5 (as in earlier attempts to simulate ELMs on the JET tokamak with the same code [172]), it has been necessary to include a facility by which the poloidal distribution of the increase may be modified.

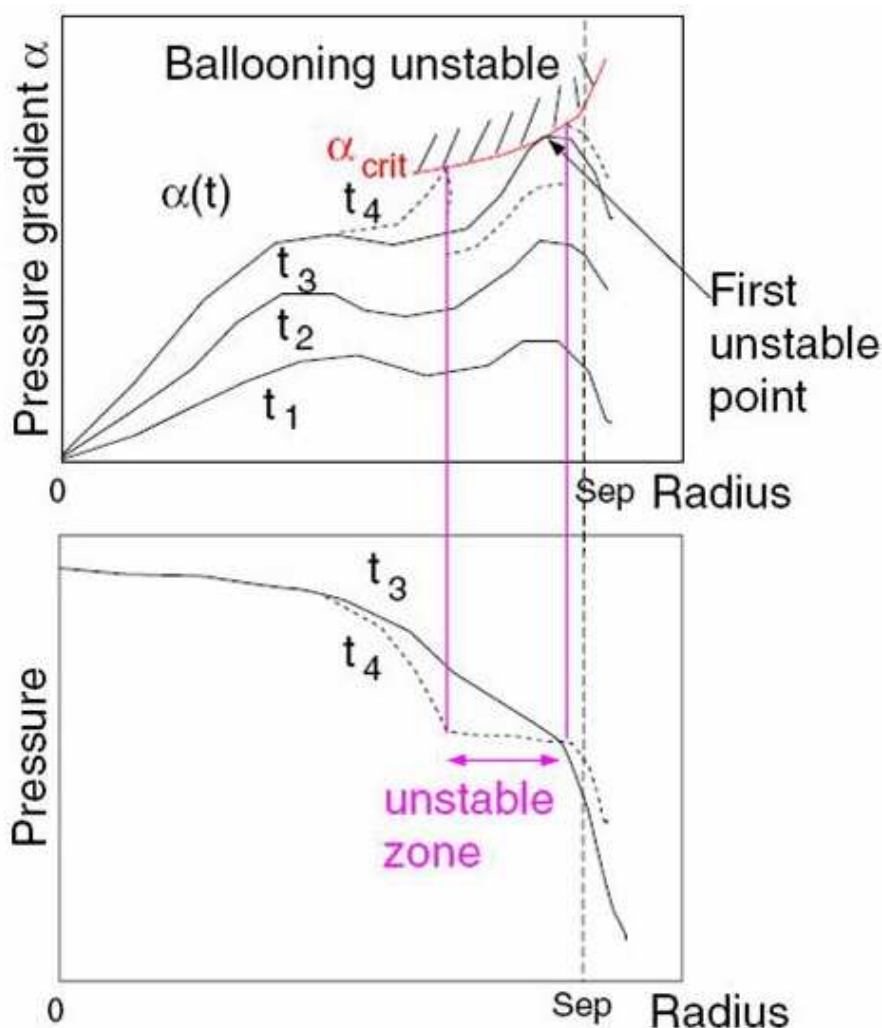


Figure 6.17. Sketch of pressure gradient (top) and pressure (bottom) for Type I ELM (extracted from [17]). The region marked “unstable zone” represents the ELM-affected area which is used in the simulation as indication of the radial extent over which transport coefficients should be enhanced.

A number of different variants have been tried for the form of the poloidal function describing this distribution. The most realistic and perhaps physically more natural is a smooth Gaussian or cosinus-like shape and not the step-like function with large, unphysical poloidal gradients of the transport coefficients. An option, enabling different types of poloidal variations (e.g. step or Gaussian functions) to be specified in

chosen localised regions (e.g. the Low Field Side), was implemented to the local version of the code for the purposes of the ELM simulations within this thesis. Moreover, new options have also been added to the code by Dr. X. Bonnin (LMHP, CNRS-UPR), enabling changes to be made to the transport coefficients during the ELM even more easily. It is now possible not only to simply multiply the transport coefficients in the selected poloidal region, but also to use the different radial profile shapes in different poloidal locations. A facility has also been added by which a Gaussian function can be used as poloidal multiplier.

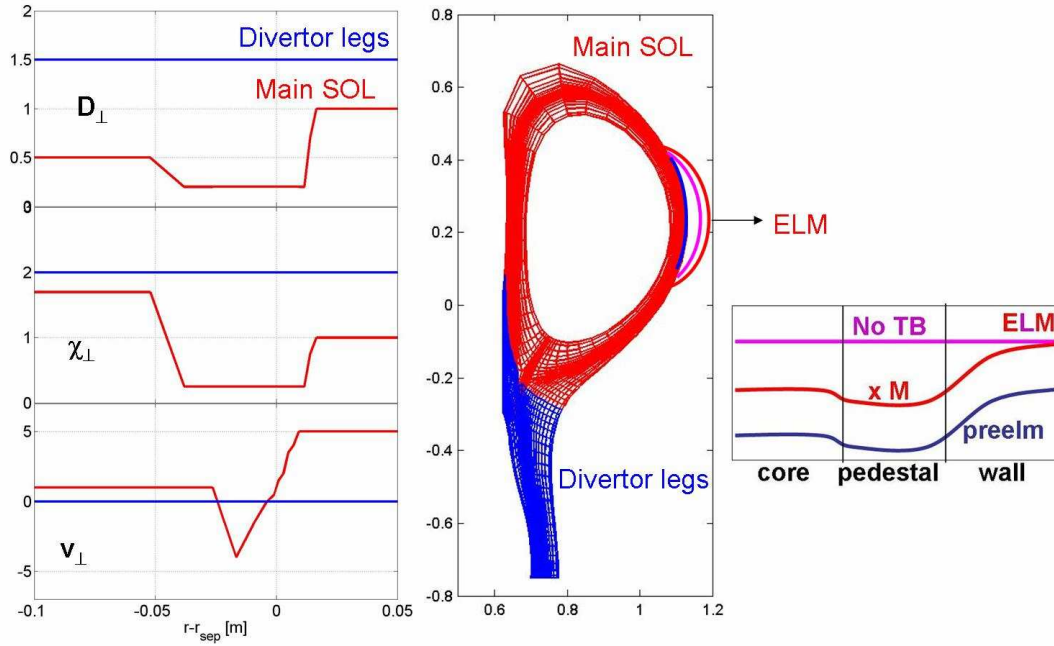


Figure 6.18. Schematics of the possible variations of the anomalous transport coefficients in space and time in SOLPS ELM simulations. Left: Examples of radial profiles of D_{\perp} , χ_{\perp} and v_{\perp} applied differently in regions of main SOL and in the divertor legs as depicted in the middle figure of the simulation grid. In addition on LFS the example of poloidal extent from which ELM can be launched with the possible schematically drawn shape of the increased transport coefficients. Right: Example possible variations of the radial profile of the coefficients during the ELM over the poloidal extent on the LFS shown in middle figure.

The various possibilities for the radial and poloidal variations of the coefficients during the time-dependent simulations are shown schematically in **Fig. 6.18**. When simulating the time-dependent ELM event three transport input files with the radial profiles of the anomalous transport coefficients (D_{\perp} , χ_{\perp} , v_{\perp}) for all the species are created for pre-ELM, ELM and post-ELM phases of the simulation. There is a possibility to choose the regions in the grid (most often the divertor legs) where these radial profiles will not be used. In these regions, a separate input file is used to impose radially flat transport coefficient profiles. In the transport input file for the ELM part of the simulation either the multiplication factors of the pre-ELM coefficients (specified in pre-ELM

transport input file), or completely new radial profiles for the ELM can be specified with the poloidal extent where they are to be applied. Moreover another arrays of the radial profiles of transport coefficients which should be applied elsewhere (outside of the ELM poloidal extent) can be specified during the ELM, otherwise they would be the same as in pre-ELM part of the simulation.

Within the poloidal extent of the ELM, the transport coefficients from the ELM transport input file can be increased by a factor of $1+G$, where G is a Gaussian profile in the poloidal direction of amplitude S , where S represents the scaling strength. The profile has a decay length of about $1/3$ of the interval over which the scaling is to be done [139]. The time when ELM starts and finishes is also chosen, corresponding to the time when these increased coefficients are applied. If multiple ELMs are simulated, the period after which the new ELM should start is also specified.

Another free parameter is the magnitude of the enhanced transport. Once the ansatz of the anomalous transport coefficients to be increased (see the discussion later – section 6.1.5.3) together with all the above described parameters has been chosen, the increased values of the transport coefficients during the ELM are systematically adjusted to match the observed loss of energy and particles and the upstream and target experimental profiles during the ELM, if available.

6.1.5.3. Diffusive vs. convective approach

The encouraging overall model-experiment agreement obtained for the steady-state, inter-ELM phase has provided a good basis for the more complex, time dependent modelling of the Type III ELM event itself. Some of the basic ELM input parameters obtained from experiment (#26730) are listed in **Tab.3.1.** In common with the pre-ELM code runs and as described below, this ELM has been simulated according to both diffusive and convective approaches. The simulations using the first approach were presented at the 34th European Physics Society Conference in Warsaw, Poland (EPS 2007) and are published in [226].

From experiment, a coherent average of the stored energy derived from a diamagnetic loop over 40 similar ELMs during the stationary phase of the discharge yields $\Delta W_{\text{ELM}} \sim 600$ J (2.5% of total plasma stored energy). The use of coherent averages is mandatory in this case given that the ELM is too small for the energy drop per ELM to be clearly distinguished. For the ELM duration, a value of $t_{\text{ELM}} \sim 100$ μs is estimated from the phase of turbulent activity on Mirnov coils located on the outboard midplane wall (see **Fig.6.34**). Unless stated otherwise, the settings for the simulations, including the basic input parameters, P_{SOLPS} , n_e^{sep} , heat flux limiters, recycling coefficients, chemical sputtering yield etc. are maintained as for the pre-ELM simulation (see section 6.1.2).

Time-dependent ELM simulations require the Monte-Carlo neutral code (EIRENE) to be run with time steps, Δt equivalent to those of the fluid code (B2.5) to avoid artificial compression of the neutral timescale [208]. Here, $\Delta t = 10^{-6}$ s has been chosen, providing 100 points during the ELM. To begin with, only a single ELM cycle has been simulated, covering a total time of 400 μs , with 100 μs before and 200 μs after. This has been later extended to several (~ 10) consecutive ELM events.

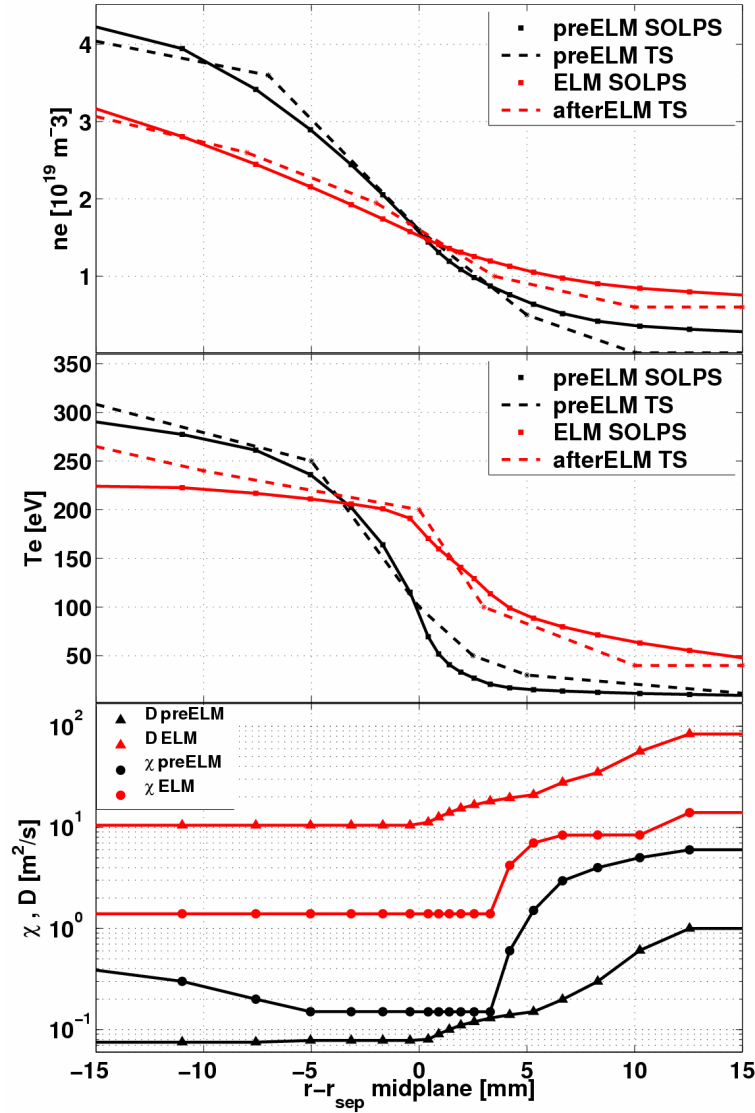


Figure 6.19 *Top and middle:* upstream n_e , T_e profiles from TS (#26393) measured before and after a Type III ELM (TS data extracted from [174]), SOLPS simulated with the “diffusive approach”.

Lower: transport coefficients D_{\perp} , $\chi_{\perp,e,i}$ used in SOLPS for the pre-ELM and ELM.

Two approaches exist in SOLPS to simulate the ELM. Either as an instantaneous local increase in the transport coefficients for particles and heat (D_{\perp} , χ_{\perp}), or as an increase in outward convective velocity v_{\perp} . In previous attempts which have been made to simulate the ELM event with fluid codes published in the literature (mostly successfully compared with experimental measurements) [172,211,225,227-229], only radial particle diffusion and radial heat conduction coefficients were increased during the ELM, setting the radial convective velocity to zero. This “diffusive” approach is therefore the first which was attempted here, in common with the pre-ELM simulations.

However, the second, more challenging case of increased v_{\perp} (referred to as “convective approach”) is likely to be a more realistic description of the ELM event, at least in the rather crude manner with which SOLPS5 is able to simulate it. The justification of this is the same which is used in section 6.1.4.2 for the ‘convective approach’ to simulate the pre-ELM steady state.

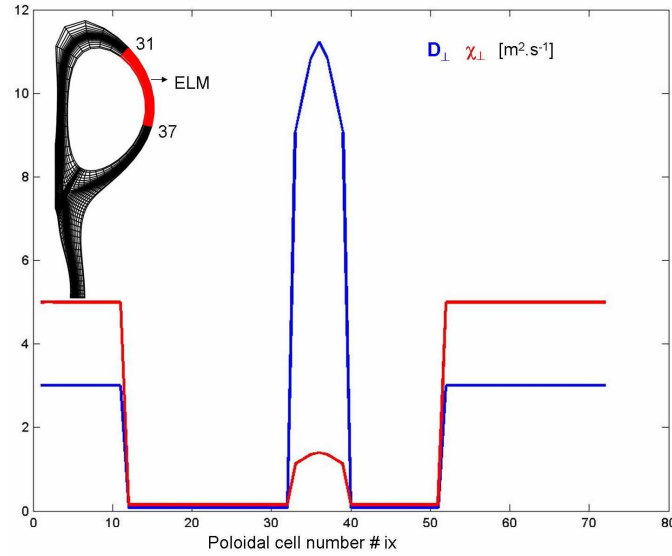


Figure 6.20. Poloidal profiles of D_{\perp} and χ_{\perp} at the separatrix during the phase of the ELM enhanced transport. The left top inset shows the poloidal extent where ELM is launched.

To estimate the required magnitude of the increase in the transport coefficients, approximate radial transport equations were solved assuming energy flow during t_{ELM} over a separatrix surface area of plasma, A_{ELM} . Assuming no velocity pinch term ($v_{\perp} = 0$) and $\chi_e \approx \chi_i$, this may be expressed approximately as

$$\frac{\Delta W_{\text{ELM}}}{2t_{\text{ELM}} A_{\text{ELM}}} = -n\chi_{\perp} \frac{dT}{dr} - \frac{5}{2} T D_{\perp} \frac{dn}{dr} \quad (6.3.)$$

For approximate values of n , T and their radial gradients at the start of the ELM, this expression can be used to pick a combination of D_{\perp} and χ_{\perp} which roughly satisfies the experimentally measured ΔW_{ELM} for given A_{ELM} and t_{ELM} . These values then determine approximately the required increase in transport coefficients to be applied in the simulation to match the ELM energy loss. This can be used as a starting point and the values later refined once a time dependent case has been run and simulated profiles are available for comparison with experimental data. An example of this data is shown in **Fig. 6.19**. The experimental TS profiles show a larger drop in n_e than T_e at the pedestal top (a feature which is even more pronounced in the coherently averaged TS profiles shown in [174]), indicating that this ELM is more convective than conductive (i.e. that $\langle T_{e,\text{ped}} \rangle \Delta n_{e,\text{ped}}$ exceeds $\langle n_{e,\text{ped}} \rangle \Delta T_{e,\text{ped}}$ in the contribution to ΔW_{ELM}). For this reason D_{\perp} has been increased more during the ELM than $\chi_{\perp,e,i}$ in the simulation. In fact, D_{\perp} is

increased everywhere by 100 times, with $\chi_{\perp,e,i}$ being increased mostly in the pedestal region (by a factor 10) and only by \sim factor 2 in the SOL. In addition to the magnitude increase, the shape of the D_{\perp} and $\chi_{\perp,e,i}$ profiles must also be modified compared with the pre-ELM values to account for the collapse of the edge transport barrier (ETB) and provide the best match to TS and target LP data.

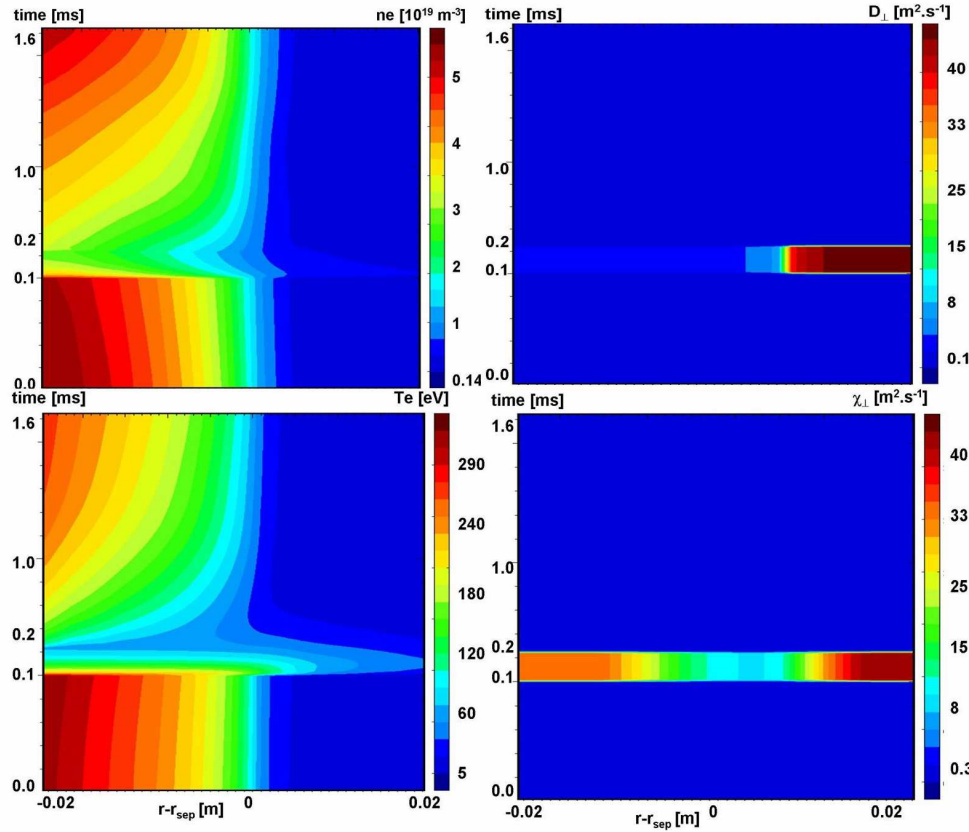


Figure 6.21. 2D profiles of n_e , T_e and D_{\perp} , χ_{\perp} during the ELM cycle as a function of time and radial position.

Several time dependent simulations have been performed varying both the radial and poloidal profile of the transport coefficients during the ELM event. Analysis testing different poloidal extents and the Gaussian scaling strengths (S) found one of the best results (in terms of agreement with experimental results) for an area of $A_{\text{ELM}} \sim 1.5 \text{ m}^2$, corresponding to the poloidal extent in the SOLPS grid from cell number ix 31 to 37, and for a Gaussian poloidal distribution centred on the outside midplane with $S=5$. The result of this exercise are the transport coefficient profiles shown in **Fig. 6.20** and an expelled energy of 690 J, reasonably close to the experimentally observed value.

The profiles of midplane n_e , T_e and corresponding transport coefficients D_{\perp} and χ_{\perp} as a function of time and radial position are shown on **Fig. 6.21** for the whole ELM cycle. One can clearly identify the recovery phase after the ELM enhanced transport coefficients are switched off.

Since the ELM is known to propagate in filaments and the radial velocity have been measured at TCV, the ELM radial transport is better approximated as a convective event for which v_{\perp} in the SOL increases during t_{ELM} . The results of the analysis of ELM events at TCV are shown on **Fig.6.22 left**. The value of radial velocity of ELMs in the TCV SOL $\sim 1 \pm 0.2 \text{ km.s}^{-1}$ has been estimated from the difference of the start of the ELM events measured by the RCP and AXUV camera [109].

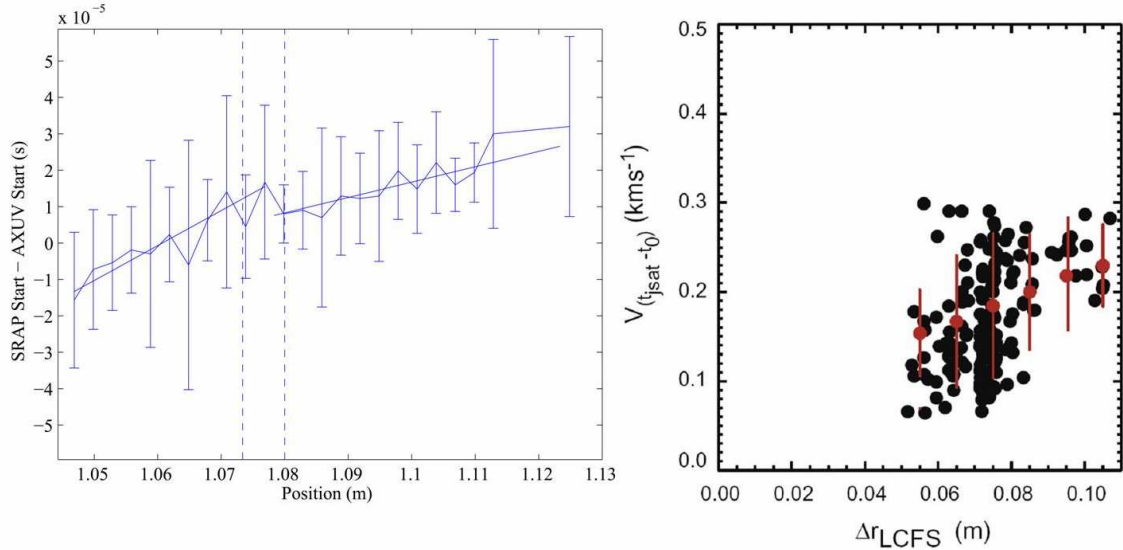


Figure 6.22. *Left:* The radial velocity measured in SOL of the TCV discharges using RCP probes and AXUV camera. The difference between the ELM start time from these two diagnostics is plotted against the wall positions. From the slope of the profile the values $\sim 1 \text{ km.s}^{-1}$ can be deduced. Supplied by R.Tye, extracted from [109]. *Right:* The radial velocity of ELM filaments on ASDEX-Upgrade determined using time of flight from the start of the ELM as a function of distance from LCFS. Extracted from [107].

In similar fashion to **Fig. 6.19**, the results of the simulations using this approach are compiled in **Fig.6.23**, Sensitivity to the poloidal extent and amplitude of the enhanced transport have again been conducted. As for the diffusive approach, it is possible to obtain very reasonable agreement with experimental upstream TS profiles and the energy expelled during the ELM ($\Delta W_{\text{ELM}} \sim 600 \text{ J}$). Obviously, larger poloidal extent requires smaller S and vice versa. Therefore as shown on **Fig.6.23** there is no unique solution and several different ansatzes give the acceptable agreement with experimental profiles. However, it is possible to be guided by “reasonable” values of v_{\perp} obtained from experiment. Nevertheless it should be noted that the shape of the v_{\perp} radial profile is approximately the same in all the cases depicted on **Fig.6.23**.

As a first approximation, the v_{\perp} to be used in the simulation was estimated as a fraction of the measured v_{\perp} reflecting the fact that the SOL volume is not continuously populated by the filaments. The fraction of the SOL volume occupied by the filaments was estimated at $\sim 50\text{-}200\%$ (assuming the width of circular cross-section of filament $\sim 1\text{-}2 \text{ cm}$ (as estimated from Fig.1 in [107]) and number of filaments $n \sim 10\text{-}20$). This yields an estimated v_{\perp} at the separatrix of $\sim 500\text{-}2000 \text{ m.s}^{-1}$ (the range encompassed by

the experimental $v_{\perp} \sim 1000 \text{ m.s}^{-1}$). The selection of possible “optimal” v_{\perp} radial profiles offered in **Fig.6.23** indicates that depending on the poloidal extent of applied enhanced transport the code requires rising v_{\perp} with values near the separatrix in range of 500-2000 m/s to fit the experimentally observed upstream profiles reasonably well.

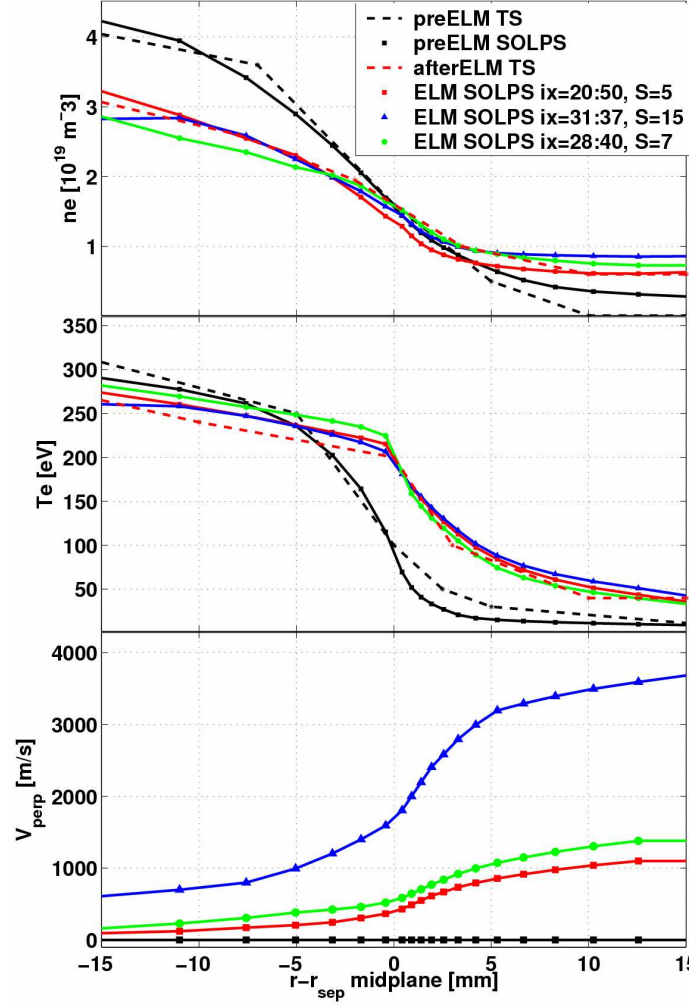


Figure 6.23 Upstream n_e , T_e profiles from TS (#26393) measured before (black dashed line) and after ELM (red dashed line) and SOLPS simulated by “convective approach” and radial velocity v_{\perp} used in SOLPS for pre-ELM and ELM. Different convective ansatzes are depicted showing that it is possible to obtain agreement with experimental upstream profiles and an energy of ELM $\Delta W_{ELM} \sim 600 \text{ J}$ using different poloidal extent and scaling of Gaussian poloidal function S .

The experimental data available together with the simplicity of the model (containing several free parameters) do not allow the problem to be properly constrained. Without more poloidally distributed measurements of the radial profiles (n_e, T_e) or more precise measurements of the radial velocity v_{\perp} itself, it is very difficult, even impossible, to identify one solution as a “best choice”.

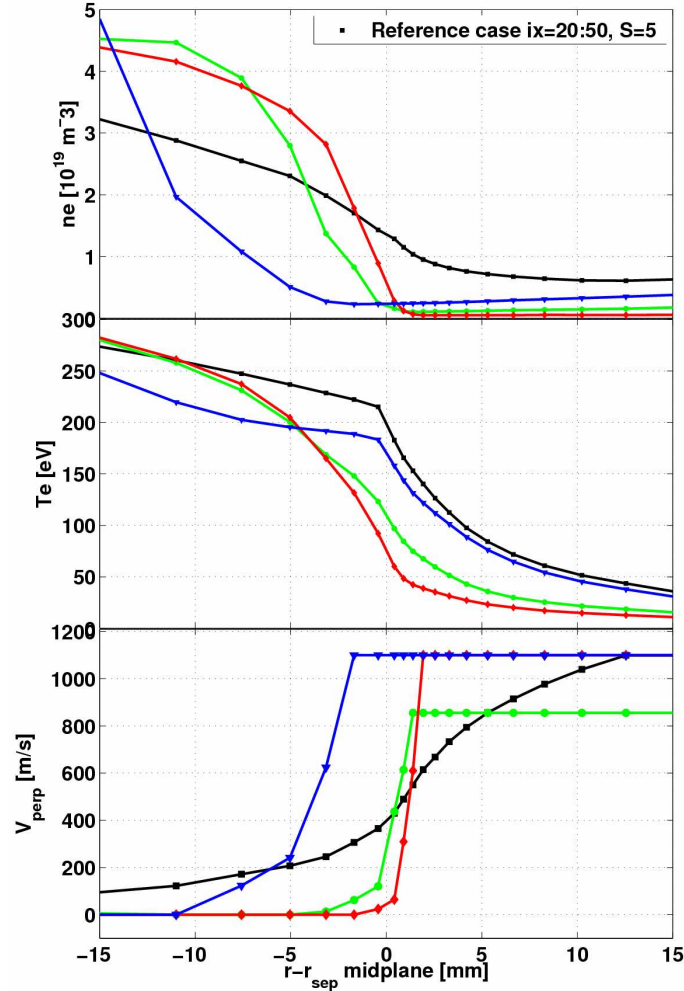


Figure 6.24 Upstream n_e , T_e profiles during ELM simulated by SOLPS using “convective approach” with different profiles of radial velocity v_\perp but with the same poloidal extent and Gaussian scaling strength S as in the “reference case” (black squares). The reference case here does not mean the best fit with the experimental data, but the one from the options shown on **Fig.6.23** with the same free parameters (poloidal extent, S) as those used in other cases on this figure.

Fig. 6.24 compiles the profiles of n_e and T_e obtained from simulations with different shapes of the v_\perp , (including the flat or step-like ansatz with zero v_\perp inside the separatrix and constant v_\perp in SOL like approach used in [103]). It appears that the reasonable agreement with experiment can be obtained only with v_\perp gradually rising near the separatrix in the radial extent approximately corresponding to the extent representing the width of the pedestal of the n_e profiles (as for example estimated by TS fitting on **Fig.6.3**). This is in agreement with the observation described in Chapter 3 and observations of [107] where acceleration of filaments at ASDEX-Upgrade as seen on **Fig.6.22 right** is reported. However, even though the simulations reported here are consistent with acceleration, the observations of ELM filaments to decelerate or move with constant velocity have been also reported (as mentioned in chapter 3).

6.1.5.4. Simulations of targets

In this section, the focus will be on the target profiles during the ELM cycle. **Fig. 6.25** shows simulated ELM and pre-ELM target profiles of j_{sat} , T_e and n_e , computed using the diffusive approach, for which the upstream match with experiment is shown in **Fig. 6.19**. The SOLPS j_{sat} data are compared with the coherently averaged LP data (40 ELMs between $t = 0.6$ and 0.8 s). Measurements of T_e are not possible on the ELM timescale with the single Langmuir probes embedded in the target and so only SOLPS5 results are shown in this case. The same reasoning applies for the experimental n_e .

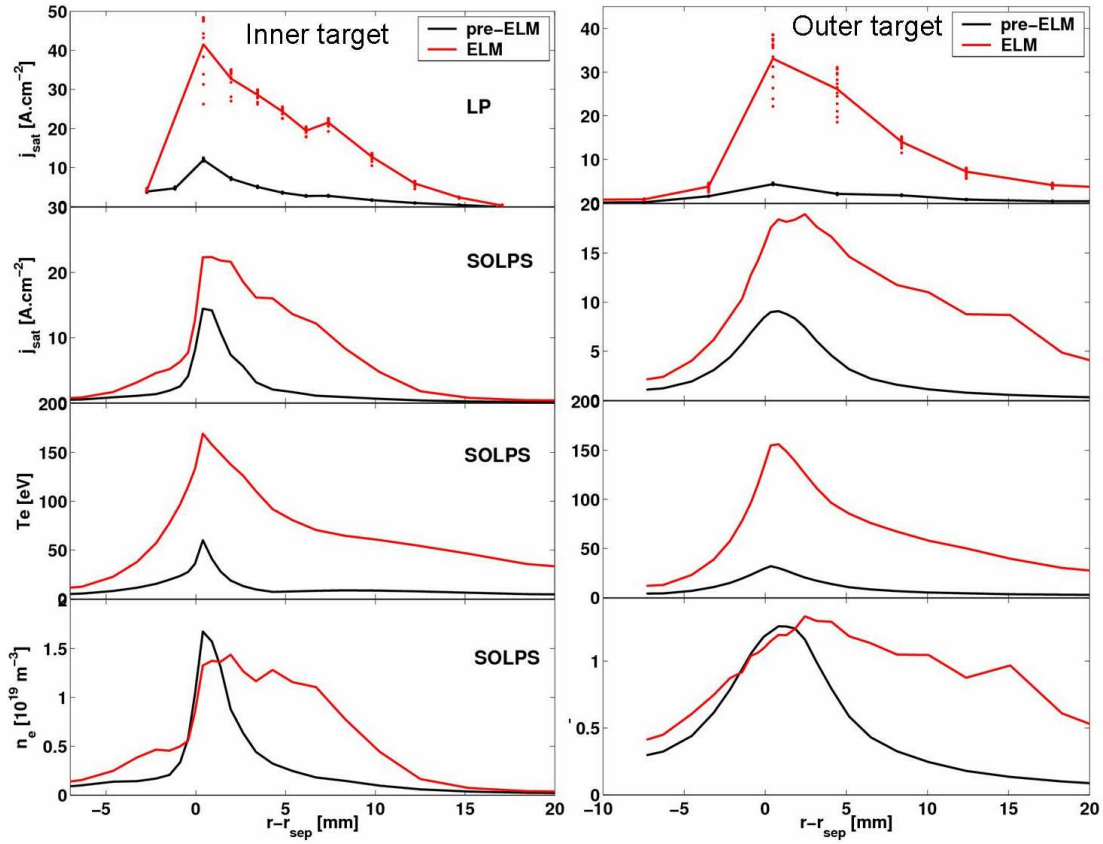


Figure 6.25. Pre-ELM (black) and ELM (red) target profiles of j_{sat} , T_e and n_e from SOLPS5 simulation #25511 using the “diffusive approach”. The top panels show the j_{sat} profiles from coherent averaging of LP experimental data for both pre-ELM and ELM. Full lines represent the averaged data.

Agreement with experimental particle fluxes is fair in magnitude (\sim factor 2) and good in profile shape. The peak target electron temperatures in **Fig. 6.25** are high, similar to the upstream midplane separatrix values (see **Fig. 6.39**) and considerably higher (\sim factor 3) than the very approximate estimates made in [177] on the basis of coherent

averaging and combination of LP signals (see **Fig. 6.26**). In contrast, as seen in **Fig. 6.27**, the simulated target profiles of ion flux broaden during the ELM cycle in much the same way as reported experimentally (see Fig.17 in [177]). It appears that the profiles are steeper during rise time of the ELM and broader at the ELM peak and relaxation phase. This is observed on both LP and SOLPS data.

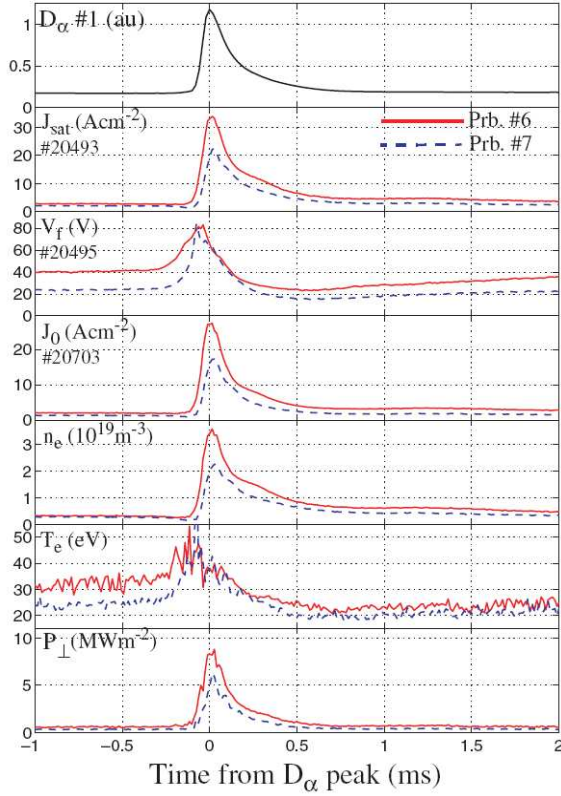


Figure 6.26. Measured j_{sat} and estimated n_e, T_e, P_{\perp} near the outer target strike point computed using the coherent ELMs averages over the period 0.5-0.8s of the TCV pulse #20493 (close repetition to #26730). Data for two probes #6 (red full lines) and #7 (blue dashed lines), nearest to the outer strike point in the common flux region are shown. The derived parameters are obtained by combining coherent signals from separate similar discharges. Extracted from [177].

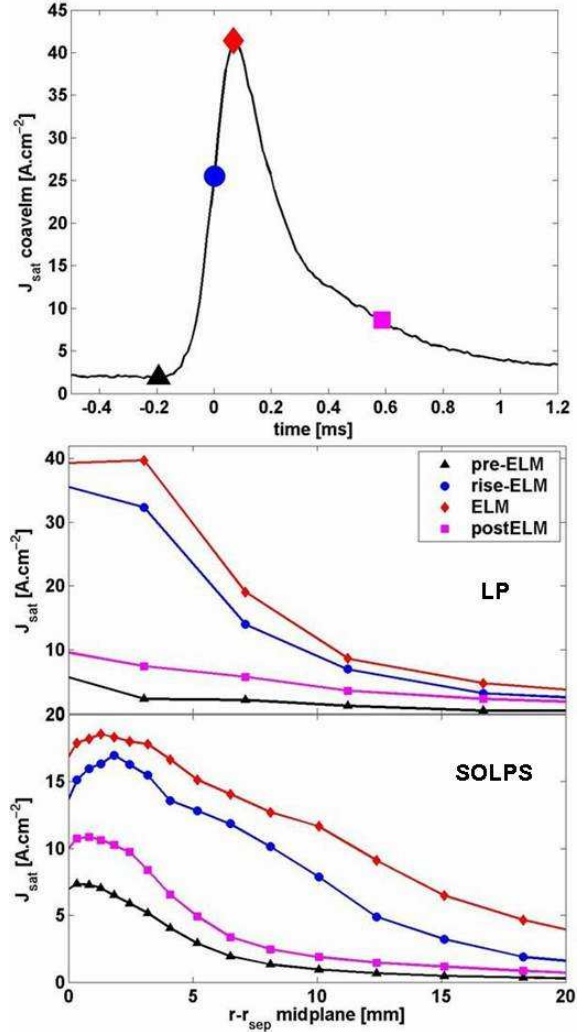


Figure 6.27. Centre: Profiles of outer target j_{sat} from #26730 obtained using the coherent averaging over the period 0.6-0.8s, encompassing 40 ELMs. Each profile corresponds to a single time in the time-dependent trace of j_{sat} from the LP closest to the outer target strike point (left upper). Lower: Corresponding SOLPS j_{sat} profiles at the outer target.

Using data from the floor viewing fast IR camera these SOLPS5 results can be compared also in terms of energy flux. Since no camera measurements are available for the reference discharge modelled here (#26730), the data from a slightly different discharge #35036 (very similar to #26730 - see the comparison shown in **Fig. 6.31**) are used. **Fig. 6.28** compares experiment and simulation.

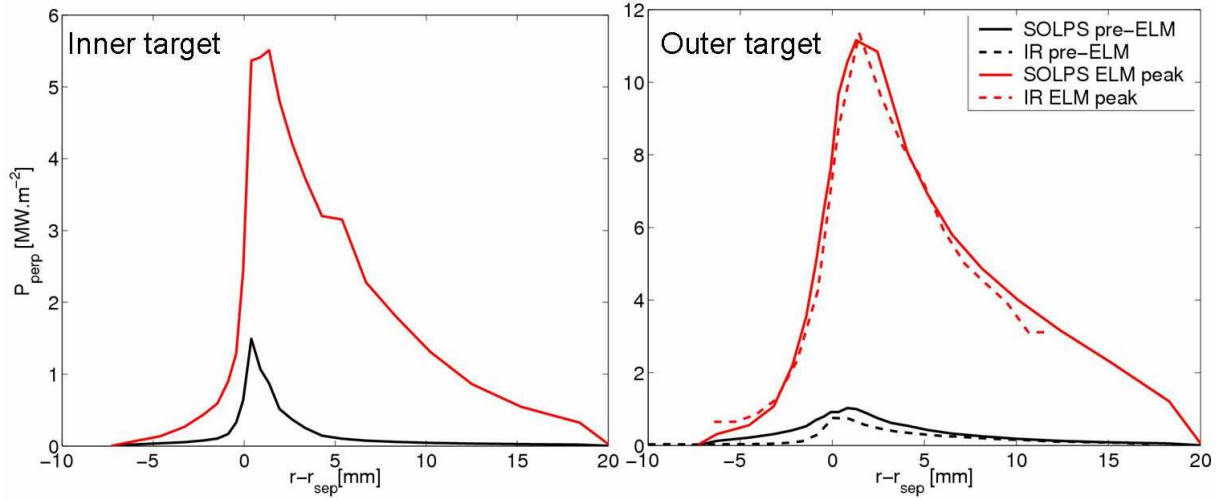


Figure 6.28. Pre-ELM (black) and ELM peak (red) target profiles of P_{\perp} from SOLPS (full lines). At the outer target the simulations are compared with the profiles from vertical viewing IR camera from #35036 (dashed lines).

As seen in **Fig. 6.28** the agreement between IR measurements and SOLPS5 power flux densities on the outer target in terms both of absolute magnitude and shape of the target profile is excellent. Moreover the results also match the estimated P_{\perp} from LP measurements shown in **Fig. 6.26**, although the ELMs in the two cases (for the discharges considered in [177] and those in pulse number #26730).

The SOLPS5 power flux profiles in **Fig. 6.28** have been obtained as an output from the code while assuming the sheath heat transmission coefficients as explained in section 6.1.2, while the γ_e is given by expression Eq.6.1 with $\gamma_e^* = 2$ and $\gamma_i = 3.5$. Contributions to the power flux come from electrons, ions and recombination at the target surface as expressed by Eq.2.62-2.64 (details of how these are derived have been given in chapter 2.) The ionic quantities are, of course, summed over all ion species included in the simulation and geometric factors are included (field line impact angles). As illustrated in **Fig. 6.29**, the contribution from recombination is quite small and the same applies for the impurities. This is consistent with hot edge plasma.

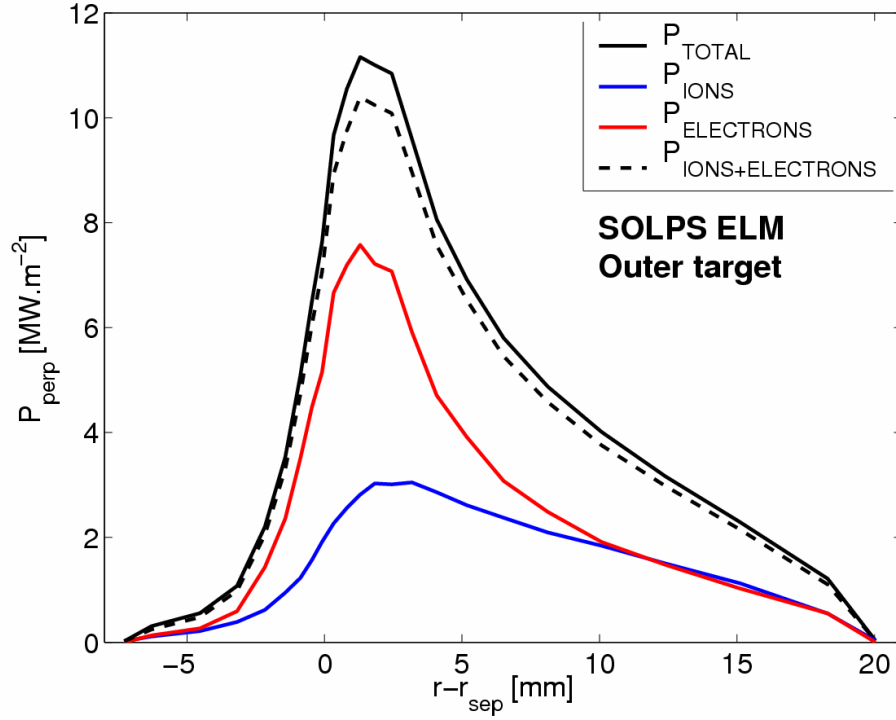


Figure 6.29. Outer target profiles of P_{\perp} from SOLPS at the ELM peak with the contributions of electrons and ions. The difference between black solid and black dashed lines corresponds to the contribution of recombination. Note, that the ratio of the contributions from electrons and ions will be discussed later in section 6.1.5.6)

The IR measured power flux naturally comprises all of the various contributions listed above (see section 5.2.1).

Fig. 6.30 compares simulated target profiles of j_{sat} , n_e , T_e and power flux density P_{\perp} at the ELM peak derived from code runs employing the diffusive and convective ansatz for the ELM radial transport (the corresponding upstream profiles for the latter are shown in **Fig. 6.23**) There is essentially no difference at the target for the two cases.

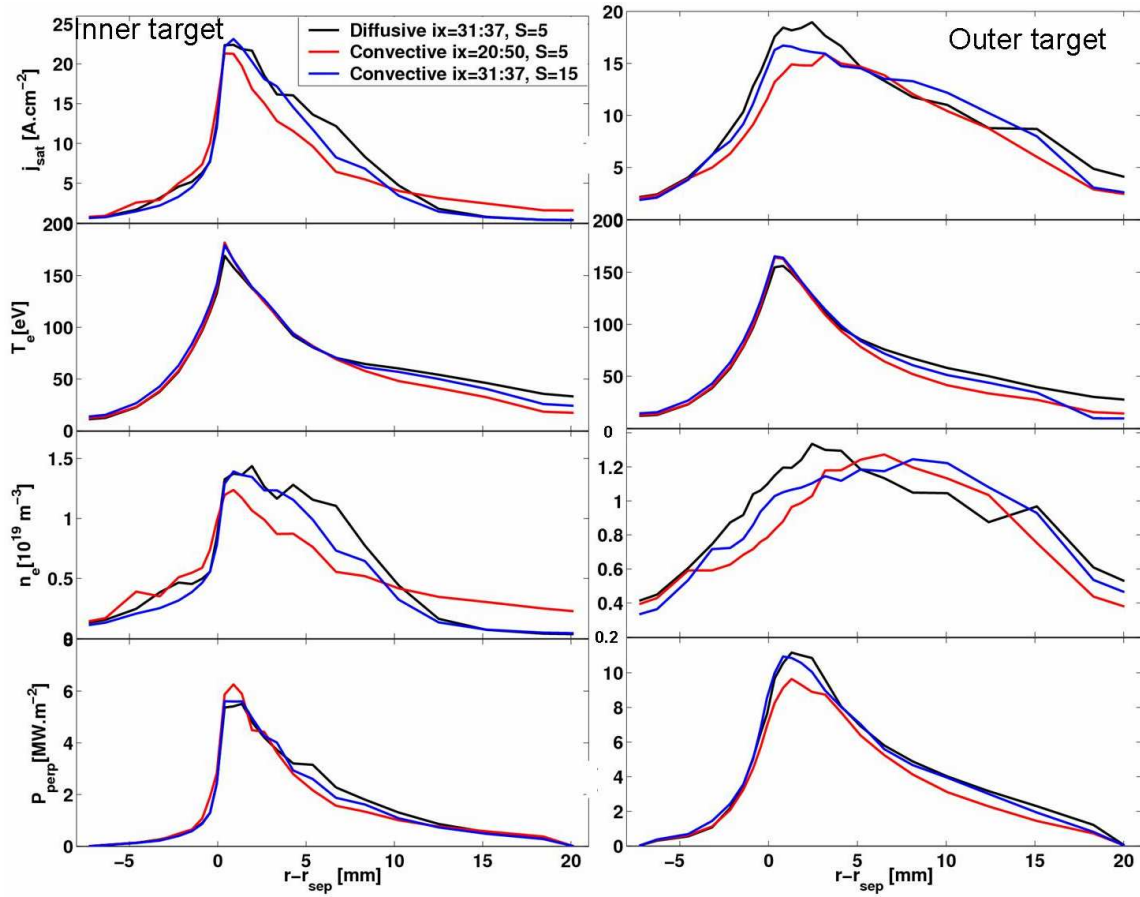


Figure 6.30. Target profiles of ELM peak j_{sat} , T_e , n_e and P_{\perp} from SOLPS simulations with different ansatzes for the ELM radial transport. The profiles obtained using “diffusive approach” (black lines) correspond to the upstream profiles shown on **Fig.6.19** and those using convective approaches (blue and red) to upstream profiles at **Fig.6.23**.

It is worth to note, that when ELM leaves the main SOL the radial power flux is mainly convective. However, the estimations of the convective and conductive contributions to the fluxes at the targets give about $\sim 70\%$ of conduction.

6.1.5.5. Time-dependent signals

The previous sections have mostly concentrated on upstream and target profiles at one instant in the ELM evolution. Here, the time-dependence of the particle and heat fluxes and temperatures (T_e and T_i) is examined in more detail. Beginning with P_{\perp} , for which excellent spatial agreement with IR is obtained (**Fig.6.28**), **Fig. 6.31** compares the experimental and simulated time evolution at the outer target strike point.

In contrast to the spatial profile, the agreement is less satisfactory in time. In particular, the IR measurements indicate a slower rise time (by approximately a factor 2) and a longer relaxation phase following the ELM peak. An obvious solution to improve

the agreement is therefore to simply increase the duration over which the ELM energy is released upstream. The result of this exercise is presented in **Fig.6.32** where 4 cases are shown with increasing ELM duration, including the reference case with $t_{\text{ELM}} = 100 \mu\text{s}$. During the first $100 \mu\text{s}$ the profiles of all ELMs depicted in **Fig.6.32** are identical (rising) and the main differences appear after these $100 \mu\text{s}$ when the relaxation phase is observed. This is consistent with what one would expect given unchanged pedestal profiles and connection length in all those simulations. It appears that the rise times between IR and SOLPS become reasonably comparable when the duration of enhanced transport is increased and the SOLPS data are averaged to $\Delta t = 10^{-4}\text{s}$. This suggests that if time-step in SOLPS is longer the agreement in time-dependent flux evolution is better (at least in the rise time).

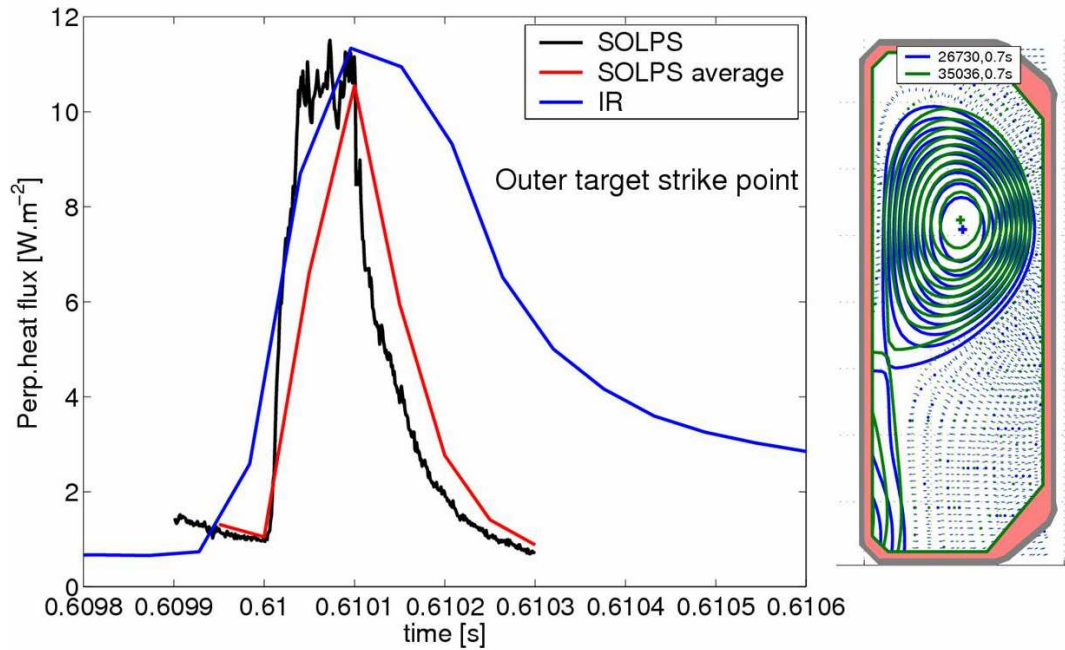


Figure 6.31. Time evolution during the ELM of P_{\perp} at the outer target strike point from SOLPS (black line – diffusive approach) and IR camera (blue line). For reference, the two equilibria (#26730 for SOLPS5 and #35036 for IR) are shown at right. The red curve is obtained from the SOLPS data with time step $\Delta t = 10^{-6}\text{s}$ whilst the IR data have 100 times lower time resolution ($\Delta t = 10^{-4}\text{s}$).

It is clear that the best agreement with IR data is obtained for the longest $t_{\text{ELM}} \sim 500 \mu\text{s}$. Whilst this is satisfying, it is evident that for constant upstream profiles and poloidal extent of the ELM energy release (as is the case in the simulations), a longer t_{ELM} must lead to a higher ELM expelled energy and therefore to an inconsistency with experimental measurements of ΔW_{ELM} . Even if after the first $100 \mu\text{s}$, the power crossing the separatrix decreases quite rapidly (see **Fig. 6.33 right**), the energy expelled after this first $100 \mu\text{s}$ is up to 65% of the total integrated energy for $t_{\text{ELM}} = 500 \mu\text{s}$. The total energy expelled by this long ELM is $\Delta W_{\text{ELM}} \sim 1300\text{J}$, about twice the experimentally estimated value.

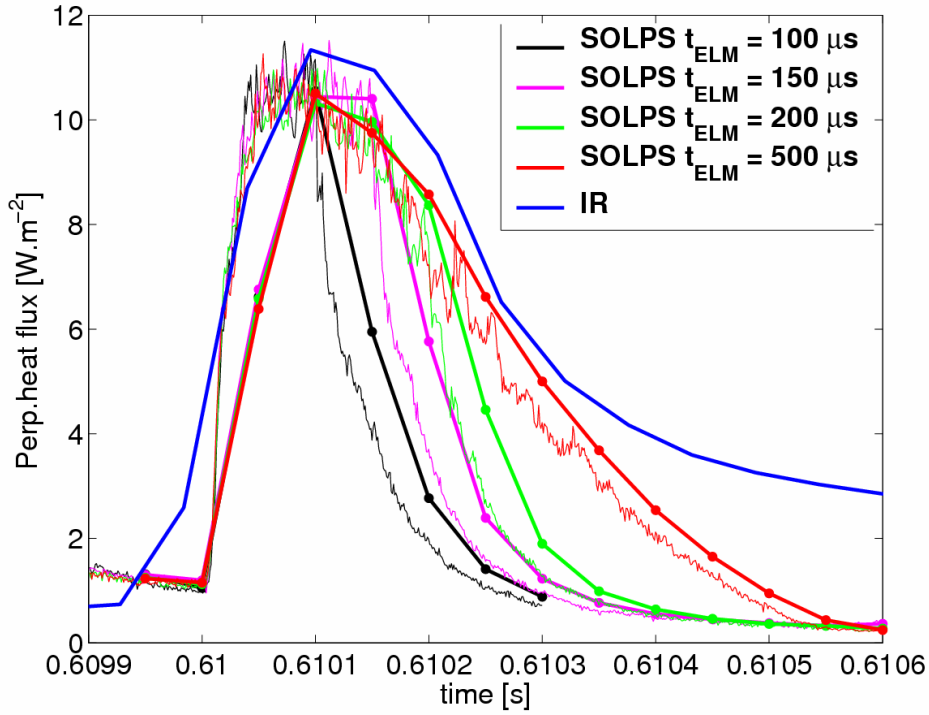


Figure 6.32. Simulated (diffusive approach) and experimental time evolution of P_{\perp} at the outer target strike point during an ELM with varying duration t_{ELM} . Thick lines with circles represent the averaged SOLPS data ($\Delta t = 10^{-6} s$). The main differences appear in the post ELM peak phase. Rise times are practically identical.

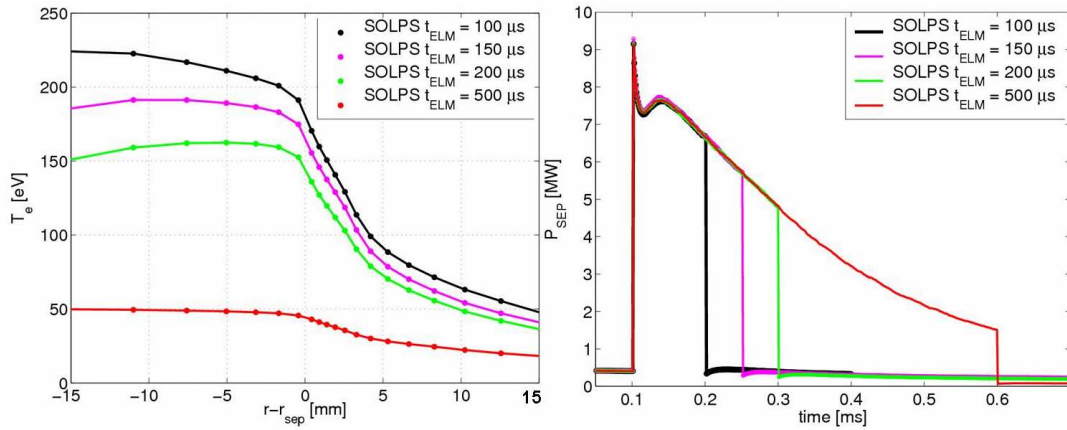


Figure 6.33. Left: upstream midplane profiles of T_e for ELMs with varying duration of the enhanced transport. Right: time dependence of the power crossing the separatrix, P_{SEP} for the 4 values of t_{ELM} .

Not surprisingly, the discrepancy also appears when a closer look is taken at the upstream n_e and T_e profiles. As seen in **Fig. 6.33**, the pedestal temperature collapses completely for the longest ELM. This is a consequence of the quick removal of the energy during the later part of this long ELM, especially by the high level of the wall

interactions (not shown). Therefore another, less radical solution is needed to keep the energy loss down whilst avoiding the pedestal collapsing too much in the tail of long ELM. A strategy to avoid this is to divide the ELM cycle not into three parts as has been the case thus far, but to add a fourth. This is straightforwardly performed by adding a fourth transport input file in the simulations. Inspired by the fact that these TCV Type III ELMs occur near the L-H transition threshold (see chapter 3), during part of the relaxation phase of the ELM the transport coefficients are raised to an “L-mode” level before being reduced again in the tail of the ELM back to the pre-ELM values. The ELM cycle thus consists of a pre-ELM part with H-mode transport coefficients, an ELM-part with ELM transport coefficients, an L-mode phase with transport coefficients lower than those of ELM part but higher than those of H-mode part and finally the H-mode again which closes the ELM cycle with the transport coefficients corresponding to those of the first, pre-ELM phase. This is shown schematically in **Fig. 6.34**.

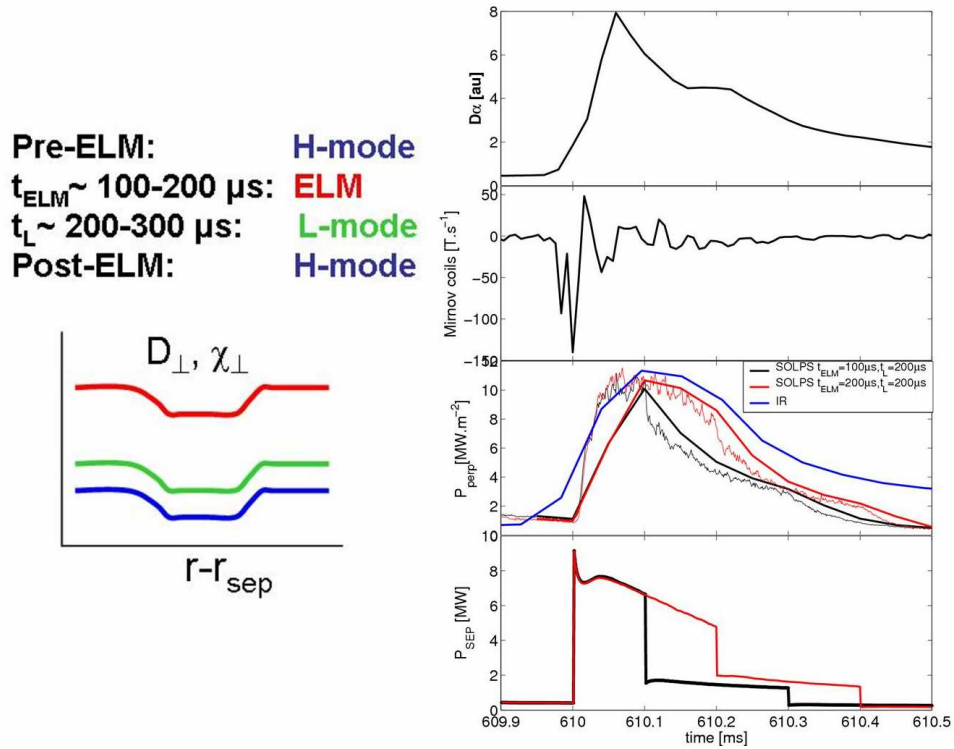


Figure 6.34. *Left:* Schematic of the transport coefficient radial profiles for simulations with an “H-ELM-L-H” ansatz. *Right:* Time-dependent signals of D_α , Mirnov coils and IR P_\perp from shot #35036 plotted with SOLPS signals of P_\perp and P_{SEP} from 2 different simulations. Black lines correspond to the case with $t_{ELM}=100\ \mu\text{s}$ and $t_L=200\ \mu\text{s}$, while red lines to that with both $t_{ELM}=t_L=200\ \mu\text{s}$. During the L-mode period of these simulations the pre-ELM profiles of D_\perp , χ_\perp are increased approximately 4x. During the ELM period they are identical to the case in **Fig.6.19**.

An indicator of the approximate ELM and L-mode phase durations, t_{ELM} and t_L is obtained from the signal of a Mirnov coil located on the outboard midplane wall. This is also shown in **Fig.6.34**, along with P_\perp and P_{SEP} from the simulations with $t_{ELM} \sim 100$ and $200\ \mu\text{s}$ and $t_L \sim 200\ \mu\text{s}$. The match with time-dependent IR profiles is very encouraging

and ΔW_{ELM} is much closer to experimental value than in case of long ELM. It is clear that this ansatz is still rather crude and a smoother decrease of transport coefficients in the relaxation phase could improve the match with the long tail seen experimentally in the IR P_{\perp} . This appears therefore to be one credible ansatz to explain the target IR measurements.

Another diagnostic against which SOLPS5 simulations can be compared is the set of photodiodes (PDs), supplying line-integrated D_{α} emission signals from viewing chords distributed around the poloidal cross-section (see **Fig. 6.35**). The bursts of D_{α} emission provoked by the ELM indicate not only changes in the local T_e and n_e provoked by the ELM, but also the enhanced recycling due to interaction with first wall and divertor surfaces. To compare with experiment, similar lines of sight have been used in SOLPS5 to extract the simulated emission. The PDs are uncalibrated but can be still directly compared with respect to the time-dependence during the ELM. **Fig. 6.35** shows such a comparison of the SOLPS and experimental D_{α} time-evolution during the whole ELM cycle, where the D_{α} signals are coherently averaged from 4 ELM cycles and time $t=0$ s corresponds to the peak values in both experimental and code data. The coherent average time base of experimental data was computed with reference to the vertical line of sight such that $t=0$ corresponds to the peak in ELM signal on this channel (#1). The inset at the top right of **Fig.6.35** shows the lines of sight superimposed on magnetic equilibrium together with the approximate poloidal extent over which light is collected by the lateral photodiodes. Compared to lateral chords the vertical chord #1 is unapertured and has a large angular divergence covering quite substantial part of the plasma cross-section. The width of the experimental chords in terms of the angular divergence and the contribution from wall-interaction which is present in the real experiment, were neglected in the SOLPS integrated signals. Nevertheless, these are less relevant for the code/experiment comparison in terms of time-dependent signals without particular interest in the absolute values of the D_{α} signals, especially when only the lateral viewing chords (#2-10) with quite narrow angular divergence are being compared with corresponding SOLPS signals on **Fig.6.35** (even though #1 is shown as well).

As it can be seen on the left side of **Fig.6.35** with experimental data, very different time-evolutions of signals from different viewing chords in the coherent ELM characterize the response of the various lines of sight. Very interesting information is given, for instance by the channels 7,6,5 whose lines of sight progressively encroach on the X-point region from above. The response is more smeared out in the time and double peaked structures are observed. The first of these peaks corresponds to the single peak observed from viewing chords 10,9,8 intersecting the long outer divertor leg and it appears slightly earlier than the peak on the first vertical channel. The signal from this reference channel #1 can be considered as an effective average of the behaviour of all channels [177]. The SOLPS time-evolutions of the signals from these chords (#5,6,7) quite well reproduce the shape observed experimentally (even with double-peaked feature). Moreover the shape of time-dependent signal of chord #2 neighbouring #7 is also captured by SOLPS. However, the other lines of sight at the top of the machine and divertor legs are too noisy in the SOLPS (suggesting the lack of the wide angular divergence in these SOLPS signals and the valid comparison with experiment cannot be done). Thus it seems to be the case that the use of a single line of sight (and not the whole cone of collection) in SOLPS is good enough approximation only in the X-point region,

where probably the majority of the emission is localized.

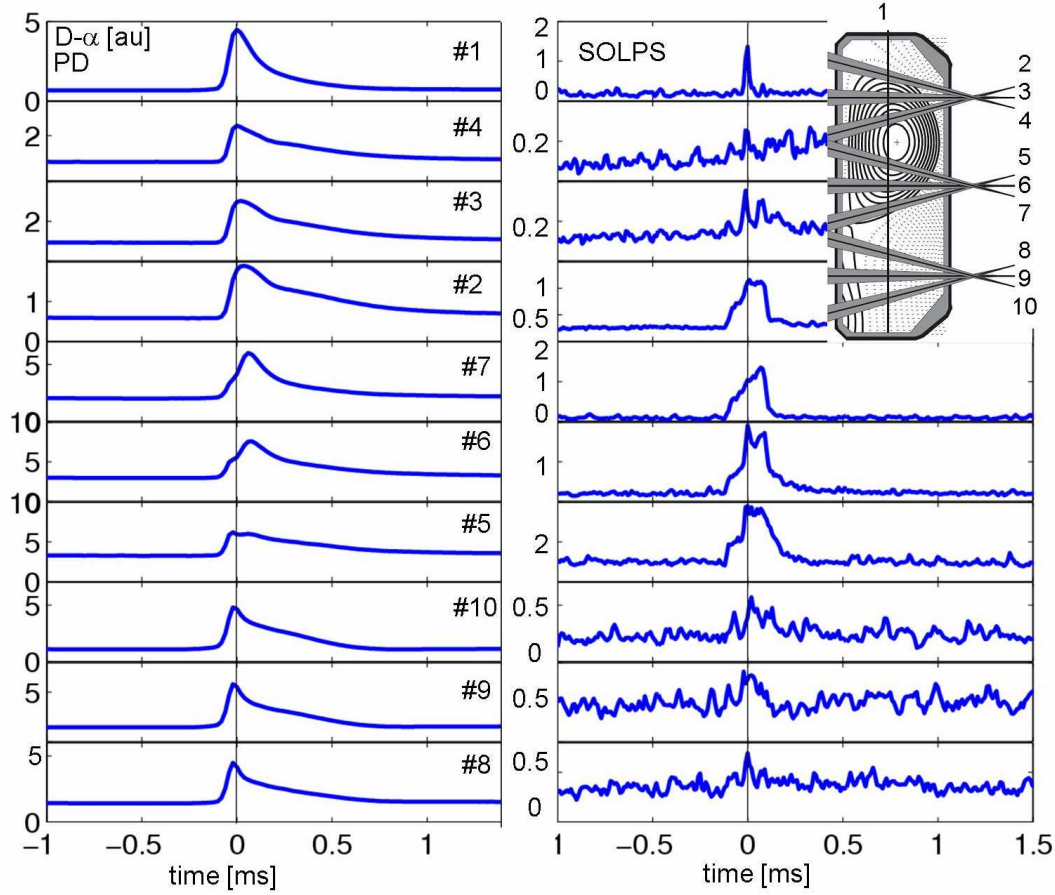


Figure 6.35. Coherent averages over the interval 0.5-0.8s of the D_α recycling emission along the line integrals across the TCV poloidal cross-section in shot #20493 (similar to #26730, for which data from PDs are not available). The channel disposition and approximate angular fields of view for the lateral channels are given in the inset at top right. The experimental signals are uncalibrated and the experimentally applied gains have not been applied. Only the time evolution of the signals is therefore important here

The SOLPS D_α emission integrated over the whole regions of the grid, namely core, SOL and both targets is shown in **Fig. 6.36**. The total D_α emission is best compared with the signal from PD 1 vertically viewing the biggest part of the plasma. The rise time of both signals is $\sim 0.1\text{ms}$, however as in the case of the target heat loads in comparison with the experimental IR data, the relaxation part of the ELM signal does not correspond to the experimental profile, what is however similarly to P_\perp approximately corrected in the simulation of longer ELM (see **Fig. 6.36 right**). One can note that for instance the integrated emission in divertors shows the peak later than $t=0$ (unlike the other parts corresponding to SOL and core), what is in line with the observations that inner target viewing signals #6,#7 and second peak on #5.

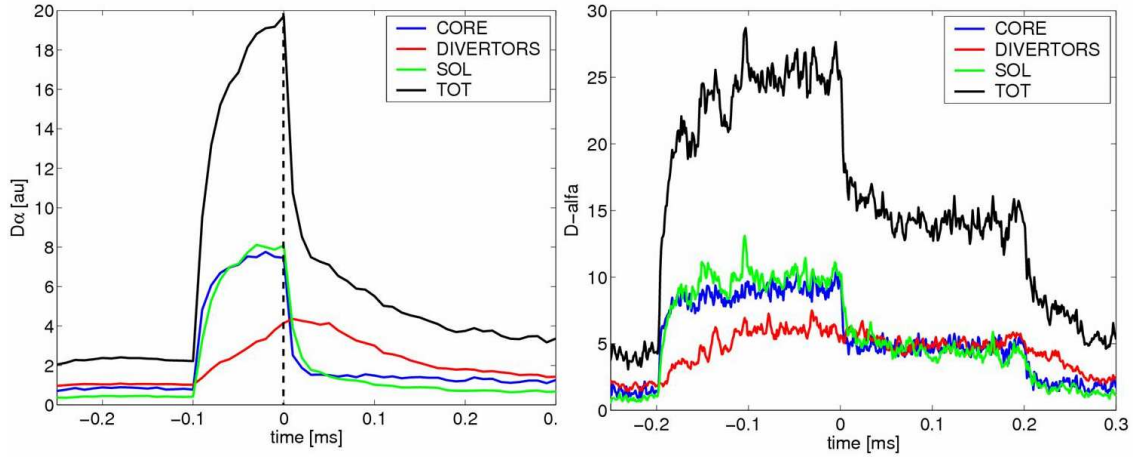


Figure 6.36. Left: D_α emission integrated over the regions of the simulation grid calculated by SOLPS. Right: D_α emission from the simulation of ELM with “H-ELM-L-H” ansatz.

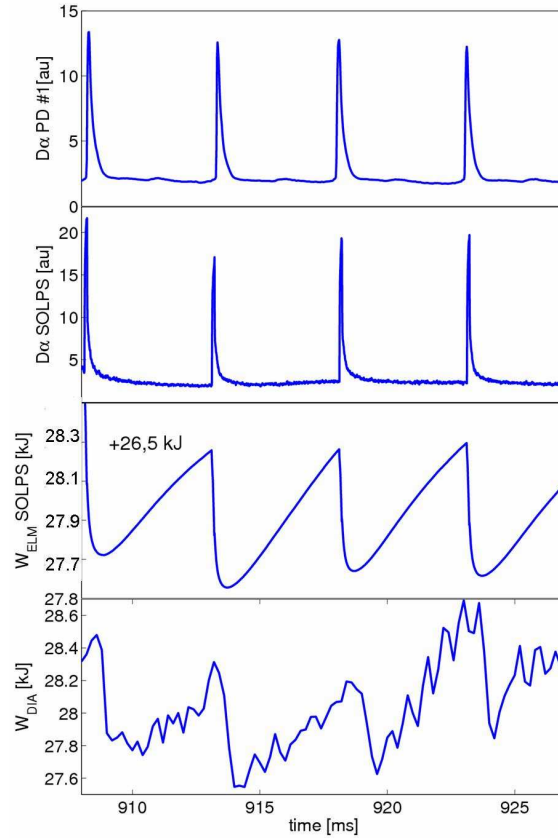


Figure 6.37. Time-traces of D_α signals and energy stored in plasma from vertically viewing photodiode PD #1 and DML respectively compared with SOLPS data. $W=26,5$ kJ corresponding to the energy in the core plasma has been added to the SOLPS5 stored energy to match the experiment (the SOLPS5 simulation does not include the core plasma). $\Delta W_{ELM} \sim 600 - 700$ J in both experiment and SOLPS simulation.

Fig. 6.37 shows the comparison of the SOLPS and experimental data for D_α and W_{plasma} (W_{dia}) during 4 multiple ELMs. One can see that simulation reproduces experiment reasonably well.

6.1.5.6. Comparison with kinetic simulations

The main limitations of the ELM simulations with SOLPS are the kinetic effects which can be only partially incorporated into the fluid code. A fluid description of the transient event normally fails if the typical timescale is less than that needed for equilibration so that plasma particles are unable to completely relax to a thermal (Maxwellian) distribution. Such situations arise, for example, in front of solid surfaces when the ELM arrives there. As it is concluded from the results of kinetic modelling [230-231], the distribution function during this phase of the fast response of the electrons due to the fast change of the target particle flux at the ELM arrival is unable to equilibrate and one gets much larger (factor of ten) heat conduction coefficients in region between the heat front and the target compared to the values expected from Maxwellian distribution. When analyzing the energy deposition at the targets both electrons and ions must be taken into account. In addition to the fast electrons, the fast ion tail also evolves during the ELM, representing another important kinetic effect. Any fast heat transport carried by the electrons will be limited by non-linear changes due to the sheath potential. The ions can come either from the hot ions traveling from upstream or previously cold dense ions in front of the target accelerated by the enhanced potential in the sheath.

In order to investigate the relevance of the fluid code results for the transient especially at the targets, where the kinetic effects manifest the most, this section compares the SOLPS5 time-dependent results for target power and particle fluxes and temperatures (T_e and T_i) with those from the 1D kinetic particle-in-cell (PiC) code BIT1. More general details on BIT1 simulations of the SOL can be found in [232]. This code includes non-linear collisions for an arbitrary number of charged particles. Collisions with neutral particle species and a linear model of plasma-surface interaction processes can be also included [233-234], but have not been used for the simulations reported here. The simulation geometry corresponds to a single magnetic flux tube bounded between inner and outer divertor plates. At the midplane, there is an ambipolar plasma source mimicking the cross-field transport across the separatrix.

The kinetic code is only 1-D, parallel to the magnetic field. To compare with the 2-D SOLPS simulations, a choice must be made as to where in the SOLPS5 target profile the comparison is to be made. A close look at the ELM and pre-ELM SOLPS5 simulations reveals that the peak of the target profile shifts outwards during the ELM and is no longer found at the nominal magnetic strike point position. From the analysis of the SOLPS diffusive ELM simulation (using “diffusive” approach and chosen as a reference case throughout this section) shown in **Fig. 6.38** it follows that the peak during the ELM is located as many as 5 radial target cells further out from the nominal SP position. In the following text the PiC data will be compared with SOLPS time-dependencies at the point of maximum flux at the ELM peak in SOLPS.

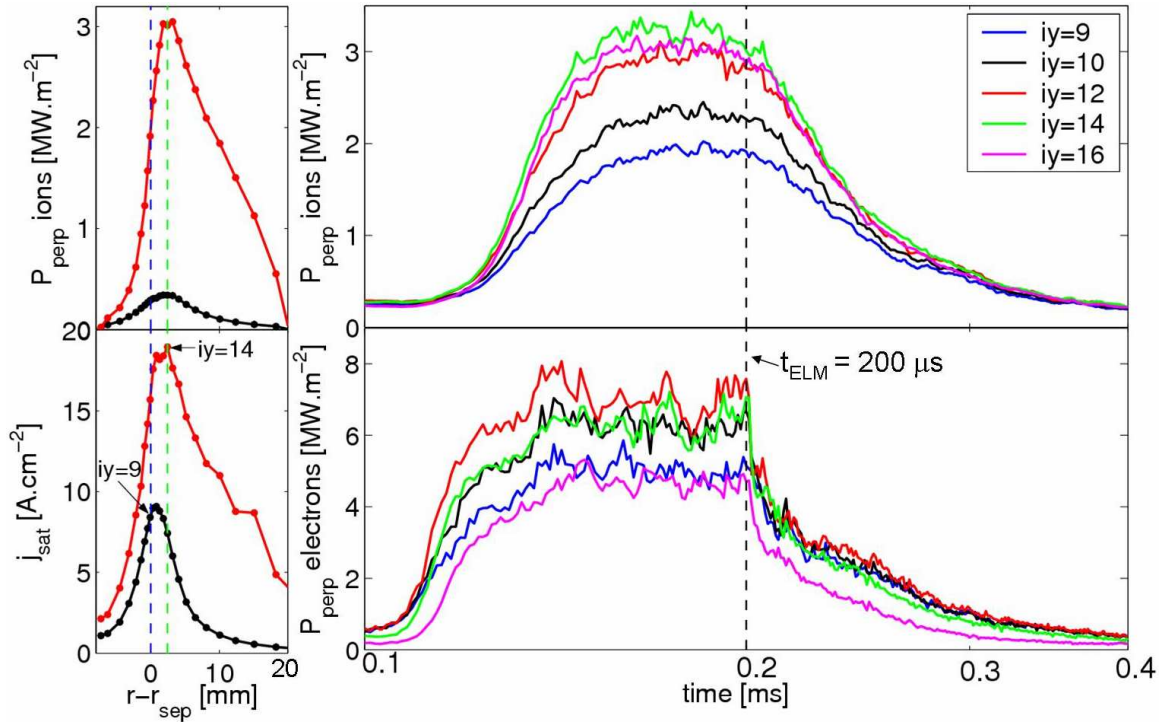


Figure 6.38. *Left:* outer target profiles of pre-ELM (black) and ELM SOLPS (red) simulated P_{\perp} deposited by ions and j_{sat} mapped to the midplane. Radial position $r-r_{\text{sep}}=0$ mm corresponds to the separatrix position (radial cell $iy \sim 9$). The profiles peak further out in the SOL (shifted about 5 cells outwards: $iy \sim 14$). *Right:* time-dependent P_{\perp} profiles of ions and electrons plotted for different radial positions at the target. There is a very clear shift in the electron time envelope in comparison with the ions (the maximum of P_{\perp} for the electrons appears at $iy=12$, about 2 radial cells closer to separatrix than for the ions).

Fig. 6.39 compiles the simulated time dependence of the upstream separatrix and downstream T_i , T_e , j_{sat} , P_{\perp} for electrons and ions at the radial position of the peak of the power flux density for the reference “diffusive” ELM. There is very little drop in T_e along the ~ 18 m of parallel connection length from upstream to target. However, T_i decreases about 4.5 times from midplane to the target, indicating strong ion cooling.

In common with the PiC simulations, the SOLPS target power flux rises on the ion and not the electron timescale. It is notable however that T_i at the target rises on a much slower timescale than its increase at the ELM onset upstream. Beyond t_{ELM} , there is an abrupt decrease in T_e on the $1 \mu\text{s}$ timescale (the approximate electron thermal transit time from upstream to pedestal τ_e). Some $10 \mu\text{s}$ later, T_i begins to fall. The same time-evolution is observed for j_{sat} . This is significantly faster than expected on the basis of ion sonic transit time ($\tau_i \sim 120 \mu\text{s}$ calculated assuming the midplane $T_{e,\text{sep}} \sim T_{i,\text{sep}} \sim 150 \text{ eV}$ – see **Fig.6.39**) and seen usually in PiC ELM simulations as [235-236]).

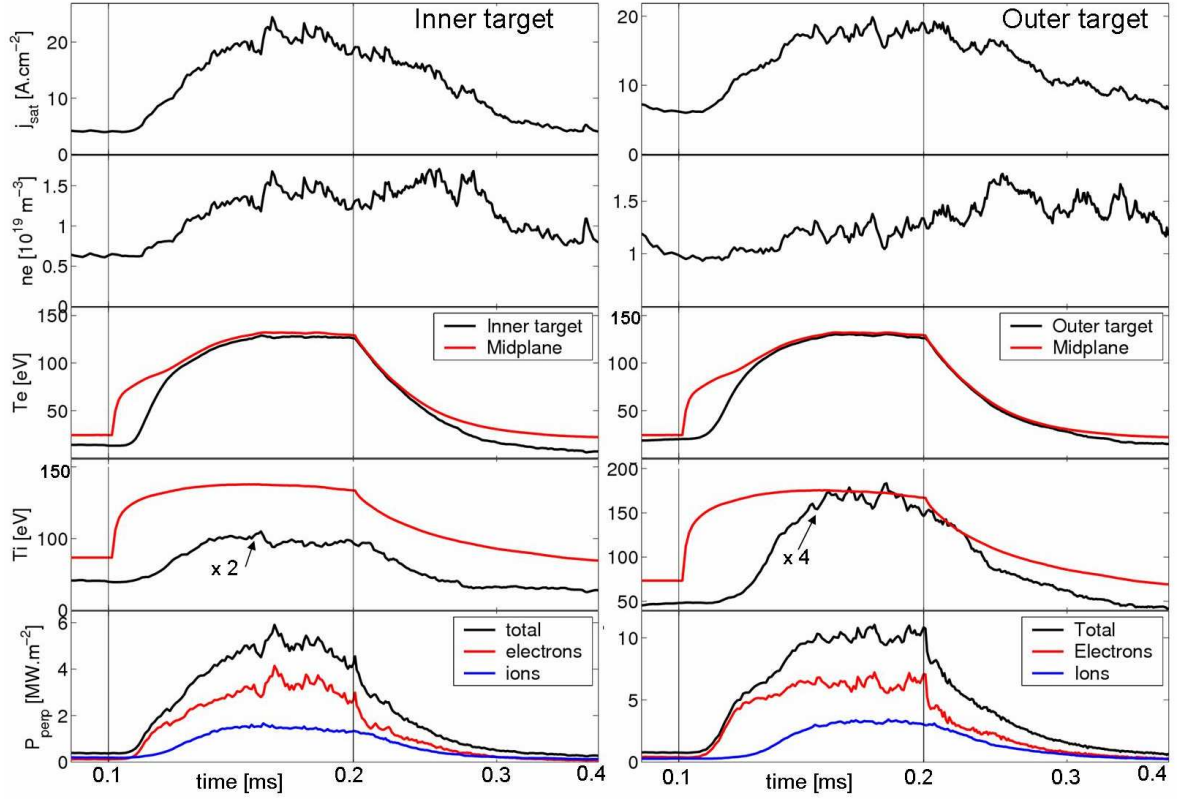


Figure 6.39. Time evolution at inner and outer targets of SOLPS5 j_{sat} , n_e , T_e , T_i and P_{\perp} at the target position of the j_{sat} peak during the ELM for the diffusive approach. The upstream T_e , T_i at the outer midplane separatrix are also plotted. Note that the T_i values have been multiplied by 2 and 4 at inner and outer target respectively. Times 0.1ms and 0.2ms represent the start and end of the enhanced transport respectively. The j_{sat} rises in time very similarly to that seen experimentally in Fig.6.26 on target LPs Results for the convective is very similar. Note the logarithmic scale on the abscissae.

To assist in the process of seeking better understanding of this behaviour, simulations with the BIT1 code have been performed by Dr. David Tskhakaya of University Innsbruck (Austrian Fusion Association) specifically for this TCV Type III ELM using the plasma background computed with SOLPS5. These kinetic simulations are CPU intensive and several weeks are required for each full calculation. The SOLPS steady state (i.e. pre-ELM) solution was used to provide input settings for the PiC simulation: the poloidal profiles of T_e , T_i , n_e at the radial position just outside the separatrix with corresponding r, z positions; the pedestal midplane values of T_e , T_i and n_e ; the total magnetic field line angle of incidence of the selected poloidal ring at both targets; the energy expelled by the ELM, ΔW_{ELM} ; the poloidal positions where the ELM was expelled and the duration of the ELM, t_{ELM} . These SOLPS5 supplied profiles do not, however, correspond exactly to the pre-ELM state of the PiC simulations. In the PiC code the plasma profiles are not controlled directly. So even though the SOLPS5 values are the initial values given to the code, the plasma profiles develop self-consistently from the

power crossing the separatrix which is estimated as:

$$P_{sep} = \frac{3}{2}(T_i + T_e)VS \quad (6.4)$$

where T_e and T_i are the pedestal temperatures, V is the SOL volume ($V = L_{pol} \cdot A$, where A is affected area in the radial-toroidal direction and L_{pol} is the poloidal extent of SOL where this energy is deposited - the value $L_{pol}=1.2m$ was used for pre-ELM PiC) and S is the intensity of these particle sources [237]. The ELM is simulated by introducing the ambipolar, Maxwellian source of particles, S distributed with pedestal temperature $T_{e,ped}$ and weighted according to a ‘pedestal’ density $n_{e,ped}$ with a cosine spatial distribution of given extent centered in the midpoint between two targets. The total ELM energy is given by

$$W_{ELM} = \frac{3}{2}(T_{i,ped} + T_{e,ped})VSt_{ELM} \quad (6.5)$$

The power crossing the separatrix has rectangular shape in time. The P_{sep} during the ELM is constant around 6 MW, corresponding approximately to the SOLPS5 case, giving the usual ~ 600 J for the Type III ELM. The parameters approximately corresponding to the SOLPS5 solution are used, even though the values of n_e , T_e , T_i in this upstream SOL are adjusted so that the ELM expelled energy has the required value from experiment. The area A depends on the radial extent of the SOL assumed by PiC. Since the latter is a 1D code, the “radial coordinate” is used only to obtain the correct approximate energy for the ELM event. In these simulations, the energy expelled by the ELM, $\Delta W_{ELM} \sim 690J$, was obtained using a poloidal extent of the power source $L_{pol} \sim 0.68m$ centered on a point 1.15m poloidally from the outer target and 1.45 m poloidally from the outer target (in SOLPS the source was centered at 1.43 m while distance to outer target from source centre is $\sim 1.17m$) and a radial extent $\sim 0.1m$ was used.

There are differences between the PiC and SOLPS codes which might play a role in the comparison of their results. No impurities or neutrals are included in these SOLPS dedicated PiC simulations. Their inclusion was intended (it is possible, in an approximate way) in a further refinement but turned out not to be feasible within the timescale of this thesis. The inclusion of impurities is not expected to make any significant difference for the rather low ΔW_{ELM} considered here. Neutrals, however can make a bigger contribution. In the PiC model there is no electron cooling and high thermal plasma densities can be observed. The total temperature at the target is defined as a mixture of both thermal and ELM plasma. In SOLPS5, with electron cooling taken into account, the temperature of thermal plasma is lower compared with the kinetic code. In contrast, the power loads are less sensitive to the thermal plasma, giving reasonable agreement between PiC ELM power flux densities and those measured with the fast IR camera. The only difference between inner and outer divertors in this 1D PiC simulation is the distance from the targets to the centre of the ELM source, while the angle of the field line is adjusted at each end of the flux tube to account for the different divertor angles.

The results of the fluid-kinetic code comparison are shown in **Fig.6.40** where the time-dependent electron and ion particle and power fluxes from SOLPS5 and PiC simulations on both targets are plotted. The agreement in terms of absolute values of total fluxes is encouraging. However, the power flux of ions is smaller than power flux of electrons in SOLPS, what is completely opposite to the PiC results.

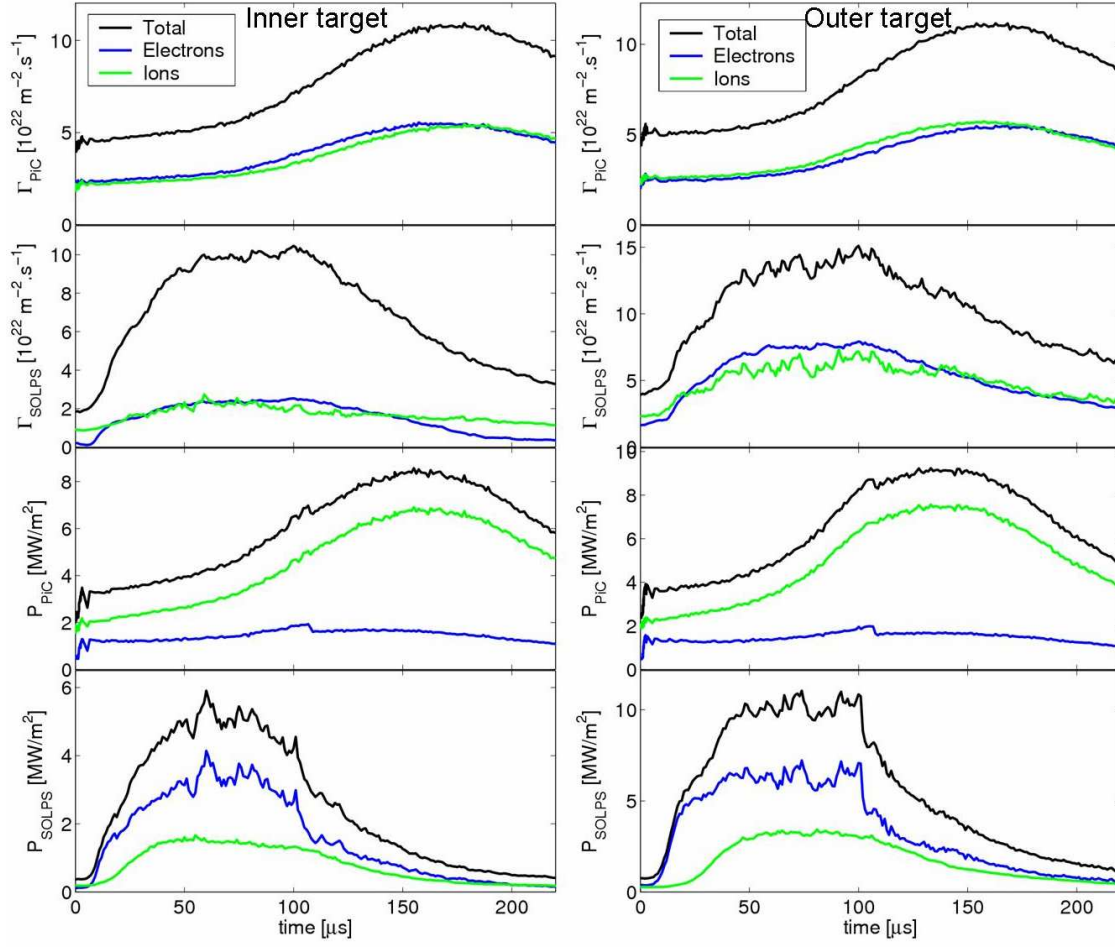


Figure 6.40. Time evolution of particle and power fluxes on targets from PiC and SOLPS5 (diffusive approximation for the ELM from same simulation as shown on Fig.6.39) including the contributions from electrons and ions. The ELM switches off at $t = 100 \mu\text{s}$

The PiC results on Fig. 6.40 clearly show abrupt rise of the electron heat flux on the electron transit timescale, followed by the main ELM front propagating on the ion sonic timescale τ_i , bringing the bulk of the ELM to the target. Thermal ions are drawn from the sheath region by the increased potential rising the ion heat flux slightly at the electron pulse arrival and after the situation stabilizes until the arrival of the bulk ion pulse on the timescale τ_i . As it was stated above, however, the peak of the SOLPS ion power flux appears much faster than the τ_i . The match of two codes is not good enough especially in the part of the ELM cycle after switching off the enhanced transport and the signature of the ion transit time is not seen in the same way as in kinetic simulations. Two possible candidate reasons for some of this discrepancy are the strong electron-ion collisional coupling and the possibility of Monte-Carlo noise in the SOLPS simulations. Electrons are much more mobile than the ions and are thus more effectively cooled. As a result of increasing collisionality the ion and electron energies become increasingly

coupled. Moreover, the assumption applied in SOLPS simulations, $\chi_e \approx \chi_i$ is likely to contribute to the argument of strong coupling between the electrons and ions. Experiment does not, however, support the speculation of full energy transfer from electrons to ions. The spikes in D_α light emission at the target indicate the presence of ions with the confidence. The experimental heat and particle fluxes rise are observed on the time scale of ions. The fact remains that the time dependence of target plate ion fluxes and power flux densities predicted by the kinetic code are in better agreement with experiment than the SOLPS5 simulations. The ion transport is thus apparently better described by the kinetic approach.

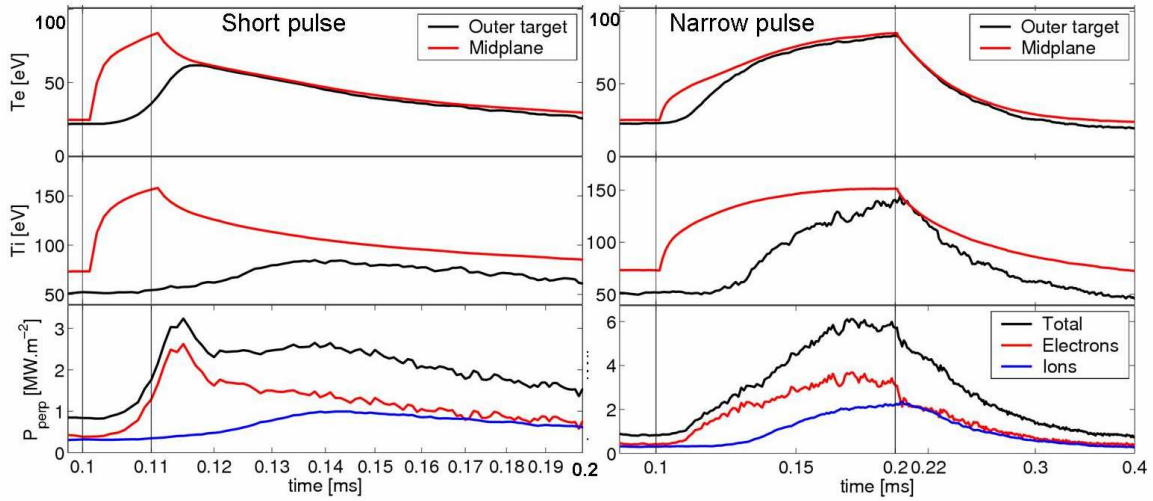


Figure 6.41. SOLPS5 Outer target and upstream time-evolution for short (left) and narrow(right) “diffusive” pulses. Vertical lines mark the start and the end of the ELM pulse.

One way to investigate these discrepancies on the SOLPS5 side is to reduce the problem to more simple situations. Instead of a long ELM with $t_{\text{ELM}} = 100 \mu\text{s}$, launched from a finite poloidal extent ($L_{\text{pol}} = 60 \text{ cm}$), two different perturbations have been studied, one with the same poloidal extent but 10x shorter duration and the second with $t_{\text{ELM}} = 100 \mu\text{s}$, but with launched from only a single poloidal cell on the SOLPS5 grid. The results are compiled in **Fig. 6.41** for the time evolution of T_i , T_e (upstream and outer target) and P_\perp (outer target). The rise times of electron and ion power fluxes at the beginning of both pulses are very close to what one would expect. The time-dependent behaviour with delay of ion pulse arrival is very clearly present in the simulation of short pulse and the ions start arriving $\sim 40 \mu\text{s}$ later than electrons. Although there is now a clear gap between an electron pulse and the peak of the ions, it is still too short compared to the expected $\tau_i \sim 120 \mu\text{s}$. The simulation of narrow pulse (in space) launched from the outer midplane (right side of **Fig. 6.41**) with $t_{\text{ELM}} = 100 \mu\text{s}$ shows that the delay in the arrival of the ion pulse is less evident than for the temporally short pulse.

In summary, two main discrepancies between the kinetic and fluid simulations have been identified:

$$1.) P_{\perp,e,SOLPS} > P_{\perp,i,SOLPS} \quad P_{\perp,e,PiC} < P_{\perp,i,PiC}$$

- 2.) The delay in the arrival of the ion pulse with respect to the electrons (expected to be on the order of the transit time, τ_i of a sonic pulse from midplane to target) is seen clearly in the PiC results but is not reproduced with SOLPS5.

An understanding of these related issues is very important for the time dependent ELM simulations to be credible. The explanation of both issues may be found in the kinetic nature of the ELM event. Parallel transport in the SOL is governed by two groups of kinetic factors. In both SOLPS and BIT1 these are the sheath heat transmission coefficients and the heat flux and viscosity limiters. It is the different way of treating the kinetic effects at the targets in both codes which causes the discrepancies between them. A closer look is therefore necessary at the places in SOLPS5 where the kinetic approximations play a role. This will be addressed in more detail in the next two sections.

6.1.5.6.1. Ion vs. electron target power fluxes

At the first sight is it striking that $P_{\perp,e} \gg P_{\perp,i}$ during the SOLPS5 simulated ELMs. This is not expected intuitively, nor is it supported by PIC simulations, which show opposite behaviour. The origin of the discrepancy may be traced to the treatment of the sheath transmission in SOLPS5. Unlike the PiC code, which includes a full kinetic treatment of the sheath through to the target surface, B2.5 uses boundary conditions at the sheath edge only. In general, parallel heat fluxes are defined in both codes as $P_{\perp,e} = \gamma_e k T_e n_e c_s$ and $P_{\perp,i} = \gamma_i k T_i n_i c_s$. However, the sheath heat transmission coefficients are treated differently in the two cases. In SOLPS, they correspond to the boundary at the entrance to pre-sheath, so that $\gamma_e = 2 + V_{SOLPS}/T_e$ (as Eq.6.1), where the potential V_{SOLPS} includes the contribution of both V_{se} (pre-sheath potential fall) and V_{sf} (sheath potential fall) as explained in chapter 2. The sheath problem is thus treated by this potential difference which appears in the heat flux of electrons. The γ_i is simply fixed at 3.5 (see section 6.1.2 and chapter 2). In contrast, the PiC code computes fluxes and energies at the target based on classical sheath kinetic expressions for the ion parallel speed (v_{\parallel}), energy fluxes at the sheath (Q_{sh}) and potential fall across the sheath ($\Delta\Phi$). These are normally:

$$v_{\parallel} = c_s = \sqrt{\frac{T_e + T_i \chi}{m_i}}$$

with χ being the polytropic constant; $Q_{sh}^{e,i} = \gamma_{e,i} \Gamma_{e,i} k T_{e,i}$; $\Delta\Phi = T_e \cdot \phi$ with $\phi = 2 + 5$; $\gamma_e = 2 + \phi$ and $\gamma_i = 2.5 + 1.5(T_e/T_i + \chi)$ [237]. The ions have been accelerated in the sheath and the term coming from the sheath potential barrier which is at the entrance to the pre-sheath included in γ_e (as in the above described case of SOLPS), after the crossing sheath belongs to the ions and is therefore transferred to γ_i . As a consequence, in the PiC simulations, $\gamma_e = 2$ approximately and $\gamma_i = 3.5 + V_{PiC}/T_i$, whilst the term from the potential drop across the sheath is approximately $V_{sf}/T_i \approx 3T_e/T_i$. It is worth stressing that the electron and ion power fluxes calculated by SOLPS thus do not take into account the transfer of energy from electrons to ions and only the fluxes at pre-sheath are given.

In other words, only total power flux on the targets given by SOLPS is comparable with real situation at the target. The total parallel heat fluxes in both PiC and SOLPS simulations are approximately $P_{\perp \text{tot}} \approx (2 + 3.5 + 3)kTn_s \approx 8.5kTn_s$, where T and n are the average temperature and density of the plasma particles. Assuming the same particle fluxes for electrons and ions, one can easily show that in the kinetic simulations, even if

$$T_e \gg T_i: \quad \frac{P_{\perp i}}{P_{\perp e}} = 1.75 \frac{T_i}{T_e} + 1.5 > 1.5$$

while in SOLPS:
$$\frac{P_{\perp i}}{P_{\perp e}} = 0.7 \frac{T_i}{T_e} < 1$$

since in SOLPS $T_e \geq T_i$ at the targets and as the ELM develops the two temperatures should equalize. Thus, the PiC code yields a much higher ion power flux deposited on the target (after the ions have been accelerated in the sheath), while SOLPS, which considers only sheath edge fluxes, shows much higher electron flux deposited at the target. Put another way, although both codes produce essentially the same total target power flux density (because the total sheath transmission factors are similar), the individual ion and electron components differ in each code as a consequence of the point at which the flux densities are specified. It is simply a question of energy exchange in the sheath, which is correctly modelled in the kinetic simulations but neglected in the fluid code.

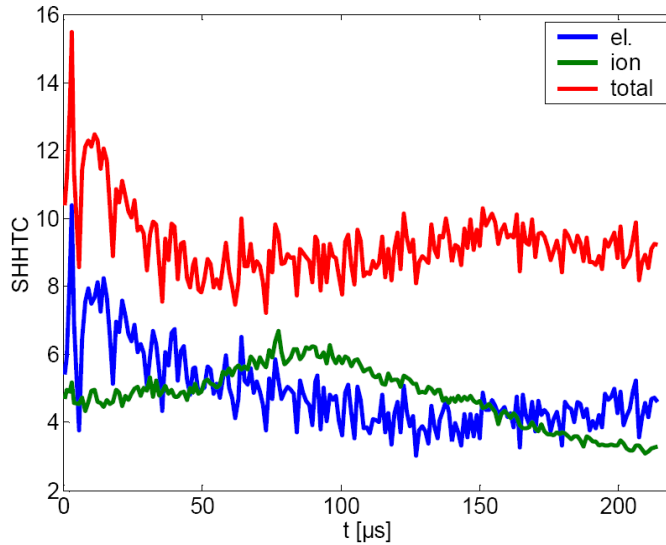


Figure 6.42. Time-dependent sheath heat transmission factors at the outer divertor sheath from PiC. Supplied by Dr. D. Tshakaya).

Fig. 6.42 shows the time-dependence of sheath heat transmission coefficients extracted from the PiC simulations. With the exception of the very early phase, corresponding to the arrival of the fast electron pulse, the coefficients do not change significantly during the ELM, providing important confirmation that the assumption of constant coefficients in the SOLPS5 simulations is justified.

Now that the reason for the power sharing discrepancy between kinetic and fluid code has been identified, a correction term can be straightforwardly applied to the SOLPS5 results. The correction has the form $eV\Gamma$ where Γ is the SOLPS parallel particle

flux at the targets and V is the sheath potential. **Fig. 6.43** shows how the application of this correction brings kinetic and fluid energy fluxes in closer agreement.

The level of agreement obviously depends on the potential V used in the correction factor. The sheath potential fall at the targets from PiC and SOLPS V_{PIC} and V_{SOLPS} are compared in **Fig. 6.44**. They are quite similar in amplitude at ELM peak but in the general over the ELM cycle the $V_{\text{PIC}} > V_{\text{SOLPS}}$, especially at outer target. The differences are particularly evident in the pre-ELM and relaxation phases and the large discrepancy in the time response between kinetic and fluid result is again clear. The sheath potential in the kinetic simulation is dominated by the arrival of fast electrons at the target, and by the local T_e in the fluid case. When electrons heat up, their neutral ionisation increases, in turn raising the local ion flux. The absence of neutrals in the PiC simulations means that a proper comparison would require neutrals to be omitted from the SOLPS simulations, an exercise which has not been performed here.

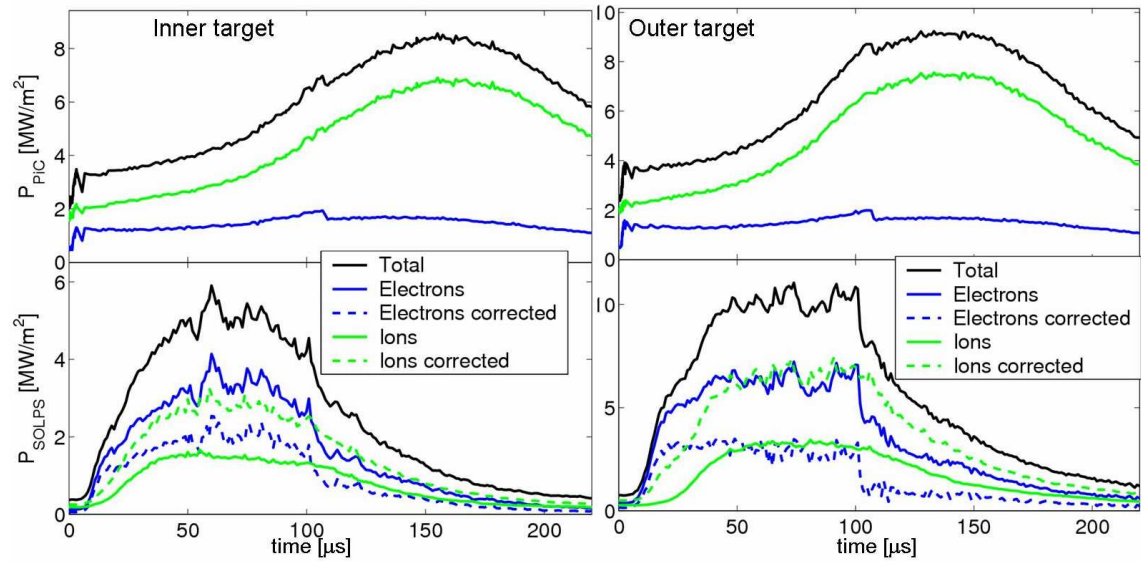


Figure 6.43. Time-dependent power fluxes on both targets from PiC (upper) and SOLPS (lower), with both corrected and uncorrected SOLPS results shown. The correction factor $eV_{\text{PIC}}\Gamma$ has been subtracted from electron power fluxes and added to ion power fluxes. Note that the total fluxes in both cases (PiC and SOLPS5) are in reasonable agreement

Another possible reason for the differences between the two codes is the simple assumption of zero parallel current ($j_{\parallel} = 0$) in the PiC simulations, whilst in SOLPS5 currents are allowed to flow from one target to another and are locally non-zero. The existence of a radial profiles of electron flux at the target in SOLPS5 attest to the existence of non-zero parallel currents included in the SOLPS5 sheath potential and thus also in the sheath heat transmission coefficient γ_e . **Fig. 6.45** shows that more ions or more electrons will be found at the target depending on radial location. Close to the strike point

electron particle fluxes much higher than ion particle fluxes, but deeper in the SOL the $\Gamma_e \sim \Gamma_i$.

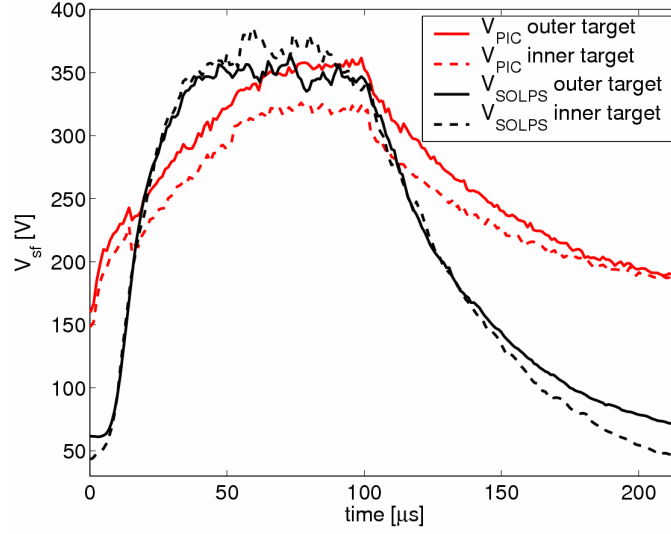


Figure 6.44. Time-dependent evolution of sheath potential drop V_{sf} from SOLPS and PiC at both targets (SOLPS $iy=14$).

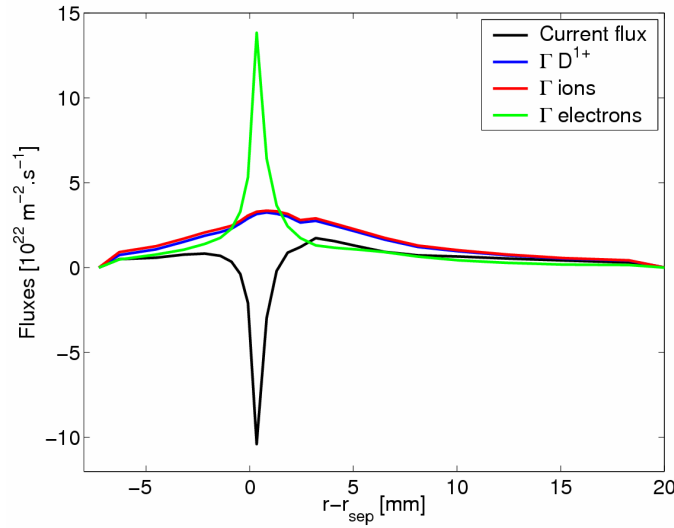


Figure 6.45. Outer target particle fluxes of electrons, ions and flux of current divided by electron charge from SOLPS simulation during the ELM. The electron particle flux profile (green) has shape strongly influences by presence of currents (black).

Apart from the distribution of the energy between electrons and ions, the most important is that the total fluxes in terms of absolute peak values agree for both kinetic and fluid simulations. This is very encouraging and confirming the agreement between SOLPS and IR measurements.

6.1.5.6.2. The influence of flux limiters

Turning to the second important discrepancy identified between the time dependent kinetic and SOLPS5 ELM simulations, namely the time evolution of the rise in ion and electron heat fluxes at the divertor targets, a partial resolution of the problem can be traced to the second group of kinetic factors playing role in the SOL parallel transport – heat flux limiters. As detailed in section 6.1.2, in all SOLPS5 simulations presented thus far the flux limiters have been fixed throughout the ELM cycle at 0.3 and 10 for electrons and ions respectively. In fact, without guidance from another source, there is no justified alternative but to choose the standard values employed for time independent simulations. Guidance is, however, now available in the form of the kinetic PiC simulations which in fact do demonstrate that the flux limiters are strongly time-dependent and change significantly during the ELM (the electron limiters even become negative). Very similar behaviour is also seen in the results of PiC simulations reported for larger ELMs at JET [235-236]. **Fig. 6.46** demonstrates this variation in the poloidally averaged values of the flux limiters from TCV Type III ELM PiC simulation.

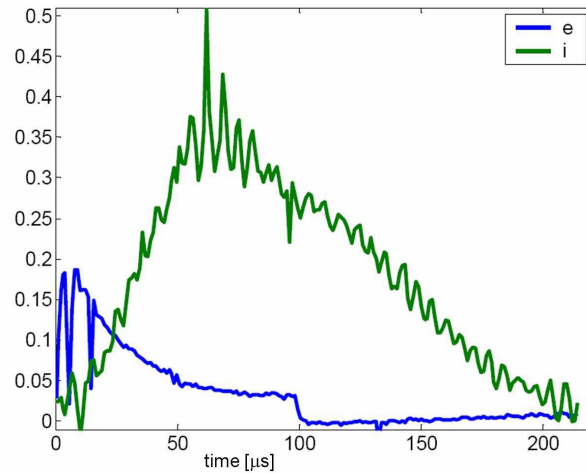


Figure 6.46 Poloidally averaged time evolution of the ion and electron flux limiters from the PiC simulation of the TCV Type III ELM. Supplied by Dr. D. Tshakaya).

To better understand the influence of flux limiters in SOLPS5, a sensitivity study, applying limiters in the range 0.01 – 10, was first performed on the steady state “diffusive” solution, followed by a similar exercise on the time dependent ELM. The first step confirmed that the behaviour of target energy fluxes in response to the flux limiter change was as expected before moving to the more complex time dependent case. Section 4.1.2.2 has already outlined how the flux limiters are expressed in SOLPS. Although they are applied everywhere on the SOLPS simulation grid, their effects are most obvious in regions with high parallel temperature gradients, $\nabla_{\parallel} T$ and hence elevated conduction heat fluxes (e.g. target vicinity) - usually in the last few poloidal cells. The extent of this effect depends on the strength of the flux limiting. In SOLPS this is performed such that the limited flux corresponds to the smaller of the two values from $Q_{SH} \sim \kappa_0 \nabla_{\parallel} T$, the Spitzer-Harm heat flux and a chosen fraction of the convected flux

$Q_{\text{lim}} \sim \alpha v_{\text{th}} nT$. The conducted heat flux in SOLPS reads as:

$$Q_{\parallel, \text{cond}, \text{SOLPS}} = \frac{1}{\frac{1}{Q_{\text{SH}}} + \frac{1}{Q_{\text{lim}}}} \quad (6.6)$$

Since $\kappa_{0,e} \approx 2000$ and $\kappa_{0,i} \approx 60$, Q_{SH} for the ions is about 30 times higher than that of electrons for equivalent temperature gradient. Additionally, since the ratio of the thermal electron and ion velocities is $v_{\text{th},e}/v_{\text{th},i} \approx 60$, Q_{lim} for electrons is 60 times higher than for ions (assuming $T_i \approx T_e$). Since electrons are more conductive, one needs to apply stronger flux limiters on electrons than on the ions, in order to see an effect on them [238]. It is very important to note, however, that energy balance must be maintained at all times so the final energy flux must correspond to the sources and losses in each part of the SOL. In the case of strong limiting (small values of $\alpha_{e,i}$), the code must therefore ultimately adjust the limited conductive heat flux by increasing it to the value corresponding to the constraints imposed by energy conservation. This can be done only by increasing the temperature in those areas where the flux limiting occurs. **Fig. 6.47** compiles the profiles of limiting measures, flm_e , flm_i , which represent the extent to which the Q_{SH} is limited and are defined as $Q_{\parallel, \text{cond}} = Q_{\text{SH}}/\text{flm}$. This means that for example, if $\text{flm}=1$, there is no flux limiting and $Q_{\parallel, \text{cond}} = Q_{\text{SH}}$ and if $\text{flm}=X$, then the heat flux corresponds to X^{-1} fraction of the Q_{SH} .

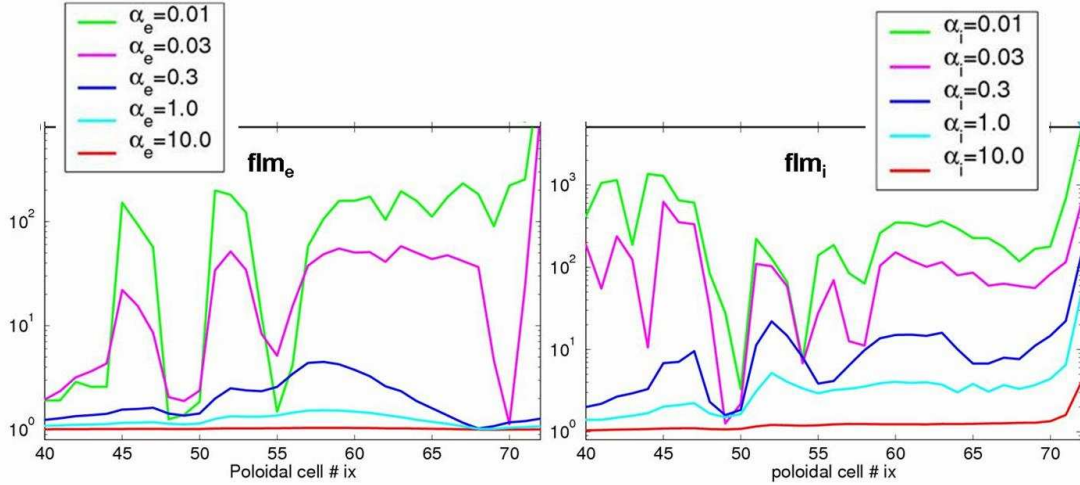


Figure 6.47. Pre-ELM poloidal profiles of the effect of the flux limiting expressed by flm_e , flm_i for the different values of flux limiting factors α_e, α_i in the range from 0.01 to 10.0. The poloidal cell $ix=72$ corresponds to the outer target and $ix=51$ to the X-point (at midplane $ix=36$).

Fig. 6.48 shows the poloidal profiles of the heat fluxes, including the convective, conductive parts and limited fluxes for the case with the strong ($\alpha_i=1$) and no ($\alpha_i=10$) ion flux limiting. In general, if $Q_{\text{lim}} < Q_{\text{SH}}$, the conductive part of the heat flux corresponds to

the fraction of convective heat flux ($Q_{\text{lim}} \sim \alpha_i v_{\text{th}} n_i T$). However, in the places where convection dominates, the flux limiting has no effect. It is also clearly seen that with strong flux limiting, the dominant fraction of the total heat flux becomes convective and in fact the SOLPS target heat fluxes in this cases are convective. On the other hand without flux limiting the situation is opposite ($Q_{\text{lim}} > Q_{\text{SH}}$) and the conduction dominates in target heat fluxes.

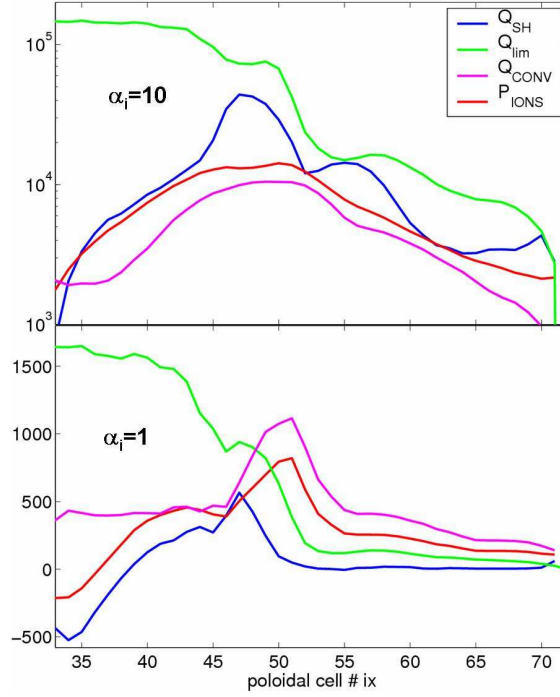


Figure 6.48. Comparison of poloidal profiles (from above midplane to outer target) of heat fluxes (given in W.m^{-2}) including Q_{SH} , Q_{lim} , Q_{CONV} and the actual SOLPS heat flux of ions, $P_{\perp i}$ (red) for the cases with ($\alpha_i = 1.0$) and without ($\alpha_i = 10.0$) flux limiting of ions.

To provide a similar sensitivity study for the time-dependent simulation, guidance was sought from the TCV PiC simulation shown in **Fig.6.46**. Inspired by the strongly changing flux limiters during the ELM cycle the original strategy was to include an approximation to the PiC values directly into the SOLPS5 code by adding new user subroutine. However, after tests performed with the time-dependent possibilities already included in the code (step-like ansatz during time from pre-ELM and ELM), it became clear that including greater complexity would not be necessary. When the same values of the flux limiters as indicated by PiC results are applied in SOLPS, namely $\alpha_{e,i} = 0.03$ for in the pre-ELM phase and $\alpha_e = 0.2$ and $\alpha_i = 0.4$ during the ELM, SOLPS5 does not reproduce the time-evolution of the target heat fluxes obtained from the PiC simulation. It is, however, necessary to take into account the uncertainty in the PiC values of flux-limiters introduced as a consequence of the poloidal averaging. Moreover, when the above mentioned simulation was compared with that in which $\alpha_e = 0.2$ and $\alpha_i = 0.4$ are fixed throughout the whole ELM cycle (including the pre-ELM phase), the same result is

obtained. This suggests that it is the ELM phase which dominates with regard to the appropriate choice of flux limiters.

With the above findings in mind, a sensitivity study to flux limiters for the time dependent problem has been performed in the same way as for the steady state: flux limiters are fixed throughout the ELM cycle, but varied from simulation to simulation in the range 0.03 - 10.0. To get closer to the PiC time evolution required in fact rather strong flux limiting; best results were obtained for $\alpha_e = 0.5$ and $\alpha_i = 1.0$. This is nicely seen in **Fig.6.49** where the PiC data are compared with the SOLPS power fluxes. The time-delays of ion power fluxes seen at both targets are very similar in both cases, from SOLPS $\sim 130 \mu\text{s}$ and $\sim 140 \mu\text{s}$ at inner and outer target respectively compared to $\sim 160 \mu\text{s}$ and $\sim 140 \mu\text{s}$ from PiC. It should be also noted, that power fluxes at the target are slightly lower than before (as seen on **Fig.6.39** and **Fig.6.40**).

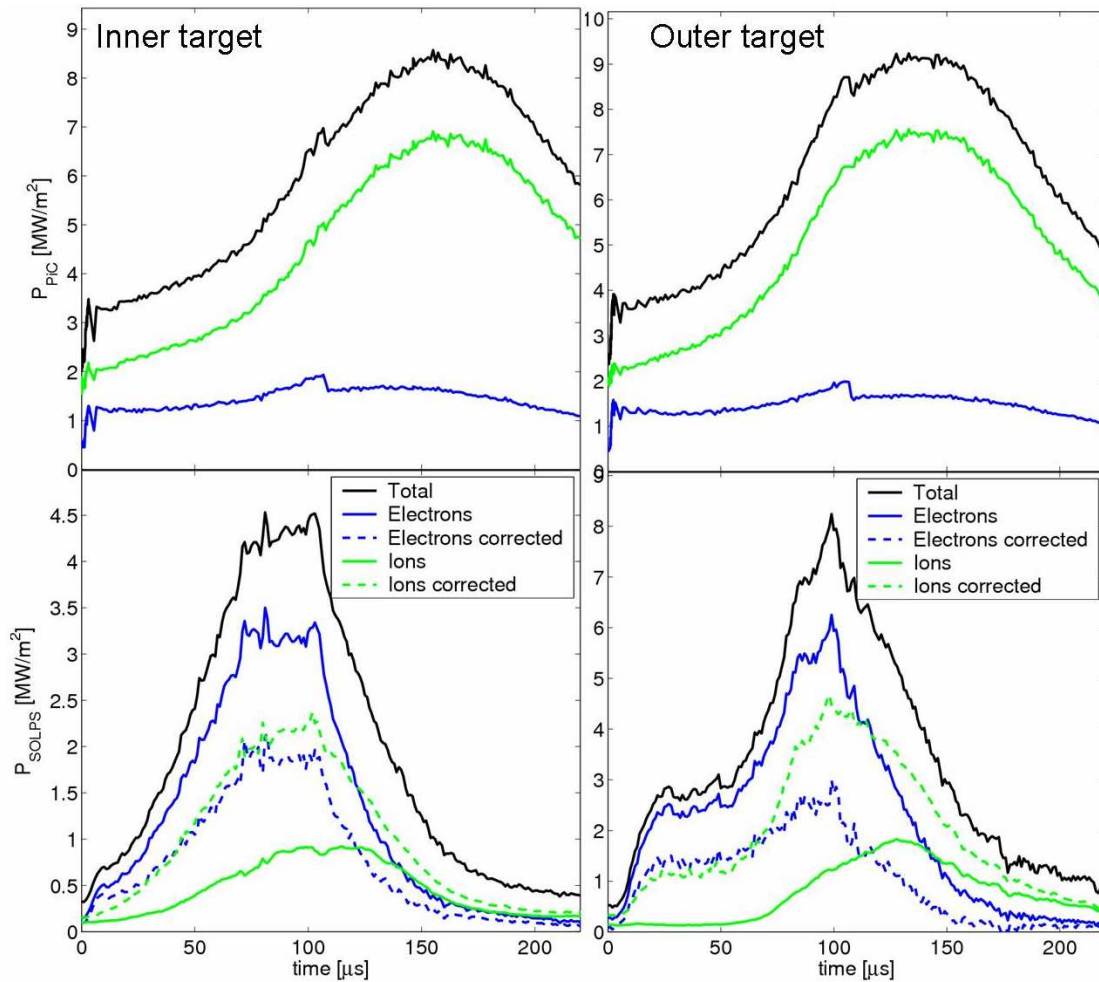


Figure 6.49. Time-dependent target power fluxes compared from PiC and SOLPS with flux limiting of $\alpha_i=1.0$ and $\alpha_e=0.5$. Plotted also the SOLPS fluxes with correction $\text{Corr} = eV_{\text{PIC}}\Gamma$ as in **Fig. 6.43** (dashed lines). Simulation #26094.

Without the flux-limiting SOLPS assumes thermal conduction leading to diffusive transport problem (particle transport equation is limited to the Fick's law). On the other hand the kinetic code solves the ballistic problem in low-collisionality when transport is convection dominated. If flux limiters are applied, parallel heat transport becomes convective and the particles behave ballistically. Obvious solution appears to be, that the flux-limiting applied to electrons and ions, would be such, that both would behave ballistically. The best solution giving the same time delays as PiC simulations was obtained with the flux limiters $\alpha_i = 1.0$ and $\alpha_e = 0.5$, agreeing with the qualitative argument above that electrons need to be limited stronger to feel the limiting effect.

Convection-dominated regimes where the heat flux is limited yield the longer delays in the arrival of ions at the targets. Similar results are seen in the detached regime when the heating mechanism is the convective heat transport into the divertor [17]. In this case the transport happens on much slower time-scale (ion convection) than the very fast timescale of electron heat conduction. This extends considerably the time over which the ELM produces changes in the heat load for the detached divertor leg. This applies also on comparison of PiC and SOLPS with the different flux limiters. The convective time scale for the energy transport is:

$$t_{\text{conv}} = \frac{L_{\parallel}}{v_{\text{th}}} \quad (6.7)$$

The conductive time scale reads as [239]:

$$t_{\text{cond}} \sim \frac{t_{\text{conv}}}{t_{\text{coll}}} \cdot t_{\text{conv}} \quad (6.8)$$

where t_{coll} is the collision time. Since the ELM $t_{\text{conv}}/t_{\text{coll}} < 1$ one gets $t_{\text{cond}} < t_{\text{conv}}$ and longer delay in the arrival of ion pulse to the targets is observed [241]. When no flux limiting is used, energy flux tends to be more conductive, and the arrival of ions occurs on the shorter conductive time scale than in PiC (where the ELM energy transport is of convective nature). Therefore without flux-limiters in SOLPS it was impossible to see the similar time signature on the ion target heat flux as it was seen in the results from kinetic PiC simulations.

Even though the time-evolution of SOLPS particles and heat fluxes depicted by solid lines in **Fig.6.49** is closer to those from PiC, it is still necessary to apply the corrections corresponding to the sheath heat potential barrier which is inherently included in the PiC and only set as boundary in SOLPS (see the corrected dashed lines in **Fig.6.49**). It is impossible to correct the SOLPS contributions of ions and electrons to fit the time-dependent PiC profiles so that the shape of time-evolution of SOLPS total flux (especially the relaxation phase of the ELM cycle) remains the same after such a correction. While in PiC the shape of total flux is dominated by the flux of ions, in SOLPS it is by the flux of electrons and therefore the SOLPS total heat flux develops always on the electron time scale. So even when with flux limiters one gets closer to the PiC time dependence (delays), the problem of power sharing between electrons and ions compared with PiC remains unresolved. This is an indication, that the origin of the discrepancy must involve other elements. It appears that the correction using flux limiting

is not the whole story and probably something more fundamental is incorrect with the SOLPS ELM description. Resolving of this issue would represent an important contribution to the insights of the benchmark between kinetic and fluid simulations (and experiment). However, until the understanding of it is not found, the SOLPS5 cannot be used predictively for ITER.

6.1.5.7. Energy analysis

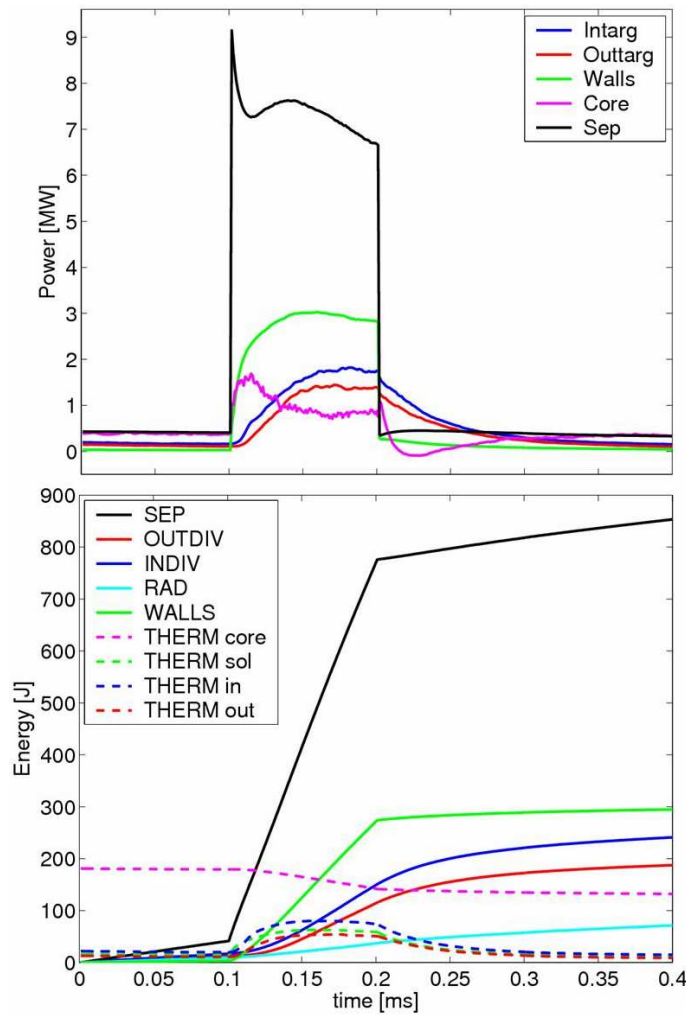


Figure 6.50. *Upper:* SOLPS powers crossing the boundaries during the ELM cycle, including the power crossing the separatrix. *Lower:* energy obtained from integration of the powers shown in the upper pane. Energy expelled through the separatrix corresponds to the drop in the W_{plasma} as indicated on **Fig.6.37**. This $\Delta W_{\text{ELM}} \sim 700 \text{ J}$ is found as a sum of E_{DEP} , E_{WALLS} , ΔE_{therm} and E_{RAD} .

Fig.6.37 shows the time evolution of the energy stored in the plasma for SOLPS5 compared with experimental data from W_{dia} for the reference Type III ELMing discharge. A correction of ~ 25.6 kJ is required on the SOLPS values to account for the fact that the simulation grid does not encompass the plasma core, where most of the plasma energy resides. The energy expelled by the ELM is very nicely reproduced and gives about $\Delta W_{\text{ELM}} \sim 700$ J.

Fig.6.50 compiles the powers crossing the SOLPS5 boundaries together with the integral of these powers to produce the energy in each component throughout the ELM cycle ($t_{\text{ELM}} = 100$ μs). The energy balance is again as in pre-ELM part very good. It is interesting but unlikely corresponding to the reality that the biggest part of this energy ($\sim 43\%$) is found on the walls ~ 280 J, slightly higher than the energy recovered at the divertor targets: ~ 220 J ($\sim 34\%$). The energy radiated during the ELM represents only 3% of the total (20 J). The missing 130 J comes from the increase of the thermal energy in the SOL part of the grid including the divertor legs. **Fig 6.51** shows the time and space dependence of power loads on the divertor targets over the full ELM cycle. The energy deposited on inner target ($\sim 130\text{J}$) is higher than at the outer ($\sim 100\text{J}$) as observed in the pre-ELM phase. This is to be expected given the lack of any drift physics in these code runs.

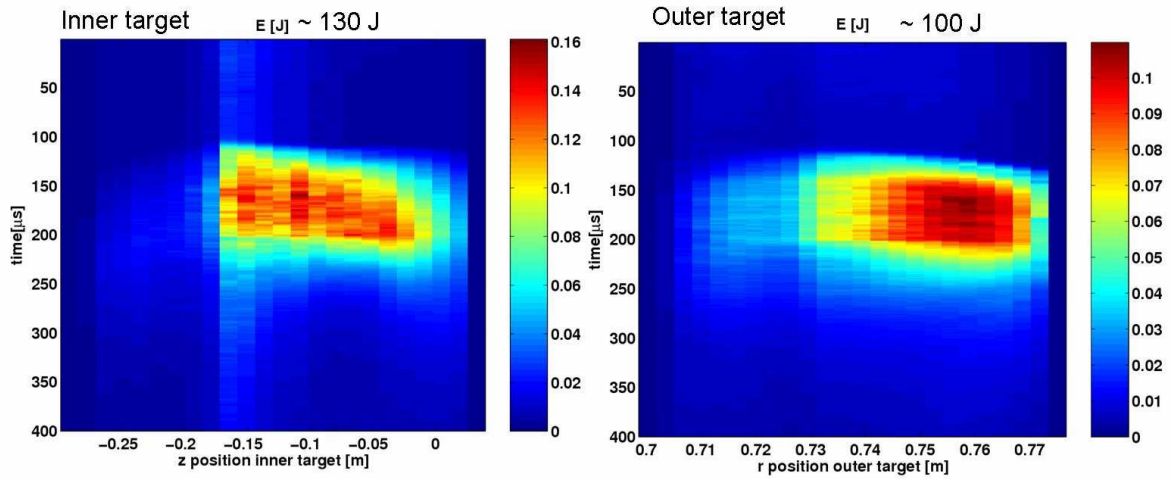


Figure 6.51. Time and space dependent evolution of the energy deposited at the targets during the ELM cycle. $E_{\text{DEP,OUT}} \sim 100$ J and $E \sim 130$ J.

One important area in which more code-experiment comparison is urgently required is that of edge radiation, which plays a critical role in power exhaust, particularly in tokamaks with high first wall surface coverage with graphite (such as the devices considered in this thesis).

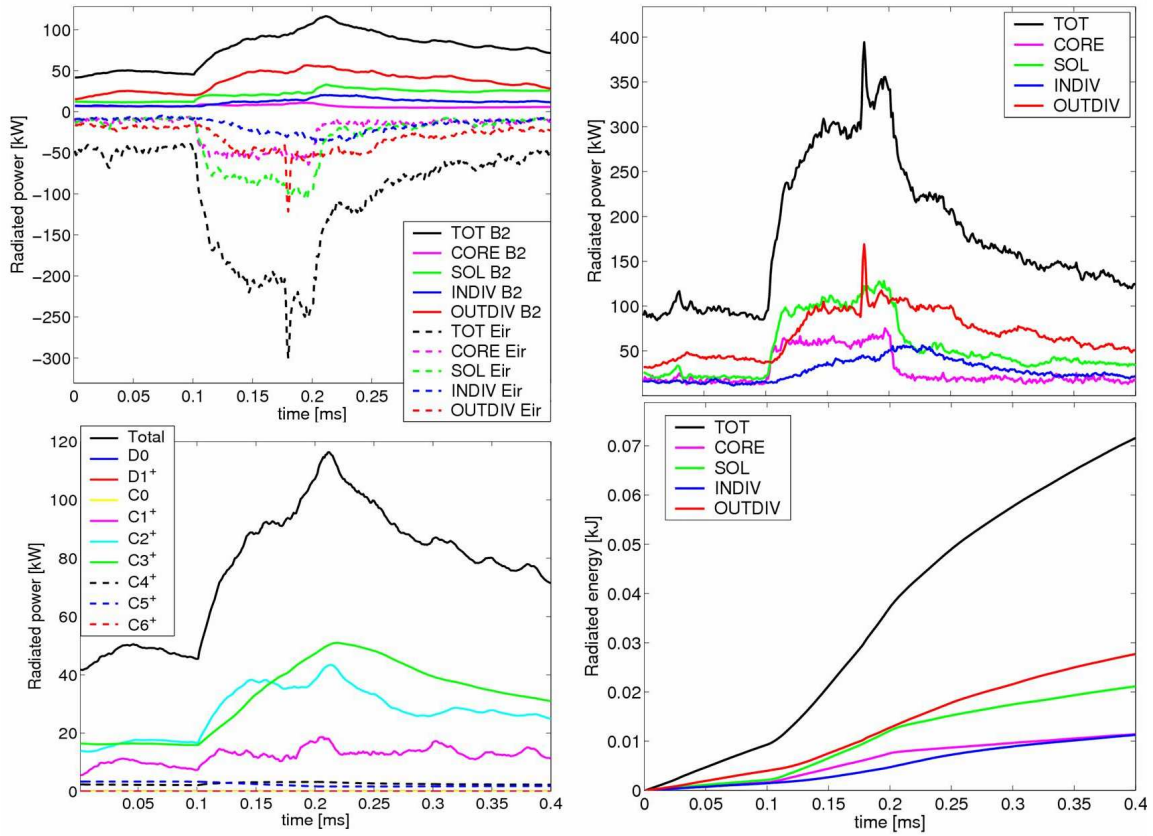


Figure 6.52. *Left upper: SOLPS radiated powers from photons (B2.5) plotted as positive and from neutrals (EIRENE) plotted as negative (for clarity only). Left lower: B2.5 radiated power as a sum of the contributions from the species. Right upper: radiated power in different regions of plasma. Right lower: energy radiated in those regions. "Diffusive ELM"*

The **Fig. 6.52** compiles a variety of information relating to the simulated radiation dynamics during the ELM. In contrast to the steady state case, the radiation from neutrals is about factor ~ 2 stronger than from the photons during the ELM. The largest fraction of the photonic radiation comes from C^{3+} , C^{2+} and C^{1+} . The total photonic radiated power only ~ 20 J during the $100 \mu s$ ELM duration. However, it should be taken into account that radiation evolves on a longer timescale to allow for the transfer to the higher ionization states. If one integrates the radiated power over the longer timescale much more radiated energy is obtained (for example ~ 150 J during 1 ms). As shown in the 2-D distributions of **Fig. 6.53**, most of the radiation is found in the divertor legs. About twice as much is released in the outer divertor leg than from inner divertor leg. This is in accordance with the results of deposited power, since the different radiation losses lead to different parallel heat conduction towards each target and enhanced radiation always results in the smaller peak of the heat load on the target [17].

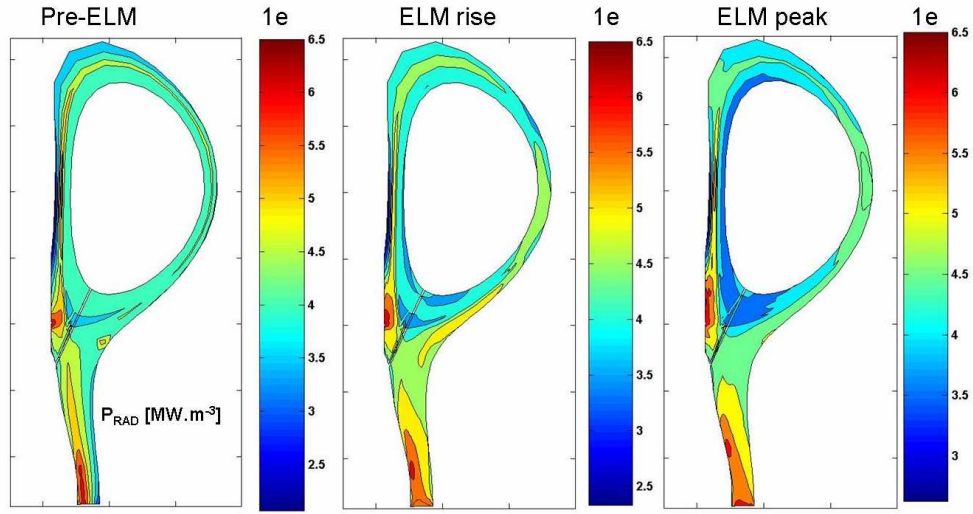


Figure 6.53. Radiated power density from SOLPS at three stages of ELM cycle, pre-ELM, ELM rise and ELM peak. Most of the radiation is found in the divertor legs.

The quality of the experimental bolometry data during the Type III ELM event was unfortunately not good enough to provide the time-dependent radiation evolution. However, the experimental radiated power from discharge #31835 (similar to #26730) supplied by B. Tal (HAS) averaged through all the ELMing part of the discharge (including inter-ELM and ELM phases) is found to be ~197 kW. This is rather well matched with the averaged value of radiated power during the simulated ELM cycle ~200kW.

6.2. Type I ELMing H-mode at TCV

Experiments at TCV with high power ECRH at the third harmonic (118 GHz) have produced large, probably Type I ELMs, on TCV for the first time [240]. There are still not many successful discharges of this type at the time of writing, but these ELMs typically exhaust $\sim 2\text{-}10$ kJ of the plasma stored energy (12-20 %) with $f_{\text{ELM}} \sim 50$ Hz. It still has not been possible to unambiguously classify the large ELMs as Type I, but it seems likely that their appearance at high powers above the L-H transition threshold qualifies such a classification.

The most important ELM-related parameters compared with those of other ELMs modeled in this thesis are summarized in **Tab 3.1** and the parameters of the discharge with these Type I ELMs can be found in **Tab 5.2**. This section presents briefly a simulation of a typical ELM from discharge #32713. The quality of the data from this discharge is not as high as for the Type III ELM on TCV, for which a great deal of experience has been gathered over the years (the ohmic H-mode on TCV has been widely studied due to its easy accessibility).

Fig. 6.54 compiles the time traces of few important plasma parameters. Although the magnetic equilibrium (see **Fig.6.54**) and density ($\bar{n}_e \approx 5.5 \times 10^{19} \text{ m}^{-3}$) are very close to the previously modeled Type III ELM discharge, the other parameters are very different. While #26730 (section 6.1) is an ohmic H-mode, pulse #32713 is additionally heated with X3 power from 2 gyrotrons (1 MW) so that $P_{\text{IN}} \sim 900$ kW, of which 300 kW is ohmic power and ~ 600 kW is absorbed ECRH power.

An attractive feature of the simulation of this discharge compared with the Type III case is the opposite sign of the plasma current ($I_p = -370$ kA) and toroidal magnetic field ($B_\phi = -1.43$ T), giving an ion $\vec{B} \times \nabla \vec{B}$ drift direction towards the X-point (FWD field). This is of particular interest with respect to in-out divertor target asymmetries and the possible effects of the drifts (which, in common with the Type III case, are not included in the simulations) As for the ELM itself, the energy, $\Delta W_{\text{ELM}} \sim 3$ kJ represents 12% of the plasma stored energy which is ~ 10 times more than small Type III ELM ($\sim 2.5\%$) and the ELM frequency is 4 times lower.

One advantage of these particular large ELM discharges is the availability of fast AXUV bolometry data (e.g. from #33563), allowing tomographic inversion of the radiated power on the ELM timescale (even if the absolute value of the total radiation cannot be derived from the AXUV system (see section 5.2.1)). Such data was unfortunately not available for the Type III H-modes. Unfortunately, however, the X3 heated discharges lack the good pedestal profile data obtained for the ohmic H-modes and have very little target profile data. Only using the best possible data extracted from several similar, but not identical discharges, can the simulations be reasonably constrained. The data from several similar discharges #32711-#32725 have therefore been used to produce the upstream n_e and T_e profiles from core and edge TS systems. These are the only data available to constrain the code upstream – no reciprocating probe data can be obtained in these much higher power shots. At the targets only very few LP measurements are available, including from some very recent repeat discharges (e.g. #37968), fast thermography data from an upgraded outer target viewing IR system.

Due to the lack of the experimental measurements to constrain the code properly at the targets, the exercise reported in this section represents only preliminary. However, it might be compared with the data which will become available in the future.

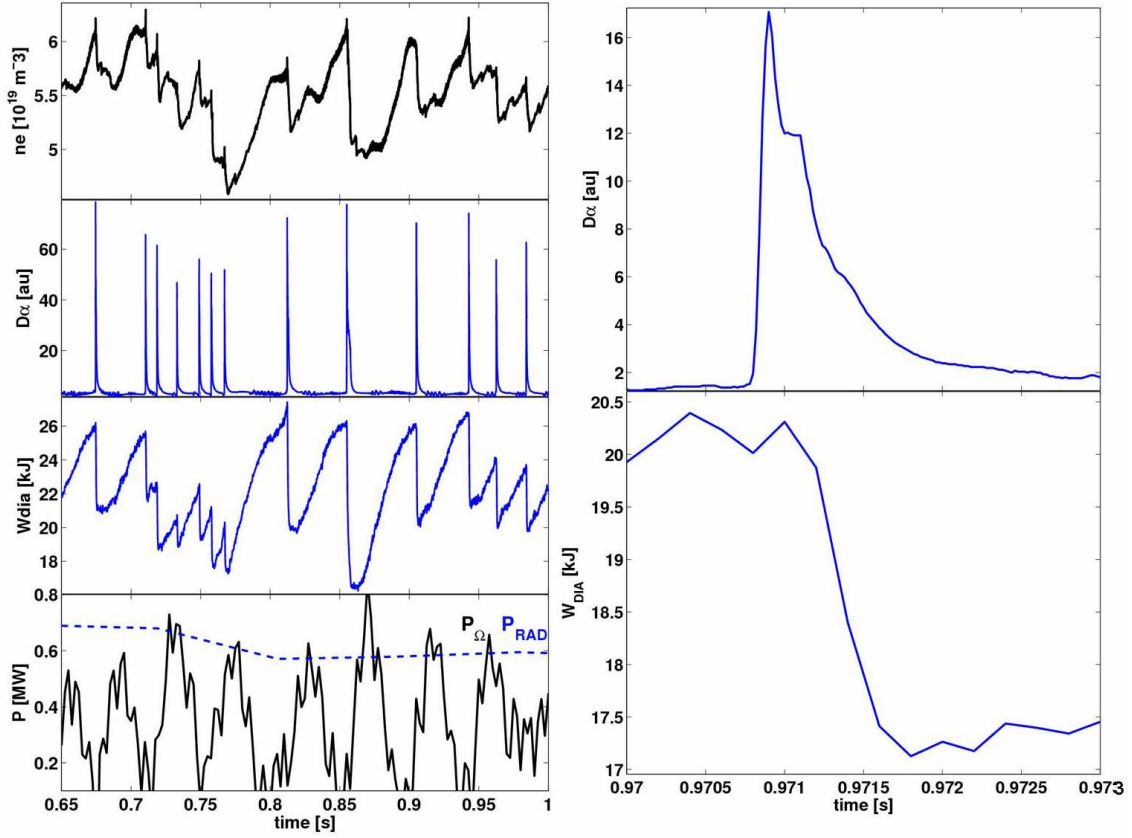


Figure 6.54. Left: selected time traces of plasma signals from the TCV Type I ELM-ing discharge #32713 simulated in this section. The pulse is characterised by ELMs of varying amplitude in the range $\Delta W_{ELM} = 2\text{-}10$ kJ. Right: wide angle D_α line of sight (see Fig. 5.5) and energy expelled by an ELM from a pulse for which good bolometry data are available (#33563, identical to #32713); $\Delta W_{ELM} \sim 3$ kJ.

6.2.1. Settings

The basic settings are the same as for the first simulations of the Type III ohmic H-mode #26730 in Section 6.1. For this higher power discharge, the energy crossing the inner grid boundary is estimated as $P_{SOLPS} = P_\Omega + P_{ECRH} - P_{RAD,CORE} = 300 + 600 - 150 = 750$ kW (distributed equally between electrons and ions), the midplane separatrix density is fixed at $n_e^{sep} = 2 \cdot 10^{19} \text{ m}^{-3}$, $\Delta W_{ELM} \sim 3$ kJ and the ELM duration, $t_{ELM} = 200 \mu\text{s}$ (approximately estimated from data on Fig. 6.54). None of the sensitivity studies described in the previous sections for the smaller ELM have been repeated here. The default values of all the settings summarized in section 6.1 are used throughout this section (e.g. flux limiters, transmission coefficients etc).

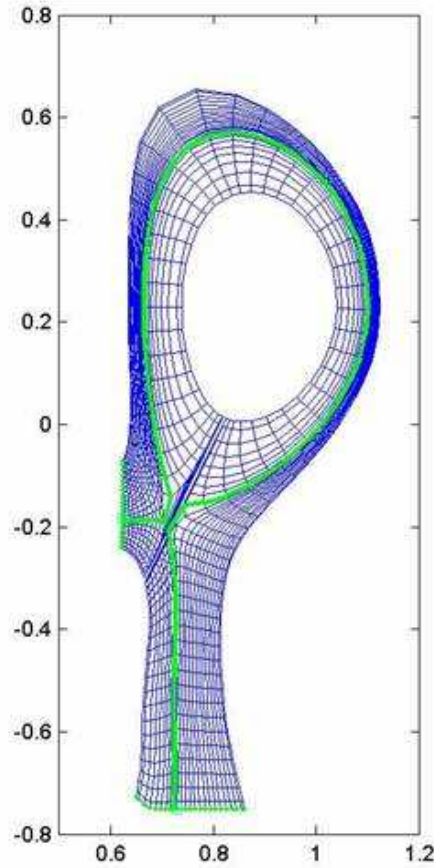


Figure 6.55. Grid used for the simulation of the TCV discharge #32713 and Type I ELM; the green line denotes the separatrix contour. Note that compared to the case of Type III ELM, this one has much bigger flux expansion at outer target (here the flux expansions are about the same at both targets).

The simulations of the TCV discharge # 32713 have been performed on the grid on **Fig. 6.55** which differs from the previously described grid only by the magnetic equilibrium used to reconstruct it. **Fig. 6.55** illustrates the simulation grid, extracted from #32713. It is similar to that used for the Type III ELM (#26730) differing slightly in outer target flux expansion and having a larger X-point to HFS wall separation. The radial extent of the grid is 3.7 cm inside and 0.6 cm outside of the midplane separatrix. A greater radial depth inside the separatrix has been used to ensure that sufficient plasma volume is available to adequately source the pedestal regions following the ELM crash.

6.2.2. Simulation of Type I ELMing H-mode at TCV

Following the example of the simulations of Type III ELM, the same strategy and modelling technique were employed for the simulation of Type I ELM here. A converged, pre-ELM solution was first obtained using “diffusive” approach, radially varying the D_{\perp} and χ_{\perp} coefficients while assuming $\chi_{\perp e} \approx \chi_{\perp i}$ and keeping $v_{\perp}=0$. As usual, the TB was switched off in the divertor legs and constant values of $1 \text{ m}^2 \cdot \text{s}^{-1}$ for both D_{\perp} and χ_{\perp} applied in the SOL. The good upstream match shown in **Fig. 6.56** was obtained after some optimisation. Interestingly, $D_{\perp} \sim 0.2$ and $\chi_{\perp} \sim 0.07 \text{ m}^2 \cdot \text{s}^{-1}$ are required to match the profiles for this larger

ELM, whilst for the smaller Type III instability, the opposite combination was found to be optimum (namely higher $\chi_{\perp} \sim 0.2 \text{ m}^2 \cdot \text{s}^{-1}$ and lower $D_{\perp} \sim 0.065 \text{ m}^2 \cdot \text{s}^{-1}$)

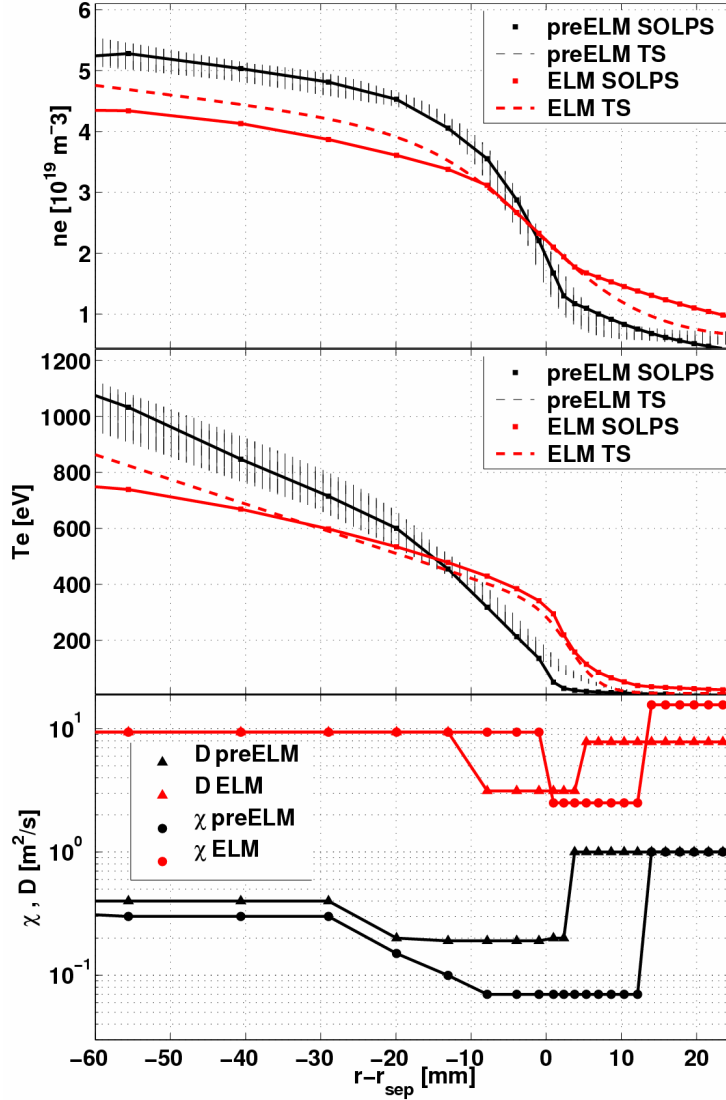


Figure 6.56. Upstream n_e , T_e profiles from TS and SOLPS5 for pre-ELM (black lines) and ELM peak (red lines) for an X3 heated H-mode. TS pre-ELM data represented by the black vertical lines represent the compilation of several profiles acquired in steady state periods between Type I ELMs in discharges #32711 - 32713. The ELM peak profile measured by TS (red dashed line) represents the data during one single transient event, e.g. ELM peak from discharge #32711 for which the best data at the ELM peak (estimated from D - α signals on **Fig.6.54**) were obtained. The lower panels show the pre-ELM (black) and ELM (red) transport coefficients D_{\perp} (triangles), $\chi_{\perp,i}$ (circles). Simulation number #29808.

This converged pre-ELM solution provides the starting point for the time dependent ELM simulation with time step $\Delta t = 10^{-6} \text{ s}$. **Fig 6.56** also shows the upstream profiles of n_e and T_e resulting from the ELM simulation for an increase of D_{\perp} and χ_{\perp} only during the ELM. These were elevated by factors of ~ 15 and ~ 35 for D_{\perp} and χ_{\perp} respectively across the full LFS poloidal extent (cells 20-48) centered on the LFS midplane using a Gaussian poloidal profile

with strength $S=15$. The inter-ELM profiles represent the compilation of many carefully selected steady-state profiles, whilst the ELM profiles are data from a particular ELM in pulse #32711 expelling $\Delta W_{\text{ELM}} \sim 3\text{kJ}$ of energy, acquired at the time of the peak of this ELM (in the D_α signals as shown on **Fig.6.54**).

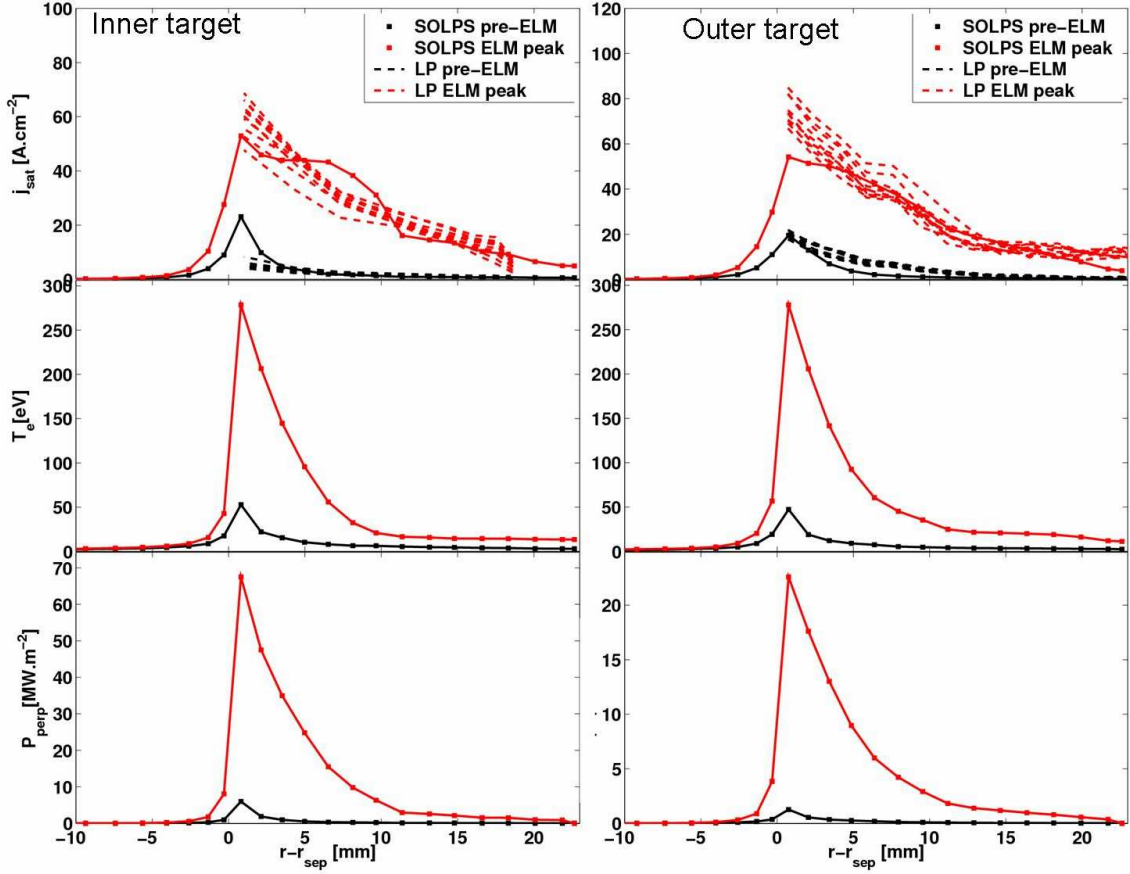


Figure 6.57. Pre-ELM (black) and ELM (red) target profiles of j_{sat} , T_e and P_\perp from SOLPS simulation. Experimental j_{sat} profiles from LP are shown for both pre-ELM and ELM of discharge #37968, repetition of #32713.

Fig. 6.57 compares the pre-ELM and ELM SOLPS and experimental profiles from LP at both targets. Voltage sweeps were not used in these discharges so that T_e cannot be derived from. Instead, a fixed negative bias was applied to the probes to allow fast acquisition, on the ELM timescale, of the ion particle flux. In any case, if the SOLPS5 simulations of the target T_e profiles in **Fig. 6.57** are correct, voltage sweeping would not have yielded useable data in the key area of interest (the strike point) as a consequence of the high local T_e which would have been beyond the probe voltage sweep capacity. The experimental data shown here are obtained from discharge #37968, a close repetition of #32713. The good upstream agreement with the TS is also found in the ion target flux profiles.

The code-predicted power flux on the inner target is higher than on outer target during both the steady state and ELM phases. This is in contradiction to the Type III ELMing case simulated in previous section (see **Fig.6.28**). The obvious reason for this is the difference in the flux expansions between two equilibriums especially at the outer target. While the Type III ELM case in section 6.1. has much higher flux expansion at inner target compared to outer,

the profile of the power flux is smeared out and thus the peak is lower there compared to the outer target even if the total deposited energy is by 30% higher at inner target. As it can be seen on **Fig. 6.55** the flux expansions at both targets are very similar for the case of Type I ELM analyses in this section. Therefore logically, the ratio in profile peak amplitudes corresponds to the ratio in the deposited energies.

6.2.2.1. Energy analysis

Fig.6.58 describes the code energy balance during the ELM cycle in an analogous manner to **Fig. 6.50** for the Type III ELM. During the pre-ELM phase, of the 750 kW injected into the simulation grid $\sim 65\%$ (480 kW) arrives at the targets, $\sim 18\%$ (150 kW) is radiated and, unlike the Type III ELM case a very low fraction leaves the outer grid boundary. This is to be expected since the SOL is wider in this simulation and the T_e is higher, making parallel conduction much more effective. As already indicated on **Fig.6.57**, the code predicts more power deposited on inner target, with a pre-ELM asymmetry of $P_{in,dep}/P_{out,dep} \sim 1.7$. The integrated energy through separatrix over the ELM duration of 200 μs amounts to $\Delta W_{ELM} \sim 3$ kJ, corresponding to the experimental plasma stored energy drop during the ELM event (**Fig.6.58**).

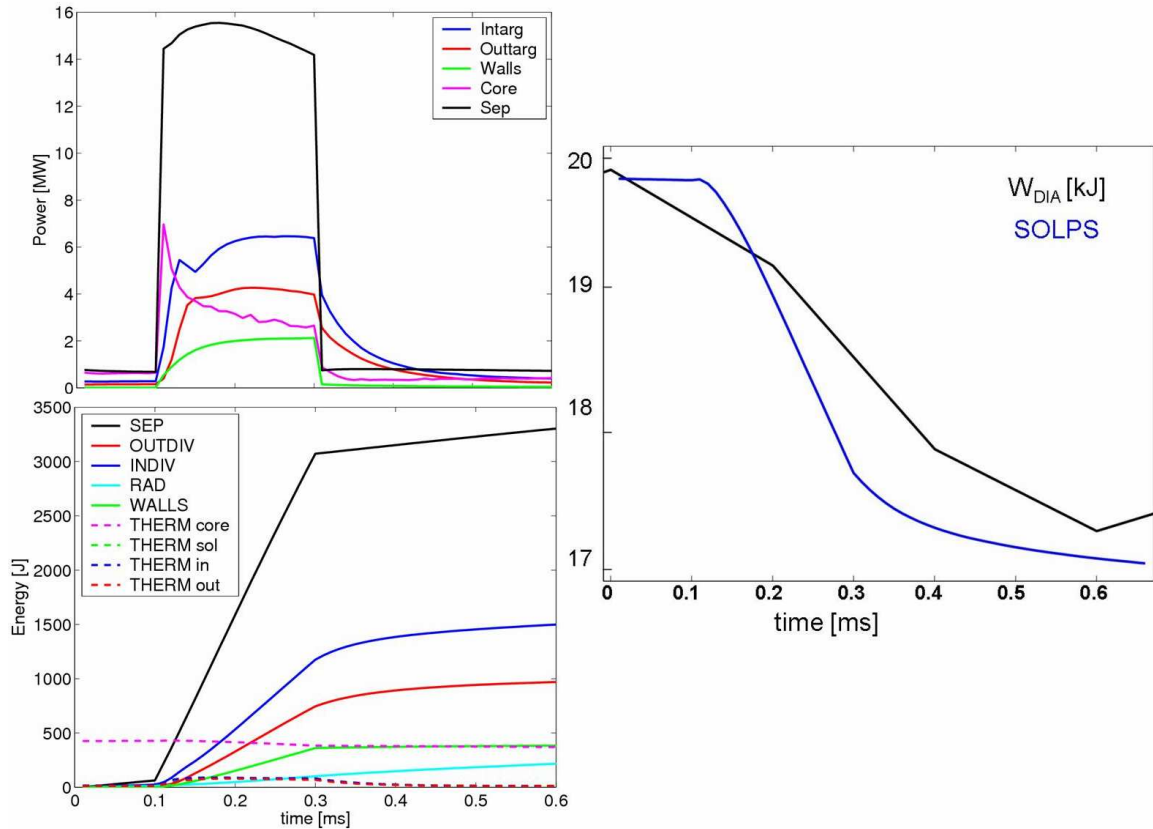


Figure 6.58. *Left upper:* SOLPS time-dependent profiles of power crossing the boundaries including the power crossing separatrix. *Left lower:* energy through the boundaries and separatrix, radiated energy and thermal energy integrated over the ELM cycle. *Right:* measured plasma stored energy from single ELM in discharge #33653 (black) compared with SOLPS (blue), corresponding to the $\Delta W_{ELM} \sim 3$ kJ obtained from the simulation.

Unlike in Type III ELM simulation, the majority of the Type I ELM energy in this simulation is deposited on the divertor targets ~ 1900 J ($\sim 63\%$) and ~ 400 J ($\sim 13\%$) leaves the outer grid boundary. The energy radiated during the ELM represents a very small fraction 3% (100 J), the same as in Type III ELM simulation suggesting very hot plasma edge. The in-out energy deposition ratio on the targets $E_{\text{in,dep}}/E_{\text{out,dep}} \sim 1.7$ is unchanged compared with the pre-ELM power asymmetry. It can be concluded that on both TCV ELMs one sees the in-out target power deposited asymmetry favouring the inner target. It is clear, that without drift effects there is no effect in SOLPS to the sign of the magnetic field and thus it is not surprising that the same asymmetry is observed in both REV and FWD field cases. As it will be reported in chapter 7, the situation is opposite for JET simulations, where the in-out asymmetry favouring outer target is found. The plausible explanation for this opposite asymmetries predicted by code at TCV and JET is the difference in the geometry of these two machines. As it was explained in chapter 5 (see **Tab. 5.2**) at TCV the connection length to inner target is ~ 14 m and to outer target ~ 18 m, what means that the inner target is closer to the midplane (the ELM source). At JET the parallel connection length to outer target is about 2 times shorter (~ 45 m) than that to the inner target (~ 80 m), what is in line with the code prediction of more power is deposited at outer target (see chapter 7). In purely kinetic situation, of course, the connection length would not play a role in the energy deposition but only in the time delays of plasma arrival to the targets. However, in SOLPS being fluid code the connection length can drive the in-out power deposition asymmetries. The indication of this is also the fact that the ratio of in-out deposited power is stronger in the Type I case where the ELM has been launched from the bigger poloidal extent with the source center somewhat closer to inner target compared to the Type III ELM.

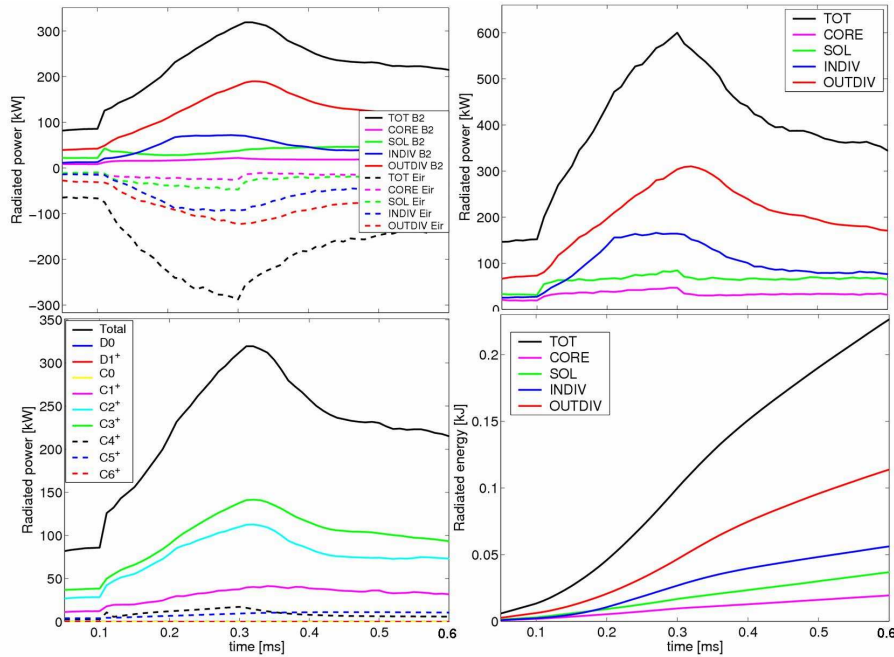


Figure 6.59. *Left upper:* SOLPS radiated powers during the ELM cycle from photons (B2.5) plotted as positive and from neutrals (EIRENE) plotted as negative (for clarity only). *Left lower:* B2.5 radiated power as a sum of the contributions from the fuel and impurity species. *Right upper:* radiated power in different regions of the plasma. *Right lower:* energy radiated in those regions.

Unfortunately, no measurement exists to constrain the code results in the time of writing and therefore all the attempts to reason the behaviour found by the code are only speculations. More on the issue of the in-out target power asymmetries can be found in the section 6.3.

Analogous to **Fig. 6.52** for the Type III ELM, **Fig. 6.59** illustrates the radiation dynamics in the X3 heated, large ELM simulation. Unlike in the Type III ELM case, neutrals radiate as much as photons during the larger ELM. It appears that the radiated power from impurities goes with the amplitude of the ΔW_{ELM} , since the peak of the power for Type I $\sim 300\text{kW}$ and for Type III $\sim 120\text{kW}$ gives roughly ratio ~ 3 , corresponding approximately to the ratio of ΔW_{ELM} of these 2 ELMs. Like the smaller ELM, most of the radiation comes from the lower charge states of carbon: C^{3+} , C^{2+} and C^{1+} . Of the total radiated energy ($\sim 100\text{ J}$) during the ELM cycle, most is found in the divertor legs (**Fig. 6.60**), with about twice as much from the outer than the inner leg (as seen in the case of Type III ELM). This is probably due to the fact that there is more volume in the outer target leg and particles spend more time spiraling down the longer connection length.

Since the impurities are transported over longer time scale roughly corresponding to the divertor plasma residence time (possibly estimated from D_α signals), the radiated power should be integrated over longer time than $200\text{ }\mu\text{s}$. For example during 1 ms , the radiated energy predicted by SOLPS is $\sim 350\text{ J}$.

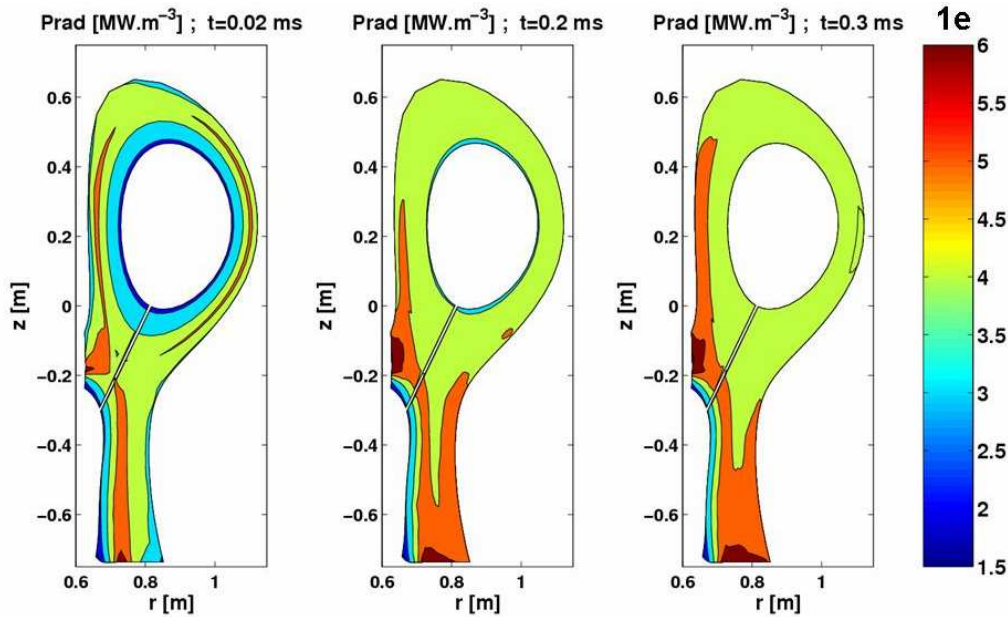


Figure 6.60. Radiated power density from SOLPS at three stages, pre-ELM, ELM rise and ELM peak. Most of the radiation is in divertor legs.

Fig.6.61 shows the radiated power from the TI of data from bolometers during the simulated discharge #32713 in different regions of plasma. The radiation from foil bolometers can be used only for the average, inter-ELM radiation. Very low time-resolution of $\sim 0.1\text{s}$ allows only for the estimates of radiation averaged over the ELM cycle. It should be reminded that about 150kW of $P_{\text{RAD,CORE}}$ has been already subtracted from P_{SOLPS} and therefore the values on **Fig.6.61** are expected to overestimate the SOLPS averaged over ELM cycle. The total radiated power is about 600 kW , the $P_{\text{RAD,BELOW}}$ part corresponding approximately to outer divertor leg shows radiation of $\sim 300\text{kW}$, and the $P_{\text{RAD,OUT}} - P_{\text{RAD,BELOW}} \sim 150\text{ kW}$

represents approximately the radiation in inner divertor. All these values roughly match the radiated power observed from SOLPS during the ELM rise, however the values from code are slightly lower. The observed ratio of $P_{in,rad}/P_{out,rad} \sim 0.5$ is well reproduced by the code.

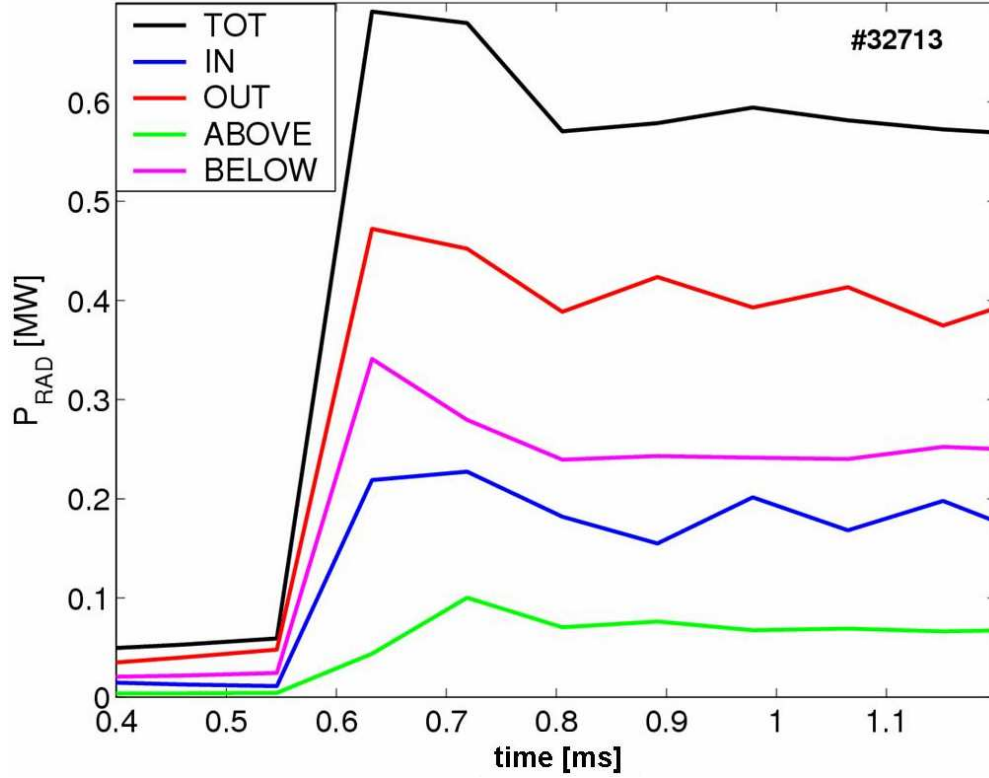


Figure 6.61. Radiated power from foil bolometers in different regions of the plasma throughout the discharge #32713 (analogy with **Fig.6.16**). “IN” stands for inside the separatrix, “OUT” stands for outside the separatrix, “BELOW” and “ABOVE” means the radiation below and above the main plasma. One can also assume that $P(IN)=P(CORE)$; $P(OUT)-P(BELOW) \sim P(\text{Inner divertor})$; $P(BELOW) \sim P(\text{Outer divertor})$.

Unlike the Type III ELM pulses, during several of the X3 heated discharges, some data from the high time and space resolution AXUV camera system are available. The AXUV diode signals were digitized at 250 kHz giving the time-resolution of $4\mu s$ allowing comparison of the radiation from the B2.5 part of the SOLPS code during the ELM cycle (since AXUV are not sensitive to non-photonic radiation). A detailed analysis of this radiation for discharge #33563 has been published in [241]. The time-evolution of the AXUV radiated power for the coherently averaged ELM from tomographic inversion (TI) is shown in **Fig. 6.62**, along with a comparison of the radiated energy corresponding to this power and the measured ELM energy drop for an ELM similar to the one modelled here with SOLPS. As much as 30% of the radiation is seen in the ELM rise phase and is localized in the outboard midplane, indicating that this early phase radiation occurs as a result of filament impact at the vessel walls [241]. The SOLPS time traces of radiated power are similar. A low fractional energy loss due to the radiation of only $\sim 8\text{-}15\%$ of ΔW_{ELM} is observed experimentally in the Type I ELM, what is in much more than with SOLPS ($\sim 3\%$). The peak in the photonic part of

the radiation from SOLPS (~ 300 kW) overestimates experimental one (170 kW) by factor of 2. This is in line with the fact that because of the non-linear response of the diodes, AXUV system is known to underestimate the total radiation by probably factor of ~ 2 at least. However, it must be taken into account that the energy of the ELM analyzed by AXUV is lower ($\Delta W_{\text{ELM}} \sim 2.3$ kJ) compared to that of simulated one (3 kJ).

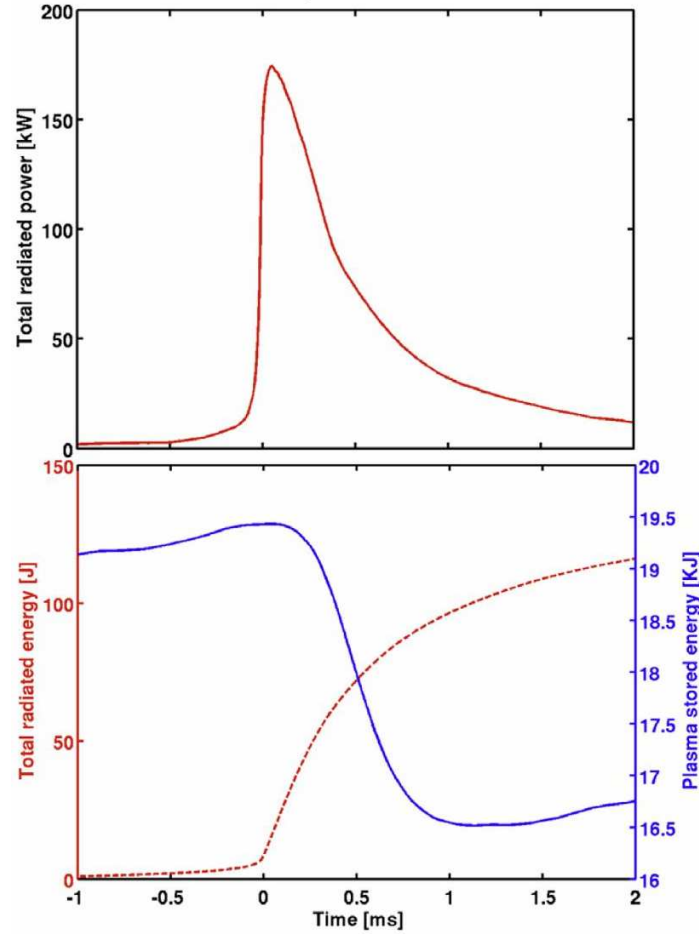


Figure 6.62. Up: Total radiated power measured by AXUV for #33563. Down: Integrated energy from AXUV and plasma stored energy W_{dia} from DML. Extracted from [241].

6.3. Toroidal pedestal rotation

In this section the question of the target power load asymmetries will be addressed. It is known from the observation in all the machines that the in-out asymmetry favours the outer target for the FWD field during the inter-ELM phase. On the other hand, the ELM is known to deposit the energy in the other direction to the pre-ELM asymmetry and since the ELM event represents a massive perturbation to the SOL, it is very unlikely that the background plasma plays any role in the ELM energy asymmetry. In fact the ELM just momentarily burns right through the divertor plasma and determines the asymmetry itself, independently from the inter-ELM situation. It is not absolutely understood which physics govern this process, but there are indications that component of the toroidal rotation might be responsible for it.

Tab.7.1 in the next chapter summarizes the in/out asymmetries obtained from the SOLPS simulations for four ELMs studied in this thesis and the experimental ratios of heat fluxes deposited at inner and outer target (given only for JET due to lack of the TCV data). Earlier sections 6.1 and 6.2 have shown that the in-out target deposited integrated energy asymmetries during the ELMs are favouring inner target in both Type III and Type I TCV ELMs with REV and FWD toroidal field directions respectively. This is to be expected since the drift effects are not included in the simulations. The asymmetry in opposite direction is observed from JET simulations, which can be probably explained by the differences in the geometry .

In general, larger fraction has been always observed to be deposited on inboard divertor and on outboard divertor in FWD and REV field configurations respectively at JET, ASDEX Upgrade and DIII-D machines [236,242]. As it follows from **Tab.7.1** and will be shown in the following chapter on JET ELMs, even though the pre-ELM power asymmetries are more closely matched, a problem still exists with the in-out asymmetry of the target plates power load during the ELM, where strong disagreement between experiment and model is observed. This discrepancy has been always seen as a general feature of the fluid codes [17]. The clear conclusion on this cannot be drawn for the simulations of TCV ELMs, since the measurements of in-out asymmetry at TCV were unfortunately not obtained in the time horizon of this thesis. Therefore only speculations can be done on the basis of the observations on the other machines. Thus, intuitively one could expect that more energy will be deposited on the inner target during the ELM in the configuration with FWD field and outer target with REV field. However, TCV geometry is asymmetric and very different to other devices. As a result, one might not expect TCV to behave completely like the other machines.

Nevertheless, an attempt to influence the in-out target power loads asymmetry obtained by the code was done in order to test the hypothesis in [242]. It has been suggested [242] that one explanation for the observed asymmetry favouring the inner target during the ELM might be the presence of a toroidal component of velocity imparted to the ELM at the moment of formation due to toroidal rotation in the pedestal region. This section describes a preliminary attempt to include this phenomenon into the SOLPS5 ELM simulations at TCV.

6.3.1. Features of target power asymmetry in SOLPS

The fluid code package SOLPS used here includes the following features, which are known to cause the in-out asymmetry, especially during the inter-ELM [17]:

- Toroidal geometry: An out-in asymmetry factor given by $A=(1+\epsilon)/(1-\epsilon)$ with ϵ being the inverse aspect ratio, is about $A \sim 1.7-1.8$ for TCV, JET and ASDEX Upgrade. This

represents that the cross-sectional area is larger on the outside than on the inner side of the poloidal cross-section.

- Shafranov shift: The flux surfaces are closer together on the outside of the poloidal cross-section and therefore if the transport is assumed to be constant in real space the radial transport is larger on the outboard side of the cross-section.
- Target geometry: geometric effects arising from the targets themselves, like for instance the length of the target legs which very probably plays an important role in the TCV with untypical geometry of the configuration with the outer divertor leg much longer than inner one. This is known to cause the different local plasma conditions in front of the target plates.
- Ballooning: If the ballooning of the transport coefficients is applied either during the steady state or in this work especially during the ELM, the distance between the localization of this ballooning area to the targets would be different for inner and outer target and would also differ for the JET and TCV (as indicated by the ratios of the connection lengths towards the targets from the outer midplane for these two machines as seen in Chapter 5.-experimental differences).
- Drift effects: from drifts (diamagnetic and $\vec{E} \times \vec{B}$) if were applied, which is not the case throughout this work.

Most of these effects are, however, applicable only to the L-mode or inter-ELM target asymmetries and are most likely to be seen at higher collisionalities (for higher densities and lower temperatures). Further possibility which can influence the in-out asymmetry during the ELM is the inclusion of toroidal rotation in the pedestal region and momentum transport from pedestal region to the SOL during the ELM [242].

6.3.2. Toroidal pedestal rotation

In [103] a kinetic approach (force-free convective transport along open field lines) is used to derive an analytic expression describing the divertor target power fluxes resulting from an upstream ELM represented by a burst of particles released into the SOL with a Maxwellian distribution at temperature T_i . This model naturally reproduces time delays at the inner and outer targets for a perturbation launched at the outboard midplane (where the ELM is known primarily to originate as a consequence of the ballooning nature of the asymmetry), due simply to the different connection lengths from origin to target arising naturally from a “symmetric” divertor configuration (as in JET for example). In a machine like TCV, where the asymmetric divertor geometry leads to roughly equal midplane to target connection lengths, no such delay is expected. However, if the Maxwellian is launched with zero mean velocity, the model cannot, defacto, lead to any asymmetry in the total energies deposited at each target, which must be equal. In [242], an extension to this model is proposed in which a drifting Maxwellian (with drift velocity characterised by a parallel Mach number $M_{||}$) is included, corresponding to a perturbation carrying a fraction or all of the toroidal rotation velocity which is known to characterise the H-mode pedestal [243]. In this so-called “free-streaming particle” (FSP) approach [242], the in-out asymmetry of the time integrated ELM energy load, seen to invert when the toroidal field direction (corresponding to an inversion of the pedestal rotation velocity) is inverted. Only ion transport time scales are considered in this approach so that the fast energy transport due to electrons is ignored. The assumption of convectively (ion) dominated energy transport is used in FSP approach and applies therefore only for the case of mainly convective ELMs. The latter are usually observed only at higher densities and small ELM amplitudes [242]. Small convective ELMs in DIII-D are reported to

be more asymmetric than larger ELMs which show a higher fraction of conductive losses [244-245]. An advantage of this approach is that no effects due to (poloidal) drifts are required to explain the in-out target power deposition asymmetry. As such, the proposal can be tested with SOLPS5 as used in this thesis (in which no drift terms are switched on for the ELM simulations).

6.3.2.1. Toroidal pedestal rotation in SOLPS

Toroidal momentum transport in the radial direction can be mimicked in SOLPS by the inclusion of a boundary condition of constant parallel (toroidal) velocity, $v_{||}$ imposed at the inner boundary ($v_{||in}=const$). Such simulations have in fact also been attempted in an earlier study [246] intended to investigate the effect of the neutral beam injection on the generation of radial transport through toroidal momentum. Once coupled into the SOL, toroidal momentum drives asymmetries in pressure and parallel fluxes, leading to differences in target heat and particle fluxes compared to the situation without such additional transport.

Transport of the toroidal momentum through the separatrix and further to the plates can be understood on the basis of a simplified slab model of the SOL with x-axis directed from inner to outer target plate and y-axis from the core to the SOL [17]. Integration of the parallel momentum balance equation over the SOL volume (neglecting the parallel and anomalous viscosity in the SOL), yields:

$$\int_{x-}^{x+} \Gamma_s^m dx = m_i \langle v_{||} \rangle_s \int_{x-}^{x+} \Gamma_s dx = m_i \int dy (\Gamma_{x+} v_{||+} - \Gamma_{x-} v_{||-}) + \int dy \frac{B_x}{B} (p_+ - p_-) \quad (6.9)$$

where the Γ_s^m is the momentum flux at the separatrix, Γ_s is the particle flux at the separatrix and subscripts '+' and '-' correspond to the outer and inner targets respectively. Eq.6.9 is a statement that the radial flux of parallel momentum through the separatrix (LHS) is transported by the poloidal particle flux to the plates and also causes pressure asymmetry. The pressure asymmetry produces the difference in the particle and energy fluxes to the target plates. This was confirmed for example by the observations in ASDEX Upgrade reported in [247].

If the toroidal velocity at the targets in Eq.6.9 is assumed to be the sound speed at the target plates:

$$v_{||,\pm} = c_{s,\pm} = \sqrt{\frac{T_{e\pm} + T_{i\pm}}{m_i}}$$

and since, in the absence of $\vec{E} \times \vec{B}$ drifts, $\Gamma_x = (B_x/B) \cdot v_{||}$, the two terms on the RHS of Eq.6.9 are equal then [17]:

$$\frac{1}{2} m_i \langle v_{||} \rangle_s \int_{x-}^{x+} \Gamma_s dx = \int dy \frac{B_x}{B} (p_+ - p_-) \quad (6.10)$$

This means that half of the radial flux of toroidal momentum generated in the core and then flowing through the separatrix is responsible for the pressure asymmetry at the plates. From the simulations in [17] it follows that the Eq.6.10 is a reasonable estimate. The effect depends on the value of the imposed toroidal velocity, since the pressure asymmetry should be of order of $\langle v_{||} \rangle_s / c_{s,\pm}$ where $\langle v_{||} \rangle_s$ is the average parallel velocity at the separatrix. When a parallel velocity is imposed as an inner core boundary condition, an additional SOL radial electric field is also generated in the separatrix vicinity. Due to the momentum transport, the average velocity in the SOL becomes more negative in the case with imposed $v_{||} < 0$ and more positive if $v_{||} > 0$. By convention, positive $v_{||}$ is directed from the midplane towards the outer target and

a pressure excess appears at the outer target. If v_{\parallel} is negative (directed from midplane to inner target), the pressure is higher at inner target compared to the outer target

By convention in this simple approach, a positive value of M_{\parallel} ($v_{\parallel} > 0$) describes toroidal rotation in the co-current direction, corresponding to the FWD field case, should drive an asymmetry in favour of the inner target. If $M_{\parallel} < 0$, the asymmetry favours the outer target. This effect is however applicable only on the convective fraction of the power loads and therefore it will strongly depend on the extent to which the heat fluxes to the targets during the simulated ELMs are convective (or conductive). The in-out asymmetries during the ELMs are seen to be most obvious as the ELM energy increases [242]. The asymmetries are very scattered and are smaller for smaller ELMs.

6.3.3. Simulations of TCV Type III ELM with toroidal pedestal rotation

This part describes the attempts made to change the in-out ELM power asymmetry by an inclusion of an adhoc toroidal rotation into the pedestal region in the SOLPS simulation of the TCV Type III ELMing discharge in RWD field configuration reported in section 6.1. As mentioned earlier, on the basis of the observations from other machines the speculation that experimentally one would find more power deposited on outer targets in this field direction will be assumed as plausible for this exercise. The in/out target power ratio found in the simulation is ~ 1.3 . In the absence of poloidal drift terms in the simulations presented here, one can refer to the situations with FWD and REV field only by imposing negative and positive v_{\parallel} respectively. Therefore the inclusion of positive v_{\parallel} is expected to change the observed asymmetry towards the outer target

In SOLPS simulations, v_{\parallel} is imposed at the core boundary and even with quite narrow simulation grid (~ 2.5 cm inside separatrix in this TCV simulation), many CPU hours are needed for v_{\parallel} to propagate outwards from inner boundary to the SOL. Therefore if v_{\parallel} is to be included in the transient ELM simulation, one needs to launch it on the top of the steady state solution where v_{\parallel} has already propagated to the separatrix.

Because of the limitations of the 2D SOLPS code, the experimentally observed toroidal rotation cannot be included as such, and only parallel component of the velocity can be applied. Therefore the strong viscous damping term arises in the momentum equation when v_{\parallel} is imposed. Thus in order to allow the v_{\parallel} perturbation to penetrate from the core boundary outwards, the parallel viscous term must be switched off otherwise the extra parallel momentum injected by v_{\parallel} is converted into heat and does not reach the separatrix. In order to remove the parallel viscous damping and obtain pure toroidal rotation, the inclusion of drifts in the simulation would be required [238]. As far as the radial transport coefficients are concerned, the values matching experimental observations have been chosen. Thus based on the turbulence measurements indicating that the ratio of parallel transport momentum and heat transport coefficient is close to unity [248], in addition to setting parallel viscosity to 0, the perpendicular viscosity, η_{\perp} was simultaneously set to $\sim \chi_{\perp} \sim 1 \text{ m}^2 \cdot \text{s}^{-1}$. With very small values of η_{\perp} ($\sim 0.01 \text{ kg} \cdot \text{m}^{-1} \cdot \text{s}^{-1}$), the parallel velocity does not develop in the SOL from a value injected at the inner core boundary.

In the simulation attempted here, parallel velocities in both directions $v_{\parallel} = +10^5 \text{ m} \cdot \text{s}^{-1}$ and $v_{\parallel} = -10^5 \text{ m} \cdot \text{s}^{-1}$ ($\sim 30\%$ of the pedestal sound speed), were injected in the simulations at the inner core boundary. From the measurements of toroidal pedestal rotation measured at ASDEX Upgrade by edge CXRS, values of $\sim 10^4 \text{ m} \cdot \text{s}^{-1}$ ($\sim 15\text{-}30 \text{ km/s}$) were found in co-current direction in the pedestal region, corresponding to $M_{\parallel} \sim 0.1$. However, it should be noted that because the toroidal momentum is generated in the core and is then transported to

the separatrix, the average parallel velocity gradually decreases towards the separatrix, while the radial flux of toroidal momentum remains almost constant (as seen also in simulations in [246]).

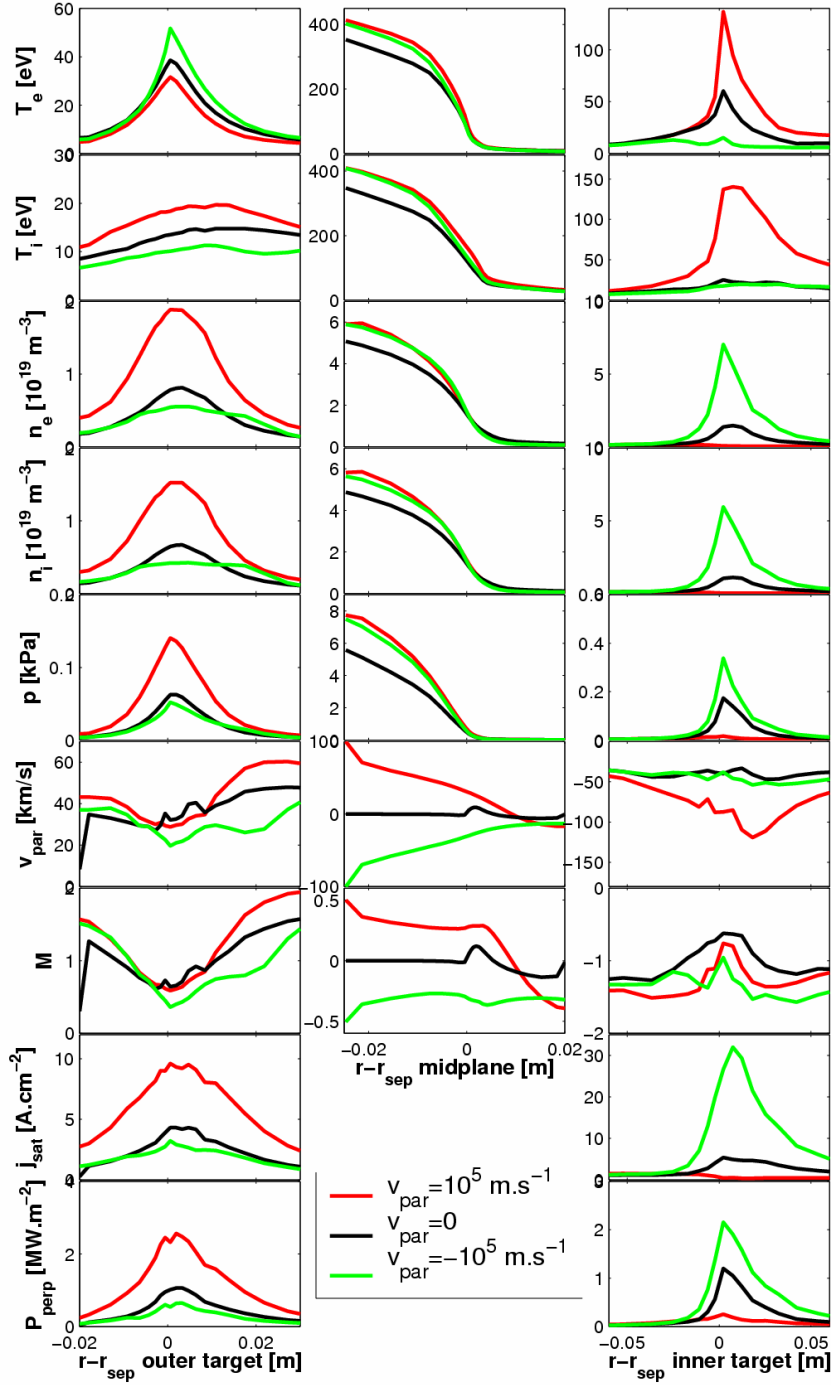


Figure 6.63. The profiles of T_e , T_i , n_e , $n_i \sim n(D^+)$, p , $v_{||}$, $M_{||}$, j_{sat} and P_{\perp} at outer target (left), outer midplane (middle) and inner target (right) for pre-ELM simulations of TCV Type III ELMing H-mode with $v_{||} = 10^5 \text{ m.s}^{-1}$ (red) and -10^5 m.s^{-1} (green) compared with the reference case without $v_{||}$ (black). Reference case is “diffusive”.

If a given $v_{||}$ is imposed at core boundary, it diffuses outwards to the pedestal region and is about 10 times lower than its initial value when it has reached separatrix. This can be clearly seen on **Fig.6.64** with spatial and time evolution of parallel velocities and on the **Fig.6.63** where the compilation of the several parameters (T_e , T_i , n_e , $n_i \sim n(D^{1+})$, p , $v_{||}$, $M_{||}$, j_{sat} and P_{\perp}) at both targets (left and right columns of **Fig.6.63**) and midplane (middle column) is shown for the three pre-ELM cases including those with positive, negative and zero $v_{||}$ imposed. At the separatrix $v_{||} = \pm 10^4 \text{ m.s}^{-1}$, a factor of 10 down on the inner core boundary value. It is very important to note that imposed $v_{||}$ does not cause changes in the upstream profiles and therefore no corrections of the anomalous transport coefficients are required in order to maintain rough agreement with experimental upstream profiles once an additional $v_{||}$ is introduced. The two cases with opposite $v_{||}$ behave asymmetrically and a change in the in-out target asymmetries are already manifest in the steady state profiles. The particles and power fluxes increase at outer target and decrease at inner target for the case with $v_{||}=10^5 \text{ m.s}^{-1}$ and vice versa for $v_{||}$ in the opposite direction.

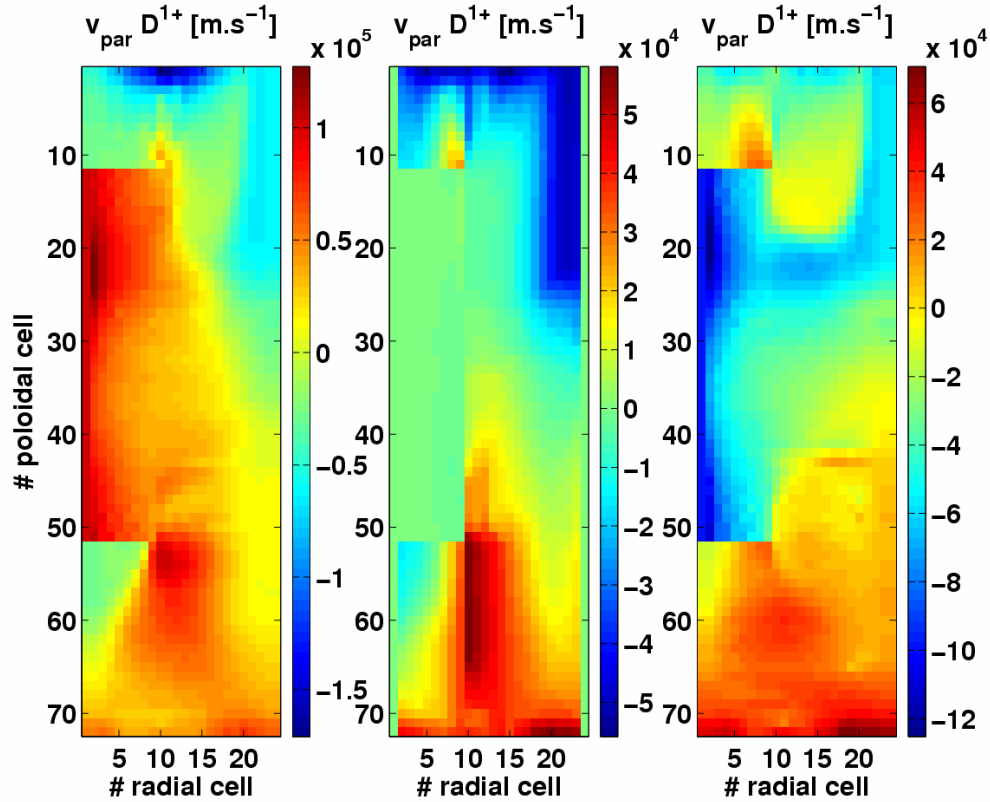


Figure 6.64. Spatial distribution of the parallel velocity in the simulation grid for the three different TCV cases in Fig.10.1. Left: $v_{||}=+10^5 \text{ m.s}^{-1}$. Centre: reference case $v_{||}=0$. Right: $v_{||}=-10^5 \text{ m.s}^{-1}$. The poloidal cells 12-51 represent the main SOL and radial cells ≥ 10 outside separatrix.

When the ELMs are launched on these steady state solutions in the same way as for the case without $v_{||}$, similarly to the simulations with $v_{||}=0$ reported in section 6.1.5.4, the radial heat fluxes crossing the separatrix are completely dominated by convection (95%). However the heat fluxes to the targets are much more conductive, with the convective fraction representing only $\sim 30\%$ (for all three cases shown in **Fig.6.63**). Nevertheless, as seen in **Fig. 6.65**, this is enough for the effect of toroidal rotation to be seen as expected on the basis of the

FSP model [242]. The ratio of energies deposited on the targets during the ELM event $E_{\text{DEP,IN}}/E_{\text{DEP,OUT}}$ increases from ~ 1.3 (reference case) to ~ 3 for the ELM with $v_{\parallel} = -10^5 \text{ m.s}^{-1}$ and decreases to ~ 0.3 for $v_{\parallel} = +10^5 \text{ m.s}^{-1}$. This is the trend in the right direction and it looks like a good start. It is worth mentioning that the flux limiting factors in these simulations are set to the default values (e.g. $\alpha_i = 10$ and $\alpha_e = 0.3$), namely weak ion flux limiting. This is the reason for the rather high conductive fraction of the heat fluxes at the targets. It follows from the analysis in the section 6.1.5.6.2, that if the flux limiting were stronger, the ELMs would be more convective and the effect of toroidal rotation would be even stronger.

It must be however, pointed out, that introduction of v_{\parallel} has radical effects on the pre-ELM solution which are clearly not correct. There is no longer any real agreement with the data of reference case with $v_{\parallel} = 0$. This would be only acceptable if this “pre-ELM” solution was taken only as a very first part of the ELM simulation. However, this is not correct either, since it is observed, that once the ELM is applied all the energy is expelled through the separatrix in first 20 μs and then the power through the separatrix drops rapidly and all the upstream profiles collapse completely. The agreement with the upstream ELM profiles (as seen on **Fig.6.19** for reference case) is obtained only at 20 μs . The target profiles are also nowhere near the experimental measurements. Moreover, the energy expelled by the ELMs has, decreased from $\sim 600 \text{ J}$ to $\sim 450 \text{ J}$ for the cases with applied finite v_{\parallel} shown on **Fig.6.65**.

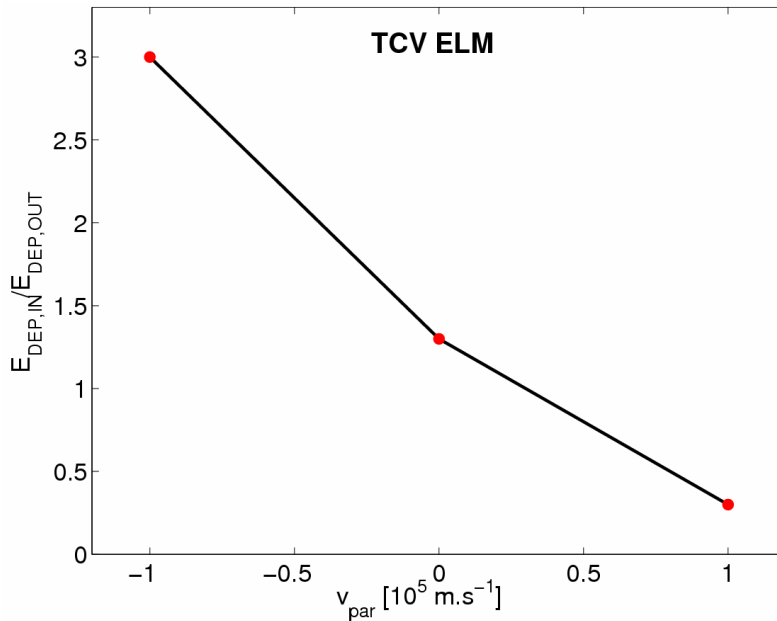


Figure 6.65. Ratio of power deposited on inner and outer target during TCV ELMs for different values of toroidal rotation. The cases with parallel velocity 10^5 and -10^5 m.s^{-1} expel only $\Delta W_{\text{ELM}} \sim 450 \text{ J}$ compared to the reference case without v_{\parallel} ($\Delta W_{\text{ELM}} \sim 600 \text{ J}$). Note, that the left part of the plot with negative x-axis corresponds to the experimental case with FWD field and the part with positive x-axis to the case with REV field.

These discrepancies suggest that even if inclusion of the v_{\parallel} seems to “solve” the in-out asymmetry problem (hypothetical, since no measurements are available to prove this), it creates another discrepancies and completely new solution with different combinations of the transport coefficients would be needed to obtain the profiles matching the experiment data. This analysis is too immature and needs to be pursued in the future in more details. In addition, the experimental measurements are needed to constrain the code and draw valid conclusions.

7. SOLPS simulations of JET ELMinG H-modes

Chapter 6 has described in detail the SOLPS5 time dependent simulations of two types of ELMs on TCV, demonstrating good correspondence with the available experimental data and using the results of PiC simulations to study the effect of kinetic corrections on the fluid predictions. This turns to much larger transients on the JET tokamak, where ELM energies are hundreds of times those experienced on TCV. The emphasis here will be on the use of these ELM simulations to benchmark two of the world's major edge code packages: SOLPS5, the tool of choice during this thesis and EDGE2D-NIMBUS, the fluid Monte-Carlo plasma boundary code suite developed over 20 years at JET and used exclusively for simulations of JET plasmas. Although a series of simpler code-code benchmarks have been attempted in the past, the study reported here represents the first attempt to perform such an exercise for a complex, time dependent situation. In addition the simulations of H-mode with ELM expelling energy close to the ITER limit $\sim 1\text{MJ}$ are reported in the second part of this chapter.

7.1. SOLPS5 – EDGE2D-NIMBUS benchmark of JET Type I ELMinG H-mode

In this section the focus will be on SOLPS modelling of a Type I ELMinG H-mode discharge at JET, characterised by ELMs with $\Delta W_{\text{ELM}} \sim 200\text{ kJ}$, a factor 200 larger than the small TCV Type III ELMs examined in Chapter 6. Motivation for this study is twofold: first because the discharge in question is part of a dedicated series of H-modes performed on JET to obtain the best (at the time) possible set of edge profile and target measurements and second because the discharge has been modelled in detail by Kallenbach [172] using the JET edge code EDGE2D-NIMBUS [132]. The exercise thus provides an excellent opportunity to test the SOLPS5 time dependent model on a larger, more relevant (to ITER) scale (compared with the TCV simulations) and at the same time satisfy an important benchmarking function. A selection of the results described here are the subject of a recently published journal article [173].

7.1.1. SOLPS vs. EDGE2D/NIMBUS

Edge modeling codes are used to understand and interpret the results of the present machines and to predictive modeling of the future tokamaks, e.g. ITER. It is therefore crucial to understand, document and resolve the differences between them whether they arise from differences in underlying physics approximations or choices of numerical treatment.

Although a benchmark of the SOLPS5 and EDGE2D-NIMBUS codes has previously been successfully attempted [249], the exercise reported here represents a more complex situation, in which impurities are included (all charge states of carbon) and a time dependent solution is sought to capture the ELM.

Both codes are fluid-Monte Carlo code packages. B2.5 and EDGE2D are stand-alone fluid codes solving the Braginskii equations for parallel transport with a diffusive/convective ansatz for cross-field transport. Each is interfaced with a neutral code (Eirene and NIMBUS) which may also be run independently, but which differ considerably from each other. For example, NIMBUS uses a cylindrical and Eirene a toroidal approximation and Eirene includes a great deal more complexity in the various atomic physics processes that are accounted for.

Each code package contains similar descriptions of physical and chemical sputtering. Even though both packages solve the overall edge fluid-neutral system in essentially the same way (i.e. based on a similar physics model), the codes are extremely complex and have been developed by many people over decades. Benchmarking one against the other is an important check of the overall level of consistency of two codes which solve the same problem with different numerical schemes. Since only one (SOLPS) has been used to provide a physics basis for the ITER divertor and SOL plasma, it is also important that the results of this code be checked against an independent package. Although EDGE2D has recently been successfully coupled to Eirene, the neutral transport code used in SOLPS5, comparison will be made here only between SOLPS5 and results from the EDGE2D-NIMBUS simulations reported in [172]; the EDGE2D-Eirene coupling had not yet been performed at the time the work in [172] was undertaken.

The complexity of the time dependent ELM case is such that a benchmark is even more important. One important difference is that time dependence is introduced in both the B2.5 and Eirene components of SOLPS5, whilst in the EDGE2D-NIMBUS, package only the fluid component is time dependent (neutrals are time independent). In EDGE2D the time-step decreases during the ELM cycle from 10^{-4} s to 10^{-7} s, in B2.5 and EIRENE the same time step is applied throughout the simulation (in the case published here it was 10^{-5} s). The highest level of complexity (namely the inclusion of drifts) is not attempted here since they were not included in the original EDGE2D-NIMBUS simulations [172].

7.1.2. Experiment and settings

The Type I ELMIg H-mode JET discharge modeled here, #58569, is a $I_p = 2.0$ MA, $B_\phi = 2$ T pulse with gas fuelling, $P_{IN} \sim 14$ MW and $W_{plasma} \sim 4$ MJ. In common with most medium to high power H-modes on JET, additional heating in the form of NBI makes up most of the heating power in this pulse. In this case, $T_{e,ped} \sim 1.25$ keV and $n_{e,ped} \sim 4 \times 10^{19} \text{ m}^{-3}$ with $f_{ELM} \sim 30$ Hz and $\Delta W_{ELM} \sim 200$ kJ, $\Delta W_{ELM}/W_{PLASMA} \sim 0.05$. Compared for example to the small Type III ELM at TCV with $\Delta W_{ELM} \sim 600$ J and about 10 times smaller deposition area, this JET Type I ELM is about ~ 30 times more powerful in terms of power deposition to the plasma-facing components. Key time traces of this discharge are shown in **Fig.7.1** and the main plasma parameters in **Tab.5.2**. The ELM-related parameters can be found in **Tab.3.1**.

As for the TCV case, the JET simulations are constrained upstream by experimental n_e , T_e and T_i profiles obtained from the diagnostics described in chapter 5, but without the benefit (in terms of spatial resolution in the pedestal region) of the HRTS system, which had not yet been installed at the time of this earlier discharge. Unlike the even higher power discharge described in the next section, however, this lower I_p discharge was run with a slow vertical rigid plasma sweep, allowing high resolution target profiles of ion flux density j_{sat} , n_e and T_e to be generated with the LP array (much higher than possible at higher I_p , where the risk of disruption is too high to allow large vertical movements). Unfortunately at the time when this discharge was produced, measurements of total radiated power were performed with the old JET bolometry system (KB1), which has too low time resolution for analysis on the ELM timescale to be attempted. A different, but very similar discharge, #73394 has therefore been used for the radiation analysis of the simulations here. The new, improved bolometer diagnostic (KB5) was available only for pulses similar to the simulated one. Therefore only an indication of the inter-ELM power fluxes at the targets have been obtained from discharge #74380 using a IR cameras with time resolution 0,1ms. Unfortunately, this discharge has quite different divertor magnetic geometry compared with the reference pulse and so the comparison with simulations is not strictly valid. It has the outer leg on the load bearing septum replacement plate (LBSRP) installed after the period in which the reference

pulse was made. This is thus a horizontal target configuration (for the outer target), in comparison to the vertical target equilibrium of the reference plasma. Nevertheless, given that good IR measurements on the ELM timescale were not available for #58569, this represents a reasonable compromise given that the main plasma parameters, including the I_p , B_ϕ and P_{IN} (and hence the same magnetic connection length) are similar. The data from this pulse have been however, used only as a cross-check of the inter-ELM power fluxes at the targets and another pulses #62222 and #62224, much closer to the simulated one in the divertor configuration (compared to above described #74380), have been used to indicate the measured energy target deposition asymmetries expected in the simulated discharge during the ELM. The ELMs examined in these pulses have higher $\Delta W_{ELM} \sim 270\text{-}300$ kJ compared to the simulated pulse, however it is again a reasonable compromise.

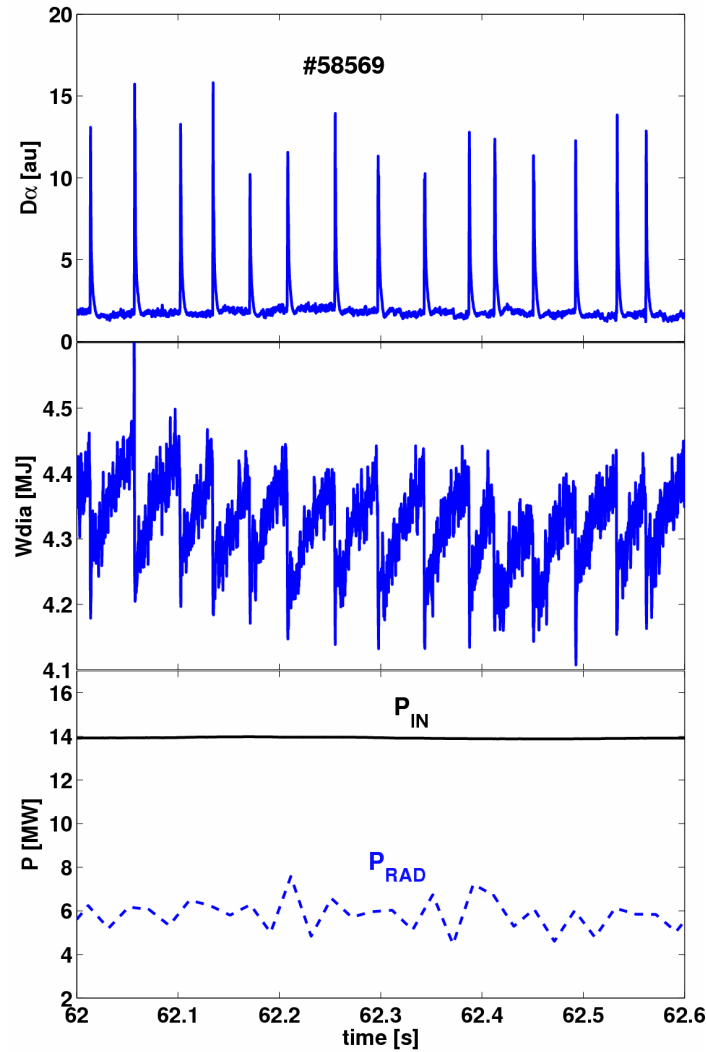


Figure 7.1. Selected time traces of the main parameters of the discharge #58569 simulated in this section. D_α signal corresponds to the line of sight at the outer divertor. The time axis corresponds to the JET time index ($t+40s$).

The boundary conditions and settings in the JET simulations are mostly the same as in the TCV cases except a few which are mentioned specifically below. As far as possible, the benchmark is performed by setting all equivalent inputs in SOLPS5 as they were for the EDGE2D model in [172]. This includes wall albedos (recycling coefficients), parallel heat flux limits, separatrix density feedback (as also used for the TCV cases) and power flux sharing in the ion and electron channels. The P_{SOLPS} power is set as the corresponding P_{SOL} value in **Tab.5.2** as 12 MW and $n_e^{\text{sep}} = 2 \times 10^{19} \text{m}^{-3}$.

Unlike the TCV simulations, where the gas puff was a point source of D_2 molecules, in the JET case, the gas puff prescribed in the EIRENE input file is a surface distributed source of particles. In common with the model in [172], no flux limiting of parallel heat fluxes was used and no sensitivity study on these parameters has been performed. As for the TCV cases, the simulations contain 9 species: deuterium and carbon neutrals and all ion species (D^+ , C^+ , C^{2+} , C^{3+} , C^{4+} , C^{5+} , C^{6+}).

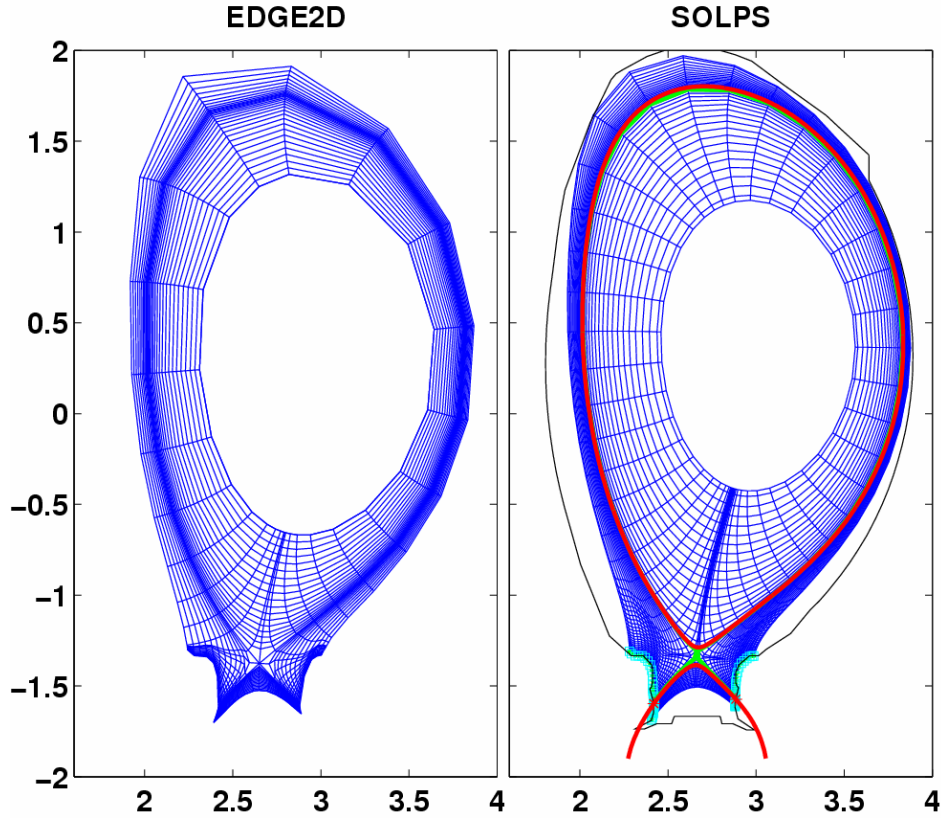


Figure 7.2. Grids used for the JET H-mode simulation (pulse #58569). The red and green lines mark the separatrix as identified by EFIT and SOLPS5 respectively

Fig.7.2 shows the SOLPS5 computational grid on which the ELMing H-mode benchmark has been performed, along with that used for the EDGE2D-NIMBUS code runs in [172]. Both are derived from the magnetic flux surfaces obtained with the magnetic equilibrium reconstruction code EFIT at $t = 29$ s into the discharge, near the end of the plasma current flat-top. The grids are not quite the same: the EDGE2D-NIMBUS grid has 48 cells poloidally, 30 radially and extends about 20 cm inside the separatrix and 5 cm outside; the SOLPS5 grid has higher spatial resolution (96 cells poloidally and 36 cells radially) and

extends much further into the core, ~ 40 cm and ~ 6 cm in the SOL. The first 24 poloidal cells cover the inner divertor, the next 48 (ix=25-72) cells the main SOL and the last 24 cells (ix=73-96) the outer divertor. The separatrix is between radial cells 19 and 20 and the outer midplane at poloidal cell 57. A true one to one benchmark would require the exercise to be performed on the same grid. The differences are sufficiently small for this not to be an issue. In addition, the wider SOLPS5 grid permits an improved study of radiation distributions (something not treated in detail in [172]).

7.1.3. Results of the benchmark exercise

To model the pre-ELM steady state, a step-like ansatz is used for the radial profile of transport parameters exactly as performed in [172], within the small differences introduced as a consequence of the imperfect grid match. In this way, the inner core region, the H-mode pedestal (edge transport barrier) and the outer SOL are represented as 3 distinct regions. Along the divertor legs, the radial profiles of the transport coefficient are flat ($D_{\perp} = \chi_{\perp e} = \chi_{\perp i} = 1 \text{ m}^2 \cdot \text{s}^{-1}$, $v_{\perp} = 0 \text{ m} \cdot \text{s}^{-1}$). Note that $\chi_{\perp i} = \chi_{\perp e}$ is assumed on the basis of similar experimental values of T_i and T_e (see **Fig. 7.3**).

The upstream profiles of n_e , T_e , T_i and transport coefficients during the pre-ELM phase are compiled in **Fig.7.3** (analogous to Fig.2 in [172]) including the previous results obtained from [172], those from the new SOLPS5 simulation and the experimental data (the experimental points have been processed slightly differently from those in [172] and may not correspond precisely). The high level of agreement between profiles from the two codes is extremely encouraging. As described in [172], if diffusive outward transport is assumed, as it is here, a strong inward particle pinch is required to match the experimental density profile. Not surprisingly, the same applies to the SOLPS5 simulations. Attempts made with SOLPS5 to find a satisfactory match without invoking a pinch term failed to produce as close agreement with experimental profiles.

In the same way as for the TCV ELM simulations and like in [172], an approximation to the ELM cycle is included using an adhoc increase in transport coefficients for an ELM duration specified from experiment; $t_{\text{ELM}} \sim 1 \text{ ms}$ on JET. Multiple ELMs are simulated as a repetitive increase of transport coefficients with frequency $\sim 30 \text{ Hz}$, corresponding to the experimental f_{ELM} . To match the observed $\Delta W_{\text{ELM}} \sim 200 \text{ kJ}$, D_{\perp} , $\chi_{\perp e}$ and $\chi_{\perp i}$ must be increased by factors of 20 and 40 respectively. This multiplication factor is applied everywhere poloidally except along the divertor legs where the pre-ELM (flat) profiles are maintained through the ELM phase. Note that, unlike the TCV cases, no poloidal localization on the LFS has been applied in these simulations. The enhanced transport moreover has been applied also at HFS in the same way as in LFS. Only a purely “diffusive” approach has been used to model this ELM and no changes are made to the radial shape of the transport coefficient during the ELM (in contrast to the case of the TCV ELM chapter 6). In addition, the D_{\perp} , χ_{\perp} have been increased radially only in the interval extending from 5cm inside to 0.5 cm outside the separatrix (corresponding roughly to the experimentally observed ELM affected area). A time step of 10^{-5} s is used in SOLPS5, yielding 100 points inside the prescribed $t_{\text{ELM}} \sim 1 \text{ ms}$.

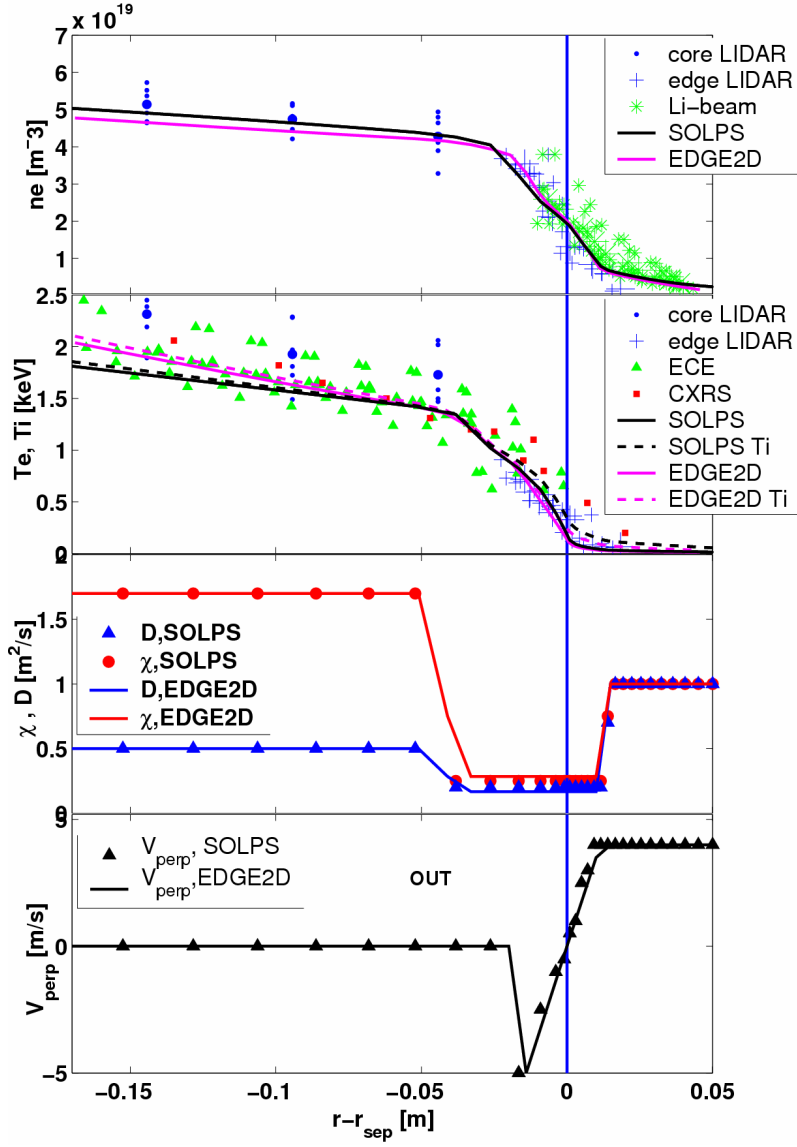


Figure 7.3. Pre-ELM n_e , T_e , T_i upstream profiles for # 58569 from experimental data, SOLPS5 and EDGE2D-NIMBUS, together with corresponding radial profiles of transport coefficients ($\chi_{\perp e} = \chi_{\perp i} = \chi$). “out” in the bottom panel indicates that positive v_{\perp} corresponds to the outward pinch and vice versa.

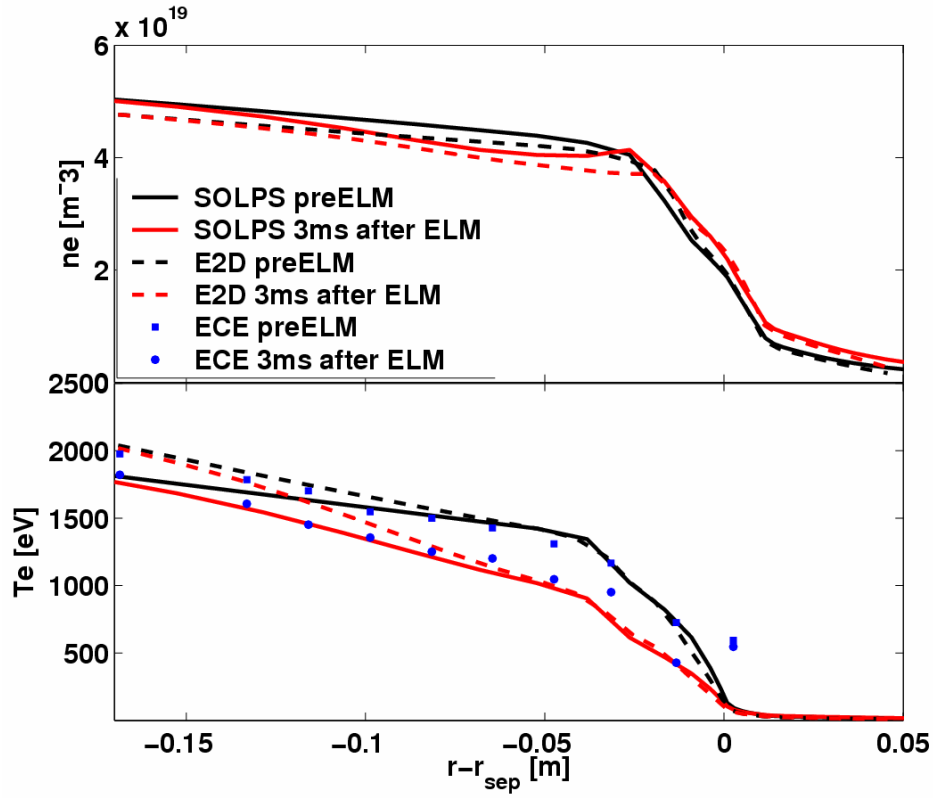


Figure.7.4. Pre- ELM and ELM upstream profiles for # 58569, upper: n_e from SOLPS and EDGE2D-NIMBUS, lower: T_e from SOLPS, EDGE2D-NIMBUS (denoted E2D) and experimental measurements from the ECE diagnostic.

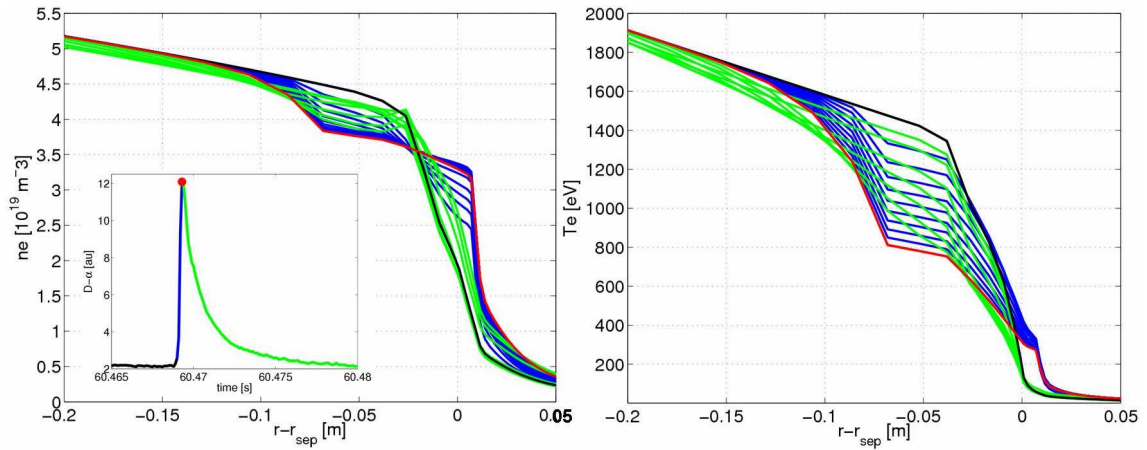


Figure.7.5. Evolution of n_e (left) and T_e (right) profiles during the ELM simulated with SOLPS. Inset on left shows the time dependent D_α signal with colors corresponding to the profiles in the particular phases of the ELM cycle; black = preELM, blue=ELM rise, red=ELM peak and green= ELM relaxation phase. Note that time axis corresponds to the $t+40s$.

Fig. 7.4 (analogous to Fig. 4b and Fig. 5 in [172]) compares the simulated upstream profiles of n_e and T_e from both codes, along with ECE data for T_e during the pre-ELM phase and 3ms after the start of the ELM. The agreement between the two codes is again very reasonable, particularly in the pedestal region. The small difference in the core is most probably due to the deeper SOLPS simulation mesh. **Fig. 7.5** shows the time evolution of the n_e and T_e profiles during the ELM cycle. The transport barrier crash is clearly seen, with the effect much stronger on the temperature than density profile.

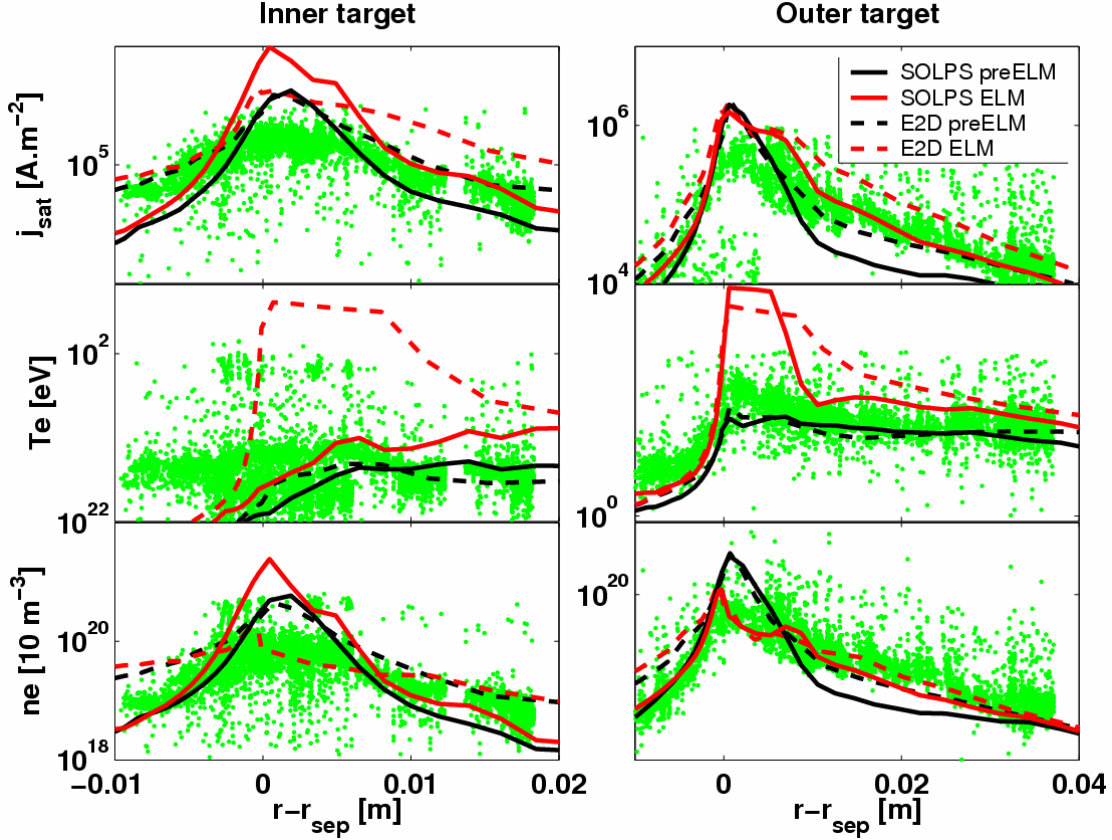


Figure 7.6. Pre-ELM (black) and ELM (red) target profiles, j_{sat}, T_e, n_e from EDGE2D-NIMBUS (dotted line) and SOLPS5 (solid line), experimental LP data (green). Simulation #24805 where, for the sake of the benchmark, no time dependence is considered in EIRENE.

At the divertor targets the code results are compared in **Fig. 7.6** with the LP profiles obtained during the vertical strike point sweeps (analogous to Fig. 6 in [172] but now also including the inner target which was not given in [172]). Both inter-ELM and ELM profiles from the simulations are plotted, where the latter corresponds to a point 0.4 ms after the transport coefficients are increased in the code. In the case of the LP data, all time points (ELM and inter-ELM) are included such that the lower and upper envelopes represent roughly the inter-ELM and ELM peak profiles. Note also that unlike the TCV case, the JET LPs can be run as triple probes, so that T_e is available on a much faster timescale (10 kHz for the example in **Fig. 7.6**).

Agreement between the two codes, especially at the outer target, is again reasonable given, for example, the different neutral models. Both are a fair match to the experimental data but both largely over-estimate the outer target T_e during the ELM. The T_e during the

ELM at inner target predicted by SOLPS5 is much lower than the one from EDGE2D-NIMBUS and thus closer to the experimental data. However, the LP signals are ELM averaged and they are known to measure low temperatures at the inner target in JET (because it is always partially detached between ELMs). The T_e drops during the ELM from the pedestal to the target about 3 times at outer and much more at inner. Indeed if one calculates the fraction if the conduction in the power fluxes more than 90 % is found. Neither of the codes predicts much of a rise in peak density at the ELM. This is obviously a counter-intuitive result, obtained with both codes, because the ELM drives a massive flux to the divertor indicated by a large increase in the D_α signal.

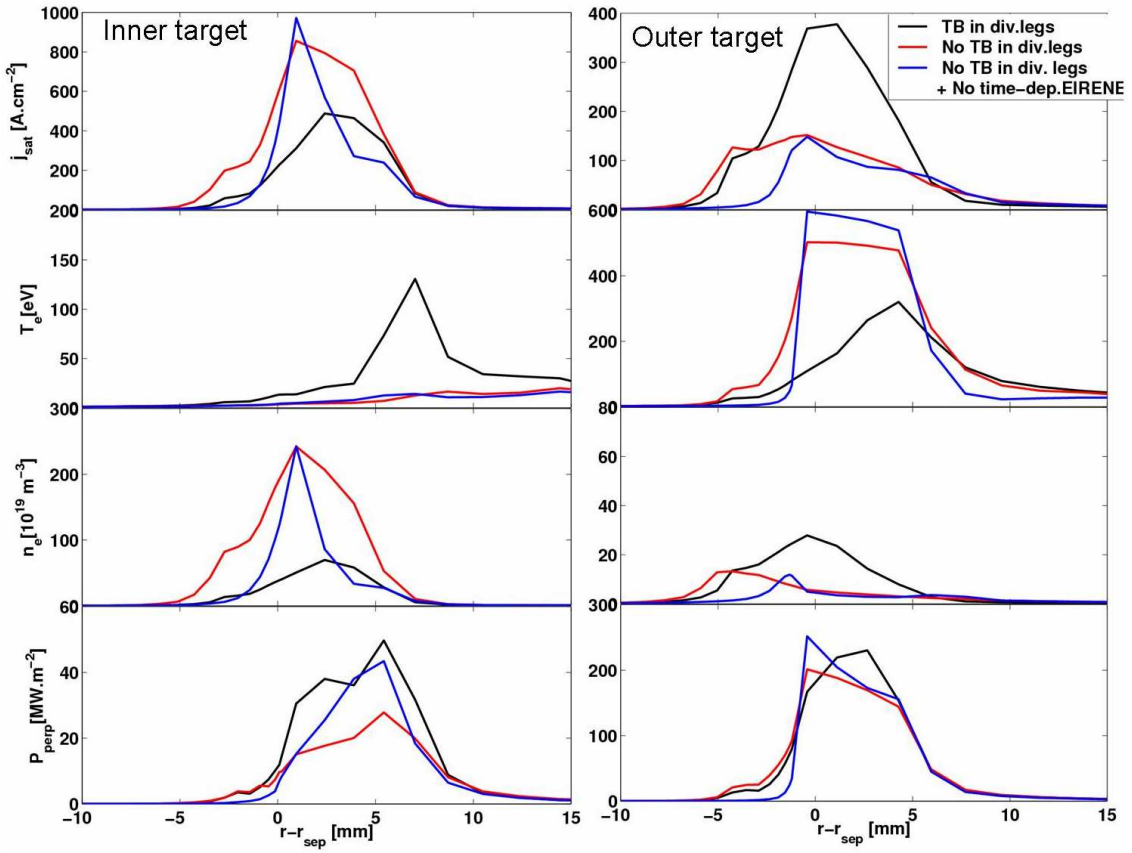


Figure 7.7. Comparison of different time target profiles during the ELM (0,4 ms after the ELM start) for the three different simulations; Black lines represent the case with TB everywhere including divertor legs and with time-dependency for the neutrals; Red lines stand for the case without TB in divertor legs but with time-dependent treatment of neutrals and the last case depicted by blue lines is the reference case from Fig. 7.6 without TB in divertor legs but with time-dependency switched off in EIRENE.

As it was mentioned in the section 7.1.1 the neutral model in EDGE2D/NIMBUS used in [172] doesn't include the time-dependence. In order to inspect this issue the simulations were performed by SOLPS both with and without time-dependent treatment of the neutrals in EIRENE part of the code package. Fig. 7.7 compiles the ELM target profiles of j_{sat} , n_e , T_e and P_\perp for three different simulations including the two cases mentioned above and the case with the time-dependently treated neutrals and same radial profiles of transport coefficients (with

TB) applied everywhere poloidally in the simulation grid. Most visible differences come from the TB in divertor legs especially for T_e , n_e and j_{sat} . Different treatment of neutral time-dependence appears to affect the profiles more in shape than in the amplitude.

7.4.1 Target power loads

In addition to the baseline benchmarking exercise, which can only check the level of agreement with the results presented in [172], the new SOLPS5 simulations can be used to study other aspects of the response to these JET Type I ELMs, profiting from improved diagnostic measurements not available to the EDGE2D-NIMBUS study.

Fig. 7.8 shows the SOLPS target power fluxes, where the simulated results have adopted the same approach with regard to sheath heat transmission coefficients as those described in section 6.1.4. Good IR measurements were not available in the reference pulse, nor do more recent identical pulses exist in which such measurements are available (see section 7.1.2).

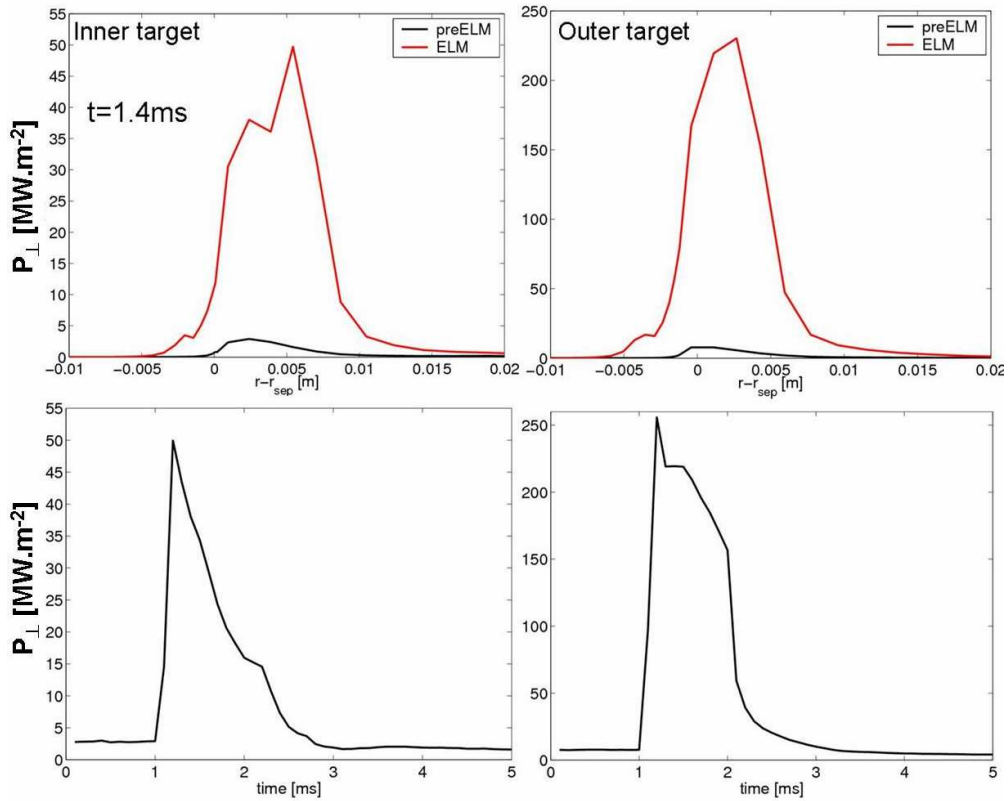


Figure 7.8. *Upper:* pre-ELM (black) and ELM (red) profiles on both targets from SOLPS
Lower: Time-dependent power fluxes at the strike point from SOLPS

Fig 7.8 upper shows the SOLPS5 simulations, which correspond to the case with no ETB in divertor legs and with the code fully time-dependent (including EIRENE), which is adopted in the following analysis as a reference case. The profiles are extracted at the peak of the ELM amplitude evolution at the strike point. This evolution is shown in the lower part of **Fig 7.8**.

The pre-ELM profiles from code match reasonably well the experimental values from the pre-ELM phase of #73480 with profile peaks values approximately $\sim 2 \text{ MW.m}^{-2}$ and $\sim 11 \text{ MW.m}^{-2}$ at inner and outer target respectively (compared to $\sim 3 \text{ MW.m}^{-2}$ and $\sim 8 \text{ MW.m}^{-2}$

from SOLPS – see **Fig.7.8 upper**). This in-out asymmetry favouring outer-target is observed in all machines during the inter-ELM phase in configurations with FWD field. The match with this trend is quite encouraging because the agreement during the pre-ELM is a key if one wants to investigate the behaviour of fluxes during the ELM event. The experimental measurements show that this inter-ELM in-out asymmetry is reversed during the ELM [177]. SOLPS5, however, shows much higher power flux densities at outer compared to inner target also during the ELM, with peak values reaching $\sim 50 \text{ MW.m}^{-2}$ and $\sim 250 \text{ MW.m}^{-2}$ at inner and outer target respectively. When integrated over the full ELM cycle the SOLPS finds the energy deposited at inner target $E_{\text{DEP,IN}} \sim 30 \text{ kJ}$ and $E_{\text{DEP,OUT}} \sim 140 \text{ kJ}$, thus giving the in-out asymmetry ratio ~ 0.21 .

This is in sharp contrast with experimentally observed total energies measured for similar discharges #62224 and #62222 (with $\Delta W_{\text{ELM}} \sim 270 \text{ kJ}$ and 300 kJ respectively) which find $E_{\text{DEP,IN}}/E_{\text{DEP,OUT}} \sim 1,65$ and 2 respectively. Even though this result is meant to be only indicative it cannot be denied that such ELM energy loading asymmetries are typically observed on JET [236] and elsewhere (e.g. ASDEX-Upgrade [250] for forward toroidal field. The target power deposition asymmetry seen at TCV cases has opposite direction in both Type I and Type III ELM simulations. This discrepancy, which is probably driven by the different geometry of the two machines was discussed in section 6.3 and the in-out asymmetry issue for the JET case will be addressed in section 7.3.

7.1.5. Energy analysis and radiation

In similar fashion to the analysis performed for the TCV ELM, the SOLPS5 JET benchmark output has been used to study the energy balance during the ELM cycle. During the pre-ELM phase in the simulation, the power crossing the core boundary $\sim 12 \text{ MW}$ is distributed mainly at the targets $\sim 65\%$, with the rest lost by radiation. The total radiated power during the pre-ELM phase is found to be $\sim 4 \text{ MW}$, in good agreement with experimental data from bolometer system (see **Fig. 7.1**).

As shown on **Fig.7.9** the measured time variation of the diamagnetic stored energy during the ELM cycles is well reproduced by the simulations, giving the observed $\Delta W_{\text{ELM}} \sim 200 \text{ kJ}$. The SOLPS values are corrected by 2.8 MJ corresponding to the core plasma volume not included in the SOLPS grid. This is somewhat less than the $\sim 3.4 \text{ MJ}$ required in the EDGE2D-NIMBUS simulations [172] as a consequence of the narrower grid used there (see **Fig. 7.2**). This drop in the energy stored in plasma in SOLPS corresponds to the time-evolution of the powers crossing the boundaries and the integrated energies during the ELM cycle plotted in **Fig. 7.9**. The energy expelled through the separatrix during the ELM (200 kJ) is balanced by the calculated energy deposited on the targets ($E_{\text{DEP}} \sim 170 \text{ kJ}$) and radiated energy ($E_{\text{RAD}} \sim 30 \text{ kJ}$). It is interesting to note, that unlike the simulations of small TCV ELMs, where a considerable fraction of ΔW_{ELM} leaves the outer boundary of the grid (and would thus correspond to power deposited on the main walls) this larger JET ELM deposits majority of its energy ($\sim 85\%$) on the targets. This can be qualitatively explained when taking into account that SOL width at JET is about twice as large as that used in TCV simulations. Since the more energetic JET ELM loses the energy faster by parallel transport (increased conduction), less energy gets to the outer boundary which is further out compared to the TCV case.

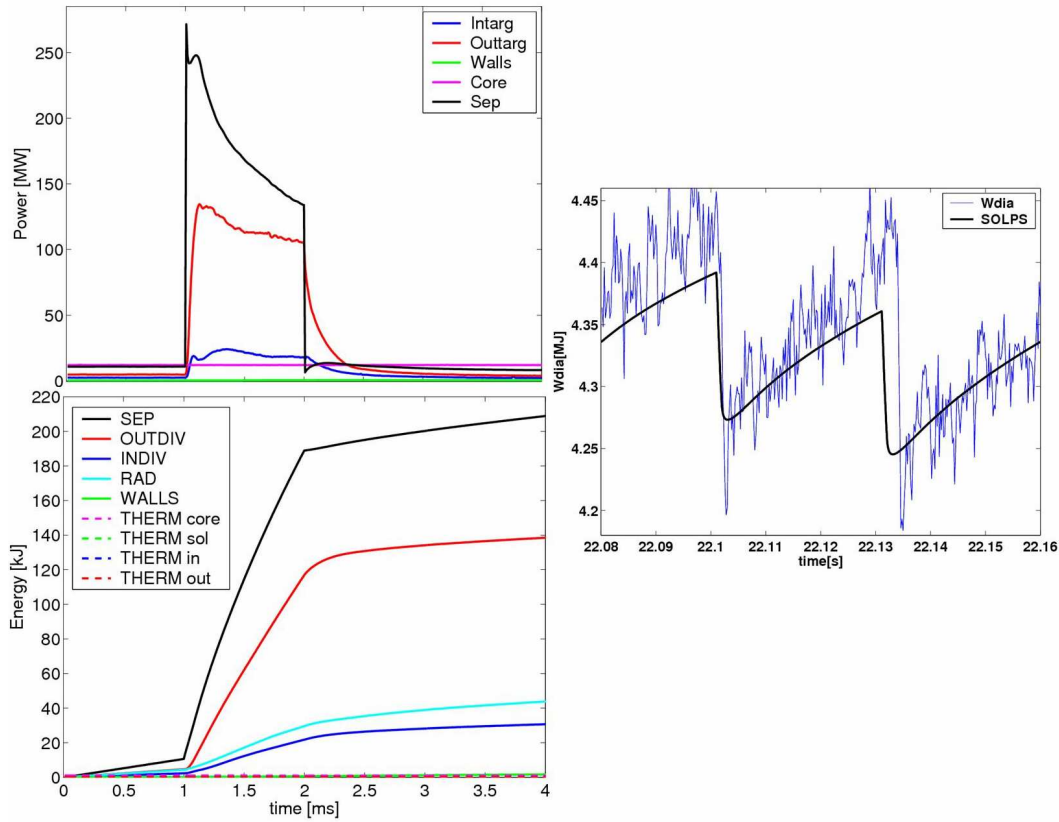


Figure 7.9. *Right:* Drop in plasma energy during the ELM from experiment and SOLPS (corrected by ~ 2.8 MJ to account for core plasma stored energy not covered by the simulation grid). *Left:* Power crossing the boundaries (upper) and corresponding integrated energies (lower).

As seen in **Fig.7.10**, the radiation from photons is about factor of ~ 5 stronger than from the neutrals – a situation very different to the smaller ELMs on TCV, where the radiation energy is more equally shared between B2.5 and EIRENE. This is connected with the low temperature at the inner target responsible for the strong radiation in that region which practically represents the main part of the radiation from B2.5. Like the TCV case, however, the dominant contribution to the photonic radiation originates from the low charge states of carbon C^{2+} , C^{3+} . **Fig. 7.10** also shows the total radiated power and energy predicted by SOLPS including the fractions corresponding to different regions of the grid. In contrast to the TCV ELMs, the radiated power is almost exclusively found at the targets and very small fraction is found in SOL with practically nothing inside the separatrix.

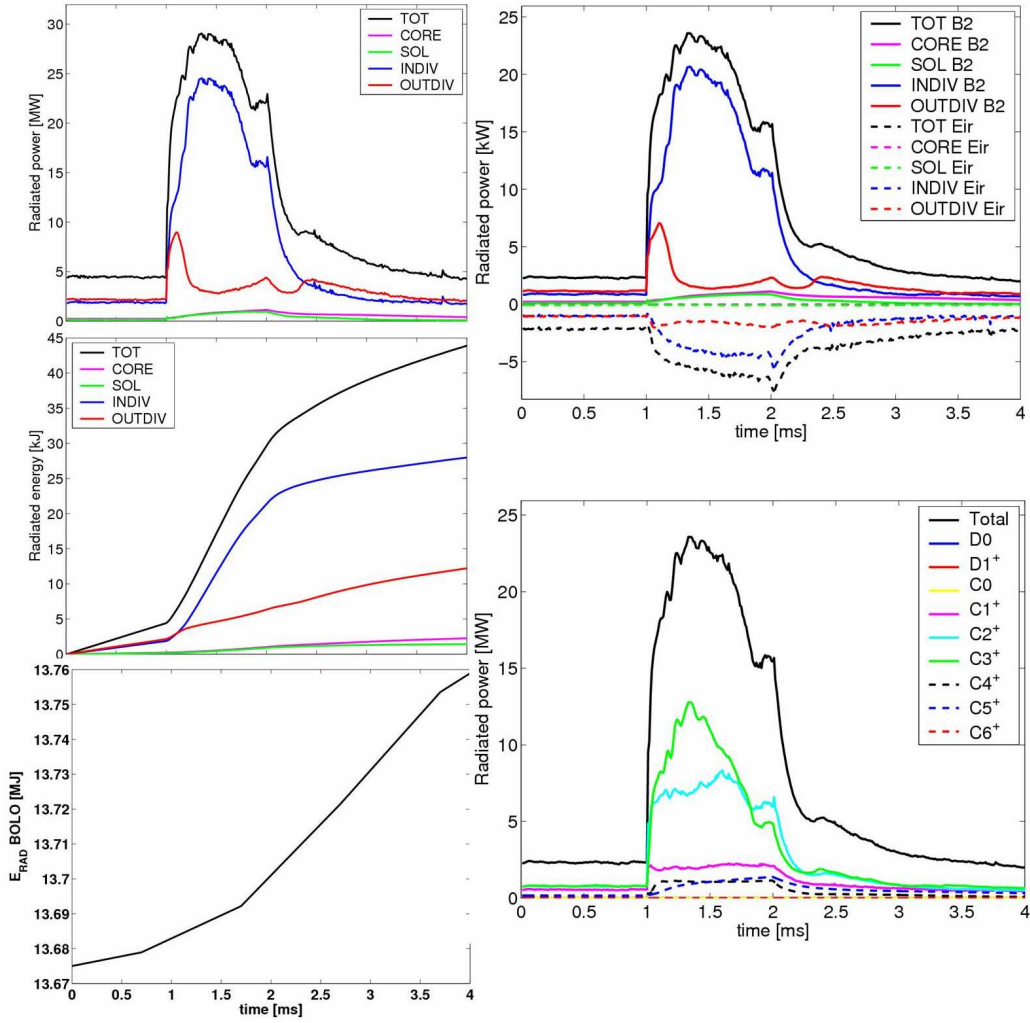


Figure 7.10. *Left upper:* radiated power in different regions of plasma. *Left centre:* energy radiated in those regions. *Left lower:* radiated energy during the ELM cycle measured by bolometers from #73394. *Right upper:* SOLPS radiated powers from photons (B2.5) plotted as positive and from neutrals (EIRENE) plotted as negative (for clarity only). *Right lower:* radiated power from B2.5 as a sum of the contributions from the species.

A recent upgrade to the JET bolometer system has enabled radiated power measurements on ~ 1 ms timescale, allowing ELM induced radiation to be at least partially studied [201-202]. **Fig.7.10 lower left**, includes the data obtained by this new system from the discharge #73394, which is a vertical target equilibrium, similar to #58569 with the exception of a slightly higher plasma current: $I_p=2.4$ MA. The experimental radiation energy during the ELM cycle is about ~ 40 -50 kJ, slightly more than the code predictions, but factor of ~ 1.5 is reasonable agreement. The SOLPS ELM provokes an asymmetric radiation distribution strongly favouring the inner divertor. This is not surprising taking into account the low T_e during the ELM there. Now it is clear why the power deposited at inner target is so much lower than at outer target. Since the inner divertor in SOLPS is very cold (see **Fig.7.6**), the radiation is very strong there thus removing all the conducted energy.

An approximately linear dependence of this in-out asymmetry on ΔW_{ELM} is reported in [236] for discharges similar to this benchmark case, giving $E_{RAD,IN}/E_{RAD,OUT} \sim 2$ for ΔW_{ELM}

~ 200 kJ. The SOLPS5 simulations overestimate this ratio by factor of ~ 2 with $E_{\text{RAD,IN}}/E_{\text{RAD,OUT}} \sim 24$ kJ/6 kJ (~ 4), but the asymmetry tendency is well reproduced. The total radiation in SOLPS thus represents only $\sim 15\%$ of ΔW_{ELM} , the rest appearing as heat flux at the targets (in the code). In experiment, $\Delta E_{\text{RAD}}/\Delta W_{\text{ELM}} \sim 0.5$ [201-202,236].

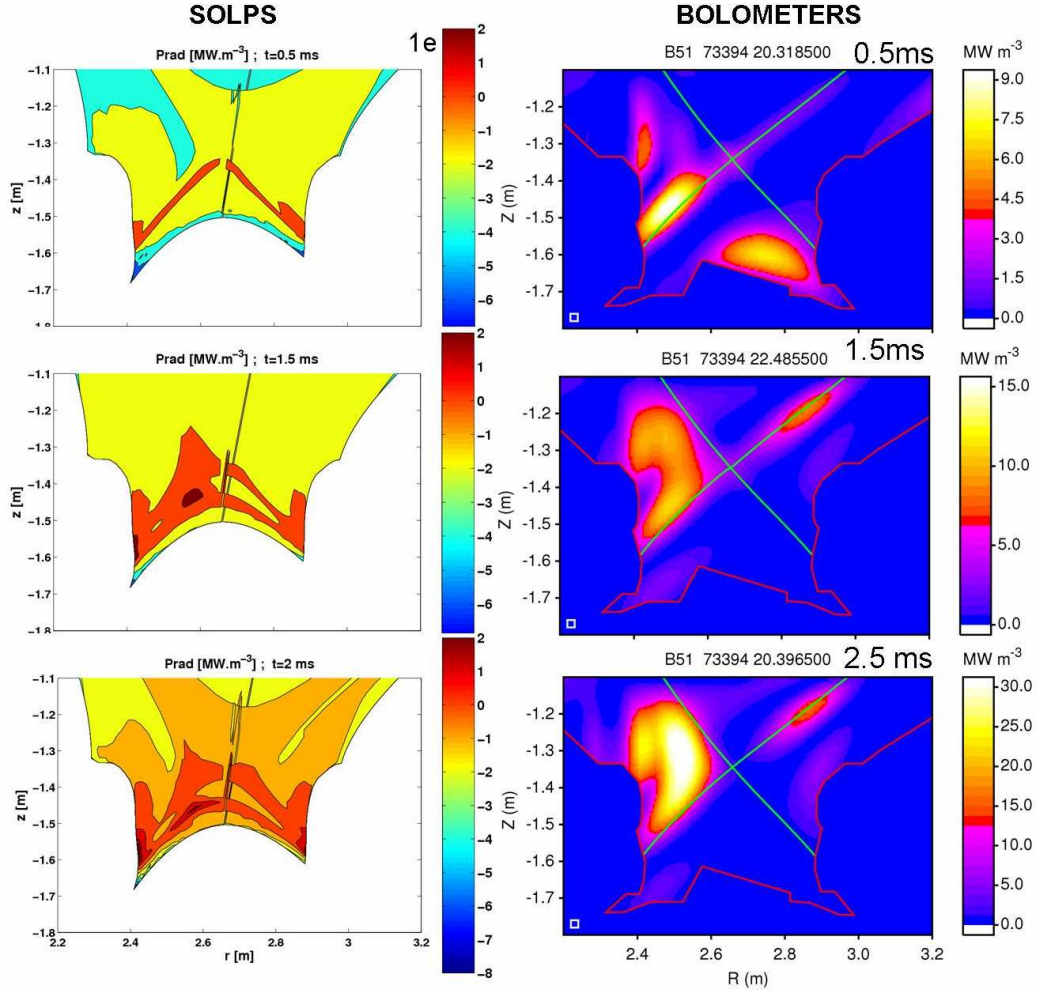


Figure 7.11. Radiated power densities in the divertor region from SOLPS (left) and bolometry from #73394 (right) at different times of the ELM cycle. Top figures correspond to pre-ELM ($t=0.5$ ms where the start of the ELM is $t=1$ ms as in Fig.6.12), middle ones to ELM rise (1.5ms) and bottom ones to ELM peak (2ms). Note, that the SOLPS data are on logarithmic scale, since the spatial resolution is about 10 times higher in SOLPS simulations than in experiment. For the experimental data the real times of the reconstruction are noted above each plot in the center. The numbers at right side indicate the time with respect to the simulated ELM start ~ 1 ms.

Fig 7.11 offers the comparison of the poloidal cross-sectional 3D radiation power density from SOLPS and experiment during the pre-ELM, ELM rise and ELM peak. Even if there is simulated asymmetry in the right direction, SOLPS results show that the radiation is concentrated mostly around the strike points and it can be concluded that SOLPS does not correctly capture the distribution in the divertor during the ELM. It is necessary to note that the bolometry reconstruction at 0.5 ms included the artefact at the outer target [251].

7.2. H-mode with large Type I ELMs at JET

To reach $Q_{DT} = 10$ fusion performance, the baseline reference operation required to satisfy the ITER mission goal, requires good quality H-mode conditions, found in current devices only for operation well above the L-H transition threshold power. Such conditions are associated in current devices with Type I ELMs which, when extrapolated to ITER using existing scaling laws, will have $\Delta W_{ELM} \sim 20$ MJ and $f_{ELM} \sim 1$ -2 Hz [110]. It is now clear, from laboratory experiments in which candidate target materials, CFC or W, are exposed to the high transient heat loads provoked by such ELMs, that material erosion will place severe restrictions on target lifetime, effectively preventing operation under these conditions [252]. The high confinement must therefore be sustained but the ELMs mitigated such that energy densities do not exceed ~ 0.5 MJm⁻² on the targets for scaled ELM deposition rise times on the order of 250 μ s [52]. This can only be satisfied for $\Delta W_{ELM} \sim 1$ MJ, corresponding to only ~ 0.3 % of the full stored energy (350 MJ) projected for the $Q_{DT} = 10$ plasma. In fact, the final ITER divertor design, with more inclined inner vertical targets [253], reduces the required ELM energy to $\Delta W_{ELM} \sim 0.6$ MJ, posing an enormous challenge to mitigation schemes.

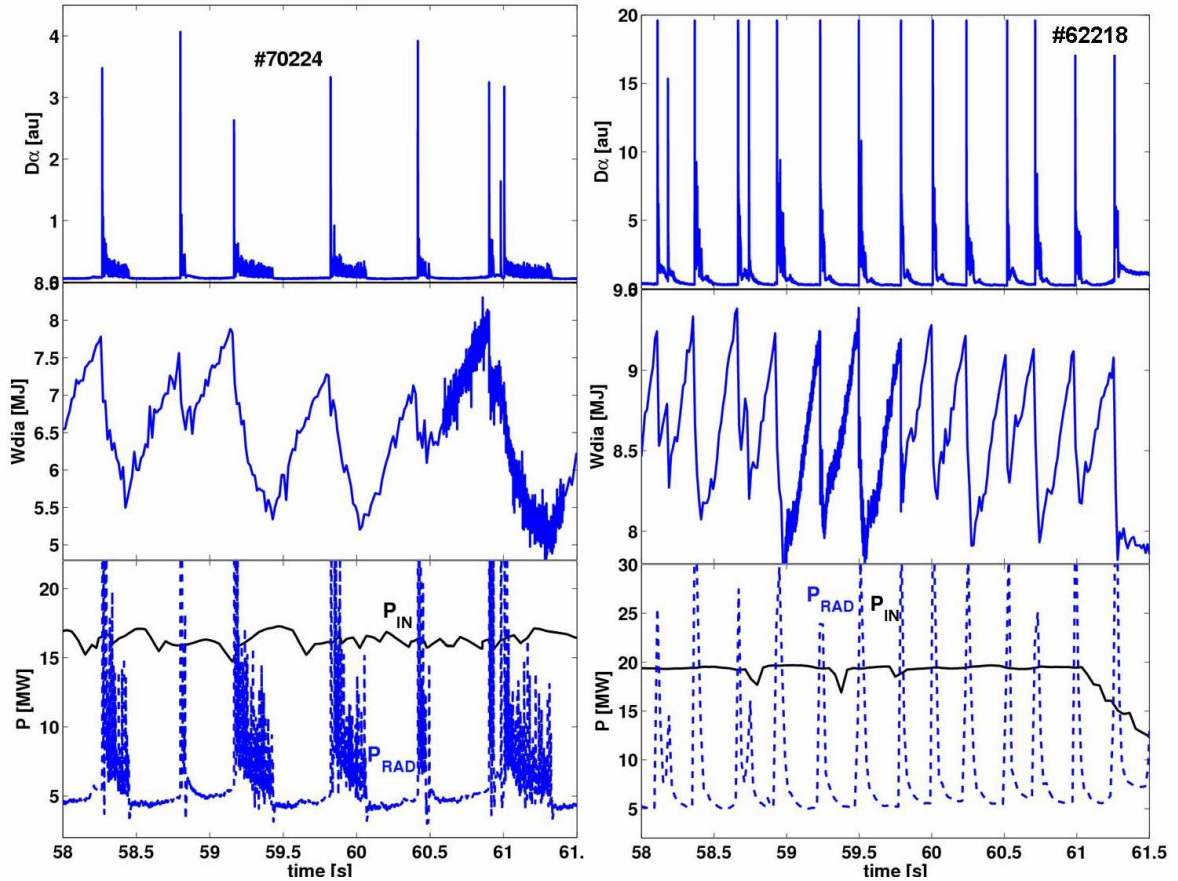


Figure 7.12. *Left:* Time traces of selected relevant parameters of discharge #70224 simulated in this section. Note the very irregular ELMs followed by compound phases. *Right:* same parameters of #62218, a very similar discharge but much more regular ELMs. They are regular enough to allow coherent averaging of IR target data, allowing ELM resolved measurements to be made and compared with SOLPS5 simulations.

Such values of ΔW_{ELM} are in fact readily achievable on JET in high current discharges, even if the pedestal conditions and stored energies of the ITER burning plasma cannot be simultaneously matched. Such discharges, with $I_p = 3.0$ MA, $B_\phi = 3.0$ T, $P_{\text{IN}} = 17$ -20 MW (supplied mostly by Neutral Beam Injection) have been run at JET in dedicated experiments designed to observe the effects of large ELMs on the plasma-surface interaction [201]. The largest ELMs are produced in pulses with little or no gas fuelling and in which $n_{e,\text{ped}}$ and $T_{e,\text{ped}}$ at the pedestal top reach $\sim 6 \times 10^{19} \text{ m}^{-3}$ and ~ 2.5 keV respectively. These parameters yield neo-classical pedestal collisionalities in the range $\nu_e^* = 0.03$ -0.08, encompassing the value expected on ITER and have plasma stored energies in the range $W_{\text{plasma}} \sim 8$ MJ. They often have large, sporadic Type I ELMs, with some events approaching an ELM energy loss of 1 MJ. Following the same procedure as for the benchmark in previous section, a first attempt has been made to simulate such ELMs with SOLPS5. The preliminary results are reported in this section.

The chosen reference discharge, #70224, has practically the same magnetic equilibrium geometry as the lower energy pulse discussed in the previous section. In fact it is simply a higher current, higher field variant of that discharge and forms one of the family of “DOC” (Diagnostic Optimised Configuration) discharges developed at JET for pedestal and plasma boundary studies in H-mode. These discharges have been used extensively to provide contributions to the understanding of the pedestal and ELM dynamics [110]. By increasing field and current at the same time, all discharges have the same edge safety factor and so ELM transport and energy losses etc can be studied, for example, at constant SOL connection length.

Relevant (to this study) time traces from the reference pulse are shown in **Fig 7.12**. Upstream, SOLPS5 is constrained by pedestal profile measurements of the pre-ELM phases from the new JET High resolution Thomson Scattering System (HRTS), the Lithium beam, ECE and CXRS diagnostics. Upstream profiles during the ELM were not available for this pulse and thus HRTS measurements from #77187, a very similar, more recent pulse, were used as an indication for the SOLPS simulations. At the targets, simulation results are compared with profiles of n_e and T_e obtained with the JET divertor Langmuir probe (LP) array. Unfortunately, many of the key probes at critical locations on the vertical targets were no longer functioning at the time of this experiment and so the data are not of very good quality. Only steady state (inter-ELM) profiles are available and even these are of limited use. Note that vertical sweeping of these high current plasmas is not permitted on JET owing to the risk of disruption and the large forces which could result. As a result, the quasi continuous radial profiles achievable for the 2.0 MA pulse discussed in the previous section are unobtainable at higher current.

The new fast bolometry system (see section 5.1.2) provides the time variation of the total radiated power, from the repeat discharge #70225. Unfortunately, the strike point positions in #70224 were placed just too low on the vertical targets for the tangentially viewing, fast IR camera (KL3B) to be able to extract surface power density profiles with sufficient spatial resolution. In addition, the erratic nature of the ELMs (see **Fig. 7.12 left**) would in any case make high time resolution measurements difficult with the tangential camera (the only system capable of proper vertical target viewing). Instead, an earlier, essentially identical 3.0 MA, 3T discharge #62218 has been used. The strike points in this DOC pulse were slightly higher and the ELMs more regular, allowing coherent averaging of the IR data and acceptable spatial resolution.

For the simulations, essentially the same input settings were used as for the benchmarked case of section 7.1. The same flux limiters as in Chapter 6 were applied, the power crossing the core boundary fixed at $P_{\text{SOLPS}} = 14$ MW and the density feedback used on a midplane separatrix value of $1 \times 10^{19} \text{ m}^{-3}$.

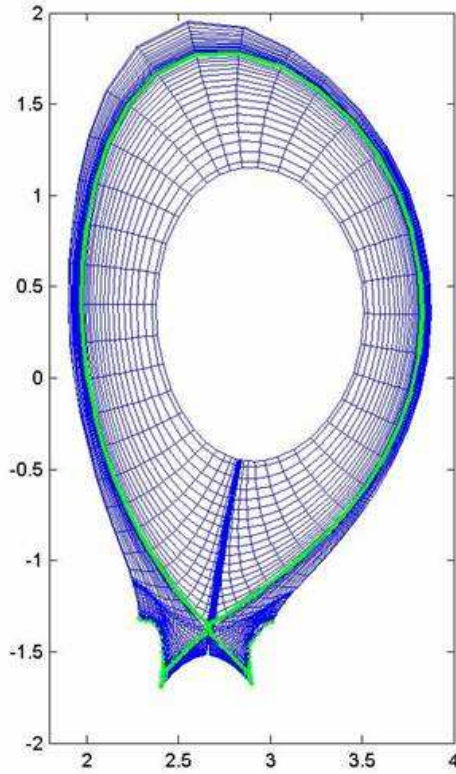


Figure 7.13. Grid used for the simulation of the JET discharge #70224 and Type I ELM; green lines represents the separatrix. This grid is very similar to the case analyzed in section 7.1 (see **Fig.7.2**), only the strike points are slightly lower here.

The simulations have been performed on the grid shown in **Fig. 7.13**, extracted from pulse #69818, of which #70224 is a repetition. Both are extremely similar to the grid used in Section 7.1 for the reference 2.0 MA pulse (both are DOC equilibria as described above). The reason for using an equilibrium from #69818 is simply that pre-ELM simulations began on this grid before the more recent pulses, with improved diagnostics, were performed. The grid is again very deep extending ~ 40 cm inside and ~ 6 cm outside the midplane separatrix. All other grid properties are identical to that used for the simulation of #58569. As before, poloidal drifts are switched off.

7.2.1. Simulation of large Type I ELM at JET

Broadly the same modelling strategy as in previous sections is used again here for the larger ELM. In the pre-ELM phase, the radial variation of D_{\perp} , χ_{\perp} and v_{\perp} coefficients is applied everywhere except in the divertor legs, where the flat radial profiles with values of $D_{\perp} = \chi_{\perp e} = \chi_{\perp i} = 1 \text{ m}^2 \cdot \text{s}^{-1}$, $v_{\perp} \sim 0 \text{ m} \cdot \text{s}^{-1}$ are set. It is worth noting that the convergence process of this simulation was the longest of those so far reported. A solution combining high input power, a rather deep grid and low $n_e^{\text{sep}} = 1 \times 10^{19} \text{ m}^{-3}$ was particularly difficult to establish for the code. Upstream results from this simulation, together with the experimental data, are compiled in **Fig.7.14**.

To achieve a reasonable match between code and experiment, values of $D_{\perp} = 0.1 \text{ m}^2 \cdot \text{s}^{-1}$, $\chi_{\perp e} = 0.5 \text{ m}^2 \cdot \text{s}^{-1}$ are required in the pedestal region (cf. $D_{\perp} = 0.007 \text{ m}^2 \cdot \text{s}^{-1}$ and $\chi_{\perp e} = 0.25 \text{ m}^2 \cdot \text{s}^{-1}$

for the TCV Type III ELMing pedestal). These higher I_p shots have low pedestal collisionality and operate at low density ($n/n_{GW} \sim 0.4$). In this case, $T_i \neq T_e$ in the pedestal region, nor do they have the same profile shape. This is in contrast to the benchmark JET case of Section 7.1 at higher fuelling and higher density, where $T_i \sim T_e$ throughout the profile. To match the very steep T_i pedestal, $\chi_{\perp i} = 0.03 \text{ m}^2 \text{ s}^{-1}$ is required there. Variation of the ratio $\chi_{\perp e} / \chi_{\perp i}$ (assuming ion-electron energy equipartition) was sufficient to find a reasonable fit to the experimental profiles of T_e , T_i .

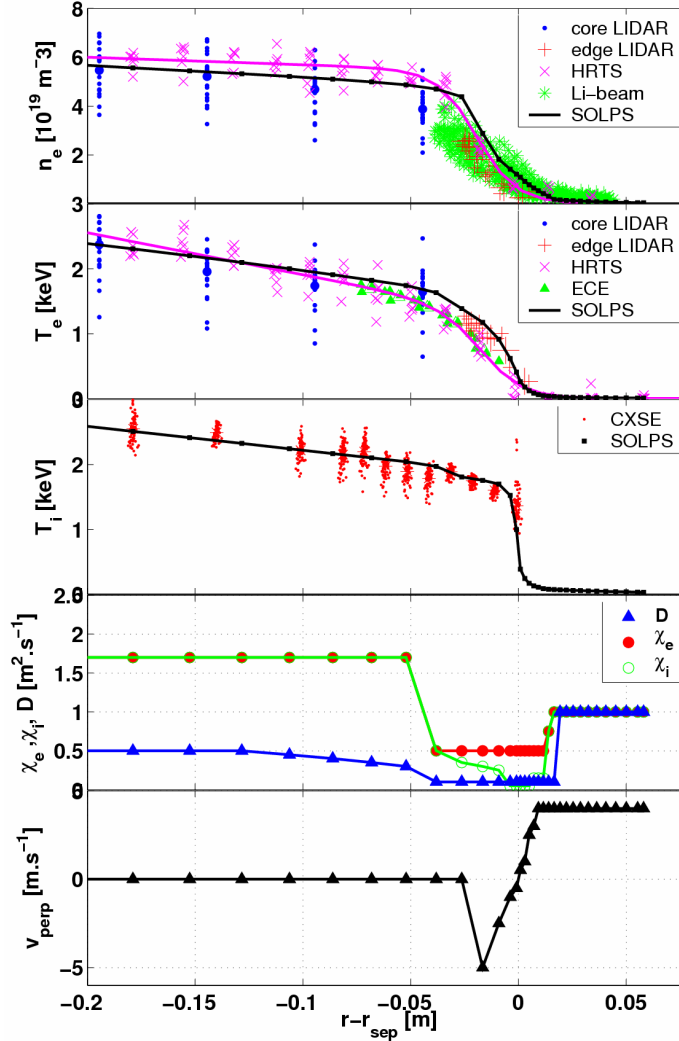


Figure 7.14. Pre-ELM upstream n_e , T_e , T_i profiles for #70224, experimental data from different diagnostics (in colours) and SOLPS data (black lines). The two lower plots show the corresponding radial profiles of D_{\perp} , $\chi_{\perp e}$, $\chi_{\perp i}$ and v_{\perp} .

In common with the lower power JET benchmark pulse and in contrast to TCV, an inward particle pinch appears to be required in the pedestal region if the steep experimental density profile is to be satisfactorily matched. It also appears to be a feature of high power H-mode shots on JET, since similar modelling with SOLPS5 of ELMing H-mode discharges on ASDEX Upgrade [211] and TCV [209] did not require a finite v_{\perp} .

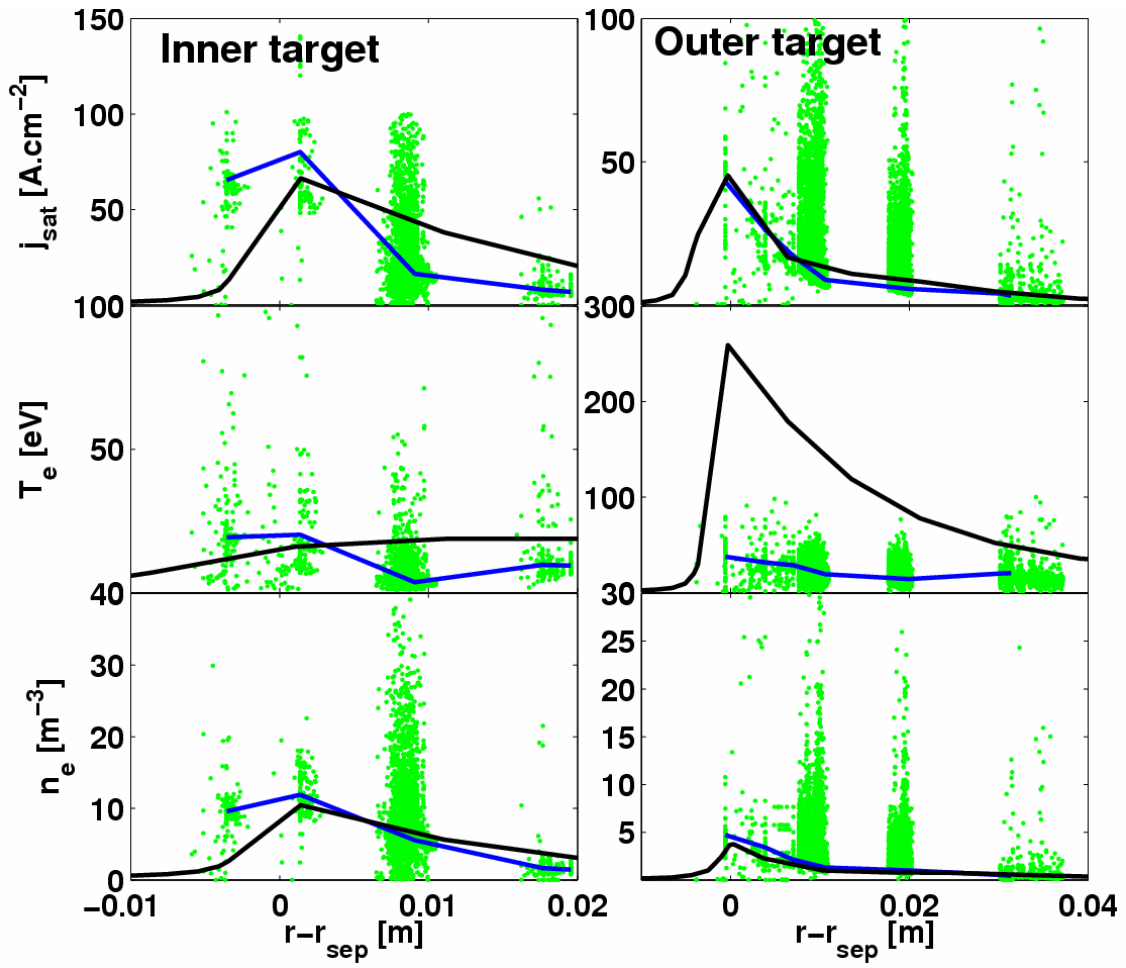


Figure 7.15. Pre-ELM target profiles of j_{sat} , T_e and n_e from SOLPS5 (black) compared with data from target LPs (green). Blue curves represent the averaged pre-ELM profiles from LPs.

Fig.7.15 shows the target profiles of j_{sat} , T_e and n_e from SOLPS compared with experimental data obtained with the JET divertor Langmuir probe (LP) array. The agreement between code and experiment is fair, although, as mentioned earlier, the lack of vertical strike point sweeps means that there are only a few points on the measured radial (LP) profiles and the agreement can only be considered indicative. At these high power levels, there is unfortunately no data in the upstream main SOL with which to better constrain the transport coefficients there. With these caveats in mind, this inter-ELM solution is nevertheless considered a good basis from which to pursue time-dependent simulations of the large Type I ELM.

The ELMs in #70224 (**Fig. 7.12**) have ΔW_{ELM} in the range 0.5 – 0.9 MJ [201]. These ELM events have been analyzed in terms of energies deposited at the targets and main walls in [201], in terms of the radiation losses in [202] and in terms of comparison with the kinetic PiC simulations in [237]. Since most of the data to be used for the comparison with the SOLPS are available for $\Delta W_{\text{ELM}} \sim 0.7$ MJ, this was the target expelled energy to aim at in the simulations through the usual mechanism of increasing the transport coefficients. The time duration of this enhanced transport is $t_{\text{ELM}} = 2$ ms (estimated from the ELM perturbation at target signals from D_α).

As in section 7.1, the simulation of this ELM proceeds by enhancing transport everywhere except in the divertor legs. The radial extent from -20 cm to +2.5 cm has been used for the enhanced transport during the ELM in order to get the reasonable n_e , T_e profiles during the ELM (in the same trend as indicated from experiment in **Fig.7.16** -see later). The coefficients D_\perp and $\chi_{\perp,e}$ have been increased in the pedestal region by factors of ~ 60 and ~ 30 respectively and $\chi_{\perp,i} = \chi_{\perp,e}$ assumed. The **Fig.7.16** shows the experimental HRTS n_e , T_e pedestal profiles at different times in the ELM cycle for an ELM in pulse #77187. The pre-ELM profiles are slightly different from those in #70224 (see **Fig. 7.14**), but can be used as a guide for the ELM phase simulations given the relative similarity of the two discharges.

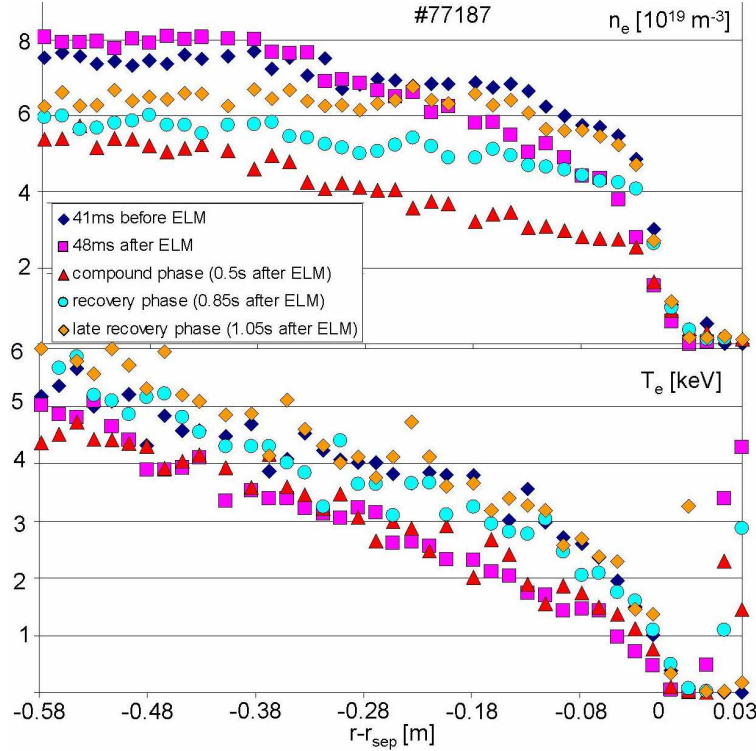


Figure 7.16. Upstream profiles of n_e and T_e from HRTS during different times within the ELM cycle of one event in pulse #77187 [254].

The upstream n_e , T_e and T_i profiles resulting from these simulations with corresponding transport coefficients are plotted in **Fig.7.17**. Since data are available only ~ 42 ms after the ELM peak, the SOLPS5 “ELM” profiles correspond to ~ 20 ms after the ELM was launched. The experimental profiles corresponding to the pre-ELM and ~ 42 ms after the ELM peak from HRTS in #77187 are also included, not really to constrain the SOLPS “ELM” profiles but as an indication of the profile behaviour during the ELM cycle. Given that the pre-ELM profiles from #77187 are slightly higher than those of #70224 matched by the simulation and that the “after-ELM” profiles from #77187 are obtained later in the cycle than those of SOLPS5, the simulated profiles, which are bounded by the experimental envelope, can be considered reasonable.

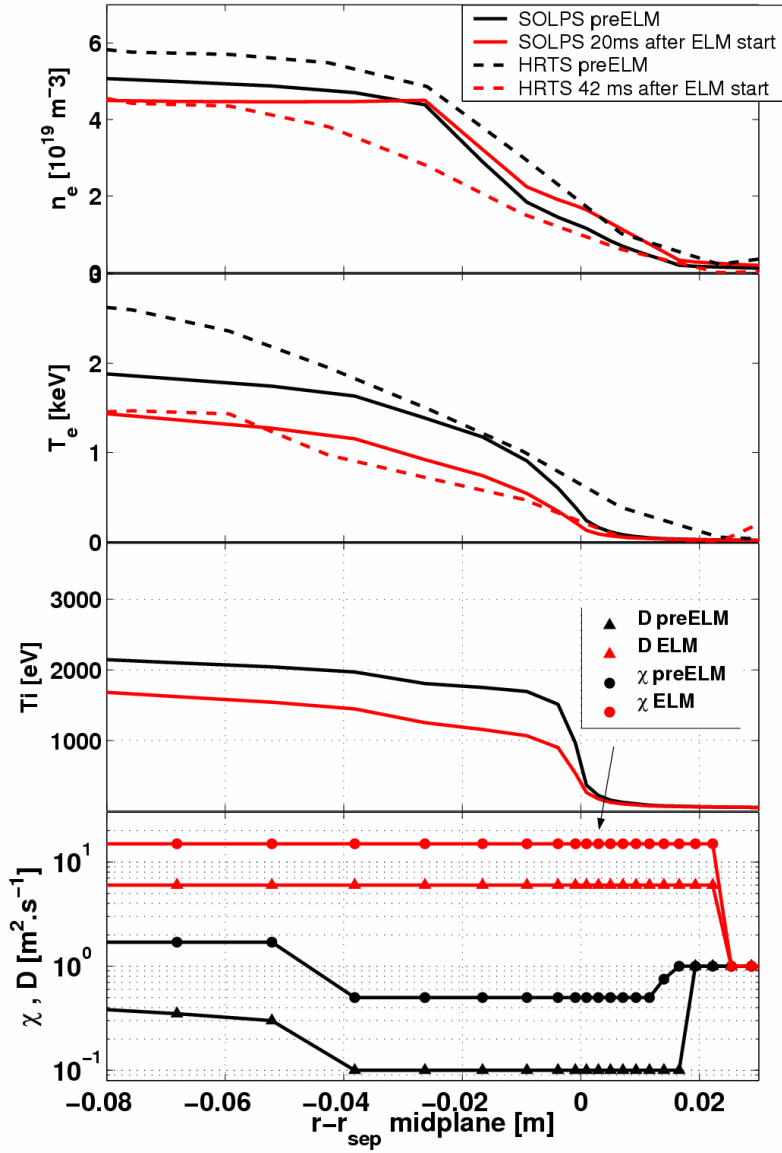


Figure 7.17. Simulated upstream profiles of n_e , T_e and T_i in the pre-ELM phase and 20 ms after the ELM start compared with the data from HRTS from a different, but similar pulse, #77187 where profiles at 42 ms after the ELM are available. The experimental data here serve only as an indication, since there are no experimental data during the ELM available from the simulated discharge #70224 for which the pre-ELM is matched by SOLPS. Simulation #29434.

Fig. 7.18 compiles the SOLPS5 j_{sat} and P_{\perp} profiles in steady state and after expected arrival of the ELM pulse in the divertor ($\sim 200 \mu\text{s}$ – corresponding to the experimentally observed peak of P_{\perp} from IR thermography – see **Fig. 7.20**). As mentioned earlier, experimental LP data during the ELM are unfortunately unavailable for these pulses and the only useful target information comes from coherently averaged IR measurements during the similar pulse #62218 with more regular ELMs at similar ΔW_{ELM} . The target power load profiles obtained from this IR analysis are shown in **Fig. 7.19**. The time evolution of the peak power flux density at both targets obtained from the same analysis, along with the corresponding SOLPS data may be found in **Fig 7.20**.

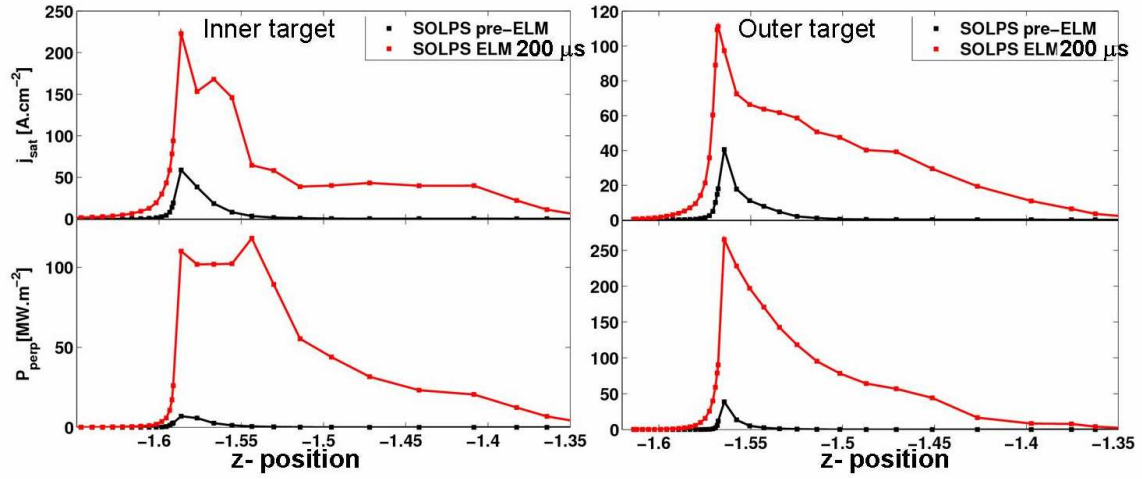


Figure 7.18. Simulated target profiles of j_{sat} (upper) and P_{\perp} (lower) during the pre-ELM and 200 μs after the transport coefficients have been increased, corresponding approximately to the experimentally observed peak of the IR derived power fluxes. Note that unlike elsewhere the profiles are plotted against the z -coordinate of the targets as it is in the case of the experimental profiles on **Fig.7.19**

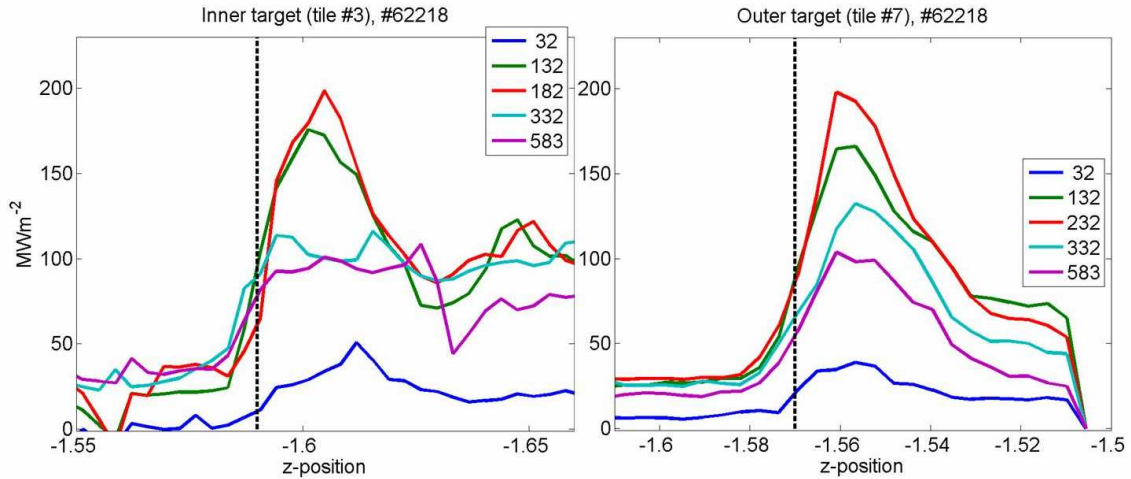


Figure 7.19. Coherently averaged power flux density profiles on the inner (left) and outer target tiles measured by the tangentially viewing IR camera at different times in the ELM cycle of discharge #62218. Extracted from [255]. Note that at inner target the x -axis is in opposite direction compared to the SOLPS plots in **Fig.7.18**.

The simulated P_{\perp} profiles at 200 μs resemble the coherently averaged IR equivalents in both shape and amplitude, particularly at the outer target, where both code and experimental peaks are $\sim 200 \text{ MWm}^{-2}$. The magnitudes are not, however, reproduced at the inner target, where experiment is approximately twice the simulated value. Interestingly, at the inner target, the simulated profile shape at 200 μs matches rather well the experimental counterpart at 332 μs . The experimental profiles appear to be broader during the ELM compared to those from SOLPS. This may well be due to the presence of strong filamentary activity in experiment – physics not included in the code. Such filaments are not present in the inter-ELM phase, where simulation and experiment match well. It is also clear, as for the

TCV ELM, that the simulations indicate a more rapid rise and fall of the power flux than observed in experiment [255-256].

The large discrepancy between code and experiment in strike point power flux densities is also evident in the time evolution shown in **Fig. 7.20**. Only at the outer target are code and experiment in reasonable agreement in so far as absolute magnitudes are concerned. Even in this case, however, the experimental outer target P_{\perp} falls much more rapidly in time than the simulation, indicating that the ansatz for the time dependence of the ELM expelled energy requires some modification (namely that a rectangular function for the enhancement of transport during the ELM is too crude). The rise time of SOLPS power fluxes is $\sim 200 \mu\text{s}$ for inner and $\sim 100 \mu\text{s}$ for outer target corresponding to the expected times of arrival of the ELM pulses to the divertor plates (estimated from the pedestal experimental values of T_e, T_i and L_{con}).

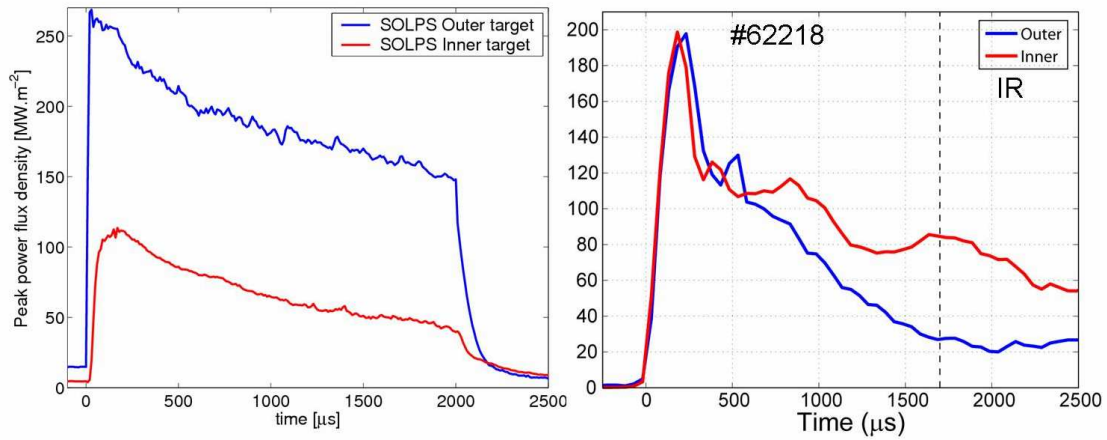


Figure 7.20. Time evolution of the peak (SP) power flux density at both targets from SOLPS5 (left) and coherently averaged IR measurements from #62218 (right) [255].

The in-out asymmetries of the target power deposition will be discussed in more details in the next section 7.2.2.

7.2.2. Energy analysis and radiation

The global energy balance for the ELM simulated here is shown in **Fig. 7.21** in the form of the time evolution of the powers crossing the various simulation boundaries, together with the energy integrated over the full ELM cycle. By definition, due to the initial assumption, the $\sim 14 \text{ MW}$ crossing the core boundary is equally distributed between electrons and ions. Almost all of this power is found on the targets in the pre-ELM phase ($\sim 4 \text{ MW}$ and $\sim 9 \text{ MW}$ on the inner and outer targets respectively). In terms of in-out asymmetry this result ($\sim 1:2$) reasonably agrees with experimental observations, where also approximately factor of 2 is found at high power. Since this is connected with Shafranov shift and greater outboard surface area [222] it is not surprising that SOLPS gets approximately right answer even without drift effect included.

The power crossing separatrix reaches its maximum at $\sim 700 \text{ MW}$ during the ELM and, 2ms ELM duration yields $\Delta W_{\text{ELM}} \sim 750 \text{ kJ}$, corresponding roughly to the experimentally measured value (**Fig 7.12**). In common with the pre-ELM phase, the largest fraction of the ELM energy is deposited on the targets 87% (650 kJ), 5% (35 kJ) is radiated and practically none leaves the outer grid boundary. This can be compared with experimental results for pulse

#70224 and other similar discharges in the same series reported in [201]. The main wall energy loads are approximately estimated using a new, wide angle IR camera system on JET [257]. On average the ELMs are found in [201] to deposit between 3-4.5% of ΔW_{ELM} on the main wall limiters, essentially independent of ΔW_{ELM} . Even this small fraction is still more than the value predicted by the simulations (which of course do not account correctly for the filamentary nature of the ELM, filaments which are seen clearly to strike the main walls).

The radiated energy obtained from the simulation is shown in **Fig.7.22**. The power radiated in the pre-ELM phase is only $\sim 2\text{MW}$, somewhat lower than experimentally observed value $\sim 5\text{MW}$. However, it must be taken into account that 5MW is the radiation from the whole plasma volume and not only the part corresponding to the grid. From experiment [202] it is found that inter-ELM radiation distribution for these discharges is always strongly weighted to the inner divertor volume, with in-out asymmetries of ~ 2 , in rather good agreement with SOLPS ($P_{\text{RAD,IN}} \sim 1\text{MW}$, $P_{\text{RAD,OUT}} \sim 0.5\text{MW}$).

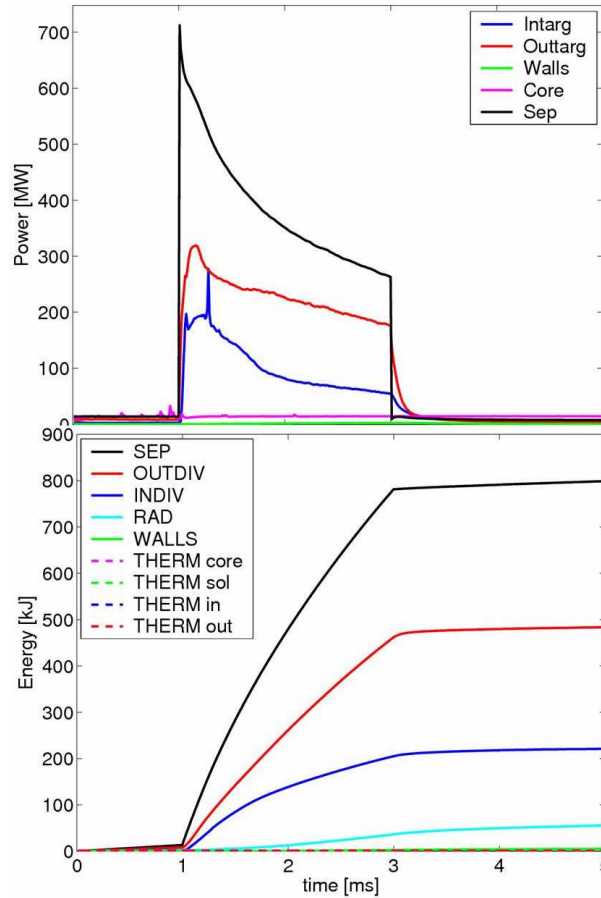


Figure 7.21. Energy balance during an ELM cycle from SOLPS5 showing contributions from different regions of the plasma.

The contribution of photons to the total radiation is slightly higher than that from the neutrals, similar to the TCV cases. During the ELM, radiation amounts to only $\sim 40\text{ kJ}$. Fast bolometry measurements of similar ELMs [201-202,254] (**Fig.7.23 left**), show, however, that $\Delta W_{\text{ELM}} \sim 0.7\text{ MJ}$, the radiated energy reaches $\Delta E_{\text{RAD}} \sim 350\text{--}550\text{ kJ}$, around an order of magnitude higher than the value predicted by SOLPS5. The rise time of the radiated power is experimentally $\sim 2\text{ms}$ (as in the simulation), but the energy is integrated over $\sim 6\text{ms}$ (in SOLPS one finds only $\sim 70\text{ kJ}$ during this time). Nevertheless the largest fraction of energy is

seen to be radiated during the ELM rise, so the two values of energy from SOLPS and bolometers can be compared [201].

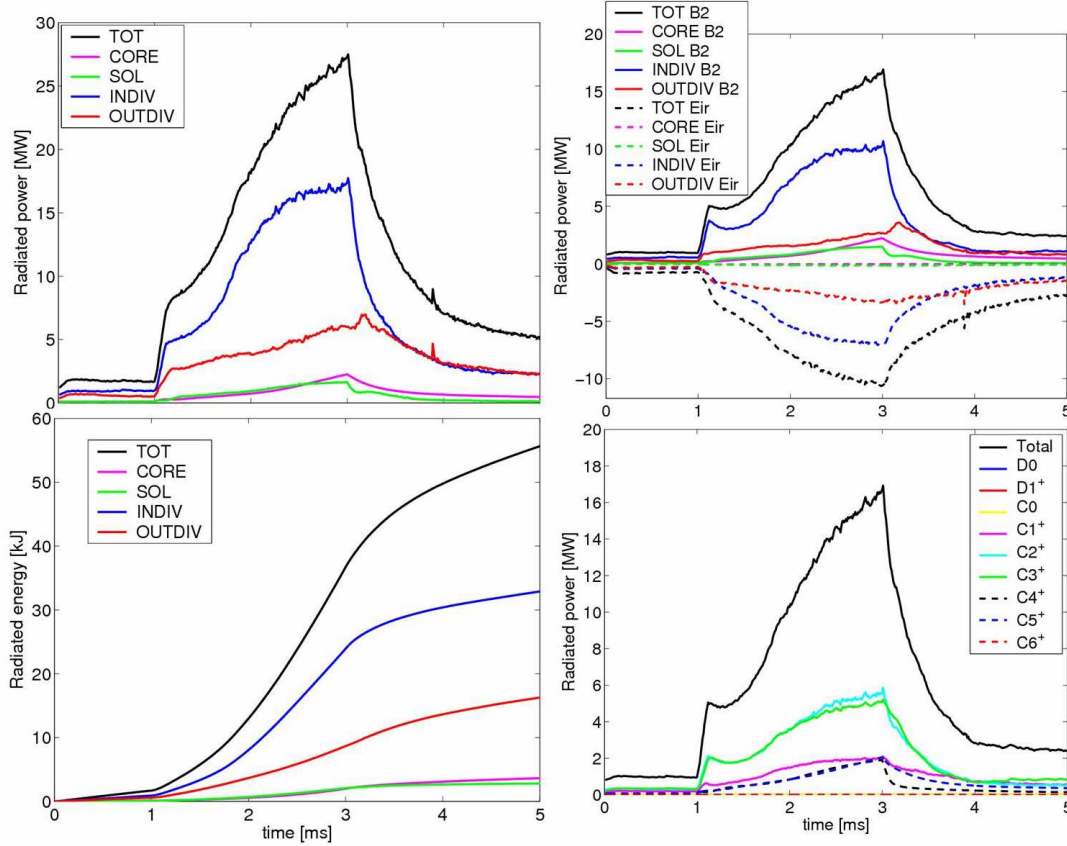


Figure 7.22. SOLPS radiated powers and energies from different regions of plasma and different species during the ELM cycle. Pre-ELM $P_{\text{RAD}} \sim 6.2$ MW from experiment #77187.

In [201-202], ΔE_{RAD} is found to increase approximately linearly with ΔW_{ELM} up to ΔW_{ELM} in the region of 0.6 MJ. This is attributed to the ablation or thermal decomposition of thick layers on the inboard target, accumulating there as a consequence of the erosion migration processes often seen in carbon dominated, single null divertor tokamaks operating with forward toroidal field [21]. Such effects are not included in the SOLPS5 description of material erosion, which considers only physical and chemical sputtering.

The SOLPS results in **Fig. 7.22** show that $\sim 94\%$ of the total radiated energy during the ELM is found in the target vicinity, strongly favouring inner target, with an in-out asymmetry of ~ 3 . The rest is found in core ($\sim 1.5\%$) and in the SOL ($\sim 1.5\%$). As seen in **Fig. 7.24**, the experimental data from fast bolometry show that the radiated fraction in the divertor region below the X-point (radiation below $z = -1.1\text{m}$) is $\sim 80\%$ for ΔW_{ELM} up to ~ 0.7 MJ. This is somewhat lower, but in the range of the simulated values. Moreover, the in-out asymmetry of the measured radiation is found experimentally to be in the range 2.5-5.5 (**Fig. 7.25**), encompassing the SOLPS prediction (~ 3 at $\Delta W_{\text{ELM}} \sim 0.7$ MJ) This agreement is probably a bit artificial taking into account that as mentioned above, SOLPS cannot possibly take into account the enhanced erosion at high ELM energy. However the asymmetry of radiated power is predicted by SOLPS in the right direction. This can be seen also on **Fig. 7.23 right**, where a tomographic reconstruction of the ELM radiation distribution averaged over the $\sim 5\text{ms}$ is shown.

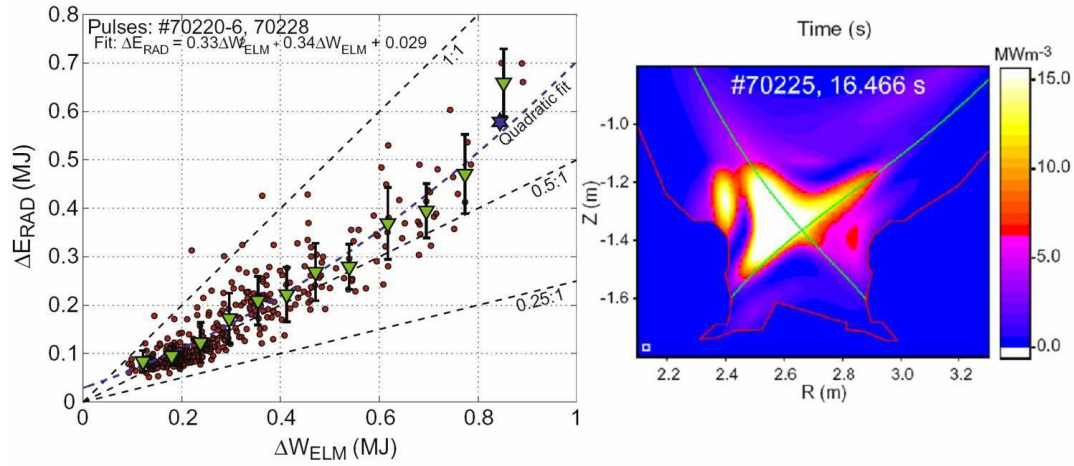


Figure 7.23. *Left:* ΔE_{RAD} at the ELM crash vs. ΔW_{ELM} for all ELMs found in a series of 3.0Ma pulses, including the reference pulse #70224. Green triangles are the mean values of the data over short intervals in ΔW_{ELM} . For $\Delta W_{ELM} \sim 700$ kJ (as in the SOLPS5 simulation) $\Delta E_{RAD} \sim 300$ -500 kJ, 10 times higher than found in the simulation. Extracted from [201]. *Right:* Tomographic reconstruction of the ELM radiation distribution averaged over first ~ 5 ms of the ELM cycle from #70225 with $\Delta W_{ELM} \sim 850$ kJ and $\Delta E_{RAD} \sim 580$ kJ. Figure from [201-202].

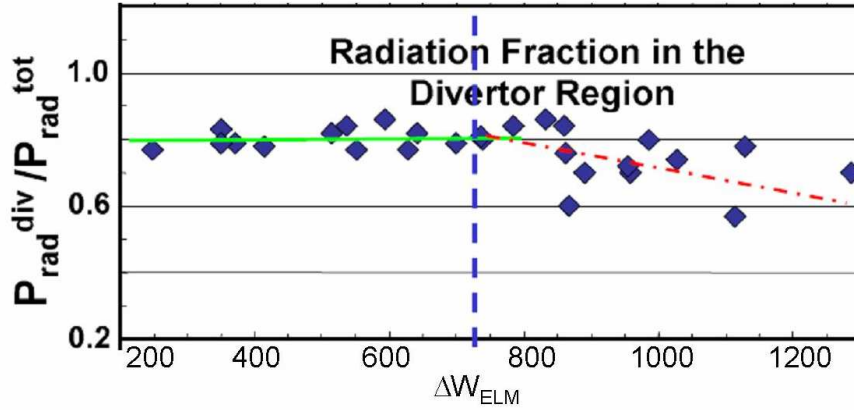


Figure 7.24. Fraction of power radiated in divertor region from the total radiation measured by bolometers. Extracted from [254].

The power deposited at the targets which represents ~ 650 kJ ($\sim 86\%$) in SOLPS. From this energy the fraction of ~ 450 kJ is found on outer and ~ 200 kJ at inner target. This yields the in-out target power load asymmetry ratio ~ 0.4 , what is in absolute disagreement with experimental measurements. Integrating of the experimental P_{\perp} (in **Fig.7.18** and **Fig.7.19**) for both targets yields an in-out target power deposition asymmetry of ~ 1.7 . This apparent in-out ELM energy asymmetry is a well known experimental result (the in/out ratio of deposited energy ~ 2 was found in [236]) and has already been alluded to in the previous section, where a similar (even worse) trend was also observed for the lower energy ELM. More details about in-out asymmetry of target deposited power loads during the ELMs are found in the next section 7.3.

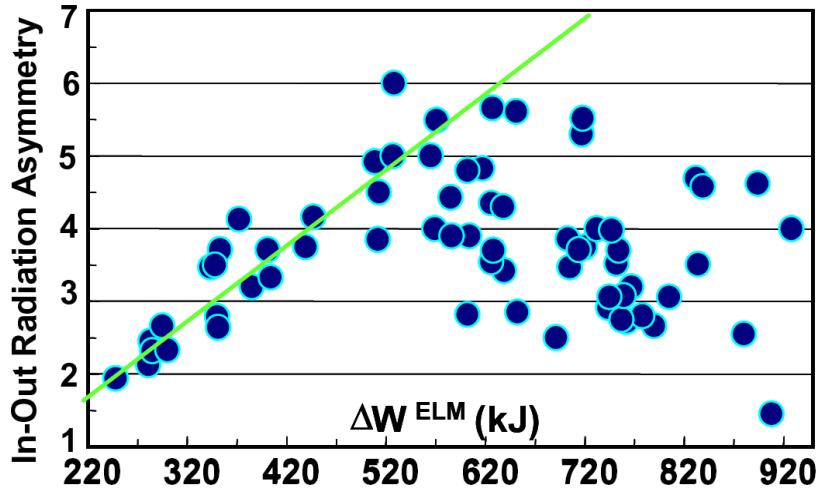


Figure 7.25. Fraction of power radiated in inner to outer divertor regions measured by bolometers for ELMs of different sizes. Extracted from [202]. For $\Delta W_{ELM} \sim 700$ kJ this ratio is between 3 and 7.

7.3. Simulations of JET ELM with toroidal pedestal rotation

Table 7.1 summarizes the experimental and simulated ratios of the heat deposited at the targets during the four different ELMs simulated in this thesis. The disagreement between experiment and SOLPS in both JET cases has been clearly reported in the previous two sections of this chapter. The TCV cases were discussed in the previous chapter and here the focus will be on JET ELMs, especially on the case with $\Delta W_{ELM} \sim 200$ kJ. In strong contradiction to SOLPS, experimentally found in/out target power ratio is ~ 1.7 - 2 for the JET ELM in FWD DOC-L configuration [236]. In order to reproduce this by SOLPS, the inclusion of negative $v_{||}$ is expected to be required [242].

	TCV		JET	
Type of ELM	Type III; RWD	Type I ; FWD	Type I; FWD	Type I; FWD
ΔW_{ELM}	~ 600 J	~ 3 kJ	~ 200 kJ	~ 700 kJ
SOLPS $E_{DEP,IN}/E_{DEP,OUT}$	~ 1.3	~ 1.7	~ 0.22	~ 0.45
Experimental $E_{DEP,IN}/E_{DEP,OUT}$?	?	~ 1.65 - 2	~ 1.7

Table 7.1. SOLPS in-out ratios of powers deposited on the targets for four different ELMs simulated in this thesis. The experimental values are given only for JET cases [255].

The pedestal rotation effects on the ELM simulation have been included to the simulation of benchmarked low power Type I ELMing H-mode #58569 by adding the different values of toroidal velocity at the inner core boundary in the same way as in the chapter 6. These simulations are very time-consuming as a consequence of the long time required for the effect of toroidal velocity to diffuse from inner core boundary to the pedestal region and therefore the simulations with $v_{||}$ had to be performed on the much narrower grid

extending only 7 cm inside LCFS (see **Fig.7.26**) compared to the rather deep one used in the benchmark simulations in section 7.1 (25 cm inside the separatrix at the midplane). It is important to note, that this narrower grid belongs to JET pulse #50401 (for which the simulations in the past were performed and therefore it was easier to readily use them for this toroidal rotation test), which as seen on **Fig.7.26**, has different divertor configuration and slightly different plasma parameters ($B_\phi=2.5\text{T}$, $I_p=2.5\text{MA}$, $\bar{n}_e = 6.5 \times 10^{19} \text{m}^{-3}$, $W_{\text{plasma}} \sim 5\text{MJ}$, $P_{\text{IN}} \sim 12\text{MW}$ and $\Delta W_{\text{ELM}} \sim 500\text{kJ}$), compared to #58569 ($B_\phi=2\text{T}$, $I_p=2\text{MA}$, $\bar{n}_e = 4 \times 10^{19} \text{m}^{-3}$, $W_{\text{plasma}} \sim 4\text{MJ}$, $P_{\text{IN}} \sim 14\text{MW}$ and $\Delta W_{\text{ELM}} \sim 200\text{kJ}$). Therefore it is not surprising that the ratio of the in/out target deposited powers during the ELM (0.6) is not exactly the same as in the benchmarked case (0.22). However, the aim here is to study the effects of inclusion of toroidal rotation to pedestal region of simulation grid.

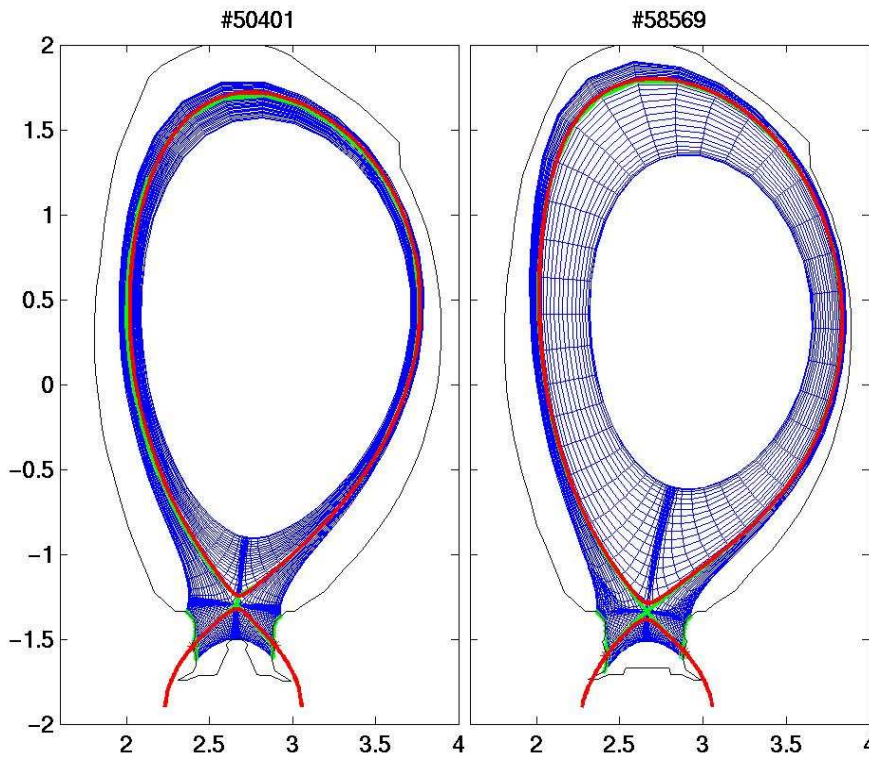


Figure 7.26. Simulation grid for JET discharge #50401 simulated with $v_{||}$ (left) and JET discharge #58569 simulated as benchmark with EDGE2D/NIMBUS (right). Compared to the grid in **Fig. 7.2** (extending 24cm inside and 4cm outside the separatrix) this one is much narrower, extending only 7cm inside and 3.7cm outside the separatrix (red line= separatrix from EFIT, green line=SOLPS separatrix). The discharges have different divertor configuration and slightly different plasma parameters.

Since the pressure in this JET ELM simulation is rather high compared to small TCV Type III ELM cases, higher values of $v_{||}$ were required to be applied in order to see the desired effect. Unlike the small TCV ELMs, the bigger JET ELM is much more conductive and already when crossing the separatrix the heat fluxes are dominantly conductive. The flux limiting coefficient 10 for ions have been applied in all the simulations what makes the ELMs even more conductive. Nevertheless, very interestingly as one can see on the **Fig.7.27** (analogy to **Fig.6.65**) the imposed $v_{||}$ affects the in/out target power asymmetries even for almost purely conductive big JET ELMs. From the ratios $E_{\text{DEP,IN}}/E_{\text{DEP,OUT}}$ for 5 cases with

values of $v_{||} = -10^6$; $-5 \cdot 10^5$; 0 ; $5 \cdot 10^5$ and 10^6 m.s⁻¹ shown on **Fig. 7.27** it can be concluded that toroidal pedestal rotation really influences the SOLPS predicted in-out target power flux asymmetries in the expected manner [242], what is indeed very encouraging outcome. As expected the negative $v_{||}$ yielded the ratio of target deposited powers of ~ 1.2 favoring inner target as observed in experiment. However, it appears that these JET ELMs are indeed too conductive for the FSP approach to be sufficient. The change in asymmetry is not as marked and the values of $v_{||}$ that need to be injected are huge.

In the same fashion as in section 6.3 with analysis of TCV ELMs, all the profiles upstream and at the targets are changed radically, but much more than in TCV case. In this JET case the parameters with completely unphysical values, very far from the experimental data are found. The particle and power fluxes at the both targets increase considerably when toroidal rotation is applied. The massive increase in the upstream and target profiles of temperatures T_e and T_i is also observed (already at the pre-ELM the values are about 10-times higher compared to experiment).

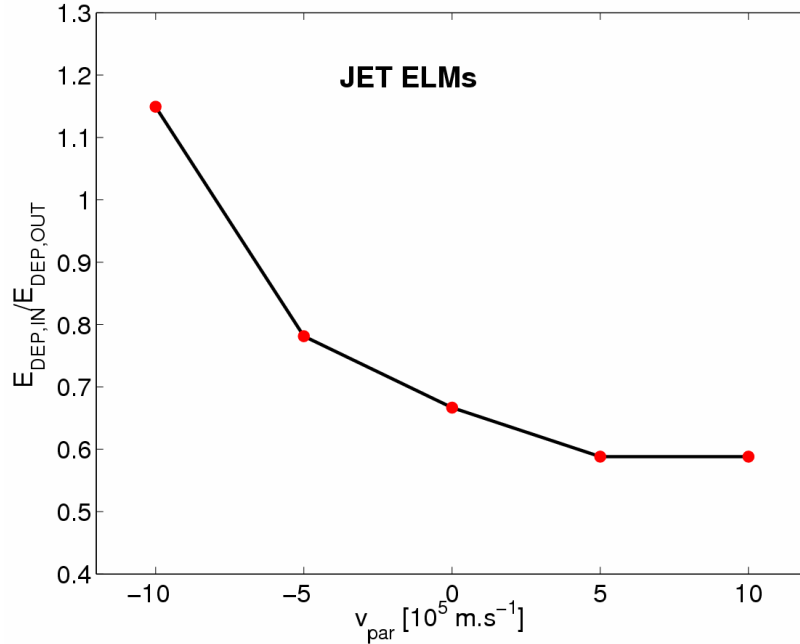


Figure 7.27. Ratios of power deposited on inner and outer target during JET ELM with different values of toroidal rotation. The cases with parallel velocity -10^6 , $-5 \cdot 10^5$, 0 , $5 \cdot 10^5$ and 10^6 m.s⁻¹ are shown. The $E_{\text{DEP,IN}}/E_{\text{DEP,OUT}}$ of reference is higher than the value reported in section 7.XX. Part of profile with negative $v_{||}$ represents case with FWD field and the one with positive $v_{||}$ represents the situation with REV field.

From the above summarized observations it seems to be the case that the inclusion of the parallel velocity to the simulations of conductive JET ELMs would not bring any improvement to the overall result of the SOLPS simulation and that the FSP model most probably cannot be successfully applied on these event with strong conductive nature.

Summary and conclusions

To be successful in designing the first wall and divertor of next step fusion reactor ITER reliable predictions of the peak power fluxes that may arise are needed, particularly during plasma instabilities, so called edge localized modes (ELMs). These modes are associated with the high confinement mode, the baseline scenario for ITER $Q_{DT} = 10$ operation. Unfortunately, however, the improved confinement comes at the price of the transient heat loading on the divertor targets due to the ELMs which, based on empirical scalings from measurements on existing machines, are predicted to deposit ~ 20 times the energy density which is currently thought to be tolerable on the basis of material lifetime. The understanding, control and mitigation of ELMs thus represent one of the primary goals of the fusion community. Despite the considerable efforts expended in this direction in recent years, understanding of the details of ELM-SOL transport and target interactions is still only emerging and considerable effort is required with regard to benchmarking the numerical modelling tools against experimental measurements. This thesis aims to make a contribution in this direction by using one of the most complex plasma boundary modelling code packages, SOLPS5, currently in use to study the time dependent ELM phenomenon and compare results against available experimental data from the TCV and JET tokamaks.

A slightly different version of the SOLPS package has been a major player in the ITER divertor design, now in the procurement stage. The simulations which have been used to guide the design have, however, been exclusively performed for steady state situations. The exercise becomes significantly more complex once time dependence is invoked and so the work described in this thesis is a useful indicator of the extent to which the ELM transient, a naturally kinetic phenomenon, can be successfully described with a fluid plasma code. To do this, a set of 4 H-mode plasmas have been studied, two each on TCV and JET, spanning Type III and Type I ELMs, from high pedestal collisionalities and to values close to those expected on ITER and across a range of ELM energy losses from ~ 700 J to 0.7 MJ. The latter is close to the energy now expected to be the tolerable limit on ITER.

Even though the large ELMs at JET are much closer to the maximum tolerable on ITER (which will require efficient mitigation schemes if they are to be obtained), the Type III ELM is also an important creature in the sense that should Type I mitigation systems fail on ITER, recourse will have to be made to smaller ELM regimes, almost certainly at the expense of confinement (and hence fusion performance). To recover some of this loss, operation at higher than baseline current (17 MA instead of 15 MA on ITER) is one option if all else fails. Despite their potential importance, Type III ELMS have hardly been studied in terms of their dynamics in the SOL. The ELM is an inherently kinetic event and therefore its simulation using a fluid description as in SOLPS can only be an approximation to the real situation. Nevertheless, the low expelled energy (~ 700 J) of the Type III ELM obtained in TCV ohmic H-modes is the “least kinetic” of all 4 events simulated in this work and has thus been treated more completely than the other, larger ELMs.

A common approach has been adopted for all cases: establish a “steady state” inter-ELM solution matching the available experimental data as closely as possible to provide a starting point for the more complex time-dependent ELM simulation. To obtain such a steady state solution, radially varying anomalous transport coefficients must be adopted, accounting for the very different transport levels in the edge and SOL regions due to the presence of the H-mode transport barrier inside the separatrix. As always, these anomalous coefficients represent one of the biggest uncertainties in the SOLPS simulations. The SOL radial particle and heat fluxes include both diffusive and convective components for which no

experimentally verified physics model exists with which their values can be specified for the use in SOLPS. The radial particle and energy fluxes can be specified by an adhoc combination of diffusivity (D_{\perp} , χ_{\perp}) and convection (v_{\perp}) or by each of these components by its own. It is not clear which mechanism drives the cross-field transport in the near SOL but in the mid to far-SOL, experimental observations of turbulent perpendicular transport in TCV SOL are a good basis for the assumption that invoking the convective component via v_{\perp} representing the intermittent nature of the observed turbulent flux is a reasonable approach. Different combinations have been attempted here, using upstream profile measurements of plasma temperature and density as the only guide.

Required values of heat diffusivity ($\chi_{\perp e} \sim \chi_{\perp i}$) in the TCV ohmic H-mode pedestal (transport barrier) region are found to be similar to neoclassical values of ion heat diffusivity in the pedestal region and reasonably consistent with the $\sim \chi_{\perp e}$ found by the core transport code ASTRA. Simulations using with a pure convective radial velocity in the SOL show that for the inter-ELM transport, the measured SOL profiles can only be reasonably matched by a radial v_{\perp} variation which rises in the SOL, consistent with direct measurements of this velocity made by turbulent transport probes. At the targets, reasonable agreement with the ion current density, temperature and density were obtained using both diffusive and convective approaches. This is only possible if the transport coefficients are varied poloidally so that transport barrier is “switched off” in the divertor regions and values of the diffusion coefficients are increased above those found in the upstream SOL. There are nevertheless discrepancies with experiment, notably concerning the plasma electron temperature at outer target which may be due to the neglect of poloidal drifts in the simulations. Concerning heat fluxes, experimental measurements are available only at the TCV outer target, but are in reasonable agreement with the simulation results. An in-out target power deposition asymmetry favouring inner target is found in the simulations, with an opposite trend in the radiation. Total radiation in the simulation grid volume seems to be in reasonable agreement with experiment.

A complete theoretical description of the evolution and transport of the complex ELM instability is not yet available and no elements of current physics models are included in SOLPS. The only possible ansatz with which to simulate the ELM is thus to increase the anomalous transport coefficients found in the pre-ELM steady state during a brief interval corresponding to the ELM duration (roughly estimated from the observed time over which the associated MHD activity is high) such that the total energy expelled during this time is compatible with that measured experimentally. The ELM is known to expel the particles and heat into the SOL on the outboard (low field) side. This has been accounted for by choosing the poloidal extent of the region with enhanced transport during the ELM and imposing a functional form for the variation in this region. However, experimental guidance in this area is relatively poor and this poloidal extent represents a free parameter.

Two approaches have been used to simulate the Type III ELM: an instantaneous local increase in the transport coefficients for the particles and heat and an increase of the outward convective velocity, each with a Gaussian poloidal distribution centred on the outside midplane. A satisfactory match has been found with the upstream profiles of density and temperature measured during the ELM using both approaches. Although, in common the pre-ELM case, it appears that an increasing radial velocity is required to fit the experimental data during the ELM, it must be concluded that there is no unique solution and the different approaches can provide acceptable agreement with the experimental profiles during both the pre-ELM and ELM phases. Less satisfactory agreement is found at the targets during the ELM event. The code overestimates the experimentally measured particle fluxes and temperatures by factor of ~ 2 -3. The heat flux at outer target agrees reasonably well with the

experimental profile, but lack of experimental data at the inner target does not allow comparison with the simulated in-out ELM power load asymmetry.

Since the ELM is above all a kinetic phenomenon, the SOLPS results at the divertor targets have been compared with those from a dedicated Particle-in-Cell (PiC) kinetic transport code calculation for the same ELM. Although reasonable agreement has been found in terms of the absolute magnitude of the total heat fluxes, the comparison reveals two main discrepancies. First, because the electron and ion power fluxes calculated by SOLPS do not take into account the transfer of the energy from electrons to the ions in the sheath, the PiC code yields much higher ion power flux deposited on the targets while in SOLPS much higher electron fluxes are found. This is known to be inconsistent with experiment (though this cannot be experimentally proven on TCV). A correction corresponding to the transfer of heat inside the sheath has been applied to the SOLPS fluxes and closer agreement with the PiC result obtained.

The second major discrepancy concerns the time behaviour of target fluxes during the ELM. The delay in arrival of the ion pulse at the target (compared to the upstream release time) is significantly faster in SOLPS5 than expected on the basis of sonic transit times from upstream to target. Delays consistent with such transport are seen experimentally and found in the PiC simulations, validating the qualitative picture of an ELM expelled on the outboard midplane followed by particles travelling at acoustic speeds to the targets. It appears that this disagreement is connected with conduction dominated heat fluxes in SOLPS which is not the case in PiC simulations. The time-evolution of the SOLPS target heat fluxes has been brought into closer agreement with PiC by modifying kinetic flux limiters in the SOLPS5 simulations, rendering the fluxes more convective. However, it does not appear possible within the scope of the sensitivity studies performed here, to simultaneously achieve expected delays and ion-electron power sharing in the fluid simulations. While in the PiC the shape of the total flux is dominated by the flux of ions in SOLPS, the electrons appear to dominate in SOLPS, shortening the timescales. This benchmark of fluid and kinetic codes has thus demonstrated that the kinetic effects are important even for the “least kinetic” ELM event of those studied here. This presumably becomes even more important as the ELM size increases, but can only be tested to the extent that the appropriate experimental data is available. As a consequence, the tentative conclusion from the work presented here is that the use of SOLPS in a predictive sense for ITER would at best provide indicative results. Much more work is required to investigate the unresolved issues raised by these simulations.

The TCV Type I ELMing H-mode has been simulated in the same manner as the Type III case above. Not only is the type and size of the ELM energy ($\sim 3\text{kJ}$) different, but also the direction of the toroidal field is reversed compared with the Type III case (forward toroidal field (-ve) compared with reversed field (+ve) in the Type III ELM case). It was originally hoped (and planned) that experimental heat flux data at both inner and outer targets would be available by the time these rather recent Type I ELM experiments were performed, but this has sadly not turned out to be the case, again preventing a study of the in-out ELM target energy loading asymmetries and comparison with the code results. The experiment-simulation comparison has thus been limited to the upstream profiles of density and temperature and target ion fluxes. Good agreement has been obtained in both cases, including on this occasion reasonable correspondence with the trends from fast total radiation measurements, unavailable for the Type III ELM. Two Type I ELMing H-modes at JET have been also simulated in this thesis. The first, with lower expelled energy ($\sim 200\text{ kJ}$) has been exhaustively modelled in earlier work with an alternative fluid-Monte Carlo code package EDGE2D-NIMBUS developed at JET over the past 20 years. In addition to the code-experiment benchmark, in this case, a comparison of the results of two major edge plasma code packages has also been performed. A comparison of this complexity (including

the all charged states of carbon impurities and a time-dependent model of the ELM) has not previously been attempted. Generally good agreement has been found between the results of the two codes, with the exception of the much lower temperature at the inner target during the ELM found in the SOLPS compared to EDGE2D-NIMBUS, a feature which is not understood.

The second JET ELM studied here expels an energy into the SOL which is close to the limit thought to be tolerable on ITER for acceptable divertor target lifetime. In common with the lower energy Type I ELM, an interesting feature of the simulations (also identified in the previously reported EDGE2D-NIMBUS work) is that an anomalous inward pinch velocity is found to be necessary to reproduce the pre-ELM density profile shape. This appears therefore to be a generic requirement for the JET pulses and is not required on TCV for either of the ELMs simulated. Nor was it necessary to reproduce pedestal profiles measured in low power Type I ELMing H-modes on ASDEX Upgrade.

Reasonable agreement with experimental profiles upstream and somewhat worse at the target plates have been found in both JET pulses. Unfortunately, the code-experiment comparison was limited since the experimentally measured ion fluxes of sufficient quality are available only for the lower ELM energy JET pulse and heat fluxes only for the higher ELM energy pulse. For the 200 kJ ELM, the radiated energy during the ELM is found to be in satisfactory agreement with experiment (by factor of ~ 1.5 less in SOLPS). In contrast, for the higher ELM energy, SOLPS about an order of magnitude lower radiation compared with measurements. One plausible explanation for this is the ablation or thermal decomposition of thick layers on the inboard target which accumulate there as a consequence of the erosion-migration processes. This is seen to occur experimentally only once a given ELM energy density threshold is exceeded. Such impurity release effects are not included in the SOLPS5 description of material erosion, which considers only physical and chemical sputtering.

Even if the absolute magnitudes are far from matched, SOLPS finds asymmetric radiation distributions favouring the inner target for both ELMs, following the experimental trend. In the lower ELM energy case this asymmetry is ~ 2 times stronger than in experiment, driven by the low inner target plasma temperature found in the simulation. Better agreement is found for the larger ELM. Whilst the situation with radiation is encouraging, the question of the in-out target power deposition asymmetry is of greater concern. It is now well known on JET that experiments in forward toroidal field observe an in-out power asymmetry favouring the outer target in between ELMs and that this situation reverses somewhat during the ELM. The ELM therefore behaves to some extent independently of the background plasma and is clearly driven by different physics in so far as the asymmetries are concerned. The SOLPS simulations find generally an in-out power asymmetry favouring the outer target in the pre-ELM phase and are in approximate agreement with experiment. During the ELM phase, however, the code, not surprisingly, predicts similar asymmetries. On TCV, simulations find, in contrast, energy asymmetries in favour of the inner target for both pre-ELM and ELM phases and for both Type III and I ELMs. This appears to be linked to the very different magnetic geometries of JET and TCV. The latter is very unconventional, with approximately equal parallel connection lengths from outboard midplane to targets and a very short X-point to inner target poloidal distance. In more conventional single null divertors, such as JET (and ITER), the midplane to inner target connection length is approximately twice that to the outer target and the X-point to target distances are similar for both targets. Since no drift terms are included in the SOLPS simulations, geometry would seem to be a dominant factor.

Concerning the observations of a reversal in energy asymmetries during the ELM, a recent development has been the suggestion that the ELM, in convecting plasma from pedestal to SOL regions, carries with it memory of the high toroidal rotation velocity known to characterise the H-mode pedestal on all devices. This hypothesis has been tested here in a

preliminary manner, and for the first time in this kind of simulation, by imposing a toroidal velocity inside the magnetic separatrix in the simulations and studying the radial transport of this toroidal momentum into the SOL. The parallel velocity has been imposed at the inner boundary of the simulation grid with positive values corresponding reversed toroidal field and negative to forward field. Applied in the first instance to the TCV Type III ELM, the indications are that transfer of this rotation into the SOL can drive target asymmetries in the direction seen experimentally, though there are significant negative consequences for the resulting target profiles in other parameters. Potential resolution of these difficulties would require protracted further study which has not been possible here.

References

- [1] Intergovernmental Panel on Climate Change (IPCC) special report on Carbon Dioxide Capture and Storage, 2005, Cambridge University Press, Cambridge, United Kingdom and New York, NY, USA, 442 pp., URL: <http://www.ipcc.ch>
- [2] International energy agency (IEA); URL: <http://www.iea.ch>;
- [3] European Fusion Development agreement (EFDA); URL: <http://www.efda.org>
- [4] EU Green Paper, “Towards a European Strategy for the Security of energy Supply” 2000
- [5] Intergovernmental Panel on Climate Change (IPCC) report, 2007, URL: <http://www.ipcc.ch>
- [6] IPCC, Special report on Emission Scenarios, IPCC, 2000, ISBN 92-9169-113-5
- [7] URL: <http://www.world-nuclear.org/info/inf01.html>
- [8] IPCC special report on carbon dioxide capture and storage, IPCC 2005, URL: www.ipcc.ch
- [9] A conceptual study of commercial fusion power plants, final report of European Fusion Power Plant Conceptual Study (PPCS), EFDA, April 2005; URL: http://www.efda.org/eu_fusion_programme/scientific_and_technical_publications/PPCS_overall_report_final.org
- [10] URL: <http://www.iter.org>
- [11] M.Q. Tran *et al.*, The potential of fusion as a future source of energy, Dec.2007 URL: <http://www.worldenergy.ch>
- [12] URL: <http://www.energyresearch.nl/energy-options/nuclear-fusion>
- [13] <https://lasers.llnl.gov>
- [14] R. A. Pitts *et al.*, Fusion the way ahead, *Physics World* **19** (2006) 20
- [15] F. F.Chen, *Introduction to plasma physics*, ISBN 0-471-55951-2, Plenum Press, New York, 1974
- [16] P.C. Stangeby, *The Plasma boundary of magnetic fusion devices*, Institute of physics publishing, Bristol and Philadelphia, 2000
- [17] R. Schneider *et al.*, *Contrib. Plasma Physics* **46** (1) (2006) 3
- [18] A. Kukushkin *et al.*, *Nuclear Fusion* **43** (2003) 716

- [19] A. Kukushkin *et al.*, *Nuclear Fusion* **45** (2005) 608
- [20] A. Loarte *et al.*, *Physica Scripta* **T128** (2007) 222
- [21] R. A. Pitts *et al.* *Plasma Phys. Control. Fusion* **47** (2005) B303
- [22] G. Federici *et al.* *Plasma Phys. Control. Fusion* **45** (2003) 1532
- [23] A. V. Chankin, *Journal of Nuclear Materials* **241-243** (1997) 199
- [24] W. Fundamenski *et al.*, *Journal of Nuclear Materials* **337-339** (2005) 305
- [25] J. D. Huba, *NRL Plasma Formulary*, Naval Research Laboratory, Washington DC
- [26] A. Bergmann, *Nuclear Fusion* **42** (2002) 1162
- [27] S. Chapman and T. G. Cowling, *Mathematical Theory of Non-uniform Gases*, Cambridge University Press, 1958
- [28] J. Wesson, *Tokamaks*, 3rd version, Oxford University Press, 2004
- [29] S. I. Braginskii, *Transport processes in Plasma*, Reviews of Plasma physics, Consultants Bureau New York 1965
- [30] R. Chodura, *Physics of Plasma-Wall interactions in Controlled Fusion*, editor D E Post and R Behirsch, New York Plenum, 1984, 99
- [31] M. A. Liebermann, *Handbook of Plasma Immersion, Ion Implantation and Deposition*, editor A. Anders, New York Wiley, 2000, 29
- [32] D. Tskhakaya *et al.*, *Theory of Fusion Plasmas* ed J.W.Connor *et al.*, Bologna Italy, Societa Italiana di Fisica, 2004, 97
- [33] G. D. Porter *et al.*, *Phys. Plasmas* **3** (5) (1996) 1967
- [34] G. D. Porter *et al.*, *Phys. Plasmas* **7**(9) (2000) 3663
- [35] A. Loarte, *Journal of Nuclear Materials* **241-243** (1997) 118
- [36] R. Simonini *et al.*, *Journal of Nuclear Materials* **196-198** (1992) 369
- [37] R. Schneider *et al.*, *Journal of Nuclear Materials* **196-198** (1992) 810
- [38] A. Loarte, *Journal of Nuclear Materials* **266-269** (1999) 1123
- [39] J. Horacek, Measurements of edge electrostatic turbulence in the TCV tokamak plasma boundary, *PhD thesis*, Centre de Recherches en Physique des Plasmas (CRPP), Lausanne, Switzerland, <http://library.epfl.ch/theses/> ; no 3524 (2006)

- [40] D. Bohm, *The characteristics of electrical discharges in magnetic fields*, editor A. Guthrie and R.K. Wakerling, McGraw-Hill, New York, 1949
- [41] B. LaBombard *et al.*, *Nuclear Fusion* **45** (2005) 1658
- [42] O. E. Garcia *et al.*, *Journal of Nuclear Materials* **363-365** (2007) 575
- [43] M. V. Umansky *et al.*, *Phys. Plasmas* **5** (9) (1998) 3373
- [44] M. V. Umansky *et al.*, *Phys. Plasmas* **6** (7) (1999) 2791
- [45] Atomic and plasma-materials interaction data for fusion, Supplements to Nuclear Fusion **2**, 1992, **3**, 1992, **4**, 1993, **6**, 1995
- [46] International Bulletin on Atomic Molecular Data for Fusion published by IAEA Vienna
- [47] J. Roth and C. Garcia-Rosales, *Nuclear Fusion* **36** (1996) 1647
- [48] J. Roth *et al.*, *Journal of Nuclear Materials* **337-339** (2005) 970
- [49] EIRENE manual, 2004, URL: <http://www.eirene.de>
- [50] H. Zohm *Plasma Phys. Control. Fusion* **38** (no 2) (1996) 105
- [51] J. Roth *et al.*, *Journal of Nuclear Materials* **390-391** (2009) 1
- [52] A. Loarte *et al.*, Power and particle fluxes at the plasma edge of ITER: Specifications and Physics Basis, 22th IAEA Fusion energy conference, 13.-18.10. 2008, Geneva, Switzerland, paper IT/P6-13
- [53] M. F. F. Nave *et al.*, *Nuclear Fusion* **37** (1997) 809
- [54] A. Kirk *et al.*, *Plasma Phys. Control. Fusion* **47** (2005) 315
- [55] C. Silva *et al.*, *Journal of Nuclear Materials* **337-339** (2005) 722
- [56] R. A. Pitts *et al.*, *Nuclear Fusion* **46** (2006) 82
- [57] A. Loarte *et al.*, *Plasma Phys. Control. Fusion* **44** (2002) 1815
- [58] S. Saarelma *et al.*, *Plasma Phys. Control. Fusion* **47** (2005) 713
- [59] F. Wagner *et al.*, *Phys. Rev. Lett.* **49** (1982) 1408
- [60] H. Zohm, *Plasma Phys. Control. Fusion* **38** (1996) 1213
- [61] J. W. Connor, *Plasma Phys. Control. Fusion* **40** (1998) 191
- [62] J. W. Connor, *Plasma Phys. Control. Fusion* **40** (1998) 531

- [63] J. W. Connor and H. R. Wilson, *Plasma Phys. Control. Fusion* **42** (2000) R1
- [64] W. Suttrop, *Plasma Phys. Control. Fusion* **42** (2000) A1
- [65] A. Becoulet *et al.*, *Plasma Phys. Control. Fusion* **45** (2003) A93
- [66] A. Herrmann *et al.*, *Journal of Nuclear Materials* **313-316** (2003) 759
- [67] T. Eich *et al.*, *Journal of Nuclear Materials* **337-339** (2005) 669
- [68] M. Becoulet *et al.*, *Journal of Nuclear Materials* **337-339** (2005) 667
- [69] G. T. A. Huysmans, *Plasma Phys. Control. Fusion* **47** (2005) B165
- [70] H. R. Wilson *et al.*, *Plasma Phys. Control. Fusion* **48** (2006) A71
- [71] A. W. Leonard *et al.*, *Plasma Phys. Control. Fusion* **48** (2006) A149
- [72] W. Fundamenski *et al.*, *Plasma Phys. Control. Fusion* **46** (2004) 233
- [73] H. R. Wilson *et al.*, *Phys. Plasmas* **9** (2002) 1277
- [74] S. C. Cowley *et al.*, *Plasma Phys. Control. Fusion* **45** (2003) A31
- [75] J. W. Connor *et al.*, *Physics of Plasmas* **5** (7) (1998) 2687
- [76] P. B. Snyder *et al.*, *Phys. Plasmas* **9** (2002) 2037
- [77] S. Saarelma *et al.*, *Plasma Phys. Control. Fusion* **42** (2000) A139
- [78] P. B. Snyder *et al.*, *Nuclear Fusion* **44** (2004) 320
- [79] L. L. Lao *et al.*, *Nuclear Fusion* **41** (2001) 295
- [80] R. O'Connell, Impurity fluid investigations on the COMPASS-D tokamak, *PhD Thesis*, University College, Dublin, 1996
- [81] V. B. Lebedev *et al.*, *Phys. Plasmas* **2** (1995) 3345
- [82] S-I. Itoh *et al.*, *Phys. Rev. Lett.* **76** (1996) 920
- [83] O. Pogutse *et al.*, Proceedings of 22nd EPS Conference on Controlled Fusion and Plasma Physics (Bournemouth), vol **19C** (1995) 247
- [84] T. Kass *et al.*, Proceedings of 24th EPS Conference on Controlled Fusion and Plasma Physics (Berchtesgaden), vol **21A** (1997) 1521
- [85] The ASDEX Team, *Nuclear Fusion* **29** (1989) 1959

- [86] G. T. A. Huysmans *et al.*, Proceedings of 22nd EPS Conference on Controlled Fusion and Plasma Physics (Bournemouth), vol **19C** (1995) 201
- [87] J. W. Connor *et al.*, *Phys. Plasmas* **5** (1998) 2687
- [88] Y-T. Lau, *Plasma Phys. Control. Fusion* **38** (1996) 1393
- [89] S. J. Fielding, *Plasma Phys. Control. Fusion* **38** (1996) 1091
- [90] O. Pogutse *et al.*, *Plasma Phys. Control. Fusion* **36** (1994) 1963
- [91] H. Sugama *et al.*, *Plasma Phys. Control. Fusion* **37** (1995) 345
- [92] A. Takayama *et al.*, *Plasma Phys. Control. Fusion* **38** (1998) 1411
- [93] B. Goncalves *et al.*, *Plasma Phys. Control. Fusion* **45** (2003) 1627
- [94] W. Fundamenski *et al.*, *Plasma Phys. Control. Fusion* **46** (2004) 233
- [95] D. L. Rudakov *et al.*, *Nuclear Fusion* **45** (2005) 1589
- [96] M. Endler *et al.*, *Journal of Nuclear Materials* **266-269** (1999) 84
- [97] M. Endler *et al.*, *Plasma Phys. Control. Fusion* **47** (2005) 219
- [98] T. Eich *et al.*, *Plasma Phys. Control. Fusion* **47** (2005) 815
- [99] J. Boedo *et al.*, *Phys. Plasmas* **12** (2005) 072516
- [100] N. Bian *et al.*, *Phys. Plasmas* **10** (2003) 671
- [101] O. E. Garcia *et al.*, *Phys. Rev. Lett.* **92** (2004) 154003
- [102] O. E. Garcia *et al.*, *Phys. Plasmas* **12** (2005) 062309
- [103] W. Fundamenski *et al.*, *Plasma Phys. Control. Fusion* **48** (2006) 109
- [104] A. Kirk *et al.*, *Plasma Phys. Control. Fusion* **47** (2005) 995
- [105] J. Marki *et al.*, *Journal of Nuclear Materials* **390-391** (2009) 801
- [106] A. Kirk *et al.*, *Plasma Phys. Control. Fusion* **46** (2004) 551
- [107] A. Kirk *et al.*, *Journal of Nuclear Materials* **390-391** (2009) 727
- [108] A. Herrmann *et al.*, *Plasma Phys. Control. Fusion* **46** (2004) 971
- [109] R. A. Pitts *et al.*, 22nd IAEA Fusion Energy Conference (FEC 2008), October 2008, Geneva, Switzerland

- [110] A. Loarte *et al.*, *Phys. Plasmas* **11** (2004) 2668
- [111] S. C. Cowley and H. R. Wilson, *Phys. Rev. Lett.* **92** (2004) 175006
- [112] C. K. Birdsall and A. B. Langdon, *Plasma Physics via Computer Simulation*, New York McGraw-Hill, 1985
- [113] T. Tajima, *Computational Plasma Physics*, New York Addison-Wesley, 1989
- [114] S. J. Zweben and R. W. Gould, *Nuclear Fusion* **25** (1985) 171
- [115] J. Boedo *et al.*, *Journal of Nuclear Materials* **337-339** (2005) 771
- [116] B. Beyer *et al.*, *Plasma Phys. Control. Fusion* **41** (1999) A757
- [117] D. A. D'ippolito *et al.*, *Phys. Plasmas* **9** (2002) 222
- [118] V. Naulin *et al.*, *New. J. Physics* **4** (2002) 28.1
- [119] W. Fundamenski *et al.*, *Nuclear Fusion* **45** (2005) 950
- [120] A. Loarte *et al.*, *Phys. Plasmas* **11** (2004) 2668
- [121] P. Tamain *et al.*, *Journal of Nuclear Materials* **390-391** (2009) 347
- [122] T. D. Rognlien *et al.*, *Contrib. Plasma Physics* **34** (1994) 362
- [123] G. J. Radford *et al.*, *Contrib. Plasma Physics* **36** (1996) 187
- [124] B. J. Braams, *A multi fluid code for simulation of the edge plasma in tokamaks*, EUR-FU/XII-80/87/68, 1987
- [125] K. Shimizu *et al.*, *Journal of Nuclear Materials* **390-391** (2009) 307
- [126] D. P. Coster, *Phys. Scripta* **T100** (2004) 7
- [127] D. P. Stotler and C. F. F. Karney, *Contrib. Plasma Phys.* **34** (1994) 392
- [128] E. Cupini *et al.*, *NIMBUS - Monte Carlo simulation of neutral particle transport in fusion devices*, EUR-FU/XII-324/9, 1984
- [129] R. Simononi *et al.*, *Plasma Phys. Control. Fusion* **33**(6) (1991) 653
- [130] D. Reiter, *PhD thesis*, Heinrich Heine Universitat Dusseldorf, Germany, 1984, KFA-Report, Jul-1947
- [131] H. Kawashima *et al.*, *Journal of Nuclear Materials* **363-365** (2007) 1498
- [132] R. Simonini *et al.*, *Contrib. Plasma Phys.* **34** (1994) 368

- [133] M. Baelmans, Code improvements and applications of a two-dimensional edge plasma model for toroidal devices, *PhD thesis*, Ecole Royale Militaire, Belgium, 1994
- [134] D. Reiter *et al.*, *Plasma Phys. Control. Fusion* **33** (1991) 1579
- [135] D. P. Stotler *et al.*, *Contrib. Plasma Phys.* **40**(3-4) (2000) 221
- [136] M. E. Rensink *et al.*, *Contrib. Plasma Phys.* **38** (1998) 325
- [137] A. Kukushkin, accepted for publication in *Contrib. Plasma Physics* 2010
- [138] D. P. Coster *et al.*, Proceedings of 19th IAEA Fusion Energy Conference, Lyon, France, IAEA-CN-94-TH/P2-13, 2002
- [139] SOLPS manual, homepage by D. Coster,
URL: <http://www.rzg.mpg.de/dpc/solps.html>
- [140] R. Marchand *et al.*, *Comp. Phys. Commun.* **96** (1996) 232
- [141] R. Schneider *et al.*, *Contrib. Plasma Phys.* **40**(4) (2000) 328
- [142] V. A. Rozhansky *et al.*, *Nuclear Fusion* **41**(4) (2001) 387
- [143] X. Bonnin *et al.*, *Journal of Nuclear Materials* **313-316** (2003) 909
- [144] L. L. Lao *et al.*, *Nuclear Fusion* **25**(11) (1985) 1611
- [145] F. Hoffmann and G. Tonetti, *Nuclear Fusion* **39**(10) (1988) 1871
- [146] P. C. Stangeby, “The plasma sheath” in “Physics of Plasma-Wall Interaction in Controlled Fusion Devices”, D. E. Post and R. Behrish editors, Plenum Press, New York, 1986, 41
- [147] D. E. Post and K. Lackner, “Plasma Models for Impurity Control Experiments” in “Controlled Fusion Devices”, D. E. Post and R. Behrish editors, Plenum Press, New York, 1986, 627
- [148] J. F. Luciani *et al.*, *Phys. Rev. Lett.* **51** (1983) 1664
- [149] M. Wischmeier, Simulating divertor detachment in the TCV and JET tokamaks, *PhD thesis*, Centre de Recherches en Physique des Plasmas (CRPP), Lausanne, Switzerland, <http://library.epfl.ch/theses/>; no 3176 (2004)
- [150] B. LaBombard *et al.*, *Phys. Plasmas* **8**(5) (2001) 2107
- [151] O. E. Garcia *et al.*, *Nuclear Fusion* **47** (7) (2007) 667
- [152] P. C. Stangeby and A. V. Chankin, *Phys. Plasmas* **2**(3) (1995) 707

- [153] C. Garcia-Rosales *et al.*, Proceedings of the 21th EPS Conference on Controlled Fusion and Plasma Physics, Montpellier, France, 1994. In E.Joffrin, P.Platz and P.E. Stott, editors, Europhysics Conference Abstracts, vol.**18B** part II, 718,Geneva,1994,EPS.
- [154] J. Küppers, *Surface Science Reports* **22**(7-8) (1995) 249
- [155] L. L. Lengyel, *Analysis of radiating plasma boundary layer plasmas*, Technical report IPP-1/191, IPP, Garching, Germany, September 1981
- [156] P. L. Bhatnagar *et al.*, *Physical Review* **94**(3) (1954) 511
- [157] C. May, *PhD Thesis*, Heinrich Heine Universitat, Germany, 1997, Jul-3486
- [158] V. Kotov *et al.*, *Plasma Phys. Control. Fusion* **50** (2008) 105012 (20pp)
- [159] E. D. Cashwell and C. J. Everett, *A practical manual on the Monte Carlo method for random walk problems*, Pergamon Press, New York, 1959
- [160] J. Spanier and E. M. Gelbard, *Monte Carlo principles and neutron transport problems*, Addison-Wesley, 1969
- [161] R. K. Janev and W. D. Langer, *Elementary processes in hydrogen and helium plasmas*, Springer Verlag, Heidelberg, 1987
- [162] W. Eckstein, *Computer simulation of ion-solid interactions*, In Springer Series in Material Science, Vol.**10**. Springer, Berlin, 1991
- [163] M. Warrier *et al.*, *Comp.Phys. Commun.* **160**(1) (2004) 46
- [164] Private communication with Dr. X. Bonnin
- [165] S. P. Hirshman and D. J. Sigmar, *Nuclear Fusion* **21**(9) (1981) 1079
- [166] URL: <https://citrix.jet.efda.org/>
- [167] D. P. Coster, Time dependent SOL modelling with SOLPS, In R.Koch and S. Lebedev, editors, Europhysics Conference Abstracts (CD-ROM, Proceedings of 30th EPS Conference on Controlled Fusion and Plasma Physics, St. Petersburg, 2003), volume **27A**, P-1.169, Geneva, 2003, EPS
- [168] <http://www.mathworks.com>
- [169] <http://www.openmosixview.com>
- [170] F. Hoffmann *et al.*, *Plasma Phys. Contr. Fusion* **36** (1994) B277
- [171] R. A. Pitts *et al.*, *Journal of Nuclear Materials* **241-243** (1997) 867
- [172] A. Kallenbach *et al.*, *Plasma Phys. Control. Fusion* **46** (2004) 431

- [173] B. Gulejova *et al.*, SOLPS5 simulations of Type I ELMI H-mode at JET, *Journal of Nuclear Materials* **390-391** (2009) 412
- [174] R. Behn *et al.*, *Plasma Phys. Control. Fusion* **49** (2007) 1289
- [175] A. Bortolon *et al.*, *Phys. Rev. Lett.* **97** (2006) 235003
- [176] J. Marki, presentation to high heat flux Special Expert Working Group of EU PWI Task Force, Slovenia, 1.-2.10. 2009
- [177] R. A. Pitts *et al.*, *Nuclear Fusion* **43** (2003) 1145
- [178] J. Horacek *et al.*, *Journal of Nuclear Materials* **313-316** (2001) 931
- [179] R. A. Pitts and P.C. Stangeby, *Plasma Phys. Control. Fusion* **32** (13) (1990) 1237
- [180] R. D. Monk *et al.*, *Journal of Nuclear Materials* **241-243** (1997) 396
- [181] G. F. Matthews, *Plasma Phys. Control. Fusion* **36** (1994) 1595
- [182] M. Kocan *et al.*, *Plasma Phys. Control. Fusion* **50**(12) (2008) 125009
- [183] A. W. Degeling *et al.*, *Rev. Sci. Instrum.* **75**(10) (2004) 4139
- [184] M. Anton *et al.*, *Plasma Phys. Control. Fusion* **38** (1996) 1849
- [185] G. Veres *et al.*, *Journal of Nuclear Materials* **363-365** (2007) 1104
- [186] J. Marki *et al.*, *Journal of Nuclear Materials* **363-365** (2007) 382
- [187] A. Herrmann *et al.*, *Journal of Nuclear Materials* **313-316** (2003) 759
- [188] K. Ereints *et al.*, *Plasma Phys. Control. Fusion* **46** (2004) 1757
- [189] R. Pasqualotto *et al.*, *Rev. Sci. Instrum.* **75** (2004) 3891
- [190] H. Salzmann *et al.*, *Rev. Sci. Instrum.* **59** (1988) 1451
- [191] C. Gowers *et al.*, *J. Plasma Fusion Res.* **76** (2000) 874
- [192] P. Buratti and M. Zerbini, *Rev. Sci. Instrum.* **66** (1996) 4208
- [193] D. V. Bartlett *et al.*, in Electron Cyclotron Emission and Electron Cyclotron Resonance Heating, Borrego Springs, California, vol. **EC-9**, 511, World Scientific Publishing, Singapore (1995)
- [194] E. de la Luna *et al.*, *Rev. Sci. Instrum.* **75** (2004) 3831
- [195] M.G. von Hellermann *et al.*, *Rev. Sci. Instrum.* **61** (1990) 3479

- [196] G. F. Matthews *et al.*, *Plasma Phys. Control. Fusion* **36** (1994) 1595
- [197] T. Eich *et al.*, *Plasma Phys. Control. Fusion* **49** (5) (2007) 573
- [198] L. C. Ingesson *et al.*, *Journal of Nuclear Materials* **313-316** (2003) 1173
- [199] K. F. Mast *et al.*, *Rev. Sci. Instrum.* **56** (1985) 969
- [200] A. Huber *et al.*, *Fusion Engineering and Design* **82** (2007) 1327
- [201] R. A. Pitts *et al.*, *Journal of Nuclear Materials* **390-391** (2009) 755
- [202] A. Huber *et al.*, *Journal of Nuclear Materials* **390-391** (2009) 830
- [203] Y. Nishimura *et al.*, *Contrib. Plasma Phys.* **4**(2-4) (2002) 379
- [204] Y. Nishimura *et al.*, Proceedings of 29th European Physical Society Conference on Controlled Fusion and Plasma Physics, Montreux, Switzerland, June 2002, vol. **26B**, 1110, Geneva, 2002. EPS
- [205] B. J. Braams, *Contrib. Plasma Phys.* **36** (2-3) (1996) 276
- [206] R. Schneider *et al.*, *Contrib. Plasma Phys.* **40** (3-4) (2000) 328
- [207] V. A. Rozhansky *et al.*, *Contrib. Plasma Phys.* **40** (3-4) (2000) 423
- [208] D. P. Coster, Proceedings of 30th EPS, St. Petersburg, ECA **27A**, 1.169 (2003)
- [209] B. Gulejova *et al.*, SOLPS5 modelling of the Type III ELMing H-mode at TCV, *Journal of Nuclear Materials* **363-365** (2007) 1037
- [210] A. Alfier *et al.*, Proceedings of 32th EPS, Tarragona, ECA **29C**, 2.002 (2005)
- [211] A. V. Chankin *et al.*, *Plasma Phys. Control. Fusion* **48** (2006) 836
- [212] W. Fundamenski *et al.*, *Nuclear Fusion* **47** (2007) 417
- [213] G. V. Pereverzev *et al.*, *Nuclear Fusion* **32** (1992) 1361
- [214] O. E. Garcia *et al.*, *Journal of Nuclear Materials* **363-365** (2007) 575
- [215] J. P. Graves *et al.*, *Plasma Phys. Control. Fusion* **47** (3) (2005) L1
- [216] M. V. Umansky *et al.*, *Phys. Plasmas* **6**(7) (1999) 2791
- [217] A. Y. Pigarov *et al.*, *Phys. Plasmas* **9**(4) (2002) 1287
- [218] A. Y. Pigarov *et al.*, *Journal of Nuclear Materials* **313-316** (1-3) (2003) 1076
- [219] A. Y. Pigarov *et al.*, *Contrib. Plasma Phys.* **44**(1-3) (2004) 228

- [220] O. E. Garcia *et al.*, *Nuclear Fusion* **47** (7) (2007) 667
- [221] Dr. D. P. Coster, private communication
- [222] R. A. Pitts *et al.*, *Journal of Nuclear Materials* **337-339** (2005) 146
- [223] I. H. Hutchinson *et al.*, *Plasma Phys. Control. Fusion* **37** (1995) 1389
- [224] A. Loarte, 18th IAEA Fusion energy conference, IAEA – CN-77, 4.-10.10.2000, Sorrento, Italy, paper ITERP/11(R)
- [225] F. Subba *et al.*, Proceedings of 30th EPS Conference on Controlled Fusion and Plasma Physics, July 2003, St. Petersburg, **27A**, P-2.85
- [226] B. Gulejova *et al.*, Time-dependent modelling of ELMing H-mode at TCV with SOLPS5, Proceedings of 34th EPS, Warsaw, Poland, 2007
- [227] D. P. Coster *et al.*, *Journal of Nuclear Materials* **241-243** (1997) 690
- [228] D. P. Coster *et al.*, Proceedings of 21st European Conference on Controlled Fusion and Plasma Physics, Montpellier, France, 1994, vol.**18B** part II, 846, Geneva, 1994, EPS
- [229] R. Schneider *et al.*, *Plasma Phys. Control. Nuclear Fusion Research* **2** (1996) 456
- [230] D. J. Sigmar *et al.*, *Contrib. Plasma Phys.* **36** (2-3) (1996) 230
- [231] O. V. Batishchev *et al.*, *Contrib. Plasma Phys.* **36** (2-3) (1996) 225
- [232] D. Tskhakaya *et al.*, *Contrib. Plasma Phys.* **48** (1-3) (2008) 89
- [233] D. Tskhakaya and R. Schneider, *Journal Comp. Physics* **225** (1) (2007) 829
- [234] D. Tskhakaya *et al.*, *Contrib. Plasma Phys.* **48** (1-3) (2008) 121
- [235] D. Tskhakaya *et al.*, Proceedings of 34th EPS, Warsaw, Poland, July 2007
- [236] R. A. Pitts *et al.*, *Nuclear Fusion* **47** (2007) 1437
- [237] D. Tskhakaya *et al.*, *Journal of Nuclear Materials* **390-391** (2009) 335
- [238] Private communication with Dr. D. Coster
- [239] Private communication with Dr. D. Tshkakaya
- [240] L. Porte *et al.*, *Nuclear Fusion* **47** (8) (2007) 925
- [241] G. Veres *et al.*, *Journal of Nuclear Materials* **390-391** (2009) 835

- [242] T. Eich *et al.*, *Journal of Nuclear Materials* **390-391** (2009) 760
- [243] P. de Vries *et al.*, *Nuclear Fusion* **48** (2008) 065006.
- [244] M. Fenstermacher *et al.*, *Plasma Phys. Control. Fusion* **45** (2003) 1597
- [245] A. W. Leonard *et al.*, *Plasma Phys. Control. Fusion* **44** (6) (2002) 945
- [246] V. A Rozhansky *et al.*, *Journal of Nuclear Materials* **290-293**(3) (2001) 710
- [247] K. Ertl *et al.*, *Journal of Nuclear Materials* **128-129** (1984) 163
- [248] X. Garbet *et al.*, *Phys. Rev. Lett.* **91** (2003) 035001
- [249] D. P. Coster *et al.*, *Journal of Nuclear Materials* **337-339** (2005) 366
- [250] T. Eich *et al.*, *Journal of Nuclear Materials* **363-365** (2007) 989
- [251] Private communication Dr. A. Huber
- [252] T. Hirai *et al.*, *Journal of Nuclear Materials* **390-391** (2009) 751
- [253] R. A. Pitts, invited paper to 12th Plasma facing materials and components for fusion applications PFMC, Julich, Germany, 11.-14.5.2009, accepted for publication in *Physica Scripta*
- [254] A. Huber *et al.*, Proceedings of 36th EPS, 2009, Sofia, Bulgaria
- [255] Private communication with Dr. T. Eich
- [256] S. Devaux *et al.*, Proceedings of 36th EPS, 2009, Sofia, Bulgaria
- [257] E. Gauthier *et al.*, *Journal of Nuclear Materials* **363-365** (2007) 1026

Acknowledgments

This thesis was born with a lot of pain, however I do not regret anything and there was no one single moment when I would have been tempted not to continue. I enjoyed the PhD work and it has been an honor for me to work for fusion. I feel a deep gratitude to many people who have played an important role on my way to accomplishing this work.

I have had the privilege of spending the last five years working under the supervision of Dr. Richard Pitts. It is rare to see such a motivating and energetic person, always dedicated and passionate about his work and moreover extremely efficient. I am sincerely grateful to him for giving me the opportunity to work with him, for his extraordinary guidance, for being always there when I needed help, for all the precious time he spent with me patiently explaining the edge plasma physics and discussing my results. I thank him for always being able to give me the motivation to pursue my work and helping to find the sense of it. I especially appreciate the fact that even when no longer at CRPP during the last one and a half years, Richard did not abandon his students and despite his excessive workload at ITER, I got a lot of help from him, in particular during the most difficult period - writing my thesis. I hold in the highest esteem all the time, energy and effort which he gave to the reading and correcting of the first draft, mostly in his “free time”, which consequently did not exist during these four exhausting months. To me Richard Pitts is a real SUPERvisor. It is not only the PhD which I have obtained thanks to him. His way of being strict, demanding and caring was doubtless a very valuable life lesson.

This work wouldn't have been possible without the considerable help of my “SOLPS supervisor”, Dr. David Coster, who has always answered all of my questions patiently and who always found solutions to my problems with the code. I highly respect his great expertise, broad knowledge of the code and of physics but also his professional attitude.

I am also grateful to Xavier Bonnin. Apart from his being highly competent in numerical modeling and physics, I always appreciated his kindness and willingness to help. My thanks go also to David Tskhakaya for our enriching collaboration, his PiC simulations, explanations and answers to all my questions. I also thank Marco Wischmeier, who introduced the SOLPS code to me.

I acknowledge the CRPP team, where many colleagues contributed to my work. I would like to thank those who provided me with the good advice and experimental data to constrain the code simulations and whose work was also vital to this thesis. In the TCV team my thanks go to Jan Horacek for the Langmuir probes data, Roland Behn and Andreas Pitzschke for the Thomson scattering data, Janos Marki for his infrared camera data, Gabor Veres and Balázs Tál for the tomographic inversion of the bolometry data, Attila Benzce for the Langmuir probes data and Olivier Sauter and Elina Asp for the ASTRA code simulations.

My thanks go also to colleagues outside of CRPP, like Arne Kallenbach for EDGE2D/Nimbus simulation data and discussions, to colleagues who have provided me with analysis of the JET experimental data needed for this work, namely Marc Beurskens for Thomson scattering data, Stefan Jachmich for Langmuir probes data, Thomas Eich for infrared camera data and Alexander Huber for the tomographic inversion of the bolometry data and always a kind help.

During my PhD I have had a chance to visit other fusion research institutes and participate in international conferences where I met many colleagues who have also contributed to my work, for which I am truly thankful. It has been always such a pleasure for me to work with colleagues from IPP Garching and from JET, especially members of Task Force E. I would like to thank to all the participants of the regular modeling month at JET, which I especially enjoyed because it gave me an opportunity to work with my favorite members of the fusion community – “the modelers”.

I would like to mention the two colleagues Jančis, who have shared an office with me during my PhD years. I would like to thank my favourite Czech colleague Jan Horáček for always being very helpful, for all his useful Matlab routines, discussions, friendship and fun. I am thankful also to my favourite Hungarian colleague Janos Marki for being a good officemate, fruitful discussions and his original way to cheer up. I thank also to my short-term officemate and favourite English colleague Robert Tye for nice discussions and his friendship.

I would like to express my thanks also to colleagues from other fusion institutes, in particular Christian Konz, Darren McDonnald, Uron Kruezi, Thomas Eich and Sukho Hong for their help, advice, discussions and friendship.

I am grateful to Xavier Llobet and Pierre Etienne for their technical help with the computers, to the CRPP electronic workshop team, especially Philippe Marmillod, Pierre Lavanchy and Blaise Marletaz for their help at the beginning of my thesis with the AXUV diagnostics and to Edith Grueter for help with the administrative tasks.

I am thankful to Olivier Sauter for becoming the co-director of my thesis at CRPP after Richard's departure to ITER and to Roland Behn and Francesco Piras for their interest in my work. I also thank Nicolas Mellet for translating the abstract, to Xavier Llobet, Silvano Gnesin and Edith Grueter for their support during the day of my thesis submission and to Basil Duval for appearing at the right moment in our office. I am also grateful to Yves Martin for giving me an opportunity to participate in the organization of 22nd IAEA FEC conference.

My thanks go to Dr. Kurt Appert and Prof. M. Quang Tran for giving me the opportunity to work at CRPP.

I am also grateful to Prof. Olivier Schneider, Dr. David Coster, Dr. Andre Kukushkin, Dr. Jonathan Graves, Dr. Olivier Sauter and Dr. Richard Pitts for accepting to be the members of my thesis jury.

Very special thanks belong to my beloved family and friends, who were always there for me and who rendered even the most difficult moments bearable. I can never thank my parents enough for everything they gave me, for their inexhaustible support and the confidence that they always had in me. Despite the distance, my mother lived all the good and hard times with me and suffered together with me. Finishing this thesis was a happy event not only for me.

In spite of the fact that the last few months of writing were the most difficult in my life, I was the luckiest girl because I had an angel who always protected me and gave me the energy to fight, Flavien. MERCI!

This work was partly supported by the Swiss National Science Foundation.

Curriculum vitae

St. Paul 10, 1004 Lausanne
+41 (0) 76 414 9687
barbora.gulejova@epfl.ch
crppwww.epfl.ch/~gulejova

14.12.1980
slovak
single



Academic Qualification

➤ **Ecole Polytechnique Fédérale de Lausanne**

PhD at Centre de Recherches en Physique de Plasmas (CRPP) **2004-2009**

➤ **Comenius University Bratislava, Faculty of Mathematics, Physics and Informatics**

	1999-2004
<i>RNDr. degree in Plasma Physics</i>	Sept. 2004
<i>Master degree in Physics</i>	June 2004
<i>Diploma in Pedagogic</i>	June 2004
<i>Bachelor degree in Physics</i>	June 2002

➤ **Comenius University Bratislava, Faculty of Management**

	1999-2004
<i>Master degree in Management</i>	June 2004
<i>Bachelor degree in Management</i>	June 2002

Languages (spoken and written)

English
French
German
Slovak
Czech
